Doctoral Thesis
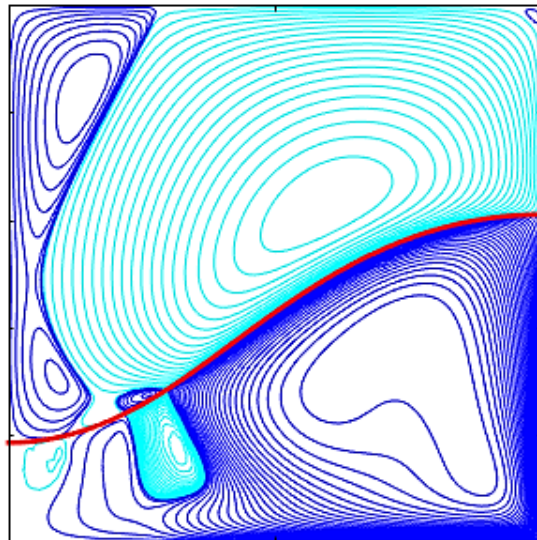
Global stability analysis of two-fluid flows

Author: Luis Miguel Carrión Matamoros
Supervisor: Miguel Ángel Herrada Gutiérrez

Departmento de Ingeniería Aeroespacial y Mecánica de Fluidos
Escuela Técnica Superior de Ingeniería
Universidad de Sevilla
2019

Doctoral Thesis

Global stability analysis of two-fluid flows

Author:

Luis Miguel Carrión Matamoros

Supervisor:

Miguel Ángel Herrada Gutiérrez

A thesis submitted in fulfillment of the requirements
for the degree of Doctor of Philosophy

Departamento de Ingeniería Aeroespacial y Mecánica de Fluidos

Escuela Técnica Superior de Ingeniería

Universidad de Sevilla

Sevilla, 2019

Tesis doctoral: Global stability analysis of two-fluid flows

Autor: Luis Miguel Carrión Matamoros

Tutor: Miguel Ángel Herrada Gutiérrez

El tribunal nombrado para juzgar el Proyecto arriba indicado, compuesto por los siguientes miembros:

Presidente:

Vocales:

Secretario:

Acuerdan otorgarle la calificación de:

Sevilla, 2019

El Secretario del Tribunal

A Dios, por su bendición.
A mi esposa Daniela.
A mis padres y hermanos.

Acknowledgements

Resumen

La presente tesis doctoral es un compendio de siete estudios dedicados al análisis numérico de la dinámica no lineal y la estabilidad lineal global de flujos de dos fluidos separados por una interfaz continua. Para esto se implementa la técnica numérica eficiente computacional desarrollada por Herrada y Montanero [1] para el estudio de la dinámica de sistemas capilares de un solo fluido. En vez de usar técnicas de aproximación para simplificar las ecuaciones de Navier-Stokes de flujos de dos fluidos obteniendo flujos básicos que dependen de una sola dirección, la aplicación de este método tiene la capacidad de modelar el conjunto completo de ecuaciones de gobierno de ambos fluidos para obtener el comportamiento hidrodinámico y el análisis de estabilidad lineal global.

El primer capítulo es una introducción para explicar los diferentes tipos de flujos multifásicos y su importancia en la industria y la tecnología. Aquí, se presta especial atención a trabajos anteriores para el análisis de estabilidad lineal global de flujos de dos fluidos, en particular aquellos que contienen una interfaz libre. También se revisan los métodos numéricos para simularlos, así como los tipos de discretización espacial.

El Capítulo 2 se centra en el estudio de un flujo de aire y agua como una aplicación en biorreactores aéreos. Este flujo estable de dos fluidos y axisimétrico es impulsado por un disco superior giratorio en un cilindro vertical sellado. La investigación demuestra la aparición de una burbuja de rotura de vórtice que aparece en el centro inferior y que se expande hacia la interfaz a medida que aumenta el número de Reynolds. Además, regiones de circulación meridional en el sentido de las agujas del reloj aparecen en el agua y en el aire, las cuales están separadas por una delgada capa de circulación en sentido contrario a las agujas del reloj adyacente a la interfaz en la región del agua. La novedad de este estudio muestra que el flujo se vuelve inestable para números de Reynolds mayores que aquellos en los que emerge la burbuja de rotura de vórtice y la capa delgada de circulación.

En el capítulo 3 es analizado la topología del flujo y el comportamiento de estabilidad que se ocultan en el trabajo experimental desarrollado por Tsai et al. [2]. El disco giratorio superior de un cilindro vertical sellado, lleno de agua y aceite de soja, genera la circulación meridional y el flujo de rotación. El análisis numérico demuestra la forma de la interfaz de superficie plana y la aparición de la ruptura del vórtice en ambos fluidos al aumentar la fuerza de rotación. También se encontró que la inestabilidad del flujo estable axisimétrico que emerge en el agua es de tipo cizalla.

Con respecto al capítulo 4, al igual que en el anterior, se analiza el flujo de rotación de dos fluidos que fue estudiado experimentalmente por Fujimoto y Takeda [3], con el objetivo de descubrir las topologías de flujo y las inestabilidades hidrodinámicas. En este caso, el contenedor cilíndrico vertical se llena con agua y aceite de silicona y sus movimientos se establecen mediante la tapa giratoria superior. El estudio numérico reproduce con precisión las complejas formas de la interfaz, llamadas en la investigación experimental como joroba, cúspide, monte Fuji y campana. Además de que la inestabilidad del flujo axisimétrico es de tipo cizalla, se encuentra que la energía de perturbación se concentra en la profundidad del agua, lo que explica la no dependencia de la forma de la interfaz en la inestabilidad.

Los patrones de múltiples vórtices y la estabilidad de un flujo de rotación se investigan en el capítulo 5. A diferencia de los casos anteriores, se utiliza un disco giratorio inferior y aire y agua como fluidos de trabajo. En base a la fracción de volumen de agua, se encuentran diferentes escenarios topológicos con características interesantes, como cadenas de vórtices de aire y agua y

vórtices de aire con forma de anillo de burbujas. Además, se demuestra que los movimientos de múltiples vórtices son estables y las inestabilidades aparecen cuando la interfaz se coloca cerca de la parte inferior o superior del contenedor.

En relación al capítulo 6, este se dedica al análisis de un sistema de aire y agua axisimétrico y estable, impulsado por un disco superior giratorio en un contenedor semiesférico. En este estudio se demuestra que el aumento de la fuerza de rotación produce un patrón de tres vórtices, donde la circulación de aire y la co-circulación de agua están separadas por una región delgada de agua que gira en sentido contrario. Además, se encuentra que la perturbación de energía crítica se localiza en la región del aire el cual es de tipo cizalla.

Finalmente, en los dos últimos capítulos, se estudia un puente líquido bajo los efectos de vibraciones de pequeña amplitud, surfactantes insolubles superficiales, gradientes térmicos y fuerza gravitacional. Específicamente, el capítulo 7 analiza la interacción entre las no homogeneidades de concentración de surfactante interfacial debido al flujo de transmisión y la convección de Marangoni. Como consecuencia, se encuentra que los patrones de flujo tienen un comportamiento no monótono al aumentar el número de Marangoni. Además, se ve que la intensidad del flujo de transmisión en la interfaz produce dos regímenes definidos cuando la amplitud de la fuerza se intensifica. En el capítulo 8, se estudia la estabilidad de la convección térmica para altos números de Prandtl con deformación de la superficie libre. Se muestra que las deformaciones dinámicas de la superficie libre del flujo base son muy parecidos a los experimentos previos y colapsan en una curva al normalizarse con su respectivo número capilar. Además, un efecto mínimo en el análisis de estabilidad es causado por la deformación interfacial.

Abstract

The present thesis is a compendium of seven studies devoted to the numerical analysis of nonlinear dynamics and global linear stability of two-fluid flows separated by a continuous interface. The computationally efficient numerical technique developed by Herrada and Montanero [1] is implemented to study the dynamics of capillary one-fluid systems. Instead of using approximation techniques to simplify the two-fluid flows Navier-Stokes equations, the application of this method has the capability of modelling the complete set of governing equations for both fluids in order to obtain the hydrodynamics behavior and the global linear stability analysis.

The first chapter is an introduction to explain the different types of multiphase flows and their importance in the industry and technology. Here, special attention is paid to previous works for global linear stability analysis of two-fluid flows, in particular those with interfaces. It is also reviewed the numerical methods for simulating them as well as the spatial discretization techniques.

Chapter 2 is focused on the study of an air-water swirling flow as an application in aerial bioreactors. This steady axisymmetric two-fluid flow is driven by a rotating top disk in a vertical sealed cylinder. It is found that a vortex breakdown bubble appears at the bottom center and spread out to the interface as Reynolds number increases. Then, clockwise meridional circulation regions appear in water and air, which are separated by a thin anticlockwise circulation layer adjacent to the interface in water. The novelty of this study shows that the flow becomes unstable for larger Reynolds numbers than those at which vortex breakdown bubble and thin circulation layer emerge.

In chapter 3, the topological flow structure and stability behaviour hidden in the experimental work developed by Tsai et al. [2] is analysed. The upper rotating disk of a sealed vertical cylinder, filled with water and soybean oil, generates the meridional circulation and swirl flow. The numerical analysis proves the flattop interface shape and the vortex breakdown emergence in both fluids by increasing the rotation strength. It is also shown that the instability of the steady axisymmetric flow emerging in the water fluid is of the shear-layer type.

With regard to chapter 4, as with to the previous one, the two-fluid swirling flow experimentally studied by Fujimoto and Takeda [3] is analyzed in order to unveil the flow topologies and hydrodynamic instabilities. In this case, the vertical cylindrical container is filled with water and silicone oil and their motions are set by the upper rotating lid. The numerical study accurately reproduces the complex interface shapes, called in the experimental investigation as hump, cusp, Mt. Fuji and bell. Besides the instability of the axisymmetric flow is of shear-layer type, it is found that the disturbance energy is concentrated in the water depth, explaining the no-dependency of interface shape on the instability.

Multi-eddy patterns and stability of a whirlpool flow is investigated in chapter 5. Unlike the preceding cases, use is made of a bottom rotating disk and air and water as working fluids. Relying on the water volume fraction, it is found different topological scenarios with interesting characteristics such as zipper-like chains of air and water eddies and bubble-ring air eddies. In addition, it is shown that multi-eddy motions are stable and the instabilities appear when the interface is placed near either bottom or top of the container.

Concerning chapter 6, it is dedidated to the analysis of a steady axisymmetric air-water driven by a rotating top disk in a semispherical container. It is found that the increasing of rotation strength produces a three-eddy pattern, where the air circulation and the water co-circulation are separated by a thin region of water counter-circulation. Moreover, the critical energy disturbance is

located in the air region, being of shear-layer type.

Finally, in the two last chapters, liquid bridges under the effects of small-amplitude vibrations, insoluble surfactants, thermal gradients and gravitational force are studied. Specifically, chapter 7 analyses the interaction between the interfacial surfactant concentration inhomogeneities due to streaming flows and Marangoni convection. It is found that the flow patterns have nonmonotone behavior with increasing Marangoni number. Furthermore, it is seen that the strength of the streaming flow at the interface produces two defined regimes when force amplitude intensifies. In chapter 8, the stability of the thermal convection for high Prandtl numbers with free surface deformation are studied. It is shown that the dynamical free surface deformations of the base flow are in good agreedment with previous experiments and collapse into one curve when normalizing with their respective Capillary numbers. Besides, a small effect on the liquid bridge stability is caused by the interfacial deformation.

Contents

List of Figures

line) and of the axial component wL of the Lagrangian mean velocity (dots). These quantities were evaluated at the liquid bridge position $(r = 1, z = 3\Lambda/2)$. The component wL was obtained from the difference between the fluid element positions at the instants t and t-T [Eq. (7.24)]. The simulation was conducted for $\Lambda = 1.25$, V = 1, C = 0.01, Ma = 0, $\omega = 2.1$, and B = 0.005. 101

List of tables

1. INTRODUCTION

Multiphase flows are systems in which different phases in solid, liquid or gas state coexist and interact simultaneously. These phenomena can be observed in a variety of industrial and technological applications, such as fluidized beds, cavitating flows, pollution controls, heat exchangers, aerosols, plasma spray coating, synthesis of nanophase materials, abrasive water-jet cutting, electrophotographic processes, to mention a few. Environmental phenomena are also typical multiphase flows, for instance, rain, snow, fog, avalanches, mudslides, sediment transport debris flows and countless more. Most biological and medical processes like blood flow, cell-fluid interface interaction, microbe locomotion, gas exchange, etc, have multiphase flows inherent characteristics.

As mentioned above, multiphase flows are presented in a variety of processes, but their complex behavior makes the analysis and study a challenge task, due to mainly the interface interaction, type of fluid, change of phases, chemical reactions and size of particles. In order to explore these phenomena, it is necessary to determine the topologies [4] involved in, which can be disperse flows and separated flows. In disperse flows [5], small particles, bubbles or droplets are spread in a continuous fluid, whereas separated flows are composed by different continuous phases limited each other by interfaces [6], [7]. Figure 1.1 depicts the different types of multiphase flows and their industrial and technological applications.

The definition of the topology is an important previous step to model the physical behavior of multiphase flows, which can be studied experimentally, theoretically and computationally. In the first one, it is used a laboratory equipment that is instrumented adequately so that the main physical characteristics can be obtained [8]; generally, empirical correlations are acquired from this experimental process. In the second approach, mathematical mechanistic equations [9], which are generally based on the main characteristics of the phenomenon, are utilized in order to model the physical behavior. Finally, computational approach studies the multiphase phenomena by applying numerical methods so as to solve the differential equations that govern them [10].

1.1 Hydrodynamic linear stability of multiphase flows

One of the most important branches of the fluid dynamics is the hydrodynamic stability, in which perturbations around a basic state flow are studied in order to analyze the transition from a stable to unstable condition[11], [12], . Basically, there are five means [13] to establish a hydrodynamic stability study: through the natural phenomena and laboratory experiments, numerical experiments, application of linear and weakly nonlinear theory, qualitative theory analysis of bifurcation and chaos and strongly nonlinear theory approach.

The study in the present thesis is devoted to the analysis of modal linear stability of two-fluid flows with a continuos interface. In this approach, the variables of the flow system such as velocity, pressure or temperature are decomposed into a steady (base flow) and an unsteady part

(perturbation), the latter being approximated by small amplitude and phase functions. These anzats, represented by $\mathbf{v}(x,t) = \bar{\mathbf{v}}(\mathbf{x}) + \varepsilon \hat{\mathbf{v}}(x,t)$ for the velocity with $\varepsilon \ll 1$ and x,t as the spatial coordinates and time respectively, are replaced into the governing equations. The resulting equations are subtracted from the base flow and the terms in ε^2 are dropped in order to yield the linearized perturbation equations. It is worth mentioning that the perturbation is considered as a superposition of many waves that do not interfere with each other.
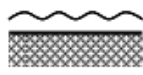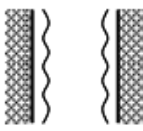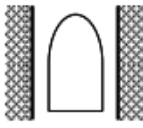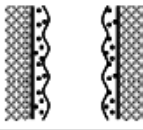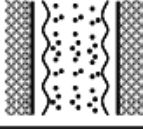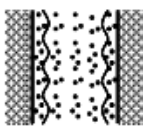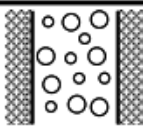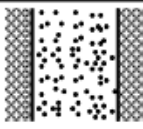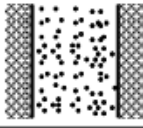
Class	Typical regimes	Geometry	Configuration	Examples
Separated flows	Film flow		Liquid film in gas Gas film in liquid	Film condensation Film boiling
	Annular flow		Liquid core and gas film Gas core and liquid film	Film boiling Boilers
	Jet flow		Liquid jet in gas Gas jet in liquid	Atomization Jet condenser
Mixed or Transitional flows	Cap, Slug or Churn-turbulent flow		Gas pocket in liquid	Sodium boiling in forced convection
	Bubbly annular flow		Gas bubbles in liquid film with gas core	Evaporators with wall nucleation
	Droplet annular flow		Gas core with droplets and liquid film	Steam generator
	Bubbly droplet annular flow		Gas core with droplets and liquid film with gas bubbles	Boiling nuclear reactor channel
Dispersed flows	Bubbly flow		Gas bubbles in liquid	Chemical reactors
	Droplet flow		Liquid droplets in gas	Spray cooling
	Particulate flow		Solid particles in gas or liquid	Transportation of powder

Figure 1.1 Types of multiphase flows [14]

Based on the flow's response to the perturbation or impulse, it can be identified both a stable and

an unstable flow. In the former one, the perturbation decays toward the base state in every direction from the source point of impulse. Conversely, if there is a growing effect of the perturbation along at least one ray emanating from the point of impulse, the flow is considered unstable.

The modal linear stability theories can be classified as: local, nonlocal and global analysis [15]. Local stability analysis focuses on flows that vary slowly in one spatial direction or parallel flows [16], [17], where the basic flow is considered homogeneous along two spatial directions [18][13]. The first studies of hydrodynamics stability were focused in local linear analysis theory and some assuptioms were imposed in order to solve the differential equations that model the physical phenomenon. For instance, the pioneering work of Kelvin-Helmholtz (1871), which used the potential flow approach, analysed the stability of two fluids of different density in two horizontal parallel infinite streams; one of the natural phenomena that can be explained by using this theory is the generation of waves. From this study, by applying an additional upward vertical acceleration to the system, the Rayleigh-Taylor instability emerged and served to explain certain processes involved in salt domes, weather inversions and in phenomena related with astrophysics and electrohydrodynamics. Rayleigh [19], in other interesting work presented in 1878, used the Euler's equations for inviscid fluids to study the linear stability leading to the break-up process of a round liquid jet under the surface tension effects.

The phase function of the perturbation is composed of the phase velocity and the wave numbers. If this numbers are real or complex, then it can be distinguish three ways [20] of leading the local, nonlocal and global stability analysis, namely, (a) through temporal approach, from which the first classical hydrodynamics theories were developed [21][22], that uses the phase velocity as a complex number and real wave numbers; (b) by using spatial approach, where use is made of complex wave numbers and real phase velocity; and (c) by means of the spatio-temporal approach, where both the wave numbers and phase velocity are complex numbers.

With respect to spatio-temporal stability analysis, special attention is given to unstable open flows, where a perturbation never passes the same point more than once. In this case, if the perturbation response grows along some rays from the point of impulse, the flow is called convectively unstable. On the other hand, if the perturbation grows at the point where it was applied, the flow is absolutely unstable. The reader interested in this subject is referred to Huerre and Monkewitz [23] for more details. The Figure 1.2 depicts a graphical description differentiation between stable and convectively/absolutely unstable flows.
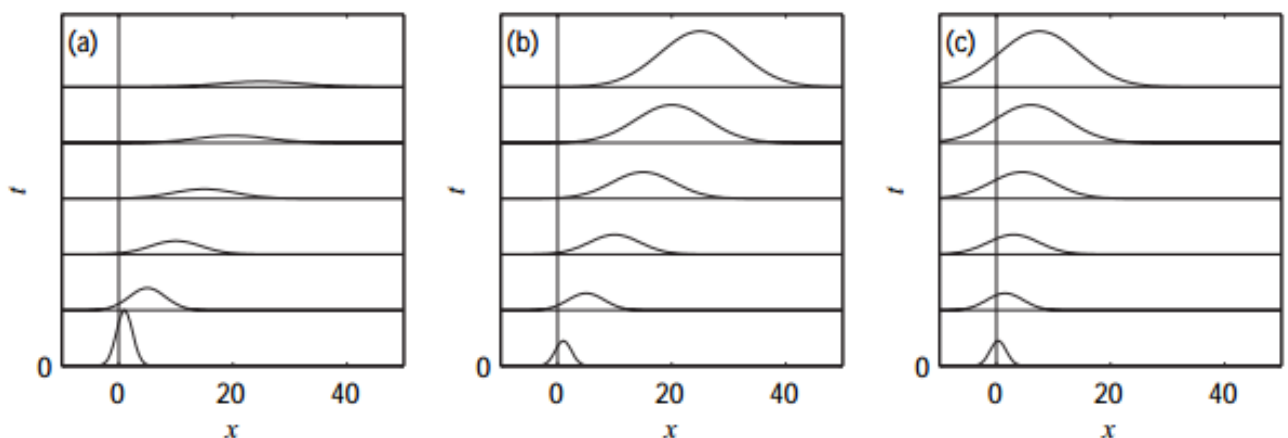
Figure 1.2 (a) Stable flow, (b) convectively unstable flow and (c) absolutely unstable flow [18].

In the nonlocal linear stability analysis, the amplitude of the perturbation, which depends only on one spatial direction for the local case, varies slowly in other one. This analysis emerged due to the fact that the local stability does not take into account both the growth of boundary layer and the

history effects related with the initial conditions. For these reasons, the so called parabolized stability equations (PSE) technique has been developed to solve this type of problems [24]. Some applications of this approach can be observed for instance in the study of Yen and Messermith [25], motivated mainly by the lack of accuracy of the local lineal stability theory to predict the natural divergence of the jet flow, where analysed the streamwise evolution of instability waves in jet flows. Bertolotti and Herbert[26] analysed the linear stability of compressible boundary layers using PSE technique, and Zhang and Zhou [27] studied the evolution of disturbances of them for subsonic and supersonic regimens, whose results from both PSE and Direct Numerical Simulation (DNS) [28] agreed with each other reasonably well. In another study in the supersonic regime, Malik [29] investigated the linear stability under the chemistry effects associated with high temperature boundary layers. Taking advantage of PSE capabilities to solve nonparallel linear stability problems, Herrada et al [30] studied the perturbations effects on the boundary layer flow over a long thin cylinder aligned with the main flow and with rotation around its axis.

As far as the global linear stability analysis is concern [31], [32], it can be identified principally two sub-categories, namely, the BiGlobal and TriGlobal linear stability theory, directly pertaining to two and three dimensional steady basic flows, respectively. In the former case, the base flow depends on two of the three spatial directions and homogeneous in the third one, which means that the disturbances are three-dimensional with a harmonic behavior along the direction in where the base flow does not vary. In this context, it is worth mentioning the pionnering study developed by Pierrehumbert [33], who explained the behaviour of two-.dimensional inviscid vortex flows under three-dimensional perturbations and discovered the short-wavelength elliptic instability nature of them. Other important stability investigations, related to the implementation of BiGlobal approach, are present in the literature for different fluid flow applications, such as the temporal and spatial stability of attachment-line boundary layers developed by Ling and Malik [34] and Heeg and Geurts [35], respectively; the three-dimensional temporal instabilities in both incompressible and compressible flows over open cavities [36], [37]; the temporal stability of pipe flows in rectangular and elliptic cross section [38], [39]; the instability of the steady flow past spheres, cylinders and airfoils [40], [41], [42], etc.

Finally, with regard to TriGlobal modal linear stability analysis, the treatment of the flow variables is made by assuming non-homogeneity on the basic flow with a total dependency on the three spatial directions, which entails applying only temporal analysis with this approach. Here it deserves to mention the work of Tezuka and Susuki [43], who were the first to use this stability approach so as to analyse a three-dimensional flow around a spheroid at varied angles of attack. In a like manner, but comparing the stability results with direct numerical simulations, Bagheri et al. [44], demonstrated the existence of self-sustained global oscillations generated by a jet in crossflow. Applying to a three-dimensional lid-drive cavity flow, Giannetti et al. [45], evaluated the critical Reynolds numbers for which the flow perturbations giving rise instabilities.

Notwithstanding a large quantity of works in the literature for studying the linear stability of hydrodynamic systems, a great percentage of them are focused on one-fluid flows, and a very little has been made to the study of immiscible multiphase flows, specially those characterized by a well-defined interface or free surface (i.e. liquid bridges [46], flow-focusing systems [47][48], electrospinnig phenomenon [49][50], two- fluids bioreactors for oxygen transport processes[51], among others). Besides, in order to yield the global linear analysis, various authors have made use of simplified momentum equations with base flows as a function of one direction, like the work developed by Herrada and Gañan-Calvo [52] so as to study the spatiotemporal stability of a confined capillary jet using exact steady unidirectional solutions for both the inner and outer fluid. Re-writing the steady Navier-Stokes equations for a two-fluid flow through the well-know slender (parabolized or boundary) approximation, Gordillo et al. [53] addressed a temporal linear stability analysis of a inviscid liquid jet surrounded by a co-flowing gas stream; using the same approximation technique, Sevilla [54] developed a spatiotemporal stability of capillary jets in order to analyse the viscous relaxation effect. In other study, Castro-Hernández et al. [55] studied the tip streaming regime using the slender-body theory approximation due to Taylor [56], in which the viscosity ratio, the velocity

ratio and the capillary number were used as control parameters. This one-dimensional approach was used by Gordillo et al. [57] to analyse the effect of the global stability on the generation of monodisperse micro and submicro emulsions from stretched jets within a coflowing stream. Likewise, Rubio et al.[58] studied experimentally and theorically the transition between jetting to dripping regime under gravitational effects; for that purpose, a global linear stability analysis was implemented by applying the dimensionless leading-order one dimensional mass and momentum equations developed by Eggers and Dupont[59] and García and Castellanos[60].

Motivaded by the fact that these approximation techniques, used to simplify the two-fluid flows Navier-Stokes equations and to generate one-direction dependent basic flows only, does not have the capability to address a global linear stability analysis using the complete set of governing equations for modelling free-interface multi-fluid flows, it is used the computationally efficient numerical method developed by Herrada and Montanero [1] for studying both the nonlinear evolution and linear stability of capillary one-fluid systems. This technique implements a mapping of the time-dependent fluid region onto a fixed numerical domain making use of a suitable coordinate transformation, a spatial discretization by means of the spectral collocation approach and a second-order backward finite differences for implicit time advancement. The most interesting and particular characteristic of this method, which helps reducing the computational cost for solving the resulting algebraic equations, is the fact that the elements of the jacobians pertaining to the discretized system of equations are symbolic functions which are evaluated numerically by means of iterative Newton-Raphson technique. Additionally, the eigenvalue problem, related to the linear stability analysis, can be solved by adapting this novel numerical procedure without significant endeavor.

This doctoral thesis is devoted to the study of the nonlinear dynamics and linear stability of two-fluid swirling phenomena and liquid bridges; for this purpose, use is made of the above-mentioned technique by considering governing equations for both phases including the kinematic and dynamic interfacial conditions.

1.2   Computational simulation of multiphase flows

1.2.1   Multiphase numerical techniques

The numerical study of multiphase flows has been in constant evolution and improvement, and, therefore, there are a large number of scientific articles devoted to investigate them. The main challenges that the multiphase numerical technique has to overcome rely mainly on modelling discontinuities and properties of different fluid through the interface, ensuring conservation of mass, momentum and energy, manipulation of complex topologies and the surface tension forces.

With regard to the scope of the present thesis, special attention is particularly paid to the study of two-phase flows, which can be mainly simulated by the following numerical methods: one-fluid model, two-fluid model, smoothed-particle hydrodynamics approach and lattice Boltzmann method.

In the one-fluid method, it is possible to analyse the two-phase flow by applying a single set of governing equations in which the mass, momentum and energy conservation laws are used to simulate the whole flow field but taking into account the different physical properties related to each fluid. The numerical methods based on this approach can be classified into two [61] categories, namely interface-capturing and interface-tracking methods.

As far the interface-capturing methods concern, the governing equations are solved, in particular, on a fixed grid and use is made of a maker function, which is advected by the flow, so as to identify the different fluids. Among them, it can be mentioned the so called Volume of Fluid (VOF) [62][63] method, where the interface is represented by a discontinuity line and whose generation is obtain from the volume fraction values; the use of the maker or auxiliary function generally entails numerical diffusion problems which can be dimish by applying suitable interface reconstruction techniques[64]. Another important maker-function advection method is the Level-Set Method (LSM)

[65][66], which has the advantage of accurately representing interfacial quantities, for instance, the curvature and interfacial normal. In order to identify the interface between the phases, a level-set function, depending on space and time, is used to represent the distance from the interface, being positive for the one fluid and negative for the other one. From this function, the physical properties of each fluid (i.e. density, viscosity) and the interface characteristics such as surface tension and curvature are determined. An important feature of LSM, is the smooth transition between phases allowing accurate discretization of the normal and the curvature, unlike VOF method in where the transition occurs in the same grid cell. The drawback of LSM with respect to VOF is the lack of conservation of mass, so that a combined method [67], [68] called coupled level set/volume-of-fluid (CLSVOF), has emerged in order to overcome the weakness of both methods. In addition to the two methods mentioned above, others have been developed to address computational multiphase flows, applying one-fluid formulation to the governing equations, for instance the constrained interpolated propagation method [69] and the phase-field method [70]. The difference relies basically on the way of the maker function is advected or how the governing equations are manipulated. Conversely, in the interface-tracking approach for one-fluid approach, the boundary between the fluids is tracked by means of marker points, which are advected with the flow, and then the maker function is generated using the interface location. Two sub-categories of this approach can be distinguish, namely the marker-and-cell (MAC) [71] and front-tracking [72] methods.

In the Two-fluid models [73], [74], whose development was particulary motivated by the safety analysis of nuclear reactors, it is a method that implements a set of governing equations for each phase representing the conservation of mass, momentum and energy. Aditionally, the physical phenomena occurring between the phases across the interface such as the transfer of mass, momentum and energy are obtained by applying an averaging method. The modelling of interface interactions is the most difficult task in the two-fluid method, due to the fact that different flow regimes [75] (for instance, bubble flow, slug flow, churn flow, annular flow, mist flow, plug flow and stratified flow) can appear depending on the flow rates of the phases and the geometric characteristics. Under these conditions, apart of implementing a rigorous mathematical model, it is necessary to develop accurate constitutive relations and empirical correlations, the latter being obtained from experiments.

Concernig smoothed-particle hydrodynamics method (SPH) [76], initially developed by Gingold and Monaghan [77] in 1977 to simulate both solid mechanics and fluid flow problems, it is a meshfree method in where the fluid is replaced by a set of particles moving in a lagrangian way. These particles interact by means of a kernel function, commonly represented by a Gaussian function, from which fluid properties at any particle can be estimated through interpolation operation within the kernel range. Considering two-phase flows [78], SPH generates a free surface between the fluids where the particles represent the denser fluid whereas the empty spaces represent the ligther fluid. Due to the meshfree nature, this method is adequate to numerically study complex boundary dynamics problems and to implement the momentum and energy equations which become a set of ordinary differential equations. In additon, since the particles themselves are considered mass, the conservation of mass is maintained. The limitations of SPH method is the difficulty of setting the boundary conditions in comparison to grid-based numerical method counterpart.

Finally, in the lattice Boltzmann (LB) approach [79], [80], use is made of the kinetic theory represented by the original Boltzmann equation at the mesoscopic level. LB method has the capacity of maintaining the microscopic kinetic principles while hydrodynamics characteristic at the macroscopic scale are retrieved. Since microscopic methods for instance molecular dynamics, dissipative particle dynamics and direct simulation Monte Carlo have high computational cost and are not really suitable for fluid dynamics problems, LB method has interesting advantages [81] even in comparison to classical numerical methods used in continuum media mechanics. These include: (a) the linear nature of convective operator, which is non-linear in the Navier-Stokes formulation; (b) the boundary conditions are implemented using mechanical rules as for example interactions between molecules and solid walls; and (c) the pressure field is obtained by means of equation of state instead of using the costly Poisson equation implemented in the typical numerical methods.

However, considering high-Mach number flows in aerodynamics, LB method still has drawbacks addressing them. In order to study multiphase flows various LB methods has been proposed, for instance the phase field approach[82] , based on the Canh-Hilliard equation, the pseudopotential method, in where the multi-fluid flow behaviour is simulated through an interparticle potential[83], the free-energy method which applies thermodynamics concepts and the color-gradient [84] method based on particle distribution functions for each fluids.

In order to increase the accuracy level of the interface evolution that can be seen in interface phenomena (i.e., liquid bridges, jets, flow focusing and electrospinning), methods based on grid lines that are aligned with the interface have been developed. These can be classified in three categories: (a) unstructured grids [85], in where the edges of triangular shaped elements (for two-dimension case) and thetrahedral elements (for three-dimension case) moving with the fluid are aligned with the interface; (b) the sharp interface method [86], based on a structured grid to represent the fluid domain, that makes use of different treatment of interface, for instance, implementing "ghost points" across the interface, using mathematical relations to take into account the jump across the interface, or rearranging the faces of the control volumes so as to maintain aligned with the interface; and (c) body-fitted grids [87] in where a time-dependent coordinate transformations is used to map the physical domain onto a fixed computational domain; in addition, the position of the interface is obtained by implementing a spatio-temporal contour function, being represented by a straight line in the numerical domain. This is precisely the multiphase method used by Herrada and Montanero [1] to study the nonlinear analysis and linear stability of capillary one-fluid flows and that is implemented in this thesis for two-fluid flows with free or continuos interface.

1.2.2   Spatial discretization

In computational fluid dynamics (CFD) and mainly in the hydrodynamic stability studies, three traditional spatial numerical discretizations can be distinguished [88], namely, finite difference method (FDM), finite element method (FEM) and finite volume method (FVM).

The FDM method approximates the differential equations by means of differential quotients resulting from Taylor series application, where the domain is partitioned in both space and time giving rise to approximate solutions at each space and time point. Some interesting works using FDM for analyzing flow stability can be cited, for instance the linear stability analysis of three-dimensional lid-driven cavity flow by Giannetti et. al. [45], where use is made of second-order accurate, staggered discretization of the three-dimensional linearized Navier-Stokes equations. Using the same approach, Shiratori et al. [89] studied the thermal effects on linear stability of capillary systems in confined zones. Morzynksi and Thiele [90] analyzed the stability of flow around a cylinder employing second-order central differences. With regard to the stability analysis of compressible flows, high order compact finite-difference methods were used by Bres and Colonius [91] in order to study the global stability of three-dimensional flow over open cavities. Likewise, Mack and Schmid [92] studied the compressibility effects on the boundary layer flows.

In FEM method, the entire physical domain is decomposed on an assembly of discrete elements, called finite elements that are interconnected by nodes. In order to obtain the approximate solution of the partial differential equations governing the phenomena, it is applied a linear combination of basic functions which are defined in each discrete element or subdomain. After assembling the subdomains, a discrete set of equations are obtained. The advantage of FEM is the capability of leading unstructured meshes that are especially suitable for nonlinear and stability analysis of flows in complex geometries. Among some typical applications, FEM has been applied to study the three-dimensional linear stability [93] and biglobal instability [94] of viscous incompressible flows. In other interesting works, a global stability analysis of 3D flow around a circular cylinder has been developed by Morzynski and Thiele [95] and a linear stability in lid-driven cavity flows [96].

As in the FEM method, in FVM approach the flow domain is divided into a number of small

control volumes. The most important characteristic of this method is that the conservation principles of mass, momentum and energy are applied to each control volume, guaranteeing global conservation during the numerical simultions. In addition, FVM can be adapted to complex geometries by employing unstructured meshes. The values of the governing equations variables are usually stored in the centre of the control volumes. Some applications in the literature include for example, a fully-implicit finite volume method that was used by Sahin and Owens [97] in order to investigate the linear stability of a lid-driven cavity flow. In other study, Gelfgat [98] used a low-order FVM to study the stability of convective flows in cavities. A parallel adaptive unstructured finite volume method were used by Sahin and Wilson [99] to analyse the linear stability of viscoelastic fluid flows and a second-order FVM were applied by Dijkstra [100] to study the global stability of the structure of cellular solutions in Rayleigh-Bénard-Marangoni flows in small-aspect-ratio containers.

Here, special attention is paid to spectral collocation methods (SCM) [101] which have been broadly implemented in hydrodynamic stability analysis. These methods are related to FEM due to the fact that the solution of the differential equations is represented as a sum of certain basis functions, such as Fourier series and Chebyshev polynomials. The main difference between these methods relies on that the basic functions used in SCM are non-zero over the whole domain, whereas those used by FEM vanish except on small subdomains. For these reasons, SCM and FEM are considered as global and local approach, respectively. Such is the importance of SCM thas was used in the pionner work by Pierrehumbert and Widnall [102] in order to develop the first global analysis of two and three dimensional instabilities of a spatially periodic shear layer considering an inviscid flow. Taking into account viscous effects, one can mention the work by Zebib [103] which employed trigonometric functions and Chebyshev polynomials to study the linear stability of an incompressible laminar flow past a circular cylinder. Recently, using parallel computing, Biglobal analysis instability for the study of laminar separation bubble phenomena was investigated by Rodríguez and Theofilis [104] and the Triglobal stability of a jet in crossflow by Bagheri et al. [44].

Throughout the present thesis the hydrodynamic equations of two-fluid flows are spatially discretized using Chebyshev spectral collocation and high-order finite different techiques. Both are able to accumulate points near the solid walls and interface in order to overcome the problems associated with the increasing effects of the hydrodynamic quantities' gradients.

1.3   Objectives and document structure

In this chapter, the different types of multiphase flows and their applications arising in the industry were introduced. Then, the classical theories of hydrodynamic stability were explained for both one-fluid and two-fluid flows, the latter being focused on those related with free or continuous interface. Finally, the numerical methods and spatial discretization in order to simulate multiphase flows were reviewed.

The principal objective of this thesis is the numerical analysis of nonlinear dynamics and global linear stability of two-fluid flows separated by a continuos interface using the efficient numerical technique developed by Herrada and Montanero [1]. The novelty of this method is the capability to model the complete set of governing equations for both fluids without applying approximations to simplify them, obtaining the hydrodynamic behavior and the global linear stability analysis of the flow with the same approach. In the next chapters, this numerical tool is used to study two-fluid swirling flows and liquid bridges behavior.

In chapter 2, it is studied a steady air-water swirling flow in a vertical sealed cylinder with a rotating top disk. The purpose is to find the relations between the appearance mechanisms of vortex breakdown phenomenon and the instability states.

The aim of chapter 3 is to unveil the topological flow structure and the stability behavior hidden in the experimental work developed by Tsai et al. [2]. This water-soybean oil swirling flow is

generated by the upper rotating disk in a sealed vertical cylinder. The goal of this study is to prove the flattop interface shape and to find the vortex breakdown emergence in both fluids while increasing Reynolds number. Besides, the type of instability and its location is investigated.

In chapter 4, similar to previous one, it is analysed the water-silicone oil swirling flow, studied experimentally by Fujimoto and Takeda [3], in order to discover the flow topologies and stability states. The main objectives are to prove the complex interface shapes found in the experiment and to discover the location of critical disturbance energy and its relation with the instability.

The goal of chapter 5 is to study the stability and multi-eddy patterns of a whirlpool flow, where the motion is yielded by a bottom rotating disk. To this end, it is varied the water volume fraction as the swirling strenght is increased. As a result, interesting topologies are found such as: zipper-like chains, air and water eddies, and bubble-ring air eddies. In addition, the influence of the interface ubiety on the instability is examined.

The objective of chapter 6 is devoted to the analysis of the steady axisymmetric air-water swirling flow in a semispherical container driven by a rotating top disk. This numerical study reveals that as the rotation strength is increasing, a three-eddy pattern appears in the flow. Also, it is studied the location of the critical energy disturbance as well as the instability of shear-layer type appearing in the air region.

In the last two chapters, the effects produced by small-amplitude vibrations, insoluble surfactants, thermal gradients and gravitational forces on the liquid bridge behavior are studied. Specifically, in chapter 7, the interaction between the streaming flow and the Marangoni convection is investigated so that to discover flow patterns with nonmonotone behavior whereas increasing Marangoni number. In chapter 8, the objective is to study the impact of the dynamical free surface deformation on the stability of thermal convection for high Prandtl numbers. Additionally, the good agreement between our numerical simulations and previous experimental works is proved, demonstrating the efficacy of the numerical technique even at micro-meter level.

The contents and results in the next six chapters have been published in the following articles:

- ✓ L. Carrión, M. A. Herrada, and V. N. Shtern, "Instability of a water-spout flow," *Phys. Fluids*, vol. 28, no. 3, p. 034107, Mar. 2016.

- ✓ L. Carrión, M. A. Herrada, and V. N. Shtern, "Topology and stability of a water-soybean-oil swirling flow," *Phys. Rev. Fluids*, vol. 2, no. 2, p. 024702, Feb. 2017.

- ✓ L. Carrión, M. A. Herrada, and V. N. Shtern, "Topology changes in a water-oil swirling flow," *Phys. Fluids*, vol. 29, no. 3, p. 032109, Mar. 2017.

- ✓ L. Carrión, M. A. Herrada, V. N. Shtern, and J. María López-Herrera, "Patterns and stability of a whirlpool flow," *Fluid Dyn. Res.*, vol. 49, no. 2, p. 025519, Apr. 2017.

- ✓ L. Carrión, M. A. Herrada, and V. N. Shtern, "Stability of an air–water flow in a semispherical container," *Eur. J. Mech. - B/Fluids*, vol. 67, pp. 377–384, Jan. 2018.

- ✓ L. M. Carrión, M. A. Herrada, J. M. Montanero, and J. M. Vega, "Mean flow produced by small-amplitude vibrations of a liquid bridge with its free surface covered with an insoluble surfactant," *Phys. Rev. E*, vol. 96, no. 3, p. 033101, Sep. 2017.

The results of the last chapter were submitted for publication in the International Journal of Multiphase Flow, with title: "Influence of the dynamical free surface deformation on the stability of thermal convection in high-Prandtl-number liquid bridges", and authors: Luis Carrión, Miguel Ángel Herrada and José María Montanero.

2. INSTABILITY ANALYSIS OF WATER-SPOT FLOW

T his chapter studies the hydrodynamic linear stability of a air-water swirling flow as a potential application in aerial bioreactors. This steady axisymmetric two-fluid flow is driven by the rotating top disk in a vertical sealed cylinder. A vortex breakdown bubble (VBB) appears at the bottom center and spread out to the interface as Reynolds number (Re) increases. Clockwise meridional circulation regions appear in water and air, which are separated by a thin anticlockwise circulation layer (TCL) adjacent to the interface in water. This study shows that the flow becomes instable for larger Re than those at which VBB and TCL emerge. Additionally, the instability is of shear-layer type in the air region but becomes centrifugal when the air volume fraction is small.

2.1. Introduction

The study of the behavior and metamorphosis that occur in swirling flow is important because of industrial and natural applications [105], [106], [107], specially for the emergence of a local circulation cells called as vortex breakdown (VB). This phenomenon has been a focus of research owing to its relevance to delta-wing aircraft, furnaces and combustion chambers, water turbines, compressors, tornadoes, and other applications [108], [109], [110]. The first studies begun in 1957 with a pionner work of Peckham and Atkison [111] in which analysed the flow over a gothic wing in a low speed wind tunnel. Since then, numerous interesting hypotheses [110] has been developed in order to uncover the mechanism behind VB phenomenon. Recently, Shtern and Borissov [112] worked in swirl-decay mechanism so that to explain the VB emergence and the ways to be controlled it [113], [114].

Unlike VB studies in single fluid flows, the reseach in two-fluid flows have attracted attention in recent years because of applications in aerial bioreactors [51], [115], where air-water flow is driving by a propeller and or a rotating lid. The air motion expands towards the reactor axis, near the interface, and produces the meridional circulation and hence the rotation of water. The air flow delivers oxygen to the interface and helps tissue culture growth and water circulation improves the mixing process of the dissolved oxygen with other ingredients. The process of tissue growth riquires a considerable interval of time under small shear stresses and slow motion of ingredients. Because of the tissue fraction is small compared to that of water, it is neglected in the flow pattern studies [51], [115]. VB phenomena is found to be important in this type of biological process [51].

The interfacial interactions occurring in two-fluid swirling flows produce interesting characteristics which are not present in single-fluid flows. One of them is a thin anticlockwise circulation layer [116], [117] (TCL) adjacent to the interface. This remarkable phenomenon, having a large surface-area-to-volume ratio, enhances significantly the heat and mass transfer and can be important in bioreactors applications.

Herrada et al. [118] studied a two-fluid flow driven by the rotating lid in a vertical sealed cylindrical container with same volumetric fractions of air and water, where the meridional circulation of air is clockwise type, which diverges from the axis near the lid and converges to the axis near the interface. Conversely, when the rotation lid is slow, the meridional circulation in the

water region is anticlockwise, converging to the axis near the interface and diverging from the axis near the bottom. The rising of speed rotation produces a vortex breakdown bubble (VBB) at the bottom center of the water region and spread out to the interface up to the thin layer anticlockwise circulation (TCL)[118].

There are vast studies related with the stability analysis of single-fluid VBB flows. For instance, Gelfgat et al. [119], [120] described the emergence of VBB in the steady axisymmetric flow as a consequence of local flow reversal without generating instabilities; therefore, there is not a direct relation between instability and the appareance of vortex breakdown. Escudier[121] and Sorensen et al. [122]–[124] found that, the emergence of VB in a steady axisymmetric flow, increasing Reynolds number, occurs for the container height-to-radius ratio H less than 3.2. For larger values of H, the flow becomes unstable with respect to 3D time oscillatory disturbances, with $m=3$ for $3.2 < H < 4.3$, $m=2$ for $4.3 < H < 5.2$ and $m=4$ for $5.2 < H < 5.5$, being m the azimuthal wave number. Recently, Herrada et al. [113] argued that the instability nature of these flows is of the shear layer type.

However, although there are detailed and rigorous instability studies of VBB single flows, no attention has been paid to the instability of two-fluid VB flow. Our study reveals that the disturbances only grow for Reynolds number being larger than those at which VBB and TCL emerge. To this end, a numerical technique has been developed for the stability investigation which can linearize efficiently the conditions at the interface.

2.2. Problem Formulation

2.2.1. Flow geometry
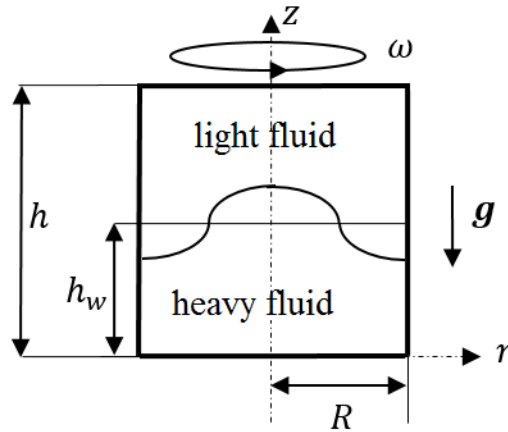
Figure 2.1 Schematic of water-spout model.

Figure 2.1 is a schematic of the problem. The lower part, $0 < z < h_w$, of the cylindrical container of radius R and height h is filled with a heavy fluid (e.g., water), the upper part, $h_w < z < h$, is filled with a light fluid (e.g., air). With no motion, the interface is flat, $z = h_w$ (thin horizontal line in Fig. 1). When the top disk (at $z = h$) rotates with angular velocity ω while the other walls are stationary, the interface becomes deformed as the curve in Figure 2.1 schematically shows. This flow mimics a water spout where swirling air raises water near the rotation axis.

One control parameter is aspect ratio $H = h/R$ which is fixed here: $H = 1$. The dimensionless height of the interface at rest is $H_h = h_w/R$ being also a volumetric fraction of the heavy fluid which varies here.   Other control parameters are the Reynolds number, $Re = \omega R^2/\nu_w$, characterizing the swirl strength, the Froude number, $Fr = \omega^2 R/g = aRe^2$, which is a centrifugal-to-gravity acceleration ratio, and the Weber number, $We = \rho_w \omega^2 R^3/\sigma = bRe^2$, characterizing the

effect of surface tension σ at the interface; $g = 9.81$ m^2/s is the gravity acceleration, ρ_w is the density of heavy fluid, $a = v_w{}^2/(gR^3)$ and $b = \rho_w v_w{}^2/(\sigma R)$. As the light and heavy fluids are specified, coefficients a and b are fixed numbers while Re varies.

We first consider the fluids, studied by Brady et al [116],[117], and imagine a physical experiment where $R = 5$ mm, $a = 5.77\times10^{-5}$ and $b = 1.42\times10^{-5}$. Then we focus on the air-water flow[118] where $v_a = 15\times10^{-6}$ m^2/s and $v_w = 10^{-6}$ m^2/s are the kinematic viscosities, $\rho_a = 1.22$ kg/m^3 and $\rho_w = 1000$ kg/m^3 are densities; subscripts "a" and "w" means "air" and "water" as well as the light and heavy fluids. Pressure on the interface at rest is atmospheric, temperature $T = 300$K and $\sigma = 0.0715$ kg/s^2. Here we imagine a physical experiment where $R = 1$ mm, $a = 1.02\times10^{-4}$ and $b = 1.39\times10^{-5}$.

2.2.2. Governing equations

Using R, ωR, and $\rho_w \omega^2 R^2$ as scales for length, velocity, and pressure, respectively, renders all variables dimensionless. We consider a flow of two viscous incompressible immiscible fluids governed by the Navier-Stokes equations [125],

$$\frac{1}{r}\frac{\partial(ru)}{\partial r} + \frac{1}{r}\frac{\partial v}{\partial \phi} + \frac{\partial w}{\partial z} = 0, \tag{2.1}$$

$$\frac{\partial u}{\partial t} + u\frac{\partial u}{\partial r} + \frac{v}{r}\frac{\partial u}{\partial \phi} + w\frac{\partial u}{\partial z} - \frac{v^2}{r} = -\rho_n\frac{\partial p}{\partial r} + \frac{v_n}{Re}\left(\nabla^2 u - \frac{u}{r^2} - \frac{2}{r^2}\frac{\partial v}{\partial \phi}\right) \tag{2.2}$$

$$\frac{\partial v}{\partial t} + u\frac{\partial v}{\partial r} + \frac{v}{r}\frac{\partial v}{\partial \phi} + w\frac{\partial v}{\partial z} + \frac{uv}{r} = -\frac{\rho_n}{r}\frac{\partial p}{\partial \phi} + \frac{v_n}{Re}\left(\nabla^2 v - \frac{v}{r^2} + \frac{2}{r^2}\frac{\partial u}{\partial \phi}\right) \tag{2.3}$$

$$\frac{\partial w}{\partial t} + u\frac{\partial w}{\partial r} + \frac{v}{r}\frac{\partial w}{\partial \phi} + w\frac{\partial w}{\partial z} = -\rho_n\frac{\partial p}{\partial z} + \frac{v_n}{Re}\nabla^2 w \tag{2.4}$$

where $\nabla^2 \equiv \frac{1}{r}\frac{\partial}{\partial r}\left(r\frac{\partial}{\partial r}\right) + \frac{1}{r^2}\frac{\partial^2}{\partial \phi^2} + \frac{\partial^2}{\partial z^2}$ is the Laplace operator for a scalar field, (u, v, w) are the velocity components in cylindrical coordinates (r, ϕ, z), t is time, and p is pressure. The coefficients, ρ_n and v_n, are both equal 1 at $n = 1$ (in the heavy fluid) while $\rho_n = \rho_w/\rho_a$ and $v_n = v_a/v_w$ at $n = 2$ (in the light fluid).

We denote the list (u, v, w, p) as $\boldsymbol{V}$, and look for a solution of the system 2.1-2.4 in the form

$$\boldsymbol{V} = \boldsymbol{V}_b(r,z) + \varepsilon\boldsymbol{V}_d(r,z)e^{(im\phi - i\omega t)} + c.c., \tag{2.5}$$

where subscripts "b" and "d" denote the base flow and a disturbance, respectively; c.c. denotes the complex conjugate of the preceding term; $\varepsilon \ll 1$ is an amplitude; integer m is an azimuthal wave number; and $\omega = \omega_r + i\omega_i$ is a complex number to be found, with frequency ω_r and growth rate of disturbance ω_i. For a decaying (growing) disturbance, ω_i is negative (positive). The equations governing the base flow result from substituting 2.5 in system 2.1-2.4 and setting $\varepsilon = 0$. The terms of order $O(\varepsilon)$ constitute equations governing infinitesimal disturbances.

2.2.3. Boundary conditions

Equations 2.1-2.4 are solved under the following boundary conditions:
(i) Regularity at the axis, $0 < z < H$, $r = 0$:

a) $u = v = 0, \partial w/\partial r = 0$ (basic flow and $m = 0$ disturbances),

b) $w_d = 0, u_d + m v_d = 0, \partial u_d/\partial r = 0$ ($m = 1$ disturbances)

c) $w_d = u_d = v_d = 0$ ($m > 1$ disturbances)

(ii) No-slip at the walls: $u = v = w = 0$ at the still disk, $0 < r < 1$, $z = 0$, and at the sidewall, $0 < z < H, r = 1; u = w = 0, v = r$ at the rotating disk, $0 < r < 1, z = H$.

(iii) Continuity of all the velocity and stress components at the interface, $z = F(r, \phi, t)$. In particular, the balance for the normal stresses yields that

$$p_w - p_a = \frac{1}{We} \nabla . \boldsymbol{n} - \frac{1}{Re} \boldsymbol{n} . (\boldsymbol{\tau}_w - \mu_r \boldsymbol{\tau}_a) . \boldsymbol{n} - \frac{1}{Fr}(1 - \rho_r) z, \qquad 2.6$$

where $\boldsymbol{n}$ is the unit vector normal to the interface, $\boldsymbol{\tau}_w$ and $\boldsymbol{\tau}_a$ are tensors of the viscous stresses in the heavy and light fluids, respectively, μ_r and ρ_r are the light-to-heavy fluid ratios of the dynamic viscosities and densities, respectively.

(iv) The kinematic equation for the interface shape, $z = F(r, \phi, t)$, yields that

$$\frac{\partial F}{\partial t} - w + u \frac{\partial F}{\partial r} + \frac{v}{r} \frac{\partial F}{\partial \phi} = 0, \qquad 2.7$$

and we look for a solution in the form $z = F_b(r, z) + \varepsilon F_d(r, z) e^{(im\phi - i\omega t)} + c.c..$

2.3. Numeric technique

To simulate the nonlinear problem for the axisymmetric basic flow and the generalized eigenvalue problem for disturbances, we use a numerical technique which is a variation of that described in detail in Ref. [1]. First, the heavy-fluid (e.g. water) and light-fluid (e.g. air) regions are mapped onto the standard square domain ($0 \leq \eta_{(w,a)} \leq 1$, $0 \leq \xi \leq 1$) by means of the coordinate transformations (a) $\eta_w = z/F$ and $\xi = r$ and (b) $\eta_a = (z - F)/(H - F)$ and $\xi = r$ for the water and air, respectively. Then, each variable (velocities, pressure field and the interface shape) and all its spatial and temporal derivatives, which appear in the transformed equations, are composed as a single symbolic vector. For example, for the axial velocity in the water flow we create a vector having 11 components: $\mathbf{x}_w = [w_w, \partial w_w/\partial \eta_w, \partial w_w/\partial \xi, \partial^2 w_w/\partial \eta^2, \partial^2 w_w/\partial \xi^2, \partial^2 w_w/\partial \xi \partial \eta, \partial w_w/\partial \phi, \partial^2 w_w/\partial \phi^2, \partial^2 w_w/\partial \phi \partial \xi, \partial^2 w_w/\partial \phi \partial \eta, \partial w_w/\partial t]$. The next step is to use a symbolic toolbox to calculate the analytical Jacobians of all the equations with respect to all the symbolic vectors. Using these analytical Jacobians we generate functions which then are evaluated point by point in the square domains. In this procedure, we used the MATLAB procedure *matlabFunction* to convert the symbolic Jacobians in MATLAB functions.

Then, we carry out the spatial and temporal discretization of the problem. The water and air domains are discretized using a set of n_w and n_a Chebychev spectral collocation points in the axial direction (along the η_w and η_a axes, respectively)[126]. The water and air domains are discretized using a set of n_ξ Chebychev spectral collocation points in the radial direction, ξ. The second-order backward finite differences are used to compute the time derivatives for the basic flow. Since the basic flow is axisymmetric, all the azimuthal derivatives are set to zero. For disturbances, we obtain the temporal and azimuthal derivatives using the representation 2.5.

The final step is to set up the numerical matrices allowing us to solve the problem by using a Newton procedure for the basic steady flow and by solving a generalized eigenvalue problem for disturbances. Details of this procedure are described in Ref. [1].

To summarize, the numeric procedure includes the mapping of water and air regions, the proper spatial and temporal discretization creating the discrete Jacobian matrix for the Newton procedure for the basic flow and two more matrices for the generalized eigenvalue problem for disturbances. For the basic flow, we get the final steady solution though an unsteady process. Starting from the rest and selecting a time step, *dt*, the solution is advanced in time until a steady state is reached. Since the nonlinear procedure used to compute the basic flow is fully implicit, *dt* can be taken sufficiently large to quickly reach the steady solution. Once the base flow is computed, and given an azimuthal wavenumber *m*, we use MATLAB subroutine *eigs* to calculate the eigenvalues (ω) of the system of discrete linear equations.

Most of the simulations presented here are done using $n_w = 25$, $n_a = 25$, and $n_\xi = 30$ (standard grid), but some runs for flows, having small circulation regions, are performed with more fine grids. Since the Chebyshev grid points concentrate near the interface from both sides, the approach is adequate to resolve thin circulation layers, located near the interface, even at moderate values of n_w, n_a, and n_ξ.

The numerical code was validated by the agreement with the results of the paper [118] where the same base flow was simulated using a different code. The stability results where validated in the paper [1] by comparison with experimental studies.

2.4. Instability of liquid-liquid flow

We first address the media studied by Brady et al. [116], where the light-to-heavy fluid density ratio is $\rho_r = 0.5284$ and dynamic viscosity ratio is $\mu_r = 0.2$. These values are larger than those for air and water by orders of magnitude that makes the interface remarkably deformed even at moderate Re values. We analyze stability features as the fraction of the heavy fluid H_h varies.

We checked the disturbances with $m = 0, 1, 2, 3$, and 4 and examined ω_i. For small Re, ω_i is negative. As Re increases, ω_i first become positive for $m = 1$ disturbances for all H_h listed in Table 2.1 which presents the results for the critical ($\omega_i = 0$) values of the Reynolds number Re, frequency ω_r and azimuthal wave number m of the leading disturbances. To better understand the instability nature, we consider the distribution of disturbance kinetic energy $E_d(r, z) = \langle |u_d|^2 + |v_d|^2 + |w_d|^2 \rangle$, normalized by its maximal value; $< >$ denote averaging with respect t and ϕ.

H_h	0.1	0.2	0.3	0.	0.5	0.	0.	0
Re	97	134	105	9	85	7	6	6
ω_r	0.0	−0.3	0.19	0.	0.2	0.	0.	0
m	1	1	1	1	1	1	1	1

Table 2.1 Dependence of critical parameters on heavy fluid fraction H_h for fluids used by Brady at al.

Table 2.1 shows that as H_h decreases from 0.8 down to 0.2, Re_{cr} grows while ω_r decreases. The physical reasoning for this trend likely is the following. The instability develops in the upper fluid Figure 2.2. As H_h decreases at a fixed Re, the upper-fluid meridional motion weakens because its volume increases while its driving does not. This stabilizes the flow resulting in the Re_{cr} growth. The limited container volume terminates this trend as the interface approaches the bottom.
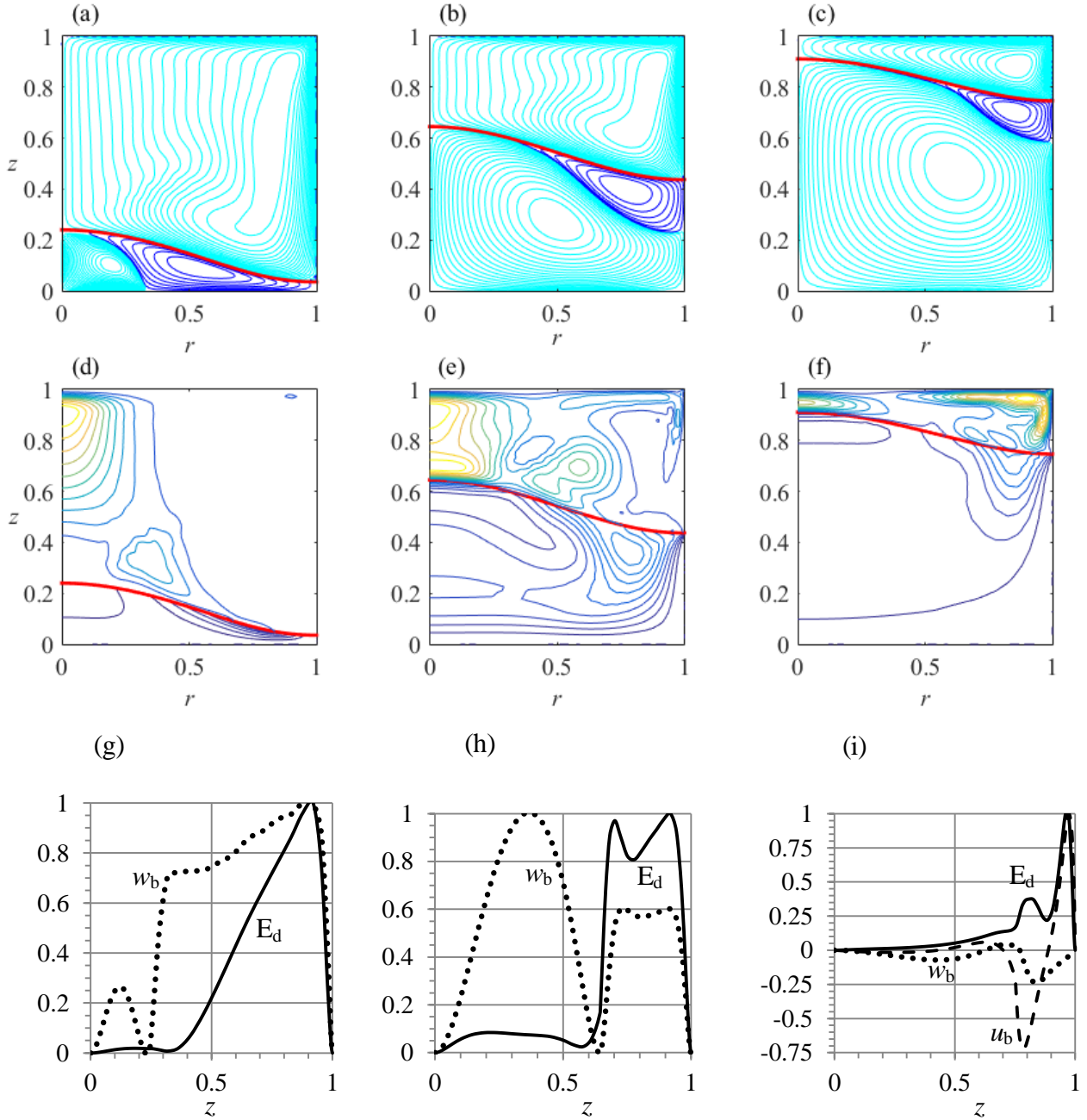
Figure 2.2 (color online) Streamline patterns at critical Re (see Table1) for heavy fluid fraction $H_h = 0.1$ (a), 0.5 (b) and 0.8 (c). The bold curves show the interface, light (dark) contours show clockwise (anticlockwise) meridional circulation. Contours of critical disturbance energy E_d for $H_h = 0.1$ (d), 0.5 (e) and 0.8 (f); z-dependence of E_d, base-flow axial w_b and radial u_b velocities at $r = r_m$ (Table 2.2) for $H_h = 0.1$ (g), 0.5 (h) and 0.8 (i).

At small H_h, the jet-like boundary layer develops near the top disk, sidewall, interface and axis (Figure 2.2(a)). The shear-layer instability typical of jets results in the Re_{cr} decrease at $H_h = 0.1$. The ω_r trend likely relates to the weakening of the upper-fluid rotation near the interface and axis as H_h decreases. This trend reverses at small H_h for the same reason as that for for Re_{cr}. The trend makes ω_r negative at $H_h = 0.2$, i.e., the critical single-helix disturbances changes the direction of its rotation.

For all H_h, the most dangerous disturbance is single-helix, $m = 1$. The simulations at $H_h = 0.9$ reveal that the flow remains stable until the interface touches the rotating lid at $r = 0$ as Re increases. Table 2.1 does not include the $H_h = 0.9$ case because our numeric technique does not allow

describing the interface disconnection from the container axis. The radial r_m and axial z_m locations of E_d absolute maximum help understand the instability nature by indicating where disturbance energy E_d focuses. Table 2.2 lists r_m and z_m values for the small ($H_h = 0.1$), middle ($H_h = 0.5$) and large ($H_h = 0.8$) fractions of the heavy fluid.

To help understand the instability nature, Figure 2.2 depicts the base-flow streamlines (a)-(c), contours of disturbance energy E_d (d)-(f), and E_d and base-flow velocity z-profiles at $r = r_m$ (g)-(i) for $H_h = 0.1$ (the first column), 0.5 (the second column) and 0.8 (the third column) at critical Re. The disturbance energy is normalized by its maximal value.

H_h	0.1	0.	0.
r_m	0.0	0	0.
z_m	0.9	0.	0.

Table 2.2 Dependence on heavy-fluid fraction H_h of radial r_m and axial z_m coordinates of absolute maximum of disturbance energy E_d.

As the locations of the absolute maximum of E_d indicate in Figure 2.2(d)- Figure 2.2(f), the instability develops in the upper fluid. This is physically reasonable since (*i*) the light-fluid viscosity is smaller than the heavy-fluid viscosity and (*ii*) the light-fluid flow, being adjacent to the rotating lid, is faster than the heavy-fluid flow since the swirl velocity rapidly decays downward[113].

The velocity difference is especially large for the shallow heavy fluid at $H_h = 0.1$. Figure 2.2(g) shows that the axial velocity of base flow w_b (normalized by its maximal value, 0.011) is significantly smaller in the lower fluid, $0 < z < z_i = 0.242$, than in the upper fluid $z_i < z < 1$. In the upper fluid, w_b is positive according to the clockwise circulation (Figure 2.2(a)) while in the lower fluid there is the small range, $0.225\ z < z_i$, where w_b is negative in the anticlockwise circulation region (where contours are dark).

The peak locations for disturbance energy E_d and w_b are very close in Figure 2.2(g) that indicates that the instability is likely related to the near-axis flow whose inflection point in the $w_b(r)$ profile causes the shear-layer instability. This feature is similar to that in the single-fluid Vogel-Escudier flow[113]. The shear-layer instability also occurs at $H_h = 0.5$ as Figure 2.2(b), Figure 2.2(e) and Figure 2.2(h) illustrate. There are two peaks of E_d located at the container axis in Figure 2.2(e) and two local peaks of w_b which are close to the E_d peaks in Figure 2.2(h).

The character of instability changes as H_h increases up to 0.8 as Figure 2.2(c), Figure 2.2(f) and Figure 2.2(i) illustrate. The location of the E_d absolute maximum shifts away from the axis and becomes close to the sidewall in Figure 2.2(f) with $r_m = 0.898$ and $z_m = 0.965$ (Table 2.2). This peak is located within the near-lid radial jet (Kármán's boundary layer[127]) as Figure 2.2(i) illustrates where the radial velocity $u_b(z)$ is depicted by the dashed curve (u_b and w_b are normalized by maximal $u_b = 0.136$).

Figure 2.2(f) also reveals a local peak of E_d which is close to the sidewall in the middle part of the upper-fluid region. This peak is likely associated with the centrifugal instability[22] which also occurs in the single-fluid Vogel-Escudier flow[113].

2.5. Instability of air-water flow

2.5.1. Instability to m=1 disturbances

Now we study the stability of the air-water flow where $\rho_r = 0.0012$ and $\mu_r = 0.018$ and therefore

the interface deformation is smaller than that for the fluids used by Brady et al.[116] at close Re values.

H	0.1	0.2	0.3	0.4	0.5	0.6	0.7	0.	0.
R	62	67	99	84	57	43	18	10	2
R	41	44	66	56	38	28	12	73	1
R	40	52	88	70	51	40	20	12	6
ω	−0.	−0.	0.0	−0.	0.0	0.0	0.0	0.	0.
m	1	1	1	1	1	1	1	1	1

Table 2.3 Dependence of marginal parameters for $m = 1$ on water fraction H_h in the air-water flow.

H_h	0.1	0.5	0.9
r_m	0.5	0.0	0,9
z_m	0.2	0,6	0,9

Table 2.4 Dependence on water fraction H_h of radial r_m and axial z_m coordinates of absolute maximum of disturbance energy E_d.

Figure 2.3, Table 2.3 and Table 2.4 show the characteristics of the air-water flow which are similar to those shown in Figure 2.2, Table 2.1 and Table 2.2 respectively. Following Sorensen at al.[123] we use terms "marginal" and "critical". Neutral disturbances corresponding to the minimal Re at prescribed m are marginal. The marginal disturbance corresponding to the minimal Re among all m values is critical. Corresponding parameters Re, ω_r and m are also named as marginal and critical.

In Table 2.3, Re and Re$_a$ are based on the water and air viscosities respectively and Re$_w = v_{bim}$Re where v_{bim} is the maximal value of the base-flow swirl velocity at the interface; Re$_a$ (Re$_w$) characterizes the strength of the air (water) base flow.

The air-water base-flow and its stability characteristics at m = 1 are similar to those for the fluids used by Brady et al.[116] at H_h = 0.1 and 0.5. The instability is likely of the shear-layer kind and develops in the upper fluid (air). Comparison of plots (g) and (h) in Fig. 3 as well as Re$_a$ and Re$_w$ values in Table 2.3 show that the water flow is drastically weaker than the air flow. In contrast, Figure 2.2 shows that the meridional flow strengths are of the same order of magnitude at marginal Re values for the heavy and light fluids studied by Brady et al.[116].

Figure 2.3 and Table 2.3 show that the H_h = 0.9 case qualitatively differs from the H_h = 0.1 and 0.5 cases with respect to both the basic flow pattern and its stability. At H_h = 0.1 (Figure 2.3(a)) and 0.5 (Figure 2.3(b)), the bulk air meridional flow is one-cellular and clockwise. It is separated from the water clockwise circulation by a thin layer of anticlockwise circulation (TCL) adjacent to the interface from below. In contrast, the air flow is two-cellular and the TCL is adjacent to the interface from above at H_h = 0.9 in Figure 2.3(c).
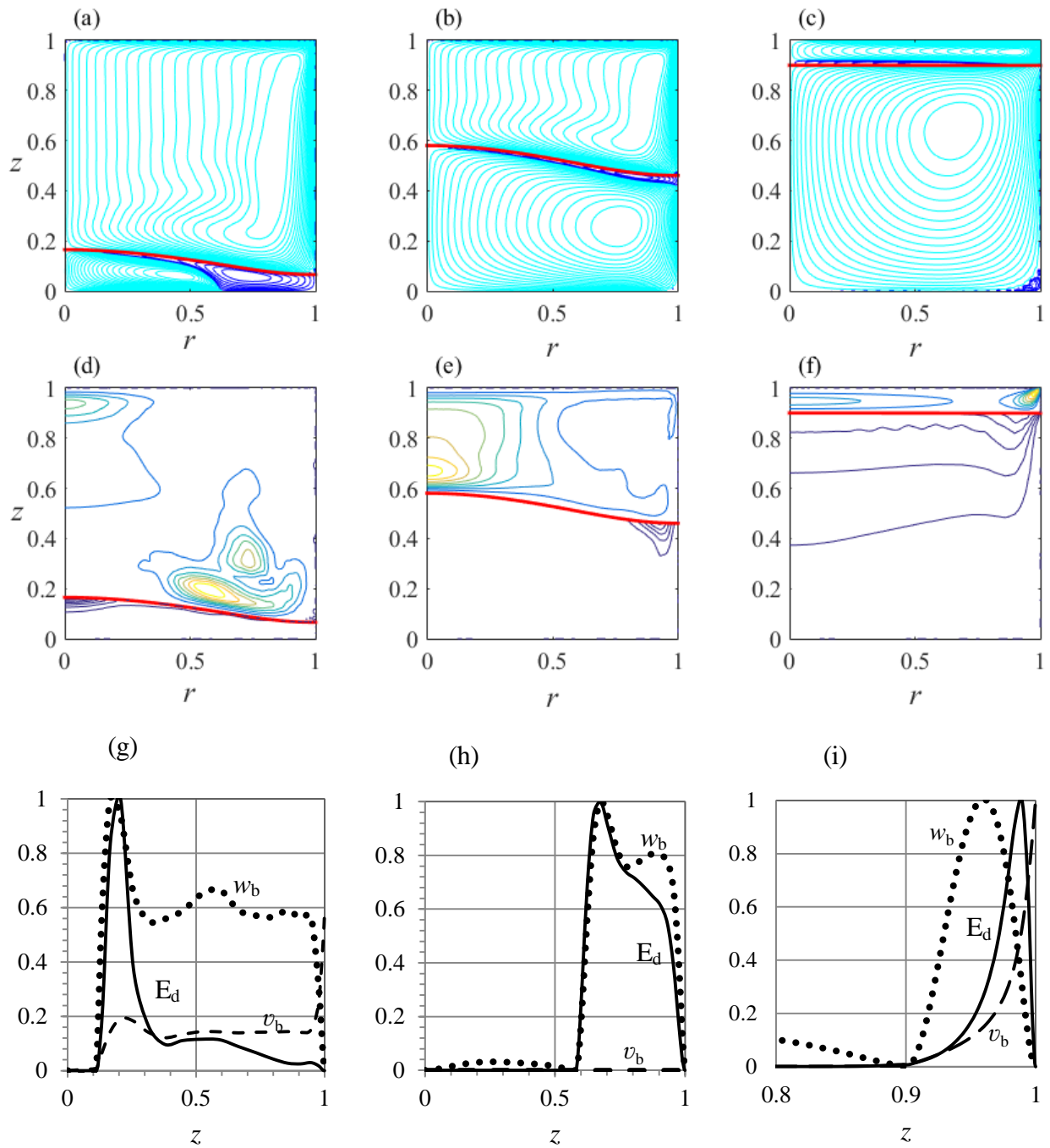
Figure 2.3 Streamline patterns of air-water flow at critical Re values (see Table 3) for water fraction $H_h = 0.1$ (a), 0.5 (b) and 0.9 (c). The bold curve shows the interface, light (dark) contours show clockwise (anticlockwise) meridional circulation. Contours of marginal disturbance energy E_d for $H_h = 0.1$ (d), 0.5 (e) and 0.9 (f); z-dependence of E_d, base-flow axial w_b and swirl v_b velocities at $r = r_m$ (see Table 4) for $H_h = 0.1$ (g), 0.5 (h) and 0.9 (i).

The $H_h = 0.8$ curve in Figure 2.4 shows that the radial velocity of base flow is negative, $u_b < 0$, that corresponds to a one-cell air flow, as Figure 2.5(a) schematically depicts. As H_h increases, u_b becomes positive near the axis, $r = 0$, up to point S, as curve $H_h = 0.825$ illustrates. Interpolation indicates that the $u_b > 0$ region emerges at $H_h = 0.8115$. This corresponds to a change in the flow topology. As Figure 2.5(b) schematically depicts, the air flow becomes two-cellular with the anticlockwise circulation in region ACa and clockwise circulation in region CCa while the water anticlockwise circulation region ACw becomes separated from the axis. All flow cells meet at the saddle point S of the meridional air-water motion.
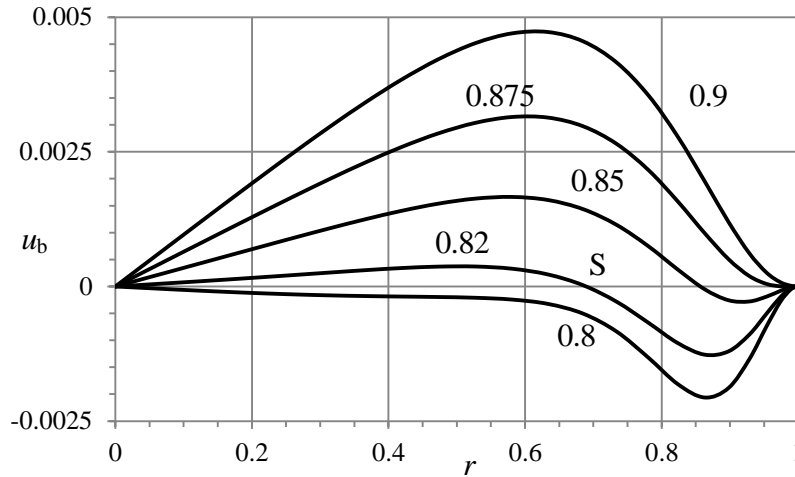
Figure 2.4 The base-flow radial velocity on the interface at H_h values shown near the curves.

In Figure 2.5, the notations CC and AC means clockwise and anticlockwise circulations in air (a) and water (w); subscripts of S denote saddle points at the interface (i), axis (a) and sidewall (w); thin curves separate regions of different circulations and show flow directions. The dashed line represents the interface.

Saddle point S moves from the axis toward the sidewall as H_h increases and reaches the sidewall at $H_h = 0.875$ (Figure 2.4). Accordingly region ACw shrinks to the sidewall-interface intersection and region ACa reaches the sidewall. For $H_h \geq 0.875$, the water flow is one-cellular and region CCa is separated from the interface as Figure 2.5(c) schematically depicts. The flow topology in Figure 2.3(c) is identical to that shown in Figure 2.5(c).
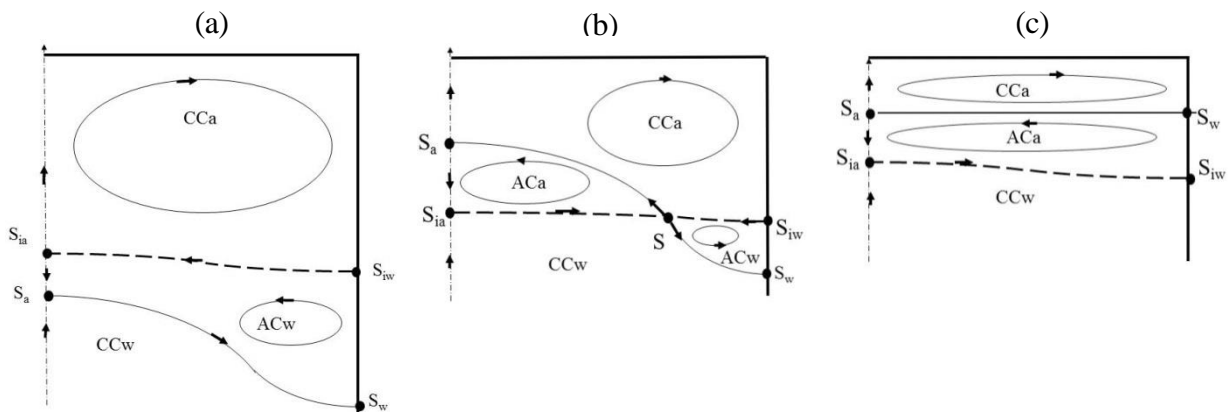
Figure 2.5 Schematics of flow topology changes as water fraction increases: $H_h = 0.8$ (a), 0.825 (b) and 0.9 (c).

These topological transformations cause that Re significantly decreases as the two right-hand columns of Table 2.3 illustrate.   The air flow becomes less stable because the radial double counterflow develops as Figure 2.5(c) illustrates. The air moving upward near the sidewall in region AC_a blocks transfer of angular momentum downward thus increasing the axial gradient of base-flow swirl velocity v_b near the lid; see Figure 2.3(i). The flow moving toward the sidewall near the interface reduces the transport of angular momentum to the axis thus increasing the magnitude of radial gradient of v_b near the sidewall as Figure 2.6 illustrates.
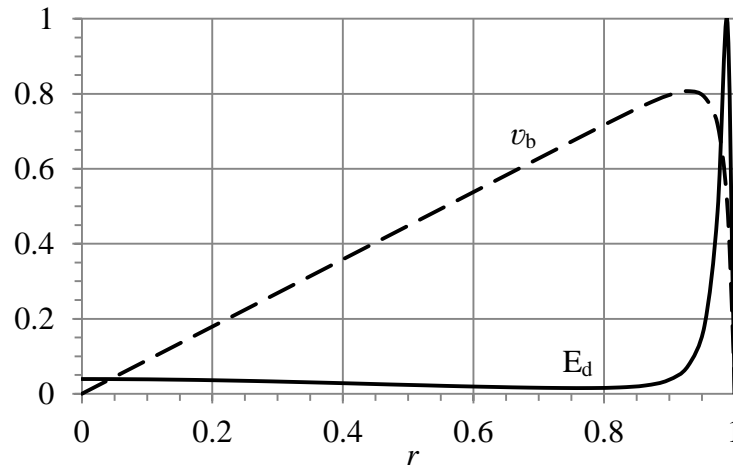
Figure 2.6 Radial profiles of basic-flow swirl velocity v_b and disturbance energy E_d at $H_h = 0.9$ and $z = z_m = 0.9894$ (see Table 4) help explain the centrifugal instability.

The sharp drop of v_b near r = 1 observed in Figure 2.6 causes the centrifugal (Taylor) instability. The necessary condition for the centrifugal instability is that $(rv)^2$ must decay as r increases [as it occurs in the Taylor-Couette flow where the inner (outer) cylinder is rotating (stationary)][22]. The v_b and E_d profiles in Figure 2.6 exactly match this Rayleigh criterion[22]: E_d peaks in the middle of near-sidewall region, where $(rv)^2$ reduces as r increases; and E_d is small in the region, where $(rv)^2$ grows with r.

2.5.2. Instability to multi-helix disturbances

Table 2.5 lists the marginal and critical (bold) values of the Reynolds number Re depending on the water fraction H_h and the azimuthal wave number m. Table 2.5 is limited to those m values which correspond to critical Re at least for one value of H_h. Frequency ω_r is shown only for critical disturbances and corresponding Re. Single-helix ($m = 1$) disturbance are the most dangerous if $H_h \geq$ 0.7. As the water fraction decreases, multi-helix disturbance become most dangerous as Table 2.5 shows.

H	Re	Re	Re	Re	ω_{rcr}
0	62718	**45699**	48620	5904	-
0	67260	50045	**39775**	5947	**0.05**
0	99045	54710	**46593**	6104	**0.03**
0	84165	61913	65861	**4832**	**0.08**
0	57492	72810	60414	**3904**	**0.09**
0	43140	65812	72495	**3985**	**0.09**
0	**18960**	51968	65199	4209	**0.03**
0	**10950**	20822	29445	3314	**0.06**
0	**2520**	5117	9684	1600	**0.26**

Table 2.5. Dependence of marginal and critical (bold) parameters on water fraction H_h and azimuthal wave number m.

Figure 2.7 depicts streamlines, (a) and (b), contours of disturbance energy E_d, (c) and (d), and z-profiles, (e) and (f), of E_d and base-flow radial velocity u_b at r corresponding to the location of maximal E_d (see Table 2.6). The first (second) column of Figure 2.6 corresponds to critical Re at H_h

= 0.1 (0.5); see Table 2.5. The results for critical Re at $H_h = 0.9$ are presented in the third column of Figure 2.3. Figure 2.7 indicates that the instability likely is of shear-layer kind and mostly develops in the jet-like air flow converging to the axis near the interface. Comparison of (a) the first two columns in Figure 2.3 and (b) Figure 2.7 shows that the single-helix (marginal) shear-layer instability develops near the axis while the multi-helix (critical) shear-layer instability develops near the interface. All instabilities, revealed in this chapter, occur in the air flow at Re values significantly larger than those at which VB and TCL emerge.
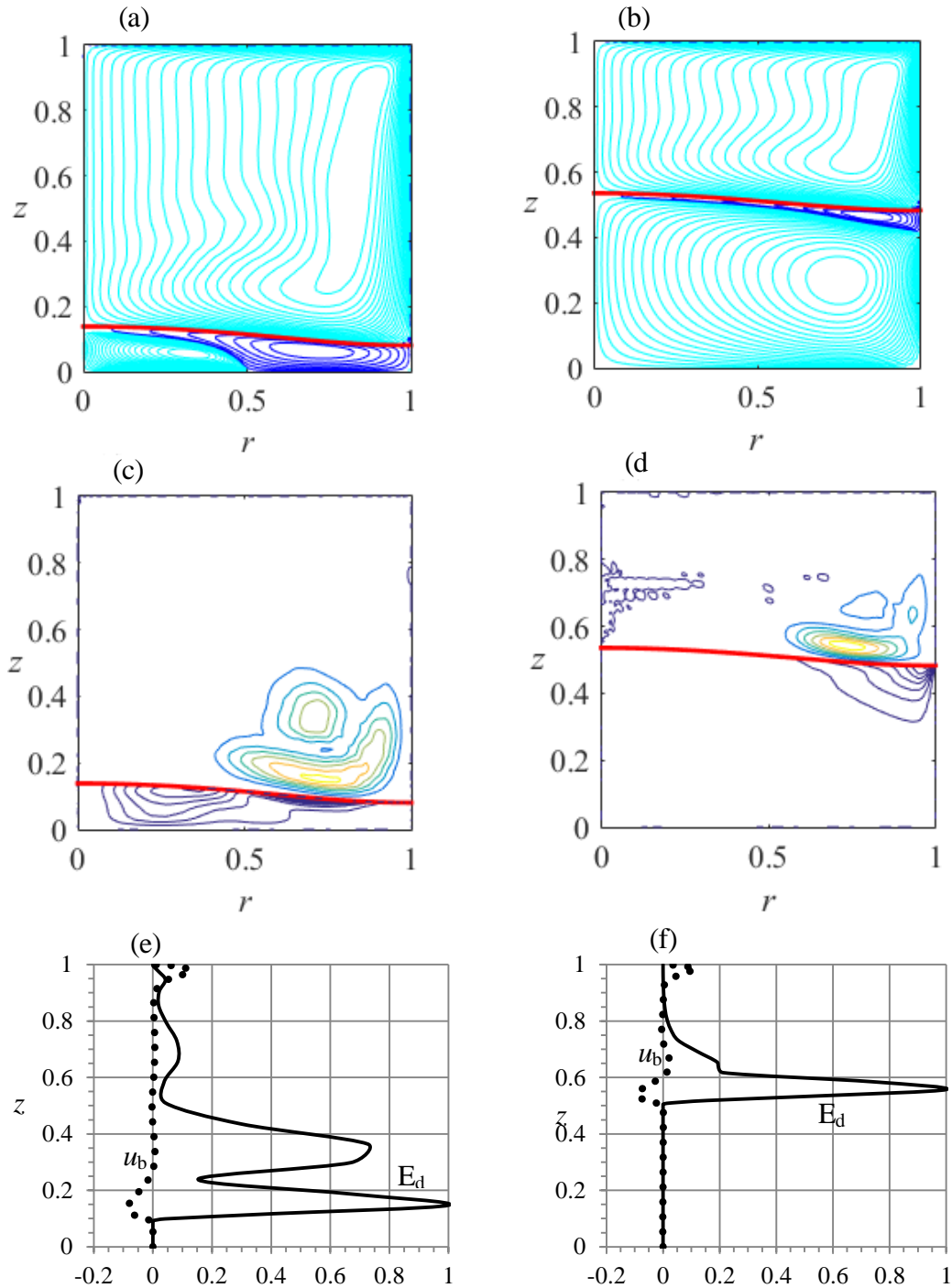
Figure 2.7 Streamline patterns of air-water flow at critical Re (see Table 2.5) for water fraction $H_h = 0.1$ (a) and 0.5 (b). The bold curve shows the interface, light (dark) contours show clockwise (anticlockwise) meridional circulation. Contours of marginal disturbance energy E_d for $H_h = 0.1$ (c) and 0.5 (d); z-dependence of E_d (solid curve) and base-flow radial velocity u_b (dots) velocities at $r = r_m$ (see Table 6) for $H_h = 0.1$ (e) and 0.5 (f).

H	0.1	0.5
r_m	0.7	0.73
z_m	0.1	0.54

Table 2.6 Dependence on water fraction H_h of radial r_m and axial z_m coordinates of absolute maximum of disturbance energy E_d for critical Re (see Table 5).

2.6. Conclusions

An efficient numerical technique is elaborated for stability studies of two-fluid flows. The key features are (a) mapping of heavy and light fluid regions in a standard square domain and (b) using a symbolic toolbox to calculate the analytical Jacobians. This helps us to linearize relation (2.6) for the stability studies. This technique is used here for flows of close densities and viscosities[117] and for air-water flows driven by the rotating lid in a sealed vertical container.

It is revealed that these flows become unstable at the Reynolds numbers significantly exceeding those at which the vortex breakdown emerges near the axis-bottom intersection and thin circulation layer develops near the interface[118]. The difference in the corresponding Reynolds numbers is especially large for the air-water flows.

As the heavy-fluid fraction decreases from 0.9 to 0.2, the critical Re grows and then drops at 0.1. For small and moderate values of heavy-fluid volume fraction, the instability likely is of shear-layer kind. For the fraction close to 1, the instability is centrifugal. In all cases investigated, the instability develops in the upper fluid. The obtained results are of fundamental interest and can be helpful in bioreactor designing.

3. TOPOLOGY AND STABILITY OF WATER-SOYBEAN-OIL SWIRLING FLOW

T his chapter reveals and explains the flow topology and instability hidden in the experimental study by Tsai et al.[2]. Water and soybean oil fill a sealed vertical cylindrical container. The rotating top disk induces the meridional circulation and swirl of both fluids. The experiment shows a flat-top interface shape and vortex breakdown in the oil flow developing as the rotation strength Re_o increases. Our numerical study shows that vortex breakdown occurs in the water flow at $Re_o = 300$ and in the oil flow at $Re_o = 941$. As Re_o increases, the vortex breakdown cell occupies most of the water domain and approaches the interface at Re_o around 600. The rest—counter-circulating—water separates from the axis as the vortex breakdown cells in the oil and water meet at the interface-axis intersection. This topological transformation of water flow significantly contributes to the development of the flat-top shape. It is also shown that the steady axisymmetric flow suffers from shear-layer instability which emerges in the water domain at $Re_o = 810$.

3.1. Introduction

Swirling two-fluid flows recently attracted the attention of researchers due to applications in aerial vortex bioreactors, a rapidly developing technology [51],[128], [115]. These flows have a number of intriguing features of fundamental interest: (i) numerous topological metamorphoses [129], (ii) multiple eddies [130], and (iii) thin circulation layers [118],[116], [117]. Fujimoto and Takeda [3] performed an interesting experiment which provided a vivid example of nonlinear physics. They visualized a flow of silicon oil and water driven by the rotating lid in a sealed cylindrical container. As the rotation strength Re_o increased, the interface became significantly deformed, taking shapes named by the authors as "hump", "cusp", "Mt. Fuji" and "bell". Similar results were obtained by Tsai et al. [2], who moreover detected vortex breakdown in the upper fluid. However, some important topological features of the lower-fluid motion remain uncovered in Refs. [2] and [3]. These features are related to the vortex breakdown in the water flow.

A topological metamorphosis of a swirling flow, which causes the emergence of a local circulation cell, often referred to as vortex breakdown (VB), has attracted the attention of researchers since 1957 due to its relevance to delta-wing aircraft, combustion, tornadoes, and other applications [109]. Many hypotheses have been suggested to interpret the VB physics [110]. A recent view is that the swirl-decay mechanism [131] explains why VB occurs and how it can be controlled [113], [114].

In contrast to the long-studied history of VB in a single fluid, two-fluid VB flows have only recently been examined. This chapter numerically investigates the flow experimentally studied by Tsai et al. [2] and reveals that the development of vortex breakdown in the upper fluid is preceded by the development of VB in the lower fluid as the rotation accelerates.

The VB cell emerges near the bottom center, expands upward, and approaches the interface near the axis. This near-axis rise of water causes a significant deformation of the interface. Next, VB occurs in the upper fluid as well. As the water and oil VB cells meet, they expand in the radial direction forming the flat-top shape of the interface.

This chapter shows that the steady axisymmetric flow suffers from shear-layer, time-oscillatory, three-dimensional instability which emerges in the water domain at $Re_o > 810$. Our stability analysis has been performed using a novel numerical technique, proving its efficiency for a two-fluid flow with a significantly curved interface [1].

3.2. Problem formulation

3.2.1. Flow geometry

Figure 3.1 is a schematic of the problem. The lower part, $0 < z < h_w$, of the cylindrical container of radius R and height h is filled with water; the upper part, $h_w < z < h$, is filled with soybean oil. With no motion, the interface is flat, $z = h_w$ (thin horizontal line in Figure 3.1). When the top disk (at $z = h$) rotates with angular velocity ω, while the other walls are stationary, the interface becomes deformed, typical of water-spouts, as the curve in Figure 3.1 schematically illustrates.
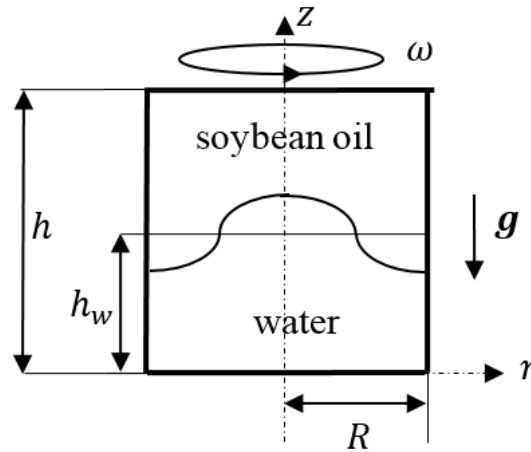
Figure 3.1 Schematic of water-spout model.

One control parameter is aspect ratio, $H = h/R$, which is fixed here: $H = 2.014$ that corresponds to Fig. 2 of Ref. [2] where $R = 7.2$ cm, $h = 14.5$ cm and $h_w = 1.5$ cm. The dimensionless height of the interface at rest, $H_w = h_w/R = 0.2083$, is also fixed here. To stay consistent with the experiment [2], we vary the Reynolds number, $Re_o = \omega R^2/v_o$, characterizing the swirl strength; v_o is the kinematic viscosity of soybean oil. It is also convenient to use $Re = \omega R^2/v_w$, v_w as the kinematic viscosity of water. Hereafter, subscripts "w" and "o" represent "water" and "oil" respectively.

The other varying parameters are the Froude number, $Fr = \omega^2 R/g = aRe^2$, which is a centrifugal-to-gravity acceleration ratio, and the Weber number, $We = \rho_w \omega^2 R^3/\sigma = bRe^2$, characterizing the effect of surface tension σ at the interface. Here, $g = 9.81$ m^2/s is the gravity acceleration, and ρ_w is the water density, $a = v_w^2/(gR^3)$ and $b = \rho_w v_w^2/(\sigma R)$. As the fluids are specified, coefficients a and b are fixed while Re varies.

To stay consistent with Ref. [2], we take $\rho_w = 1000$ kg/m^3, $\rho_o = 920$ kg/m^3, $v_w = 10^{-6}$ m^2/s. $v_o = 65.22 \times 10^{-6}$ m^2/s, and $\sigma = 0.02$ kg/s^2. This yields that $a = 2.731 \times 10^{-10}$ and $b = 6.944 \times 10^{-7}$.

3.2.2. Governing equations

Using R, ωR, and $\rho_w \omega^2 R^2$ as scales for length, velocity, and pressure, respectively, renders all variables dimensionless. We consider a flow of two viscous incompressible immiscible fluids governed by the Navier-Stokes equations [17],

$$\frac{1}{r}\frac{\partial(ru)}{\partial r} + \frac{1}{r}\frac{\partial v}{\partial \phi} + \frac{\partial w}{\partial z} = 0, \tag{3.1}$$

$$\frac{\partial u}{\partial t} + u\frac{\partial u}{\partial r} + \frac{v}{r}\frac{\partial u}{\partial \phi} + w\frac{\partial u}{\partial z} - \frac{v^2}{r} = -\rho_n\frac{\partial p}{\partial r} + \frac{\nu_n}{Re}\left(\nabla^2 u - \frac{u}{r^2} - \frac{2}{r^2}\frac{\partial v}{\partial \phi}\right), \tag{3.2}$$

$$\frac{\partial v}{\partial t} + u\frac{\partial v}{\partial r} + \frac{v}{r}\frac{\partial v}{\partial \phi} + w\frac{\partial v}{\partial z} + \frac{uv}{r} = -\frac{\rho_n}{r}\frac{\partial p}{\partial \phi} + \frac{\nu_n}{Re}\left(\nabla^2 v - \frac{v}{r^2} + \frac{2}{r^2}\frac{\partial u}{\partial \phi}\right), \tag{3.3}$$

$$\frac{\partial w}{\partial t} + u\frac{\partial w}{\partial r} + \frac{v}{r}\frac{\partial w}{\partial \phi} + w\frac{\partial w}{\partial z} = -\rho_n\frac{\partial p}{\partial z} + \frac{\nu_n}{Re}\nabla^2 w, \tag{3.4}$$

where $\nabla^2 \equiv \frac{1}{r}\frac{\partial}{\partial r}\left(r\frac{\partial}{\partial r}\right) + \frac{1}{r^2}\frac{\partial^2}{\partial \phi^2} + \frac{\partial^2}{\partial z^2}$ is the Laplace operator for a scalar field, (u, v, w) are the velocity components in cylindrical coordinates (r, ϕ, z), t is time, and p is pressure. The coefficients, ρ_n and ν_n, are both equal to 1 at $n = 1$ (in water) while $\rho_n = \rho_w/\rho_o$ and $\nu_n = \nu_o/\nu_w$ at $n = 2$ (in oil).

We denote the list (u, v, w, p) as $\boldsymbol{V}$, and look for a solution of the system 3.1 - 3.4 in the form

$$\boldsymbol{V} = \boldsymbol{V}_b(r, z) + \varepsilon \boldsymbol{V}_d(r, z)e^{(im\phi - i\omega t)} + c.c., \tag{3.5}$$

where subscripts "b" and "d" denote the base flow and a disturbance, respectively; $c.c.$ denotes the complex conjugate of the preceding term; $\varepsilon \ll 1$ is an amplitude; integer m is an azimuthal wave number; and $\omega = \omega_r + i\omega_i$ is a complex number to be found, with frequency ω_r and growth rate of disturbance ω_i. For a decaying (growing) disturbance, ω_i is negative (positive). The equations governing the base flow follow from substituting 3.5 in system 3.1 - 3.4 and setting $\varepsilon = 0$. The terms of order $O(\varepsilon)$ constitute equations governing infinitesimal disturbances.

3.2.3. Boundary conditions

Equations 3.1 - 3.4 are solved under the following boundary conditions:
(i)   Regularity at the axis, $0 < z < H,\ r = 0$:

   a) $u = v = 0, \partial w/\partial r = 0$ (base flow and $m = 0$ disturbances),

   b) $w_d = 0, u_d + v_d = 0, \partial u_d/\partial r = 0$ ($m = 1$ disturbances)

   c) $w_d = u_d = v_d = 0$ ($m > 1$ disturbances)

(ii)   No-slip at the walls: $u = v = w = 0$ at the still disk, $0 < r < 1, z = 0$, and at the sidewall, $0 < z < H, r = 1; u = w = 0, v = r$ at the rotating disk, $0 < r < 1, z = H$.

(iii)   Continuity of all the velocity and tangential stress components at the interface, $z = F(r, \phi, t)$. The balance for the normal stresses yields that

$$p_w - p_o = \frac{1}{We}\nabla.\boldsymbol{n} - \frac{1}{Re}\boldsymbol{n}.(\boldsymbol{\tau}_w - \mu_r\boldsymbol{\tau}_o).\boldsymbol{n} - \frac{1}{Fr}(1 - \rho_r)z, \tag{3.6}$$

where $\boldsymbol{n}$ is the unit vector perpendicular to the interface, $\boldsymbol{\tau}_w$ and $\boldsymbol{\tau}_o$ are tensors of the viscous stresses in the water and oil, respectively, and μ_r and ρ_r are the light-to-heavy fluid ratios of the dynamic viscosities and densities, respectively.

(iv) The kinematic equation for the interface shape, $z = F(r, \phi, t)$, yields that

$$\frac{\partial F}{\partial t} - w + u \frac{\partial F}{\partial r} + \frac{v}{r} \frac{\partial F}{\partial \phi} = 0,$$

3.7

and we look for a solution in the form $z = F_b(r,z) + \varepsilon F_d(r,z) e^{(im\phi - i\omega t)} + c.c..$

3.3. Numeric Technique

To simulate the nonlinear problem for the axisymmetric base flow and the generalized eigenvalue problem for disturbances, we use a numerical technique which is a variation of that described in detail in Ref. [1]. First, the water and oil regions are mapped onto the standard square domain ($0 \leq \eta_{(w,o)} \leq 1$, $0 \leq \xi \leq 1$) by means of the coordinate transformations (a) $\eta_w = z/F$ and $\xi = r$ and (b) $\eta_o = (z - F)/(H - F)$ and $\xi = r$ for the water and oil, respectively. Then, each variable (velocities, pressure field, and the interface shape) and all its spatial and temporal derivatives, which appear in the transformed equations, are composed as a single symbolic vector. For example, for the axial velocity in the water flow, we create a vector having 11 components: $\mathbf{x}_w = [w_w, \partial w_w/\partial \eta_w, \partial w_w/\partial \xi, \partial^2 w_w/\partial \eta^2, \partial^2 w_w/\partial \xi^2, \partial^2 w_w/\partial \xi \partial \eta, \partial w_w/\partial \phi, \partial^2 w_w/\partial \phi^2, \partial^2 w_w/\partial \phi \partial \xi, \partial^2 w_w/\partial \phi \partial \eta, \partial w_w/\partial t]$. The next step is to use a symbolic toolbox to calculate the analytical Jacobians of all the equations with respect to all the symbolic vectors. Using these analytical Jacobians, we generate functions which then are evaluated point by point in the square domains. In this procedure, we used the MATLAB procedure *matlabFunction* to convert the symbolic Jacobians in MATLAB functions.

Then, we carry out the spatial and temporal discretization of the problem. The water and oil domains are discretized using a set of n_w and n_o Chebychev spectral collocation points in the axial direction (along the η_w and ξ_o axes, respectively) [126]. The water and oil domains are discretized using a set of n_ξ Chebychev spectral collocation points in the radial direction, ξ. The second-order backward finite differences are used to compute the time derivatives for the base flow. Since the base flow is axisymmetric, all the azimuthal derivatives are set to zero. For disturbances, we obtain the temporal and azimuthal derivatives using the representation (3.5). This helps overcome the technical difficulty of linearizing relation (3.6) for the linear stability study of two-fluid flows.

The final step is to set up the numerical matrices, allowing us to solve the problem by using a Newton procedure for the base steady flow and by solving a generalized eigenvalue problem for disturbances. Details of this procedure are described in Ref. [1]

To summarize, the numeric procedure includes the mapping of water and oil regions, the proper spatial and temporal discretization creating the discrete Jacobian matrix of the Newton procedure for the base flow, and two more matrices for the generalized eigenvalue problem for disturbances. For the base flow, we get the final steady solution through an unsteady process. Starting from rest and selecting a time step, *dt*, the solution is advanced through time until a steady state is reached. Since the nonlinear procedure used to compute the base flow is fully implicit, a sufficiently large *dt* can be taken to quickly reach the steady solution. Once the base flow is computed and given an azimuthal wavenumber *m*, we use MATLAB subroutine *eigs* to calculate the eigenvalues (ω) for the system of discrete linear equations.

Most of the simulations presented here are done using $n_w = 60$ and $n_o = 25$ in the axial direction and $n_\xi = 40$ in the radial direction (standard grid), but due to their small circulation regions, some simulations for flows at large Re, are performed with finer grids. The larger n_w compared with n_o is used because the oil viscosity is significantly larger than the water viscosity.

Since the Chebyshev grid points concentrate near the interface from both sides, the approach is adequate to resolve thin circulation layers located near the interface, even at moderate values of n_w, n_o, and n_ξ. The Chebyshev grid points also concentrate near the axis and all walls, helping to resolve the small flow cells located near them.

To analyze the flow topology, we use the Stokes stream function Ψ, $w = r^{-1}\partial\Psi/\partial r$ and $u = -r^{-1}\partial\Psi/\partial z$, and plot streamlines of the meridional motion, i.e., contours $\Psi = $ constant.

3.4. Topologycal metamorphoses of water flow

3.4.1. Moffatt and near-interface eddies
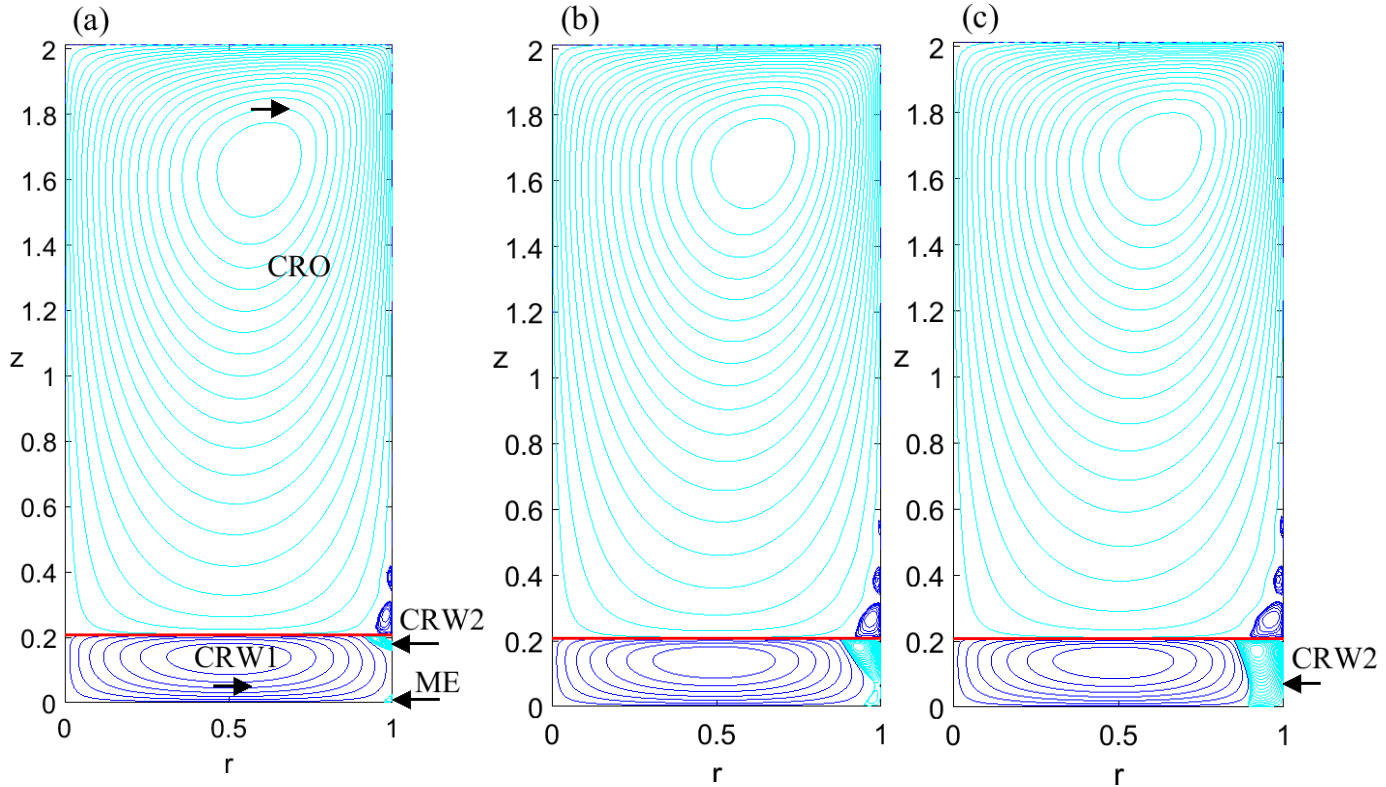
Figure 3.2. (color online) Patterns of meridional motion at $Re_o = 1$ (a), 40 (b) and 60 (c).

It is instructive to start with a creeping flow and to gradually increase Re_o. Figure 3.2 depicts streamlines at $Re_o = 1$ (a), 40 (b), and 60 (c). The bold (red online) curve denotes the interface. The clockwise (anticlockwise) circulation is shown hereafter by light (dark) contours which are blue online. Figure 2(a) depicts the pattern of the creeping flow. The rotating lid pushes the upper fluid to periphery near the lid and thus drives the clockwise circulation in CRO; CR is an abbreviation for "circulation region" and O denotes the oil. Near the interface, the oil moves toward the container axis.

The water flow is driven by two factors: (*i*) swirl and (*ii*) meridional velocities at the interface, both provided by the oil motion. The factors (*i*) and (*ii*) push the water in opposite directions; the swirl (meridional) velocity tends to drive the clockwise (anticlockwise) meridional circulation. For $Re_o = 1$, the swirl velocity at the interface is very small, as discussed in more detail below. Therefore, factor (*ii*) dominates over (*i*) and drives the bulk anticlockwise circulation marked as CRW1 in Figure 3.2(a), where W denotes the water.

This circulation induces the Moffatt eddies near the sidewall-bottom intersection, as Figure 3.2(a) illustrates. Moffatt [132] revealed that a flow in a corner (between two inclined planes with a sufficiently small angle) has an infinite set of eddies whose strength and scale diminish to zero as the edge is approached. Since the outmost eddy size is small compared with the cylinder radius, see ME in Fig. 2(a), the sidewall can be approximated by a tangential plane thus reducing the cylindrical geometry to the corner between orthogonal planes. The corner angle, 90°, is sufficiently small for the Moffatt eddies to occur [132]. Our numerical grid only resolves the outmost Moffatt eddy, denoted as ME in Figure 3.2(a).

The Moffatt eddies also develop near the interface-sidewall intersection [133]. Our numerical grid only resolves the outmost near-interface eddy in water, marked as CRW2 in Figure 3.2(a). CRW2 drives the small counter-circulation cell right above CRW2 in the oil flow. In turn, this cell induces one, in Fig. 2(a), or two, in Figure 3.2(b) and Figure 3.2(c), near-sidewall small eddies. As Re_o increases, ME and CRW2 expand in z-direction, touch each other, as Figure 3.2(b) illustrates, and merge. The merged cell is denoted again as CRW2 in Figure 3.2(c).

3.4.2. Vortex breakdown in water flow

The water moves upward in the bulk flow near the sidewall and thus blocks the downward transfer of the angular momentum from the interface. The angular momentum is transported toward the axis along the interface and then downward near the axis in the water domain. Therefore, the swirl effect is the strongest near the axis-bottom intersection where the VB cell emerges as Re_o increases and factor (i) strengthens. The VB cell is denoted as CRW3 in Figure 3.3(c).
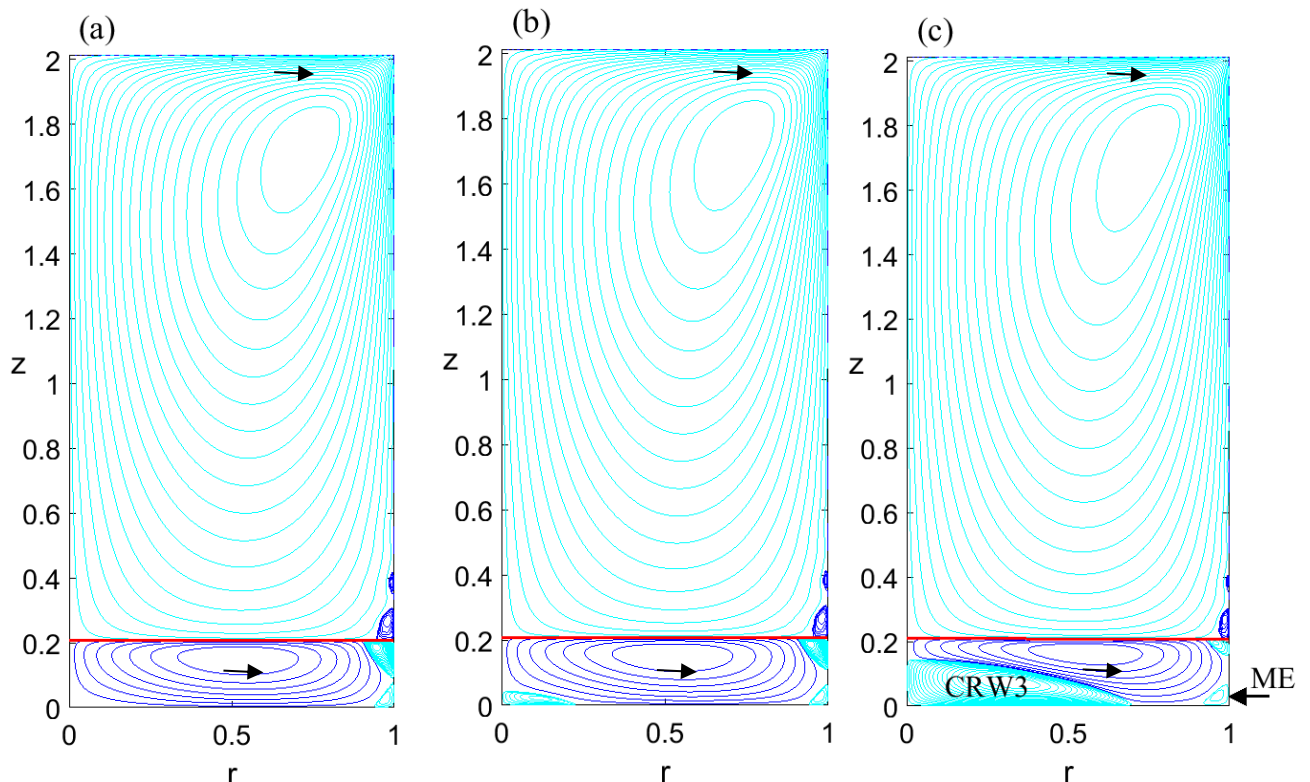
Figure 3.3 (Color online) Patterns of meridional motion at $Re_o = 300$ (a), 310 (b) and 370 (c) show formation of VB cell CRW3 in water.

Figure 3.4 shows the distribution of velocity w at the axis in water at $Re_o = 250$ (dashes), 300

(solid curve), and 305 (dots). To better observe small-magnitude velocity near the bottom, $z = 0$, Figure 3.4 plots $w^{1/3}$. As Re_o increases, the $w > 0$ range that corresponds to the VB water cell appears. Interpolating $\partial w/\partial z$ at $r = z = 0$ as a function of Re_o yields that CRW3 emerges at $Re_o \approx$ 300. Figure 3.5 depicts the dependence of the maximal value of swirl velocity at the interface, v_{si}, on Re_o. This dependence helps understand why the VB in water occurs at $Re_o = 300$. At small Re_o, the water rotation is very weak, $v_{si} = 0.0015$. The v_{si} value starts to significantly grow for $Re_o > 100$ and becomes nearly 0.07 at $Re_o = 300$, which corresponds to the inflection point of the curve in Figure 3.5
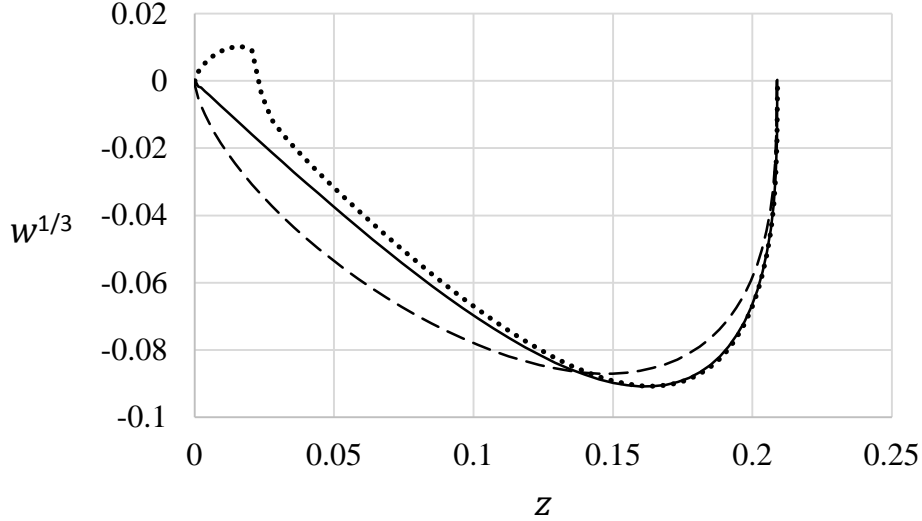
Figure 3.4 Distribution of velocity w at the axis in the water domain at $Re_o = 250$ (dashes), 300 (solid curve), and 305 (dots).
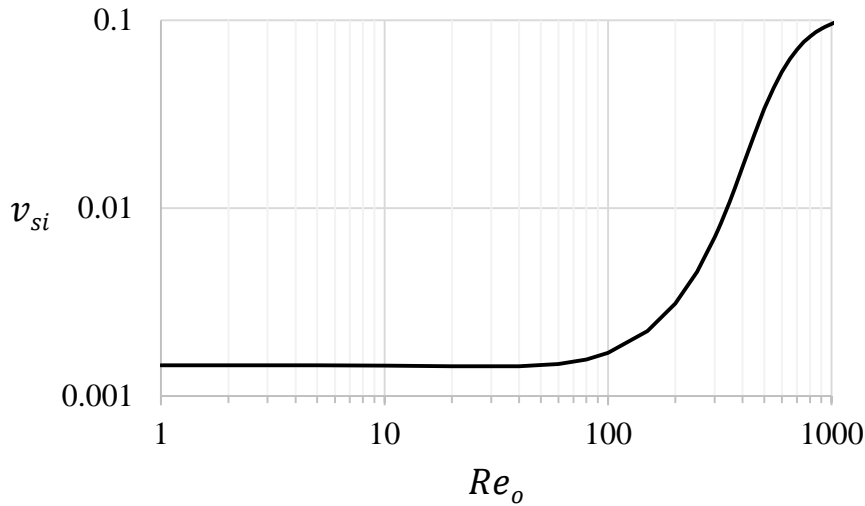
Figure 3.5 Dependence of maximal swirl velocity at the interface v_{si} on the Reynolds number.

    The Reynolds number, based on v_{si} and the water viscosity v_w, is $Re_w = 1370$ at $Re_o = 300$, i.e., the water rotates sufficiently fast for the nonlinear terms to become important in equations (3.2)-(3.4). As the rotating fluid meets a normal wall, the secondary flow develops [134]. This flow radially converges to the rotation axis near the wall and goes away from the wall near the axis. The driving mechanism for the secondary flow is the radial gradient of pressure. It develops away from the wall to balance the centrifugal force: $\partial p/\partial r = \rho v^2/r$. Near the wall, $\partial p/\partial r$ is not balanced by the centrifugal force (because it has the second-order zero since $v = 0$ at the wall) and pushes the fluid radially inward. This tornado-like secondary motion becomes sufficiently strong to overcome

the anticlockwise circulation of water near the axis-bottom intersection at $Re_o = 300$.

3.4.3. Formation of thin anticlockwise circulation layer in water

As Re_o further increases, the vortex breakdown cell CRW3 and the outmost Moffatt eddy ME, shown in Figure 3.3(c), merge and form the clockwise circulation, denoted again as CRW3 in Figure 3.6(a). The anticlockwise circulation CRW1 separates from the bottom, as Figure 3.6(a) illustrates at $Re_o = 400$, and becomes a thin layer, as Figure 3.6(b) illustrates at $Re_o = 600$. The z-extent of CRW1 at the axis, $r = 0$, becomes very small: 0.007 at $Re_o = 600$.
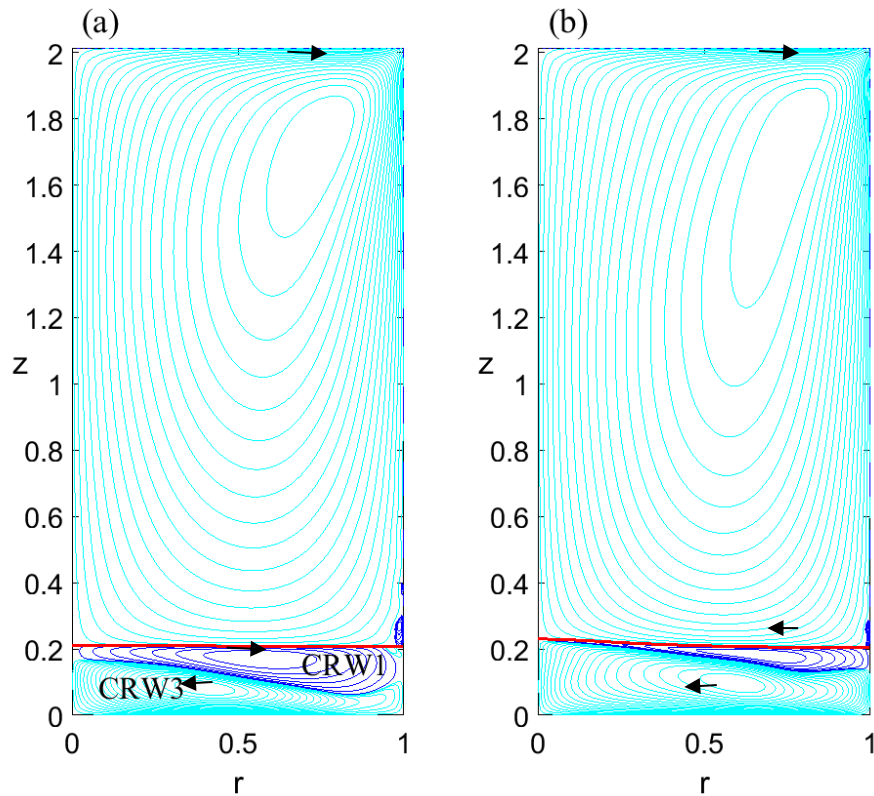
Figure 3.6 (color online) Patterns of meridional motion at $Re_o = 400$ (a) and 600 (b) show formation of thin anticlockwise circulation layer in water.

3.4.4. Growth of the interface height at the axis

This reduction results in the significant rise of the interface near the axis, driven by the water up-flow in region CRW3, as Figure 3.6(b) illustrates. Figure 3.7 depicts this trend in more detail by showing the dependence of the interface height at the axis, z_i, on Re_o.
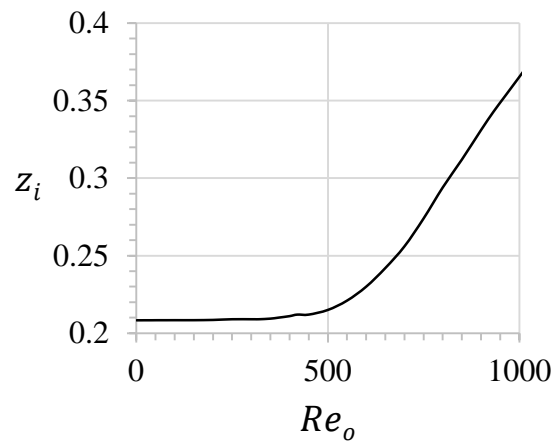
Figure 3.7 Dependence of interface height at the axis z_i on the rotation speed Re_o.

3.4.5. Formation of a bulge in the anticlockwise layer
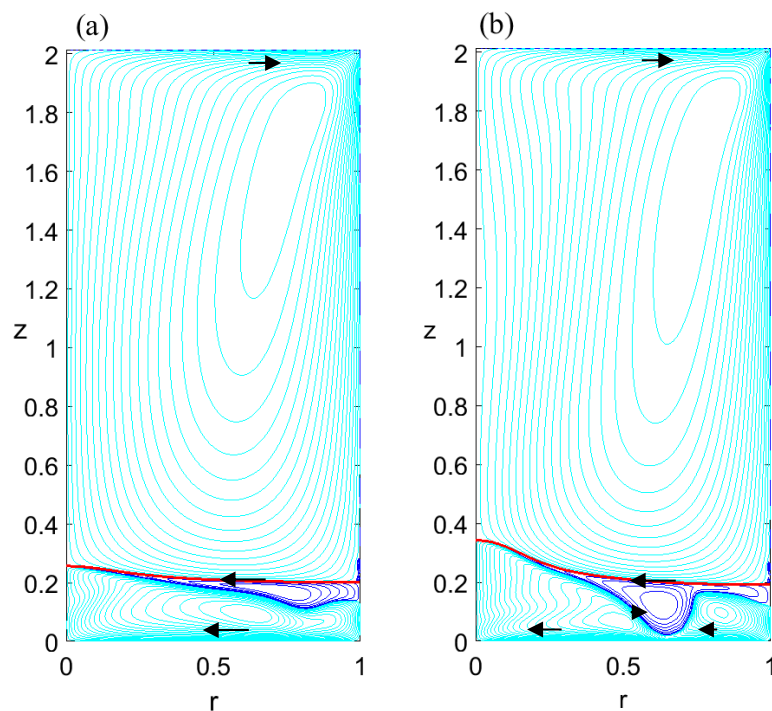
Figure 3.8 (color online) Patterns of meridional motion at $Re_o = 700$ (a) and 933 (b) show formation of a bulge in anticlockwise circulation layer in water.

The interface rises in the axis vicinity but remains nearly flat for $r > 0.3$, as Figure 3.8 illustrates. This causes an intriguing effect: the formation of a bulge in the anticlockwise water circulation. At $Re_o = 700$, the water motion is pretty fast, since $Re_w = 3742$. A strong jet forms near the interface. The interface peak at the axis makes this jet inclined downward. The inertia force separates the jet from the interface, where the interface becomes nearly flat, resulting in the bulge observed in Figure 3.8(b). The bulge divides the clockwise water circulation in the near-axis and near-sidewall parts in Figure 3.8(b). Figure 3.8(b) also shows that oil streamlines have a swelling near the axis for z close to 1.2. This swelling is a precursor of vortex breakdown in the oil flow discussed below.

3.5. Vortex breakdown in oil flow

3.5.1. Accumulation of swirl near the axis-interface intersection

Figure 3.8 indicates the formation of a jet radially converging toward the axis near the interface in the oil flow. This intensifies the swirl near the axis-interface intersection. The dashed ($Re_o = 700$) and solid ($Re_o = 850$) curves in Figure 3.9 show that the swirl velocity v at the interface increases with Re_o and its peak location shifts closer to the axis. This significantly increases the centrifugal acceleration, v^2/r, and consequently the radial gradient of pressure, resulting in a local pressure minimum near the axis-interface intersection.
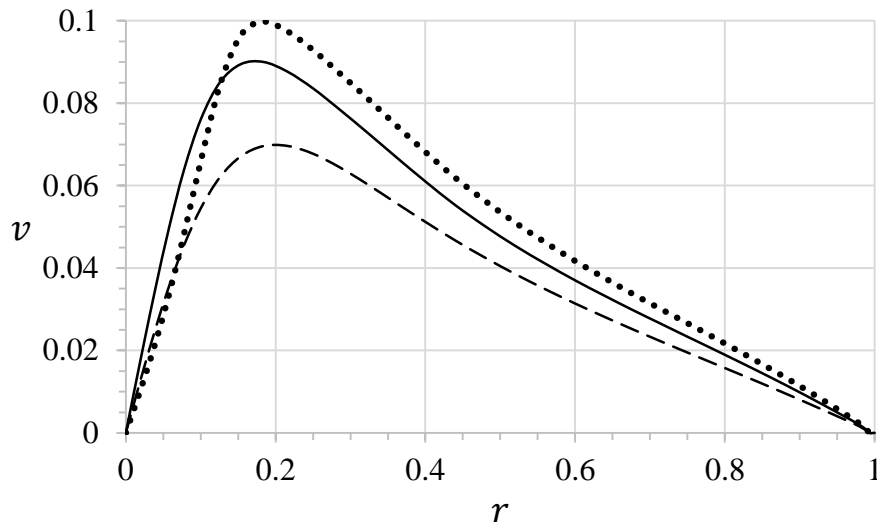
Figure 3.9 Distribution of swirl velocity at the interface at $Re_o = 700$ (dashes), 850 (solid curve) and 1082 (dots).
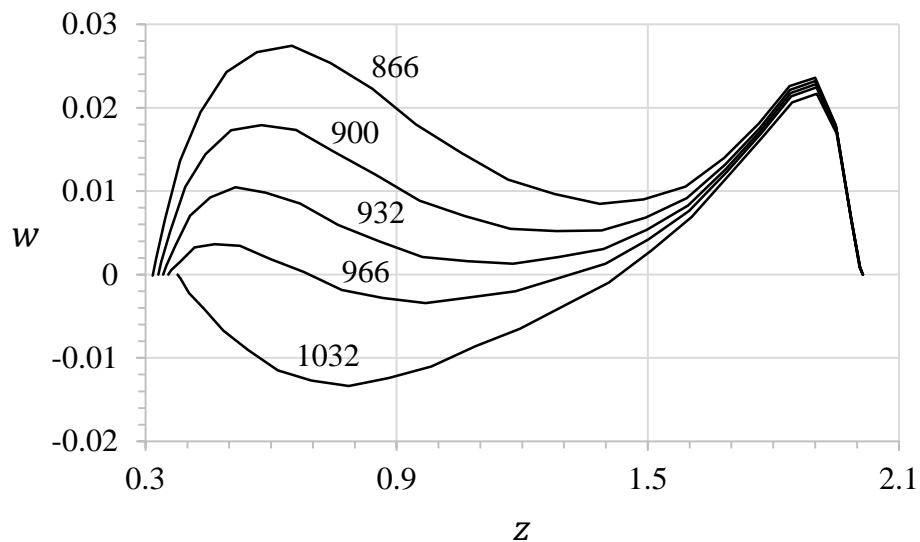
Figure 3.10 Distribution of oil velocity at the axis at Re_o values shown near the curves.

3.5.2. Distribution of velocity at the axis in the oil flow

The reduced pressure sucks the downstream oil, decelerating the upward oil motion near the axis. Figure 3.10 illustrates this trend by depicting the distribution of oil velocity at the axis at the Re_o values shown near the curves. A local minimum of w forms, its location approaches the interface, and its value decreases as Re_o increases.

3.5.3. Emergence and development of vortex breakdown in the oil flow

Interpolation of the local-minimal w value as a function of Re_o yields that vortex breakdown in oil occurs at $Re_o = 941$. The VB cell in oil emerges at the axis near $z = 1$ and then extends in both radial and axial directions. Interpolating of $\partial w/\partial z$ at the interface as a function of Re_o yields that the vortex breakdown cell reaches the interface at $Re_o = 1000$. Figure 3.11 depicts the vortex breakdown patterns at $Re_o = 966$ (a) and 1033 (b).

As the VB oil cell reaches the interface, it meets the VB water cell. Next, the stagnation saddle point S separates from the axis, as Figure 3.11(b) illustrates. The anticlockwise circulation region in water detaches from the axis as well. All bulk flow regions meet at S for $Re_o > 1000$. The vortex breakdown patterns in the oil flow, depicted in Figure 3.11, agree with the experimental vortex breakdown patterns shown in Figure 3.2(b) and (b*c) of Ref. [2].

In contrast, the striking pattern of the water flow is not resolved in Ref. [2]. An advantage of numerical simulations is that they help investigate a flow in fine details. In particular, our study reveals the complicated structure of the water flow, which plays an important role in the development of the flat-top shape (named as "Mt. Fuji" shape in Ref. [3]) of the oil-water interface.
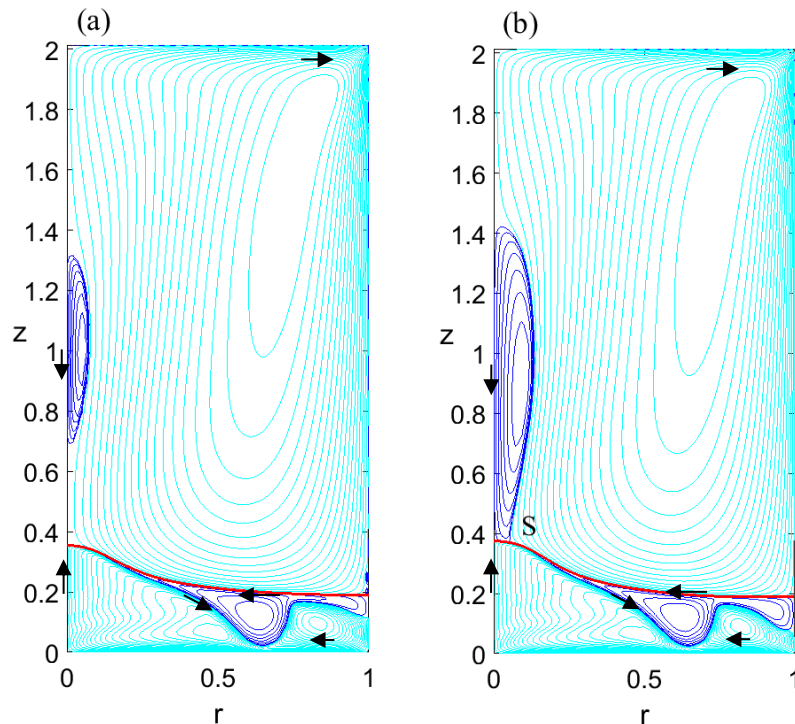
Figure 3.11 (color online) Patterns of meridional motion at $Re_o = 966$ (a) and 1033 (b) show vortex breakdown cell in oil.

3.6. Stability analysis

m	ω_r	Re	Re	v_{si}	v_{tm}	r_m	z_m
1	0.073	85	48	0.0827	-0.0342	0	0.0261
2	**0.0097**	**81**	**43**	**0.0867**	**-0.0315**	**0.714**	**0.153**
3	0.0241	84	46	0.0854	-0.0329	0.874	0.106
4	0.0388	84	47	0.0859	-0.0332	0.874	0.111

Table 3.1 Marginal ($\omega_i = 0$) and critical (bold) stability characteristics.

We refer a reader to Refs. [1] and [135] for technical details of the stability study and discuss the results summarized in Table 3.1. It lists the characteristics corresponding to the marginal disturbances at the azimuthal wave number $m = 1$, 2, 3, and 4. The marginal disturbances are neutral, $\omega_i = 0$, corresponding to Re_o at which all other eigenvalues have $\omega_i < 0$ for a prescribed m.
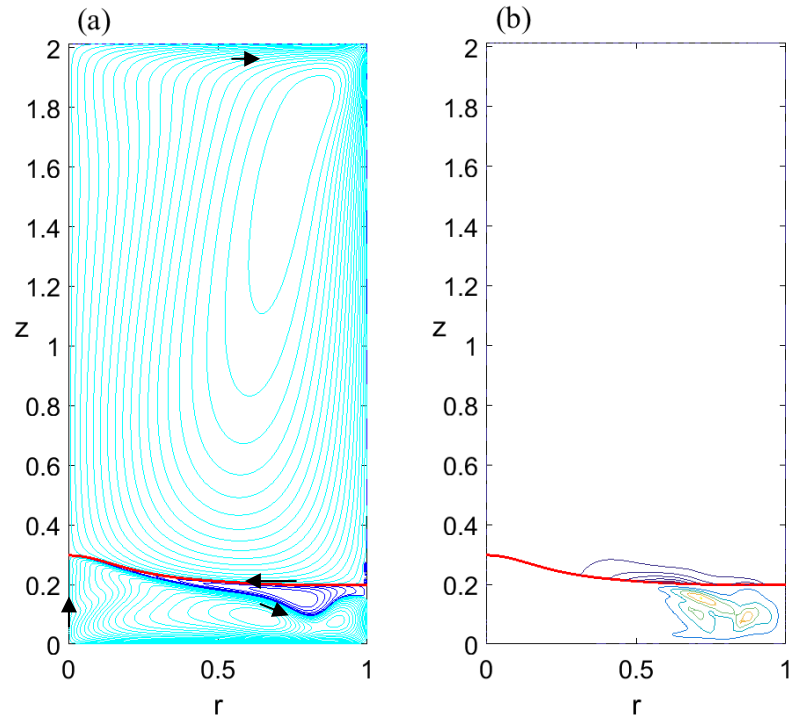
Figure 3.12 (color online) (a) Meridional motion and (b) contours of constant energy of critical disturbances at $Re_o = 810$ and $m = 2$.

The critical disturbance is the marginal one, corresponding to the minimal Re_o for all m. The critical characteristics are shown bold in Table 3.1. The Reynolds number of the water flow, Re_w, is based on the water viscosity, ν_w, and the maximal azimuthal velocity at the interface, whose dimensionless value, v_{si}, is also presented in Table 3.1. The minimal meridional tangential velocity at the interface, v_{tm}, is negative in Table 3.1 because it is directed toward the axis as Figure 3.12(a) illustrates. The location of peak marginal-disturbance squared velocity modulus, E_d, corresponds to $r = r_m$ and $z = z_m$ shown in the last two columns of Table 3.1. Here, $E_d = \langle |u_d|^2 + |v_d|^2 + |w_d|^2 \rangle$ where the brackets denote averaging with respect to time and azimuthal angle. E_d is normalized by its maximal value in the entire domain. A distribution of E_d indicates where the disturbance magnitude is maximal indicating where it most production occurs.

Other m values not presented in Table 3.1 correspond to larger Re_o. Thus, the flow becomes unstable with respect to time-oscillating three-dimensional disturbances for $Re_o > 810$.

Figure 2.1 depicts (a) streamlines of meridional motion and (b) contours E_d = constant at the critical $Re_o = 810$ and $m = 2$ and reveals that E_d is focused in the water domain. Figure 3.13 illustrates this feature in more detail by depicting z-distribution of base-flow radial velocity (v_r, solid curves) and disturbance energy (E_d, dashed curves) at $r = r_m = 0.714$ (see Table 3.1). For convenient observation in one figure, v_r is normalized by its maximal value in Figure 3.13.
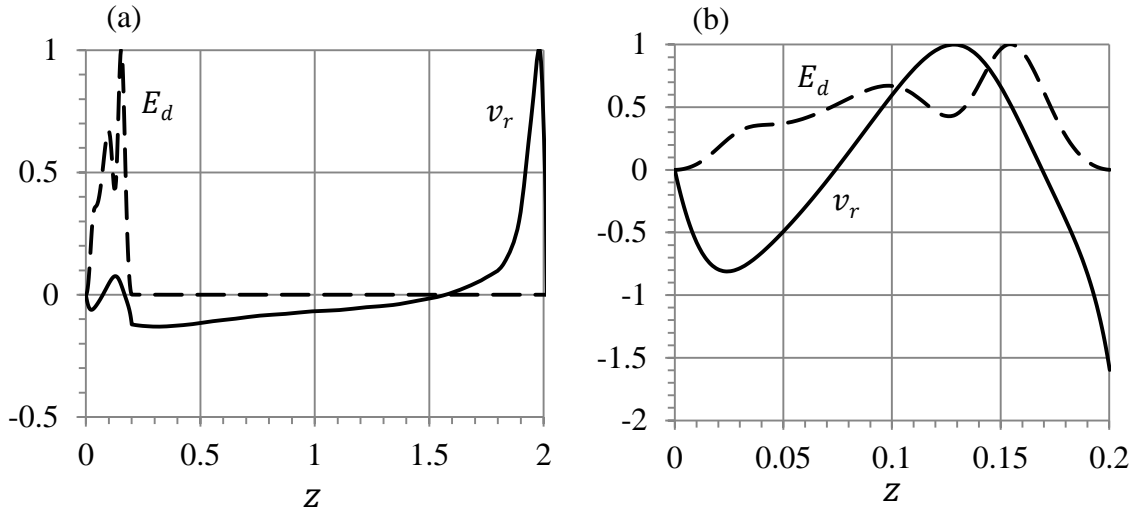
Figure 3.13 (a) z-distributions of bases-flow radial velocity v_r and critical disturbance energy E_d

at $r = 0.714$, $Re_o = 810$ and $m = 2$; (b) close-up of (a) for the water flow only.

The peak of radial velocity near $z = 2$ in Figure 3.13(a) corresponds to the jet-like oil flow near the rotating disk where the Kármán boundary layer [127] develops, which is well observed in Figure 3.12(a). The swirl and radial velocity magnitudes are significantly smaller near the interface (see the fifth and sixth columns in Table 3.1). The large value of $Re_w = 4371$ is due to the water viscosity being smaller by two orders of magnitude compared with the oil viscosity.

For the same reason, the disturbance energy in the oil is negligible compared to that in the water, as Figure 3.13(a) illustrates. This explains why in experiment [2], where the oil flow was only visualized, no effect was observed of time-oscillating three-dimensional water motion.

Figure 3.13(b) is a close-up of Figure 3.13(a) showing the water-flow features in more detail. The v_r profile depicts a well-developed counterflow with inflection points, one near $z = 0.08$ and the other at the interface, which is likely responsible for the found instability. The two local maxima of E_d, observed in Figure 3.12(b), are located in the two circulation water cells, observed in Figure 3.12(a). This supports our view that the instability is of shear-layer type.

3.7. Concluding remarks

a) This numerical study reveals the flow topology and instability hidden in the experimental study [2]. It shows that vortex breakdown occurs in the water flow at the Reynolds number, $Re_o = 300$, which is significantly smaller than $Re_o = 941$ corresponding to vortex breakdown in the oil flow.

b) For small Re_o, the bulk oil meridional circulation is clockwise and the water circulation is anticlockwise except in small Moffatt eddies occurring near the sidewall-bottom and sidewall-interface intersections (Figure 3.2a). The water-flow vortex breakdown causes the emergence of clockwise circulation near the bottom center (Figure 3.3). As Re_o increases, this circulation occupies most of water domain and approaches the interface at Re_o around 600 (Figure 3.6). The anticlockwise water circulation shrinks into a thin layer attached to the

entire interface.

c) The near-axis uprising water flow, emerging due to vortex breakdown, pushes the interface up and thus causes its significant deformation near the container axis (Figure 3.8).

d) At $Re_o = 810$, the flow becomes unstable with respect to time-oscillating three-dimensional disturbances with the azimuthal wave number $m = 2$ (Table 3.1). The disturbance energy focuses in the water flow near $r_m = 0.714$ and $z_m = 0.153$ where two cells of clockwise circulation develop (Figure 3.12). The disturbance energy drastically diminishes in the oil flow (Figure 3.13).

e) As the Reynolds number further increases, the vortex breakdown cells in oil and water meet at the interface-axis intersection at $Re_o = 1000$ and expand in the radial direction, forming the flat-top interface shape. Therefore, the observed topological transformations of water flow significantly contribute to the development of flat-top shape (Figure 3.11).

f) It seems that the water pulsations do not significantly affect the oil motion even for Re remarkably larger than 810 since the unsteadiness was not recognized in the experiment [2]. Figure 3.13(a) supports this conjecture indicating that E_d is concentrated in the water domain and is drastically reduced in the oil flow. The pulsations are damped by the oil viscosity which is 65 times the water viscosity. This explains why our results describing the topology transformations of oil flow agree with experiment.

4. METAMORPHOSIS IN A WATER-OIL SWIRLING FLOW

T his chapter reveals the flow topology hidden in the experimental study by Fujimoto & Takeda [3]. Water and silicone oil fill a sealed vertical cylindrical container. The rotating top disk induces the meridional circulation and swirl of both fluids. The experiment shows a striking deformation of interface as the rotation strength Re increases. Our numerical study reveals that the water motion is two-cellular and the upper cell is a thin circulation layer attached to the entire interface for Re values at which the striking deformation occurs. The layer has an unusual topology being a bubble-ring in the range of Re specified in the paper. In addition, our study reveals that the steady axisymmetric flow suffers from the shear-layer instability before the interface becomes remarkably deformed.

4.1. Introduction

Swirling two-fluid flows have a number of intriguing and practically important features absent in one-fluid flows. Among them are numerous topological metamorphoses [129], the formation of multiple eddies [130] and thin circulation layers [118],[116], [117]. One application is aerial vortex bioreactors which is a rapidly developed technology [128],[51],[115]. An advantage of studying these flow phenomena in a sealed container is well-defined and controlled boundary conditions allowing for meaningful comparisons of experimental and numerical results.

A topological metamorphosis of a swirling flow, related to the emergence of a local circulation cell, which often referred to as vortex breakdown (VB), has attracted the attention of researchers starting from 1957 due to its relevance to delta-wing aircraft, combustion, tornadoes, and other applications [109]. Many hypotheses have been suggested to interpret the VB nature [110]. A recent view is that the swirl-decay mechanism [112] explains why VB occurs and how it can be controlled [114],[113].

In contrast to the long-history studies of VB in a single fluid, two-fluid VB flows have been addressed only a few years ago. An interesting experiment, providing a vivid example of nonlinear physics, was performed by Fujimoto and Takeda [3]. They visualized a flow of silicone oil and water driven by the rotating lid of a sealed cylindrical container. As the rotation strength Re increases, the interface becomes significantly deformed taking shapes named by the authors as "hump", "cusp", "Mt. Fuji" and "bell". They also observed generation of water droplets. Similar results were obtained by Tsai et al [2] who also detected vortex breakdown in the upper fluid. Here we show that VB occurs in the lower fluid as well.

This and some other important topological features of the lower-fluid flow remain uncovered in Ref. [3]. This investigation shows that (a) the water flow is two-cellular, (b) the upper cell has a bubble-ring shape and (c) the flow suffers from the shear-layer instability. These features develop at smaller values of the Reynolds number Re than those at which the interface becomes remarkably deformed. They might affect the phenomena observed in Ref. [3]. Our stability analysis of this flow has been performed using a novel numerical technique proved its efficiency for a two-fluid flow with a curved interface [1].

The physical reason for the two-cell water flow is the competing driving factors: (a) swirl and (b) meridional velocities of oil at the interface. For small water fraction H_w, factor (b) dominates and the bulk water flow circulates in the opposite direction to the oil circulation. As H_w and Re increases, factor (a) causes the co-circulation of water near the bottom. The counter-circulation near the interface becomes a thin layer with a paradoxical—bubble-ring—topology.

The instability emerges near the center of water co-circulation. We argue that this instability likely is of the shear-layer kind and caused by inflection points in the radial distribution of axial velocity. The instability is time-oscillatory and three-dimensional with the azimuthal wave number m = 4. The instability develops at Re being around three times smaller than that at which the interface becomes of "Mt. Fuji" shape in the experiment [3].

4.2. Problem formulation

4.2.1. Flow Geometry

Figure 4.1 is a schematic of the problem. The lower part, $0 < z < h_w$, of the cylindrical container of radius R and height h is filled with water; the upper part, $h_w < z < h$, is filled with silicone oil. With no motion, the interface is flat, $z = h_w$ (thin horizontal line in Figure 4.1). When the top disk (at $z = h$) rotates with angular velocity ω, while the other walls are stationary, the interface becomes deformed, typical of water-spouts, as the curve in Figure 4.1 schematically shows.
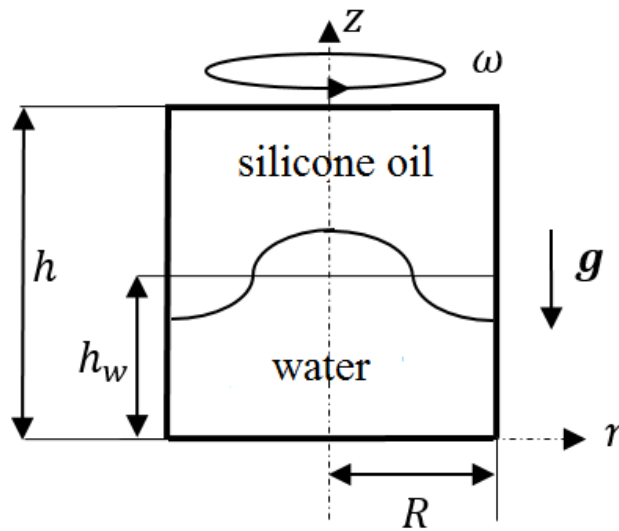
Figure 4.1 Schematic of water-spout model.

One control parameter is aspect ratio $H = h/R$ which is fixed here: $H = 2.3$ that corresponds to the results shown in Fig. 2 of Ref. [3]. The dimensionless height of the interface at rest is $H_w = h_w/R$. We vary H_w in order to explain how the two-cell water flow develops. Other control parameters are the Reynolds number, $Re = \omega R^2/\nu_w$, characterizing the swirl strength, the Froude number, $Fr = \omega^2 R/g = aRe^2$, which is a centrifugal-to-gravity acceleration ratio, and the Weber number, $We = \rho_w \omega^2 R^3/\sigma = bRe^2$, characterizing the effect of surface tension σ at the interface; $g = 9.81$ m^2/s is the gravity acceleration, ρ_w is the density of water, $a = \nu_w^2/(gR^3)$ and $b = \rho_w \nu_w^2/(\sigma R)$. As the fluids are specified, coefficients a and b are fixed while Re varies.

According to Ref. [3], we take $R = 0.095$ m, $\rho_w = 1000$ kg/m^3, $\rho_o = 965$ kg/m^3, $\nu_w = 10^{-6}$ m^2/s. $\nu_o = 137.5 \times 10^{-6}$ m^2/s (we use the middle value of the ν_o range indicated in Ref. [3]), and $\sigma = 0.042$ kg/s^2. This yields that $a = 1.19 \times 10^{-10}$ and $b = 2.51 \times 10^{-7}$. Hereafter, subscripts "w" and "o" mean

"water" and "oil" respectively.

4.2.2. Governing equations

Using R, ωR, and $\rho_w \omega^2 R^2$ as scales for length, velocity, and pressure, respectively, renders all variables dimensionless. We consider a flow of two viscous incompressible immiscible fluids governed by the Navier-Stokes equations [125],

$$\frac{1}{r}\frac{\partial(ru)}{\partial r} + \frac{1}{r}\frac{\partial v}{\partial \phi} + \frac{\partial w}{\partial z} = 0, \tag{4.1}$$

$$\frac{\partial u}{\partial t} + u\frac{\partial u}{\partial r} + \frac{v}{r}\frac{\partial u}{\partial \phi} + w\frac{\partial u}{\partial z} - \frac{v^2}{r} = -\rho_n\frac{\partial p}{\partial r} + \frac{v_n}{Re}\left(\nabla^2 u - \frac{u}{r^2} - \frac{2}{r^2}\frac{\partial v}{\partial \phi}\right), \tag{4.2}$$

$$\frac{\partial v}{\partial t} + u\frac{\partial v}{\partial r} + \frac{v}{r}\frac{\partial v}{\partial \phi} + w\frac{\partial v}{\partial z} + \frac{uv}{r} = -\frac{\rho_n}{r}\frac{\partial p}{\partial \phi} + \frac{v_n}{Re}\left(\nabla^2 v - \frac{v}{r^2} + \frac{2}{r^2}\frac{\partial u}{\partial \phi}\right), \tag{4.3}$$

$$\frac{\partial w}{\partial t} + u\frac{\partial w}{\partial r} + \frac{v}{r}\frac{\partial w}{\partial \phi} + w\frac{\partial w}{\partial z} = -\rho_n\frac{\partial p}{\partial z} + \frac{v_n}{Re}\nabla^2 w, \tag{4.4}$$

where $\nabla^2 \equiv \frac{1}{r}\frac{\partial}{\partial r}\left(r\frac{\partial}{\partial r}\right) + \frac{1}{r^2}\frac{\partial^2}{\partial \phi^2} + \frac{\partial^2}{\partial z^2}$ is the Laplace operator for a scalar field, (u, v, w) are the velocity components in cylindrical coordinates (r, ϕ, z), t is time, and p is pressure. The coefficients, ρ_n and v_n, are both equal 1 at $n = 1$ (in water) while $\rho_n = \rho_w/\rho_o$ and $v_n = v_o/v_w$ at $n = 2$ (in silicone oil).

We denote the list (u, v, w, p) as $\boldsymbol{V}$, and look for a solution of the system 4.1- 4.4 in the form

$$\boldsymbol{V} = \boldsymbol{V}_b(r, z) + \varepsilon \boldsymbol{V}_d(r, z)e^{(im\phi - i\omega t)} + c.c., \tag{4.5}$$

where subscripts "b" and "d" denote the base flow and a disturbance, respectively; $c.c.$ denotes the complex conjugate of the preceding term; $\varepsilon \ll 1$ is an amplitude; integer m is an azimuthal wave number; and $\omega = \omega_r + i\omega_i$ is a complex number to be found, with frequency ω_r and growth rate of disturbance ω_i. For a decaying (growing) disturbance, ω_i is negative (positive). The equations governing the base flow result from substituting 4.5 in system 4.1- 4.4 and setting $\varepsilon = 0$. The terms of order $O(\varepsilon)$ constitute equations governing infinitesimal disturbances.

4.2.3. Boundary conditions

Equations 4.1 - 4.4 are solved under the following boundary conditions:
(i)   Regularity at the axis, $0 < z < H$, $r = 0$:

   d) $u = v = 0, \partial w/\partial r = 0$ (base flow and $m = 0$ disturbances),

   e) $w_d = 0, u_d + v_d = 0, \partial u_d/\partial r = 0$ ($m = 1$ disturbances)

   f) $w_d = u_d = v_d = 0$ ($m > 1$ disturbances)

(ii)   No-slip at the walls: $u = v = w = 0$ at the still disk, $0 < r < 1$, $z = 0$, and at the sidewall, $0 < z < H, r = 1$; $u = w = 0, v = r$ at the rotating disk, $0 < r < 1, z = H$.

(iii)   Continuity of all the velocity and tangential stress components at the interface, $z =$

$F(r, \phi, t)$. The balance for the normal stresses yields that

$$p_w - p_o = \frac{1}{We} \nabla . \boldsymbol{n} - \frac{1}{Re} \boldsymbol{n}.(\boldsymbol{\tau}_w - \mu_r \boldsymbol{\tau}_o).\boldsymbol{n} - \frac{1}{Fr}(1 - \rho_r)z, \qquad 4.6$$

where $\boldsymbol{n}$ is the unit vector perpendicular to the interface, $\boldsymbol{\tau}_w$ and $\boldsymbol{\tau}_o$ are tensors of the viscous stresses in the water and oil, respectively, and μ_r and ρ_r are the light-to-heavy fluid ratios of the dynamic viscosities and densities, respectively.

(iv)   The kinematic equation for the interface shape, $z = F(r, \phi, t)$, yields that

$$\frac{\partial F}{\partial t} - w + u \frac{\partial F}{\partial r} + \frac{v}{r} \frac{\partial F}{\partial \phi} = 0, \qquad 4.7$$

and we look for a solution in the form $z = F_b(r, z) + \varepsilon F_d(r, z) e^{(im\phi - i\omega t)} + c.c..$

4.3. Numeric Technique

To simulate the nonlinear problem for the axisymmetric basic flow and the generalized eigenvalue problem for disturbances, we use a numerical technique which is a variation of that described in detail in Ref. [1]. First, the water and oil regions are mapped onto the standard square domain ($0 \leq \eta_{(w,o)} \leq 1, 0 \leq \xi \leq 1$) by means of the coordinate transformations (a) $\eta_w = z/F$ and $\xi = r$ and (b) $\eta_o = (z-F)/(H-F)$ and $\xi = r$ for the water and oil, respectively. Then, each variable (velocities, pressure field and the interface shape) and all its spatial and temporal derivatives, which appear in the transformed equations, are composed as a single symbolic vector. For example, for the axial velocity in the water flow we create a vector having 11 components: $\mathbf{x}_w = [w_w, \partial w_w/\partial \eta_w, \partial w_w/\partial \xi, \partial^2 w_w/\partial \eta^2, \partial^2 w_w/\partial \xi^2, \partial^2 w_w/\partial \xi \partial \eta, \partial w_w/\partial \phi, \partial^2 w_w/\partial \phi^2, \partial^2 w_w/\partial \phi \partial \xi, \partial^2 w_w/\partial \phi \partial \eta, \partial w_w/\partial t]$. The next step is to use a symbolic toolbox to calculate the analytical Jacobians of all the equations with respect to all the symbolic vectors. Using these analytical Jacobians we generate functions which then are evaluated point by point in the square domains. In this procedure, we used the MATLAB procedure *matlabFunction* to convert the symbolic Jacobians in MATLAB functions.

Then, we carry out the spatial and temporal discretization of the problem. The water and oil domains are discretized using a set of n_w and n_o Chebyshev spectral collocation points in the axial direction (along the η_w and ξ_o axes, respectively) [126]. The water and oil domains are discretized using a set of n_ξ Chebyshev spectral collocation points in the radial direction, ξ. The second-order backward finite differences are used to compute the time derivatives for the basic flow. Since the basic flow is axisymmetric, all the azimuthal derivatives are set to zero. For disturbances, we obtain the temporal and azimuthal derivatives using the representation (5).

The final step is to set up the numerical matrices allowing us to solve the problem by using a Newton procedure for the basic steady flow and by solving a generalized eigenvalue problem for disturbances. Details of this procedure are described in Ref. [1].

To summarize, the numeric procedure includes the mapping of water and oil regions, the proper spatial and temporal discretization creating the discrete Jacobian matrix for the Newton procedure for the basic flow and two more matrices for the generalized eigenvalue problem for disturbances. For the basic flow, we get the final steady solution though an unsteady process. Starting from the rest and selecting a time step, dt, the solution is advanced in time until a steady state is reached. Since the nonlinear procedure used to compute the basic flow is fully implicit, dt can be taken sufficiently large to quickly reach the steady solution. Once the base flow is computed, and given an azimuthal

wavenumber *m*, we use MATLAB subroutine *eigs* to calculate the eigenvalues (ω) of the system of discrete linear equations.

Most of the simulations presented here are done using $n_w = 50$, $n_o = 25$, and $n_\xi = 40$ (standard grid), but some runs for flows, having small circulation regions, are performed with more fine grids. Since the Chebyshev grid points concentrate near the interface from both sides, the approach is adequate to resolve thin circulation layers, located near the interface, even at moderate values of n_w, n_o, and n_ξ.

To analyze the flow topology, we use the Stokes stream function Ψ, $w = r^{-1}\partial\Psi/\partial r$ and $u = -r^{-1}\partial\Psi/\partial z$, and plot streamlines of the meridional motion, i.e., contours $\Psi = $ constant.

4.4. Topological metamorphoses of water flow

4.4.1. Creeping flow

It is instructive to start with a creeping flow, where the flow topology only depends on the fluid fractions. Figure 4.2 depicts streamlines at $Re = 1$, $H = 2.3$ and $H_w = 0.9$ (a), 0.93 (b), 0.95 (c).
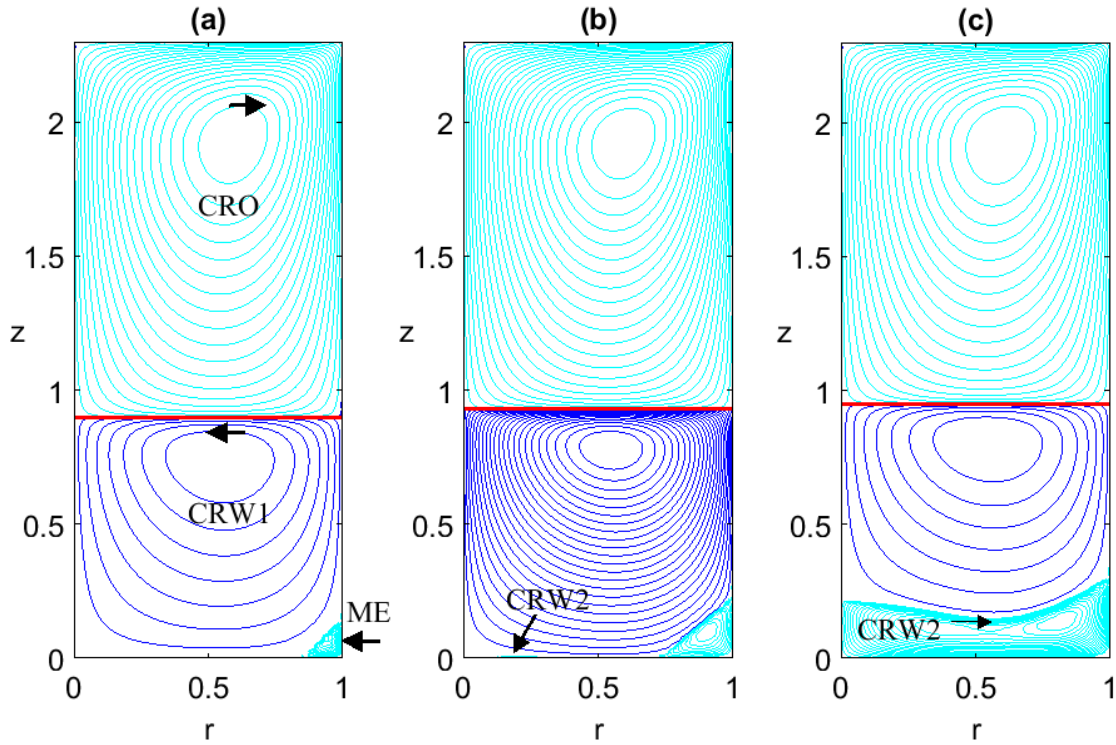
Figure 4.2 Patterns of creeping flow at water height $H_w = 0.9$ (a), 0.93 (b) and 0.95 (c).

Figure 4.2(a) shows the simplest flow pattern. The rotating lid pushes the silicon oil to periphery and thus drives the clockwise circulation in CRO; CR is an abbreviation for "circulation region" and O denotes the oil. Near the interface, the oil moves toward the container axis.

The water flow is driven by two factors: (a) swirl and (b) meridional velocities at the interface, both provided by the oil motion. The factors (a) and (b) pushes the water in opposite directions: the swirl (meridional) velocity tends to drive the clockwise (anticlockwise) circulation. For small H_w, factor (b) dominates [114], and the bulk water circulation is anticlockwise as Figure 4.2(a) shows in CRW1; here W denotes the water flow.

The water circulation induces the Moffatt eddies (ME) near the sidewall-bottom intersection. Moffatt [132] revealed that a flow in a corner (between two inclined planes with a sufficiently small

angle) has an infinite set of eddies whose strength and scale diminish to zero as the edge is approached. Since the outmost eddy size is small compared with the cylinder radius, e.g., see ME in Figure 4.2(a), the sidewall can be approximated by a tangential plane thus reducing the cylindrical geometry to the corner between orthogonal planes. The corner angle, 90°, is sufficiently small for the Moffatt eddies to occur. Our numerical grid only resolves the outmost Moffatt eddy: ME in Figure 4.2(a).

The water moves upward to the interface near the sidewall and thus blocks the downward transfer of the angular momentum there. The angular momentum is transported toward the axis near the interface and then downward near the axis. Therefore, the swirl effect is the strongest near the axis-bottom intersection where, as H_w increases, factor (a) generates CRW2 shown in Figure 4.2(b). Interpolating the velocity distribution at the axis yields that CRW2 emerges at H_w being very close to 0.93 that explains why CRW2 is so small in Figure 4.2(b).

As H_w further increases, CRW2 and ME expand. They merge into a single region denoted again as CRW2 in Figure 4.2(c). This feature is similar to that described in Ref. [130]. The merger occurs at $H_w = 0.938$ as interpolation of w(z) yields at r = 0.4.

4.4.2. Topological changes as rotation speeds up

Now we fix $H_w = 1$ (as in Ref. [3]) and increase Re. For convenient comparison with the results of Ref. [3], we introduce $Re_o = \omega R^2/\nu_o = Re/137.5$ based on the oil viscosity. Figure 4.3 depicts the flow patterns at $Re_o = 1$ (a), $Re_o = 50$ (b) and $Re_o = 350$ (c).

As Re increases, CRW2 expands upward and CRW1 shrinks toward the interface as Figure 4.3 illustrates. Table 4.1 lists the dependence on Re_o of the following flow characteristics: the interface height at the axis z_i, the CRW1 width at the axis $z_i - z_s$, see Figure 4.3(b), the maximal swirl velocity at the interface v_{mi}, the minimal tangential-meridional velocity at the interface v_{tm}, and the Reynolds number of water flow $Re_w = v_{mi} Re$; Re_w is based on the maximal swirl velocity at the interface and water viscosity.
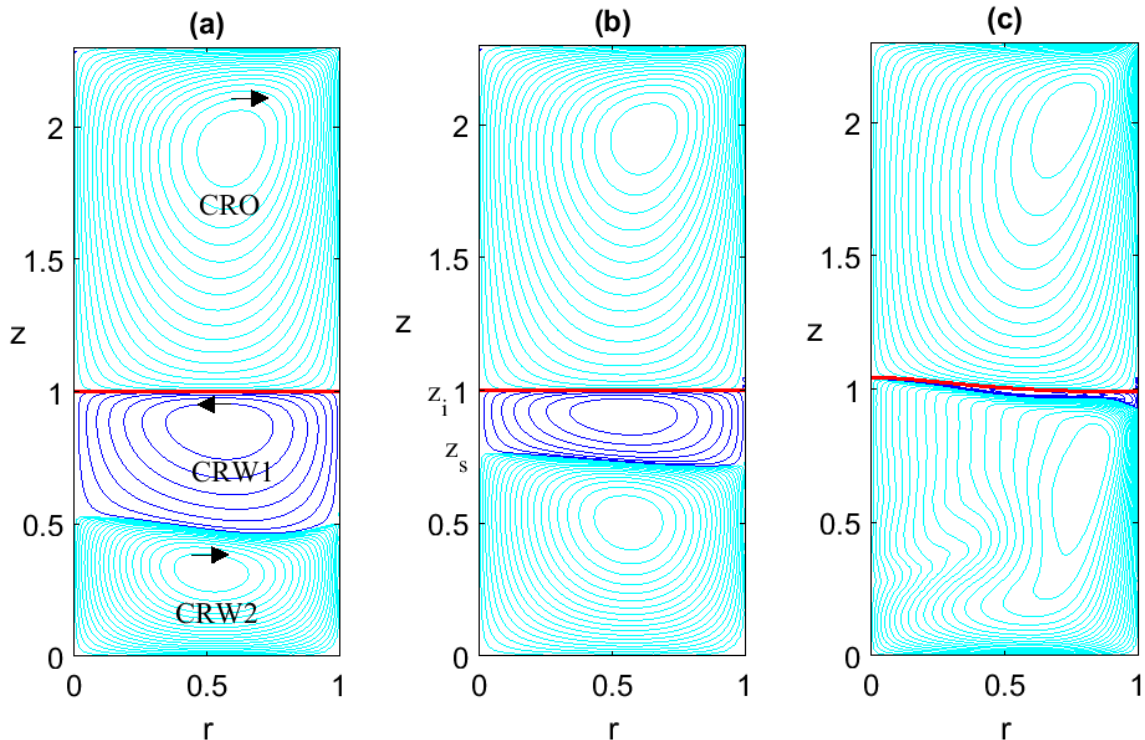
Figure 4.3 Flow patterns at water height $H_w = 1$ and $Re_o = 1$ (a), 50 (b) and 350 (c).

Re_o	z_i	z_i-z_s	v_{mi}	v_{tm}	Re_w
0	1	0.47719	0.01022	-0.00025	0
50	1.0004	0.23842	0.01040	-0.00793	73
100	1.0011	0.12863	0.01235	-0.00933	173
150	1.0021	0.07607	0.01647	-0.01115	346
200	1.0044	0.04343	0.02347	-0.01429	657
250	1.0097	0.02296	0.03423	-0.01847	1198
300	1.0212	0.00495	0.04817	-0.02333	2023
350	1.0431	0	0.06296	-0.02692	3085
400	1.0777	0	0.07571	-0.03451	4240

Table 4.1 Dependence on Re_o of interface height z_i, width of CRW1 at the axis z_i-z_s, maximal swirl v_{mi} and minimal tangential-meridional v_{tm} velocities at the interface and the Reynolds number of water flow Re_w.

Figure 4.4 depicts the radial profiles of (a) the tangential-meridional and (b) swirl velocities at the interface, normalized by their respectively minimal and maximal values, for the Re_o values indicated on the plots. Figure 4.4(a) reveals that the profile of the meridional velocity is nearly Re-independent. Figure 4.4(b) shows that the location of the maximal swirl velocity shifts closer to the axis for large Re_o.
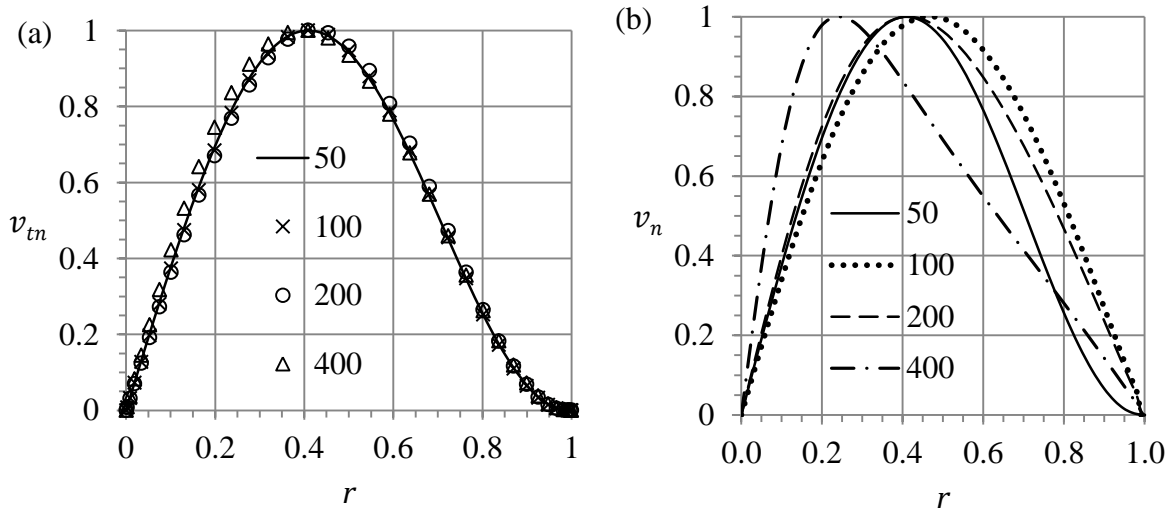
Figure 4.4 Radial distribution at the interface of normalized (a) tangential-meridional $v_{tn} = v_t/v_{tm}$ and (b) swirl $v_n = v/v_m$ velocities at Re_o values shown on the plots.

4.4.3. Formation of a robust bubble-ring

A striking feature is the shape of CRW1 for large Re. Figure 4.3(c) shows that CRW1 becomes a thin circulation layer (TCL) adjacent to the interface. The third column in Table 4.1 lists values of z_i-z_s which is the z-extent at the axis of CRW1. As Re increases, z_i-z_s reduces, becomes zero at $Re_o = 314$ and remains zero for larger Re_o. Therefore, TCL topologically is a bubble for $Re_o < 314$ and a bubble-ring for $Re_o \geq 314$. Typically, a bubble-ring is a transient shape. A small variation of a control parameter transforms a bubble-ring either in a bubble or in a ring. However here, CRW1 is a

bubble-ring in the range of $Re_o > 314$ shown in Table 4.1, i.e., TCL is a robust bubble-ring (RBR).

Figure 4.5 confirms that TCL is a bubble-ring at $Re_o = 350$ by depicting the distribution of velocity at the axis. The dots show w(z) in the water region and the solid curve shows $w(z)$ in the oil region. Figure 4.5(b) is a close-up of Fig. 5(a) near the interface. Figure 4.5 shows that $w(z)$ is zero but not tangent to the $w = 0$ line at $z = z_i$. The derivative, $\partial w / \partial z$, has a jump at $z = z_i$ being negative (positive) in the water (oil) region. The jump is due to different densities and viscosities of the oil and water.
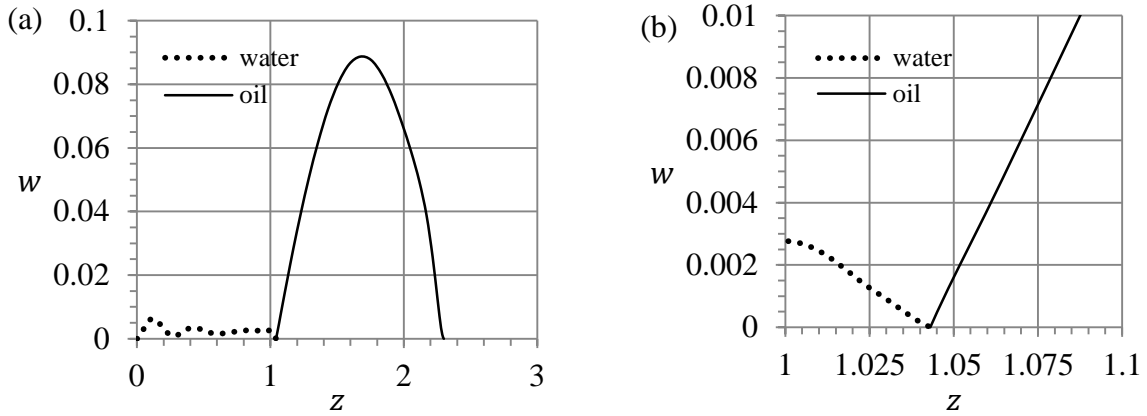
Figure 4.5(a) Distribution of velocity at the axis for $Re_o = 350$, (b) is a close up of (a) near the interface, $z = z_i = 1.0431$.
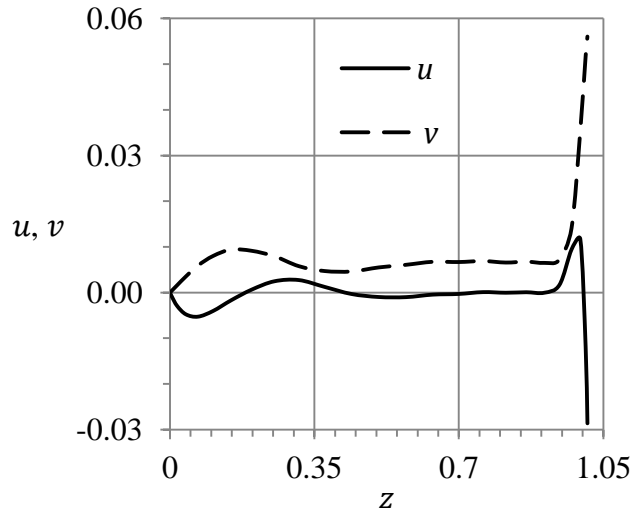
Figure 4.6 Dependence on z of swirl (dashes) and radial (solid curve) velocities in water at $r = 0.4$ and $Re_o = 350$.

The TCL is a region of large shear as Figure 4.6 illustrates depicting profiles of swirl $v(z)$ (dashes) and radial $u(z)$ (sold curve) velocities in water at $r = 0.4$ and $Re_o = 350$. TCL, shown in Fig. 3(c), is located between the peak and valley of $u(z)$ near $z = z_i = 1.0431$ in Figure 4.6. The swirl velocity also significantly changes within TCL. The magnitudes of $\partial u / \partial z$ and $\partial v / \partial z$ are maximal at the interface, $z = z_i$.

These large shear stresses likely contribute to the striking shapes of the interface shown in Fig. 2 of Ref. [3]. However, before these shapes develop, the steady flow can suffer from an instability, because the Reynolds number of the water flow Re_w is rather large at $Re_o \geq 350$ according to the values of Re_w in the last column of Table 4.1. In addition, the water flow includes a jet forming near the interface as Figure 4.3(c) illustrates at $Re_o = 350$. This jet forms below TCL,

goes to the sidewall and then downward near the sidewall and toward the axis near the bottom. These features are similar to those observed in Ref. [135]. The solid curve in Figure 4.6 has a number of inflection points that typically causes the shear-layer instability. This motivates us to perform a stability study, whose results are reported below.

4.5. Stability analysis

4.5.1. Marginal and critical characteristics

Our simulations show that the most dangerous disturbance corresponds to the azimuthal wave number $m = 4$. Table 4.2 lists eigenvalues, $\omega = \omega_r + i\omega_i$, for a few values of Re_o at $m = 4$. Interpolation yields the critical values: $Re_o = 324$, $\omega_r = 0.0391$ and $\omega_i = 0$. Disturbances with $m = 1, 2,$ and 3 becomes growing for larger Re_o as Table 4.3 shows listing the marginal (corresponding to $\omega_i = 0$) values. For $m > 4$, marginal Re_o values also are larger than the critical Re_o at $m = 4$.

Re_o	300	336	368	400
ω_r	0.0358	0.0407	0.0441	0.0465
ω_i	−0.000464	0.000245	0.000927	0.001536

Table 4.2 Dependence of $\omega = \omega_r + i\omega_i$ on Re_o for the most dangerous disturbance at $m = 4$.

Re_o	324	368	400	614
ω_r	0.0391	0.0318	0.0381	0.0244
m	4	3	2	1

Table 4.3 Critical ($m = 4$) and marginal ($m = 1, 2$ and 3) values of the Reynolds number (Re_o) and frequency (ω_r) at $\omega_i = 0$.

4.5.2. Basic-flow streamlines and disturbance energy contours
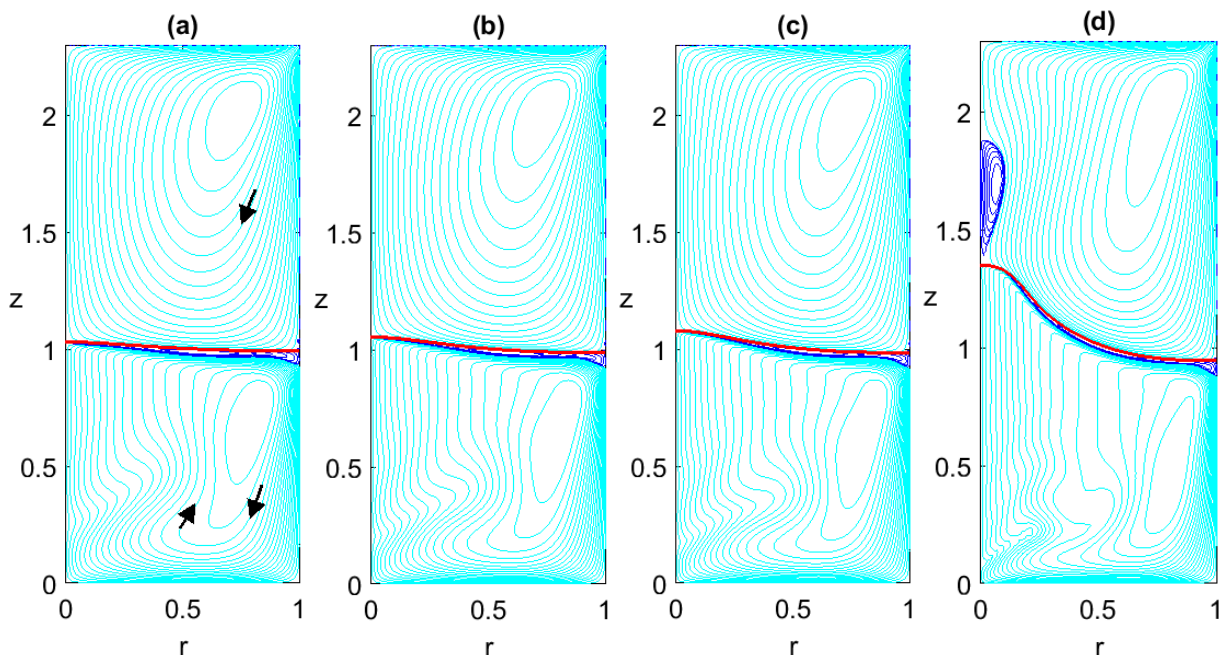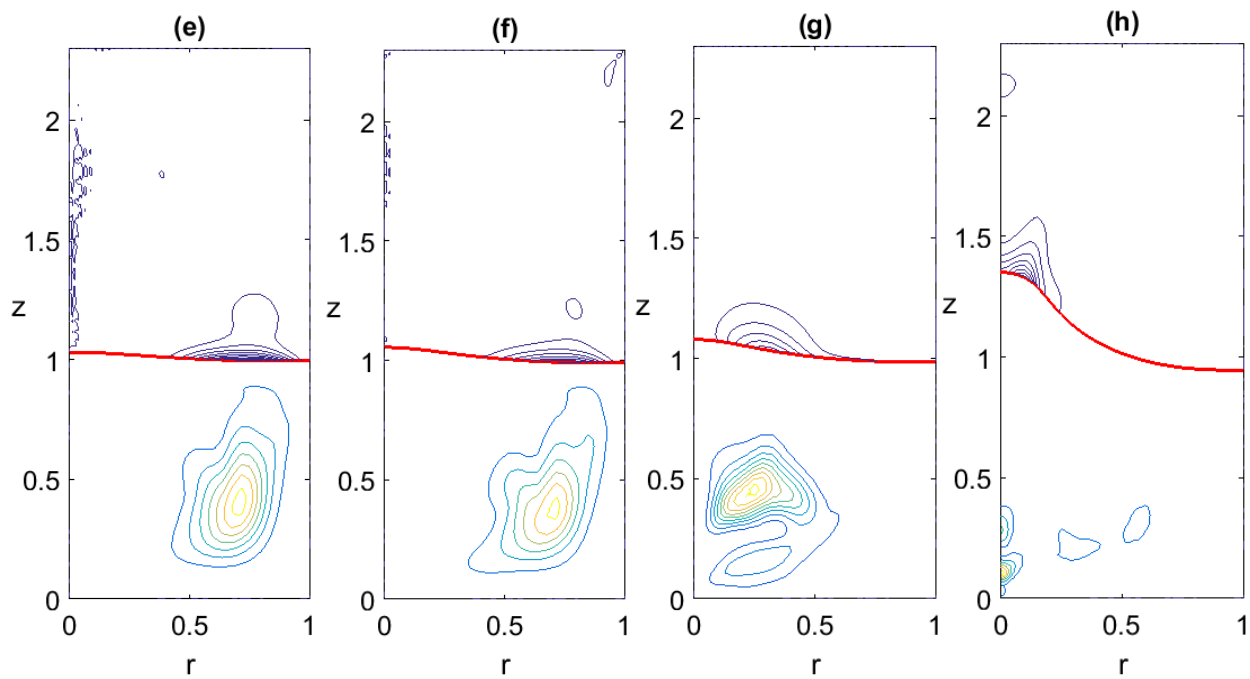
Figure 4.7 Streamlines of basic flow (a)-(d) and contours of disturbance energy (e)-(f) for parameters listed in Table 3: $Re_o = 324$ (a, e), 368 (b, f), 400 (c, g) and 614 (d, h).

Figure 4.7 depicts streamlines of the basic meridional motion, (a)-(d), and contours of disturbance energy E_d = constant for critical, (a, e), and marginal parameter values listed in Table 4.3. Here $E_d = \langle |u_d|^2 + |v_d|^2 + |w_d|^2 \rangle$ where the brackets denote averaging with respect to time and azimuthal angle and E_d is normalized by its maximal value in the entire domain.

At critical $Re_o = 324$, the energy peak is located near the middle of the water domain as Figure 4.7(e) shows. The outmost energy contour in the water domain corresponds to $E_d = 0.1$, i.e., the disturbance energy is focused between the water down-flow, going along the sidewall, and the water up-flow, going near $r \approx 0.5$ as the pair of arrows indicate in Figure 4.7(a).

4.5.3. Shear-layer character of instability
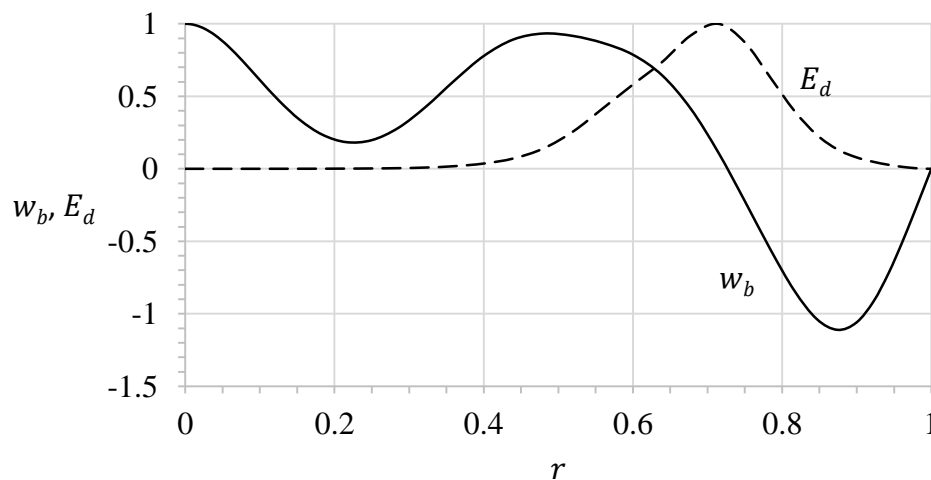
Figure 4.8 Radial distribution of the basic-flow axial velocity (solid curve) and energy (dashed curve) of critical disturbance at $z = 0.405$, $Re_o = 324$ and $m = 4$.

Figure 4.8 shows this in more detail by depicting the radial profiles of the basic-flow axial velocity $w_b(r)$ (solid curve) and the energy of critical disturbances $E_d(r)$ (dashed curve) at $z = z_m$ = 0.405 (z_m is the axial coordinate of the E_d peak in Figure 4.7(e)), Re_o = 324 and m = 4. The velocity is normalized by its maximal value for the convenient comparison with $E_d(r)$ in Figure 4.8. The radial location of E_d peak, $r = r_e$ = 0.714, is close to the inflection point of $w_b(r)$ located at $r = r_i$ = 0.76. This indicates that the instability likely is of shear-layer type, corresponding to the inflection point in the counterflow marked in Figure 4.7(a) by the arrows in the water domain.

A smaller energy peak exists in the oil domain near the interface, which likely can be related to the radial counterflow in the thin circulation layer shown by the dark curves in Figure 4.7(a). As Re_o increases, the E_d peaks shift toward the axis both in the water and oil domains. An interesting feature is the development of vortex breakdown bubble (VBB) in the oil domain shown by the dark contours in Fig. 7(d). This VBB development looks similar to that experimentally observed by Tsai et al. (Fig. 2 in Ref. [2]).

4.5.4. Iso-surfaces of critical disturbance vorticity and pressure
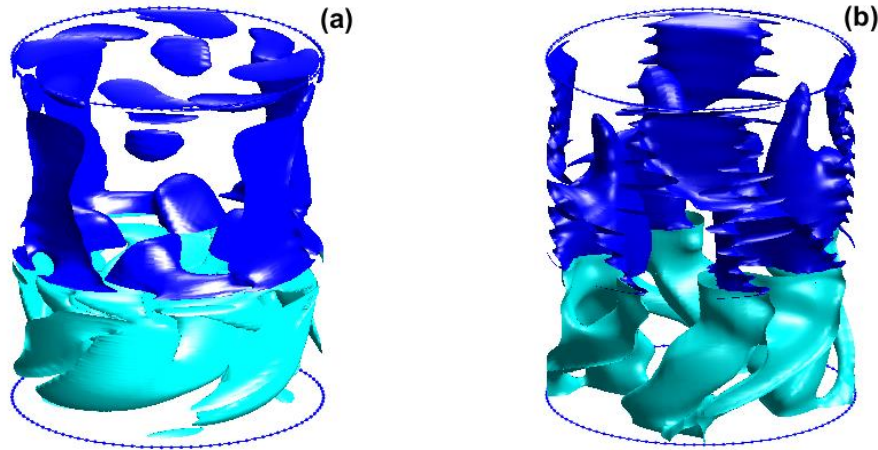
Figure 4.9 Surfaces of constant (a) azimuthal vorticity and (b) pressure of the critical disturbance at Re_o = 324 and m = 4.

Figure 4.9 depicts surfaces of constant (a) azimuthal vorticity and (b) pressure for the critical disturbance (the first column in Table 4.3). The light (dark) color corresponds to the water (oil) domain and 0.2 (0.02) values of maximal (a) vorticity and (b) pressure values. The surfaces visualize the four-branch patterns of the m = 4 disturbance fields.

4.6. Concluding remarks

Our numerical study indicates that the striking shapes of the interface, observed by Fujimoto & Takeda [3], develop in unsteady three-dimensional flow states. The instability develops at Re_o = 324 at which the interface deformation is small and has the "hump" shape typical for a slow motion. This instability likely is of the shear-layer type, corresponds to time-oscillating disturbances with the azimuthal wave number m = 4, and emerges in the lower-fluid (water) domain.

It is also revealed that even at this rather small Re_o, the water flow has a non-trivial topology, consisting of the bulk meridional circulation of the same direction, as the upper-fluid (oil) flow has, and a thin counter-circulation region adjacent to the interface.

It is shown how this topology develops as Re_o increases starting from the creeping ($Re_o \ll 1$)

flow. The creeping flow is also multicellular and its topology depends of fluid fractions.

The physical reason for the two-cell bulk water flow is in the competing driving factors: (*i*) the oil meridional circulation which tends to induce the counter-circulation in water and (*ii*) the oil swirl which tends to induce the co-circulation in water. For small water fraction (H_w) and slow rotation (Re), the meridional driving (*i*) dominates. As H_w and Re increases, the swirl driving (*ii*) intensifies, causing the water co-circulation. It emerges near the bottom center, then expands and occupies nearly the entire water domain except a thin layer of counter-circulation adjacent to the interface. The layer z-thickness near the axis diminishes to zero at the axis. The water up-flow, resulting from the co-circulation, contributes to the significant rise of the interface near the container axis observed in the experiment [3].

5. PATTERNS AND STABILITY OF A WHIRLPOOL FLOW

T his numerical study reveals stable multi-eddy patterns of a steady axisymmetric air-water flow driven by the rotating bottom disk in a vertical sealed cylindrical container. As rotation strength Re increases, eddies emerge, coalesce, separate, and disappear in both air and water. The topological scenario varies with water volume fraction H_w according to the results obtained for $H_w = 0.3$, 0.5, and 0.8. Interesting features are (a) zipper-like chains of air and water eddies forming near the bent interface and (b) bubble-ring air eddies existing in the Re ranges specified in the paper. The stability analysis, performed with the help of a novel efficient technique for two-fluid flows, shows that these multi-eddy motions are stable. The shear-layer instability develops as the interface approaches either the top or bottom of container and some eddies vanish. The physical reasoning behind the eddy formation and the flow instability is provided. The results are of fundamental interest and can have applications in bioreactors.

5.1. Introduction

An intriguing and important fluid-mechanics phenomenon is the emergence of a local circulation cell in a swirling flow, often referred to as vortex breakdown (VB). VB applications include delta-wing aircraft, where VB is dangerous causing an abrupt change in lift and drag, combustion chambers, where VB is beneficial stabilizing flame, and natural swirling jets like tornadoes, where VB decreases the twister strength. Escudier[108] performed a comprehensive review of early VB studies. More recent works, including VB control strategies, are discussed in Shtern [109].

Vogel [136] and Escudier[121] initiated fundamental VB studies in a sealed cylindrical container with one end disk rotating. An advantage is the closed domain with well-defined and controlled boundary conditions allowing for meaningful comparisons of experimental and numerical results. They well agree as was first shown by Lopez [137]. The analysis of the Vogel-Escudier flow helps understand the VB nature. A recent view is that VB develops via the swirl-decay mechanism (Shtern *et al.* [109]).

While one-fluid VB flows have been studied rather in detail, two-fluid VB flows have not attracted much attention until recent time. The situation changed with the development of aerial bioreactors where air-water flows are used for the growth of tissue culture [138]. The air flow transports the oxygen, required for tissue growth, to the interface and the water circulation enhances mixing of the dissolved oxygen with other ingredients. The tissue fraction is small compared with that of water and is neglected in the studies of flow patterns. The bioreactor applications stimulated the experimental investigations by Lo Jacono *et al.* [115]and the numerical simulations by Liow *et al.* [51], [128]. Early numerical studies modeled the gas-liquid interface as a symmetry plane [139] and as a deformable stress-free surface [140]. The first work, which is free from these idealizations of the interface, was performed by Brady *et al.* [116], [117].

Two-fluid VB flows have a number of unusual features absent in single-fluid flows. One striking feature is the existence of a thin circulation layer (TCL) adjacent to the interface. A TCL attached to the entire interface develops in a water-spout flow [118]. Another striking feature is the emergence of an off-axis VB ring in the depth of a lower fluid [141]. Since eddies arise in both fluids, their

variety is rich and their transformations are numerous. For example, eighteen topological metamorphoses follow each other as the water volume fraction increases in a truncated conical container where a creeping air-water flow is induced by the slowly rotating top disk [129].

Multiple eddies in both upper and lower fluids in a whirlpool flow driven by the rotation of bottom disk in a sealed vertical cylindrical container have not been studied. Our study partially fills this gap describing and explaining the development of VB cells, TCL, and other eddies. We reveal two more interesting features: (a) zipper-like chains of near-interface eddies and (b) robust bubble-rings (RBRs).

A bubble-ring typically is a transitional state between bubble and ring shapes. A variation of a control parameter transforms a bubble-ring into either a bubble or a ring. A RBR first was found in a creeping water-spout flow [130]. There RBR occurs in some range of water fraction. The current study shows that RBRs also develop as the rotation strength Re increases in the whirlpool flow. These RBRs exist in wide ranges of Re, listed in the study.

The resulting rather complicated topology raises a question about the flow stability. The stability of one-fluid VB flows in a cylindrical container has been investigated rather in detail. The numerical study of Gelfgat et $al.$ [119], [120] showed that the Vogel-Escudier flow can become unstable at either smaller or larger Re than that, at which VB emerges, depending on the length-to-radius ratio, H.

The experimental and numerical studies by Escudier [121]and Sorensen et $al.$ [122]–[124] documented that, as Re increases, the steady axisymmetric VB bubble first develops for $H < 3.2$. For larger H, the flow first becomes unstable with respect to 3D time-oscillatory disturbances with $m = 3$ for $3.2 < H < 4.3$, $m = 2$ for $4.3 < H < 5.2$, and $m = 4$ for $5.2 < H < 5.5$; m is the azimuthal wave number. Herrada et $al.$ [113] found that this instability is of the shear-layer type developing for $H > 5.5$ as well.

Here we consider a two-fluid flow and $H = 1$ because this H value is close to that used in bioreactors [138]. A technical difficulty of studying the stability of a two-fluid flow is the linearization of a rather complicated relation describing the balance of normal stresses at the bent interface. Herrada & Montanero [1]elaborated an efficient routine which resolves this problem and facilitates numerical simulations. The routine includes (i) mappings converting the time-dependent upper and lower fluid regions onto fixed squared domains, (ii) a symbolic toolbox to calculate the analytical Jacobians, and (iii) the Chebyshev grid in both radial and axial directions.

The Chebyshev grid, which concentrates near the interface from both sides, helps observe small bubbles, bubble-rings, and TCLs. The grid also concentrates near the axis and all walls. This helps resolve small circulation cells, emerging near the axis and walls, by using a moderate number of grid points. Herrada & Montanero [1]proved the method efficiency in their study of liquid-bridge dynamics. Here this numerical technique is modified and applied for the whirlpool problem that helps investigate and understand the base-flow topology and the instability nature.

Our study provides physical explanations of different topological scenarios as Re increases at H_w = 0.3, 0.5, and 0.8; H_w is the water volume fraction. It is found that the instability emerges in a jet-like flow forming in the water. This jet originates in the Kármán boundary layer near the rotating disk, turns upward along the sidewall and then goes toward the axis near the interface. As the jet meets a VB region, it decelerates, diverges and becomes unstable.

5.2. Problem formulation

5.2.1. Flow geometry
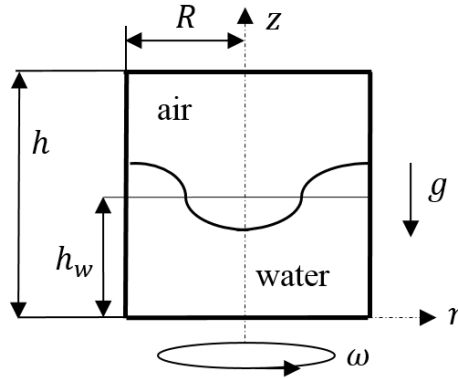
Figure 5.1 Geometry of the whirlpool model.

Figure 5.1 is a schematic of the problem. With no motion, the lower part, $0 < z < h_w$, of the vertical sealed cylindrical container is filled with water, the upper part, $h_w < z < h$, is filled with air. The air-water interface is flat, $z = z_i = h_w$, as the thin horizontal line depicts in Figure 5.1; h is the cylinder height and g is the gravity acceleration. If the bottom disk (at $z = 0$) rotates with angular velocity ω, while the other walls are still, the interface deforms downward near the axis and upward near the sidewall, as the curve schematically depicts in Figure 5.1. Such deformation of interface is typical of whirlpools.

One control parameter is aspect ratio $H = h/R$; R is the radius of the cylinder, which serves as a length scale here. Since h and R typically are close in bioreactor applications [138], we use $H = 1$. The dimensionless height of water at rest is $H_w = h_w/R$, which is also the water volume fraction. Other control parameters are the Reynolds number, $Re = \omega R^2/\nu_w$, characterizing the swirl strength, the Froude number, $Fr = \omega^2 R/g$, which is a centrifugal-to-gravity acceleration ratio, and the Weber number, $We = \rho_w \omega^2 R^3/\sigma$, characterizing the effect of surface tension σ at the interface. Here, $\nu_w = 10^{-6}$ m²/s is the kinematic viscosity of water, $\rho_w = 1000$ kg/m³ is the water density, $\sigma = 0.0715$ kg/s² at T = 300K, and g = 9.81 m²/s. We assume that pressure on the interface at rest has its atmospheric value and the air density is $\rho_a = 1.22$ kg/m³.

Our numerical simulations model a physical experiment where the all the physical properties are fixed while ω eventually increases. Therefore, Re, $Fr = aRe^2$, and $We = bRe^2$ also increase. Here $a = \nu_w^2/(gR^3)$ and $b = \rho_w \nu_w^2/(\sigma R)$ are fixed numbers, $a = 10^{-4}$ and $b = 1.4 \times 10^{-5}$ [141], while Re varies. We explore changes in the flow topology as Re increases for the water volume fraction $H_w = 0.8, 0.5$ and 0.3. In addition, we study the stability of the corresponding flow patterns.

5.2.2. Governing equations

Using $R, 1/\omega, \omega R$, and $\rho_w \omega^2 R^2$ as scales for length, time, velocity, and pressure, respectively, renders all variables dimensionless. We consider flows of two viscous incompressible immiscible fluids governed by the Navier -Stokes equations [125],

$$\frac{1}{r}\frac{\partial(ru)}{\partial r} + \frac{1}{r}\frac{\partial v}{\partial \phi} + \frac{\partial w}{\partial z} = 0, \qquad\qquad 5.1$$

$$\frac{\partial u}{\partial t} + u\frac{\partial u}{\partial r} + \frac{v}{r}\frac{\partial u}{\partial \phi} + w\frac{\partial u}{\partial z} - \frac{v^2}{r} = -\rho_n\frac{\partial p}{\partial r} + \frac{v_n}{Re}\left(\nabla^2 u - \frac{u}{r^2} - \frac{2}{r^2}\frac{\partial v}{\partial \phi}\right), \qquad 5.2$$

$$\frac{\partial v}{\partial t} + u\frac{\partial v}{\partial r} + \frac{v}{r}\frac{\partial v}{\partial \phi} + w\frac{\partial v}{\partial z} + \frac{uv}{r} = -\frac{\rho_n}{r}\frac{\partial p}{\partial \phi} + \frac{v_n}{Re}\left(\nabla^2 v - \frac{v}{r^2} + \frac{2}{r^2}\frac{\partial u}{\partial \phi}\right), \qquad 5.3$$

$$\frac{\partial w}{\partial t} + u\frac{\partial w}{\partial r} + \frac{v}{r}\frac{\partial w}{\partial \phi} + w\frac{\partial w}{\partial z} = -\rho_n\frac{\partial p}{\partial z} + \frac{v_n}{Re}\nabla^2 w, \qquad 5.4$$

where $\nabla^2 \equiv \frac{1}{r}\frac{\partial}{\partial r}\left(r\frac{\partial}{\partial r}\right) + \frac{1}{r^2}\frac{\partial^2}{\partial \phi^2} + \frac{\partial^2}{\partial z^2}$ is the Laplace operator for a scalar field, (u, v, w) are the velocity components in cylindrical coordinates (r, ϕ, z), t is time, and p is the reduced pressure. The coefficients, ρ_n and v_n, are both equal 1 at $n = 1$ (for the water flow) while $\rho_n = \rho_w/\rho_a$ and $v_n = v_a/v_w$ at $n = 2$ (for the air flow); $v_a = 15v_w$ is the kinematic viscosity of air.

We denote the list (u, v, w, p) as $\boldsymbol{V}$, and look for a solution of the system 5.1- 5.4 in the form

$$\boldsymbol{V} = \boldsymbol{V}_b(r, z) + \varepsilon\boldsymbol{V}_d(r, z)e^{(im\phi - i\omega t)} + c.c., \qquad 5.5$$

where subscripts "b" and "d" denote the base flow and a disturbance, respectively; $c.c.$ denotes the complex conjugate of the preceding term; $\varepsilon \ll 1$ is an amplitude; integer m is an azimuthal wave number; and $\omega = \omega_r + i\omega_i$ is a complex number to be found, with frequency ω_r and growth rate of disturbance ω_i. For a decaying (growing) disturbance, ω_i is negative (positive). Disturbances with $\omega_i = 0$ are neutral. We are looking for minimal Re at $\omega_i = 0$. The equations governing the base flow result from substituting 5.5 in system 5.1- 5.4 and setting $\varepsilon = 0$. The terms of order $O(\varepsilon)$ constitute equations governing infinitesimal disturbances.

5.2.3. Boundary conditions

Equations 5.1- 5.4 are solved under the following boundary conditions:
(i)   Regularity at the axis, $0 < z < H$, $r = 0$:
      a) $u = v = 0$, $\partial w/\partial r = 0$ (basic flow and $m = 0$ disturbances),
      b) $w_d = 0$, $u_d + mv_d = 0$, $\partial u_d/\partial r = 0$ ($m = 1$ disturbances)
      c) $w_d = u_d = v_d = 0$ ($m > 1$ disturbances)
(ii)   No-slip at the walls: $u = v = w = 0$ at the still disk, $0 < r < 1$, $z = H$, and at the sidewall, $0 < z < H$, $r = 1$; $u = w = 0$, $v = r$ at the rotating disk, $0 < r < 1$, $z = 0$.
(iii)   Continuity of all the velocity and tangential stress components at the interface, $z = F(r, \phi, t)$. The balance for the normal stresses yields that

$$p_w - p_a = \frac{1}{We}\nabla.\boldsymbol{n} - \frac{1}{Re}\boldsymbol{n}.(\boldsymbol{\tau}_w - \mu_r\boldsymbol{\tau}_a).\boldsymbol{n} - \frac{1}{Fr}(1 - \rho_r)z, \qquad 5.6$$

where $\boldsymbol{n}$ is the unit vector normal to the interface, $\boldsymbol{\tau}_w$ and $\boldsymbol{\tau}_a$ are tensors of the viscous stresses in the heavy and light fluids, respectively, μ_r and ρ_r are the light-to-heavy fluid ratios of the dynamic viscosities and densities, respectively.
(iv)   The kinematic equation for the interface shape, $z = F(r, \phi, t)$, is

$$\frac{\partial F}{\partial t} - w + u\frac{\partial F}{\partial r} + \frac{v}{r}\frac{\partial F}{\partial \phi} = 0, \qquad 5.7$$

that provides the water and air mass conservation. We look for a solution of 5.7 in the form

$$z = F_b(r,z) + \varepsilon F_d(r,z)e^{(im\phi - i\omega t)} + c.c.$$

5.8

In our stability studies, all the boundary conditions, including 5.6 and 5.7 also are linearized by using 5.5 and 5.8 and extracting terms of order $O(\varepsilon)$ in the system governing infinitesimal disturbances.

5.3. Numerical technique

To simulate the nonlinear problem for the basic flow and the generalized eigenvalue problem for disturbances, we use a numerical technique which is a variation of that described in detail by Herrada & Montanero [1]. First, the heavy-fluid (water) and light-fluid (air) regions are mapped onto the standard square domain, $0 \leq \eta_{(w,a)} \leq 1$, $0 \leq \xi \leq 1$, by means of the coordinate transformations (a) $\eta_w = z/F$ and $\xi = r$ and (b) $\eta_a = (z-F)/(H-F)$ and $\xi = r$ for the water and air, respectively. Then, each variable (velocities, pressure and the interface shape) and all its spatial and temporal derivatives, which appear in the transformed equations, are composed as a single symbolic vector. For example, for the axial velocity in the water flow, w_w, we create a vector having 11 components: $\mathbf{x}_w = [w_w, \partial w_w/\partial \eta_w, \partial w_w/\partial \xi, \partial^2 w_w/\partial \eta^2, \partial^2 w_w/\partial \xi^2, \partial^2 w_w/\partial \xi \partial \eta, \partial w_w/\partial \phi, \partial^2 w_w/\partial \phi^2, \partial^2 w_w/\partial \phi \partial \xi, \partial^2 w_w/\partial \phi \partial \eta, \partial w_w/\partial t]$. The next step is to use a symbolic toolbox to calculate the analytical Jacobians of all the equations with respect to all the symbolic vectors. Using these analytical Jacobians we generate functions which then are evaluated point by point in the square domains. In this procedure, we used the MATLAB tool *matlabFunction* to convert the symbolic Jacobians in MATLAB functions.

Then, we carry out the spatial and temporal discretization of the problem. The water and air domains are discretized using a set of n_w and n_a Chebychev spectral collocation points in the axial direction (along the η_w and η_a axes, respectively). Next, the water and air domains are discretized using a set of n_ξ Chebychev spectral collocation points in the radial direction, ξ. The second-order backward finite differences are used to compute the time derivatives for the basic flow. Since the basic flow is axisymmetric, all the azimuthal derivatives are set to zero. For disturbances, we obtain the temporal and azimuthal derivatives using (5.5) and (5.8).

The final step is to set up the numerical matrices allowing us to solve the problem by using a Newton procedure for the basic steady flow and by solving the generalized eigenvalue problem for disturbances.

To summarize, the numeric procedure includes the mapping of water and air regions, the proper spatial and temporal discretization creating the discrete Jacobian matrix for the Newton procedure for the basic flow and two more matrices for the generalized eigenvalue problem for disturbances. For the basic flow, we get the final steady solution though using an unsteady scheme. Starting from the rest and selecting a time step, the solution is advanced in time until a steady state is reached. Since the nonlinear procedure used to compute the basic flow is fully implicit, the time step can be taken sufficiently large to quickly reach the steady solution. Once the base flow is computed, and given an azimuthal wavenumber m, we use MATLAB subroutine *eigs* to calculate the eigenvalues (ω) of the system of discrete linear equations.

Most of the simulations presented here are done using $n_w = 25$, $n_a = 25$, and $n_\xi = 30$ (standard grid), but some runs for flows, having small circulation regions, are performed with finer grids. For $Re > 1000$, we use $n_{\eta w} = 35$, $n_{\eta a} = 35$, and $n_\xi = 50$ (fine grid). Since the Chebyshev grid points concentrate near the interface from both sides, the approach is adequate to resolve thin circulation layers, located near the interface, even at moderate values of n_w, n_a, and n_ξ. More information on the checkup of numerical accuracy is in Appendix. The numerical code also was verified by reproducing the results of Mougel et al. [142]. The reproduced base flow and stability characteristics, obtained by our code, well agree with those in (Mougel et al. [142]).

5.4. Deep whirlpool

First, we consider the $H_w = 0.8$ case and describe changes in the flow topology, occurring as Re increases. Next, we study the nature of instability which develops at larger Re. To analyze the flow topology we use the Stokes stream function Ψ, $w = r^{-1}\partial\Psi/\partial r$ and $u = -r^{-1}\partial\Psi/\partial z$, and plot streamlines of the meridional motion, i.e., contours $\Psi = $ constant.

5.4.1. VB emergence in water depth

Figure 5.2 depicts the streamline patterns at $Re = 350$ (a) and 360 (b). The swirling disk (at $z = 0$) induces the centrifugal force which pushes water to the sidewall near the bottom [127] and thus develops the anticlockwise circulation in CR1 of Fig. 2(a); CR is an abbreviation for "circulation region". This water motion drives the air clockwise circulation in CR2 of Figure 5.2(a). Hereafter the clockwise (anticlockwise) meridional circulation is depicted by light (dark) contours. The pattern shown in Figure 5.2(a) remains topologically invariant as Re decreases down to zero. In contrast as Re increases, a VB bubble emerges in the water depth near $r = 0$ and $z = 0.545$ at $Re = Re_{d1} = 359$. This VB bubble is observed as CR3 in Figure 5.2(b) at $Re = 360$. The meridional circulation in the bubble is clockwise and $w > 0$ at $r = 0$ according to the velocity distribution on the axis shown in Figure 5.3(a). The streamline pattern and w-velocity profile help us to understand the VB nature.

The physical reasoning behind the VB development is the swirl decay mechanism similar to that working in the single-fluid case [109][113]. The near-interface water flow transports the angular momentum toward the axis and thus develops a deep local minimum of pressure near the axis-interface intersection. The reduced pressure sucks the downstream water that causes the deceleration and local reversal of near-axis downflow. Figure 5.3(a) shows details of the velocity reversal at the axis, i.e., the emergence of CR3.
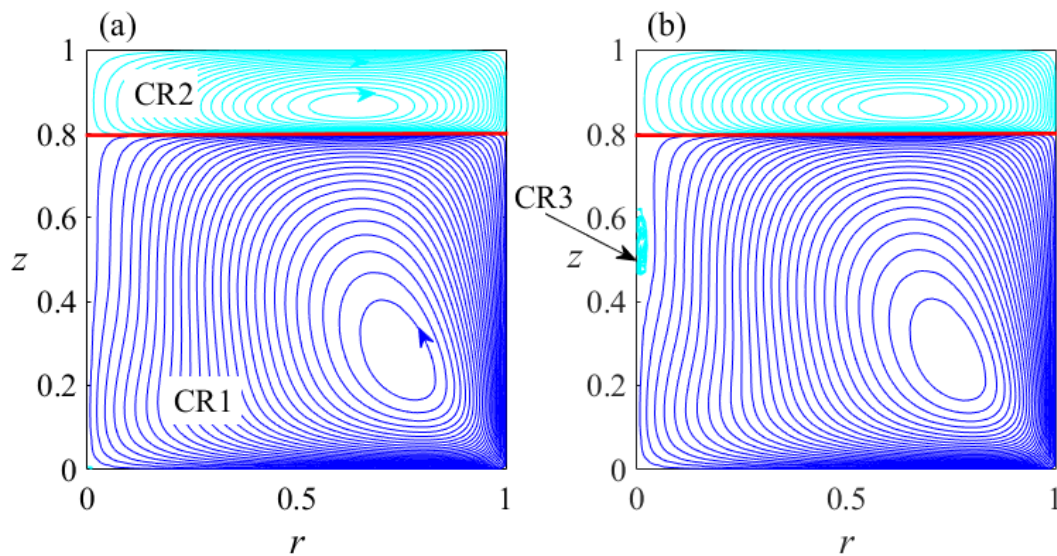
Figure 5.2 Streamline patterns at $Re = 350$ (a) and 360 (b) show appearance of VB region CR3.
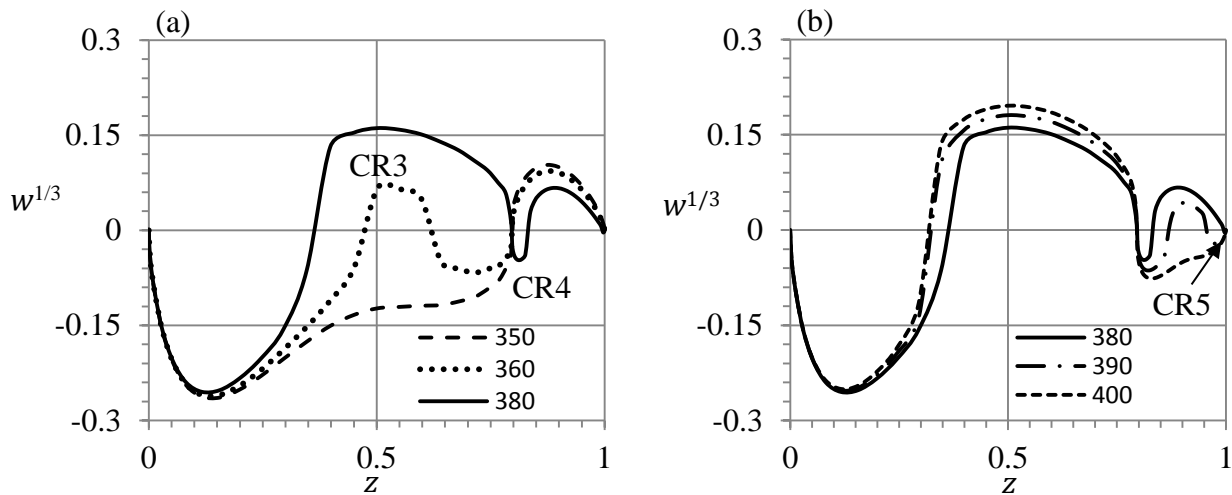
Figure 5.3 Distributions of velocity on the axis at $Re = 350\text{-}400$ illustrate (a) development of VB regions in water (CR3) and air (CR4) and (b) development of CR5 and its merging with CR4.

Figure 5.3 depicts $w^{1/3}$ to better observe small w in the separation regions. At Re slightly larger than 350, a local maximum of $w(z)$ develops in water near $z = 0.55$. The maximum value is negative for $Re < 359$, zero at $Re = 359$, and positive for $Re > 359$. As Re increases, the $w > 0$ range in the water flow rapidly expands in the z-direction as curves $Re = 360$ and 380 illustrate in Figure 5.3(a).

5.4.2. Emergence of two-fluid VB bubble

At $Re = Re_{d2} = 365$, expanding VB bubble CR3 reaches the interface and becomes a corner eddy. This is the second change in the flow topology. The scenario is similar to that described by Brøns *et al.* [143]. The difference is that here a corner eddy develops in air as well. Meridional velocity at the interface v_t reverses and becomes positive near the axis for $Re > 365$ as the curves $Re = 370$ and $Re = 400$ illustrate in Figure 5.4(a). The reversed v_t drives CR4 in air, shown at $Re = 380$ in Figure 5.5(a). Thus the VB bubble becomes two-fluid.
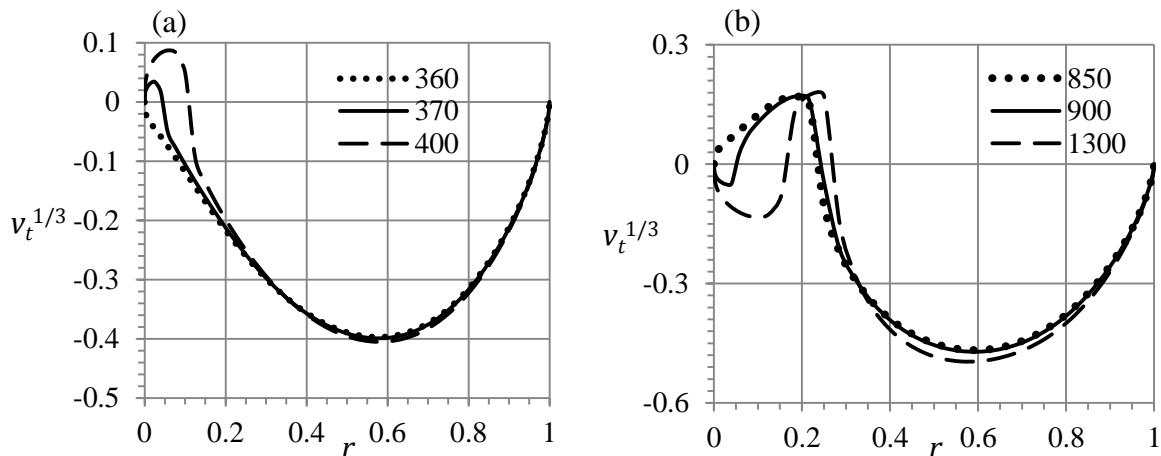
Figure 5.4 Distributions of meridional velocity at the interface (v_t) for Re from 360 up to 1300 illustrate (a) the first and (b) the second v_t reversals near the axis.
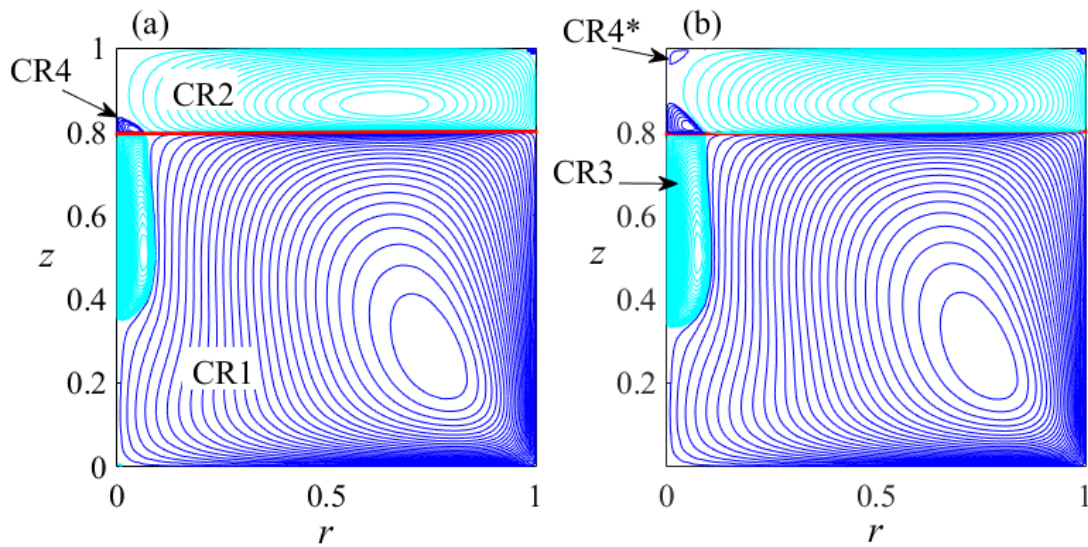
Figure 5.5 Streamline patterns at $Re = 380$ (a) and 390 (b) show appearance of VB regions CR4 (a) and CR4* (b) in the air flow.

Region CR4 in Figure 5.5(a) corresponds to the thin $w < 0$ range of the $Re = 380$ curve in Figure 5.3(a). As Re increases, region CR4 expands as comparison of curves at $Re = 380$ and $Re = 390$ in Fig. 3(b) illustrates.

5.4.3. Vortex breakdown near the top disk

The third change in the flow topology is the emergence of circulation region CR4* near the center of the top disk at $Re = Re_{d3} = 377$. Figure 5.5(b) depicts CR4* at $Re = 390$. Physical reasoning behind this VB development is the following. As a rotating fluid meets a normal wall, the secondary flow develops which converges to the rotation axis near the wall and goes away from the wall near the axis [134]. The secondary flow is weak for small Re, but becomes stronger and overcomes the bulk CR2 circulation near the axis-top intersection as Re increases (Figure 5.5). The secondary flow is amplified here by the presence of region CR4 that makes shorter trajectories of particles transporting the angular momentum from the interface to the center of top disk. As Re increases, region CR4* rapidly expands downward.
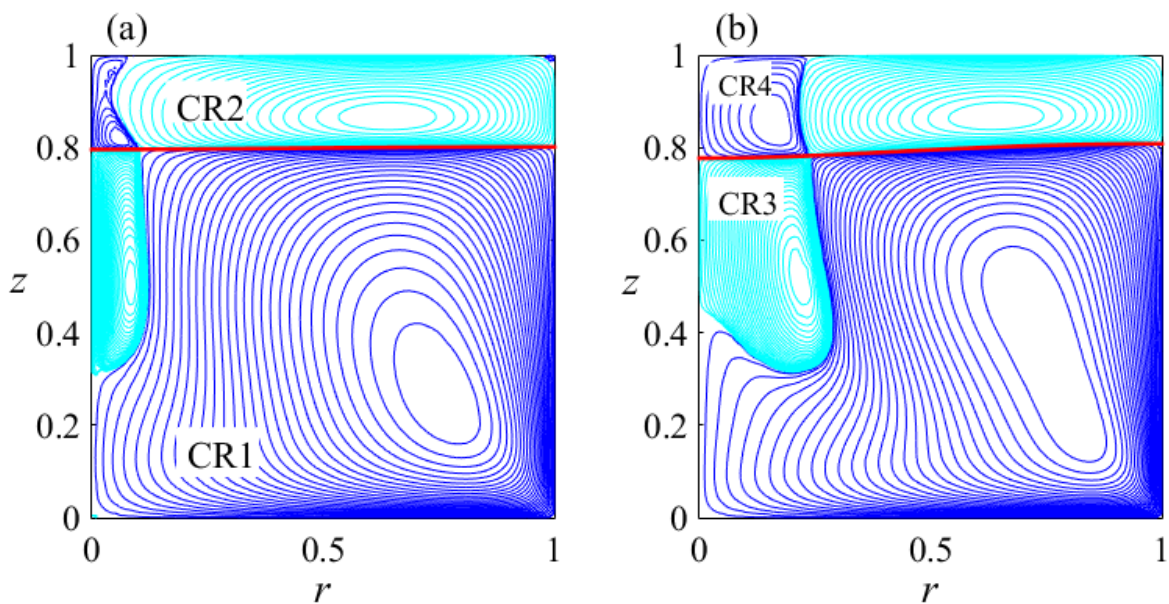
Figure 5.6 Streamline patterns at $Re = 400$ (a) and 800 (b) show radial expansion of regions CR3

and CR4.

5.4.4. Merging of near-axis cells in air

As Re increases, regions CR4 and CR4* merge at $Re = Re_{d4} = 394$. This is the fourth change in the flow topology. Figure 5.3(b) illustrates this merger: the $w > 0$ range, located near $z = 1$ and observed in the $Re = 390$ curve, is absent in the $Re = 400$ curve. We denote the merged region again as CR4. Figure 5.6 depicts CR4 at $Re = 400$ (a) and 800 (b). The Bödewadt pumping and the $v_t > 0$ water flow at the interface work together, driving the anticlockwise circulation of air in CR4, resulting in its expansion in the radial direction as Re increases (Figure 5.6).

5.4.5. Separation of water VB bubble from axis

The fifth topological metamorphosis is the separation of CR3 from the axis. The boundary between CR1 and CR3 moves up near the axis as Re increases (Fig. 6), reaches the interface at $Re = Re_{d5} = 873$ and moves away from the axis for larger Re. This transformation occurs together with the second reversal of the meridional velocity at the interface: v_t becomes negative for small r as curve $Re = 900$ in Fig. 4(b) illustrates. Figure 7(a) depicts the resulting streamline pattern at $Re = 1000$.
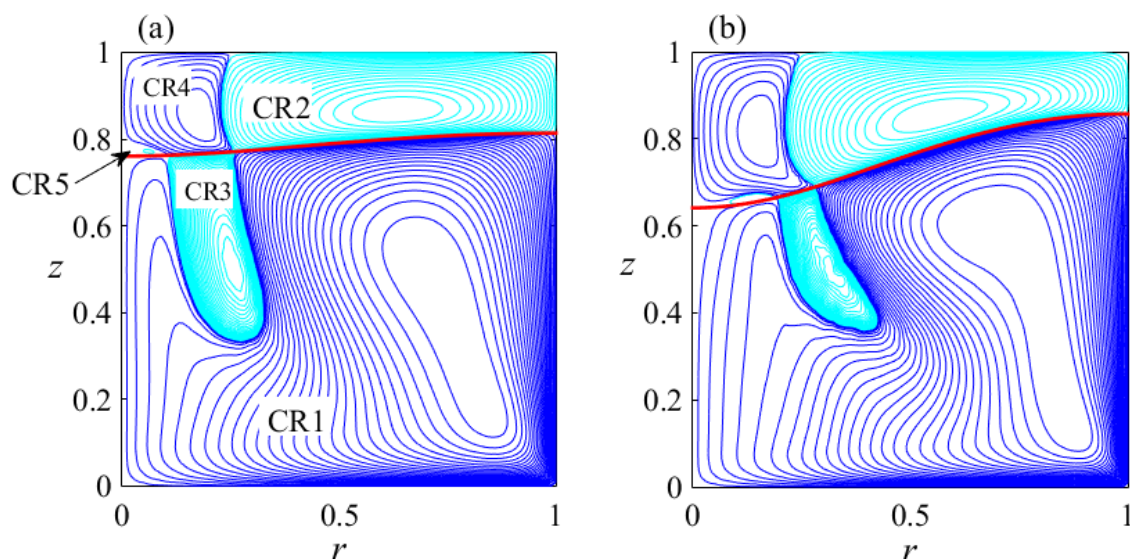
Figure 5.7 Streamline patterns at $Re = 1000$ (a) and 1800 (b) correspond to the transformation of region CR5 from a bubble (a) into a bubble-ring (b).

The scenario of this VB development in water is similar to that occurring in the one-fluid flow with the stress-free fixed upper surface, described and explained by Brøns et al. [143]. The difference is that here the VB development in the air flow occurs as well. This development, in particular, includes the appearance of new circulation region CR5 in air depicted in Figure 5.7(a) and induced by the second reversal of meridional velocity at the interface shown in Figure 5.4(b). Region CR5 emerges as a bubble and then transforms into a bubble-ring, as discussed below in more detail.

5.4.6. Emergence of the robust bubble-ring
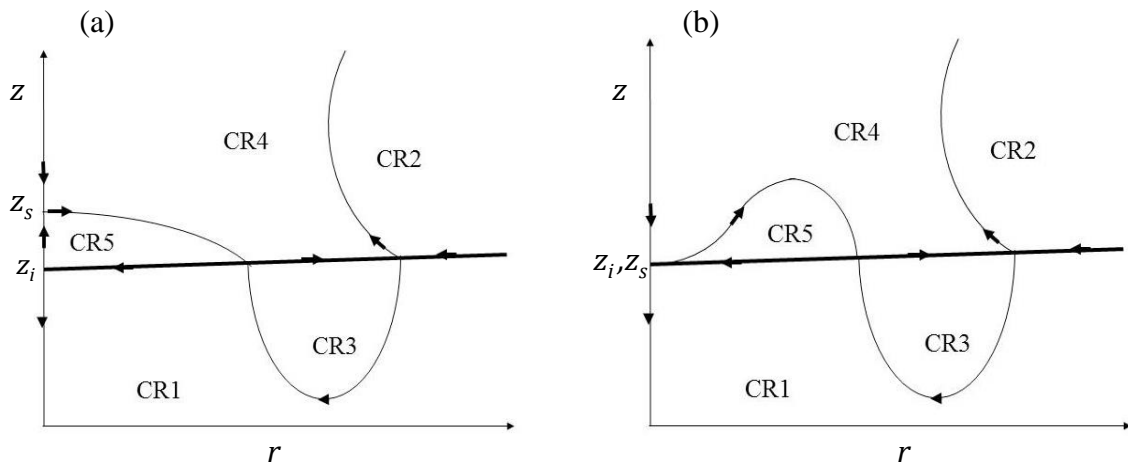
Figure 5.8 Schematics showing the flow topology in (a) Figure 5.7(a) and (b) in Figure 5.7(b).

Re	z_i	z_s	$z_s - z_i$
$Re_{d5} = 873$	0.7716	0.7716	0
950	0.7654	0.7874	0.0220
1000	0.7609	0.7927	0.0318
1100	0.7511	0.7939	0.0428
1200	0.7400	0.7853	0.0454
1300	0.7274	0.7699	0.0424
1500	0.6980	0.7246	0.0266
1700	0.6620	0.6693	0.0073
Re_{d6} =	0.6459	0.6459	0
1900	0.6180	0.6180	0
2000	0.5923	0.5923	0
2200	0.5344	0.5344	0
Re_{d7} =	0.482	0.482	0
2400	0.4574	0.4631	0.0057
2500	0.4088	0.4256	0.0168

Table 5.1 Dependence on Re of z_i, z_s, and CR5 thickness on axis $(z_s - z_i)$ reveals that CR5 is a bubble-ring for $Re_{d6} \leq Re \leq Re_{d7}$.

Though Figure 5.7(a) and Figure 5.7(b) look similar, the important difference is that the flow pattern, depicted in Figure 5.7(a), corresponds to the schematic shown in Figure 5.8(a) while the flow, depicted in Figure 5.7(b), corresponds to the schematic shown in Figure 5.8(b), as it follows from Table 5.1. Accordingly, CR5 is a bubble in Figure 5.7(a) and a bubble-ring in Figure 5.7(b).

Table 5.1 lists z-values on the axis for (a) the interface (z_i), (b) the boundary, separating regions CR4 and CR5 (z_s), see Figure 5.7(a), and (c) thickness of CR5 at the axis ($z_s - z_i$) for Re shown in the first column. It is clear from Table 1 that region CR5 is a bubble in the range, $873 = Re_{d5} < Re < Re_{d6} = 1779$, and is a bubble-ring in the range, $Re_{d6} \leq Re \leq Re_{d7} = 2348$, because its thickness $(z_s - z_i)$ is zero at the axis. The transformation of CR5 from a bubble into a bubble-ring is the sixth

topological change.
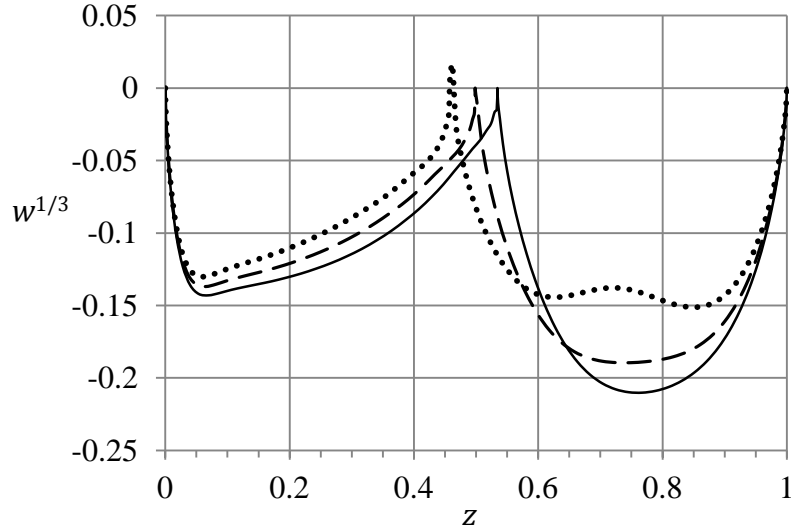
Figure 5.9 Distribution of velocity on the axis at $Re = 2200$ (solid curve) 2300 (dashes) and 2400 (dots).

Figure 5.9 confirms the existence of robust bubble-ring by depicting the profile of velocity w at the axis for $Re = 2200$ (solid curve) and $Re = 2300$ (dashed curve). The velocity w is negative, i.e., directed downward both in water, $0 < z < z_i$, and in air, $z_i < z < 1$; being zero only at the bottom, $z = 0$, interface, $z = z_i$, and top, $z = 1$. This corresponds to the topological pattern shown in Figure 5.8(b). As increasing Re passes $Re_{d7} = 2348$, the thin $w > 0$ region emerges near the interface in the air domain as the dotted curve depicts at $Re = 2400$ in Figure 5.9. We use $w^{1/3}$ to conveniently observe the $w > 0$ region in Figure 5.9 where w is very small. Therefore, CR5 again becomes a bubble corresponding to the schematic shown in Figure 5.8(a).

5.4.7. Reversal of topological transformations

The disappearance of the robust bubble-ring at $Re = Re_{d7} = 2348$ is the seventh event and the first back step among the changes in the flow topology. The eighth change is the coalescence of regions CR2 and CR5, shown in Figure 5.10(a), into new region CR2, which extends up to the axis as Figure 5.10(b) depicts. The transition from the pattern in Figure 5.10(a) to that in Figure 5.10(b) has a number of intermediate changes in the flow topology which were systematically described by Brøns [144]. We refer a reader to this instructive paper for details. The ninth change is the splitting of CR4 into CR4a and CR4b as Figure 5.10(c) illustrates at Re = 2500. The tenth change is the disappearance of CR4b; see Figure 5.10(d).
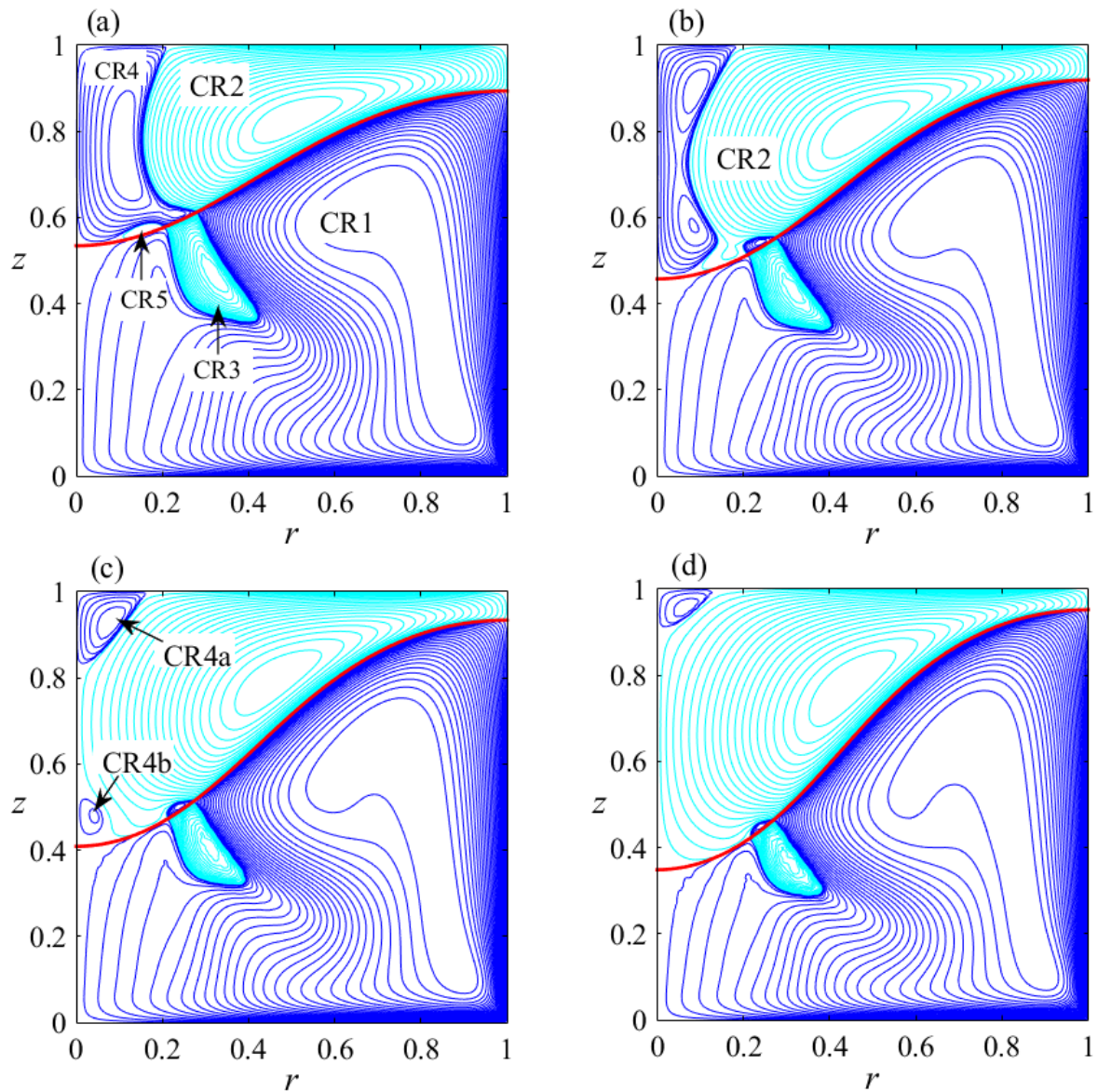
Figure 5.10 Streamline patterns at $Re = 2200$ (a), 2400 (b), 2500 (c) and 2600 (b) show reduction of VB regions.

5.4.8. Instability nature

Table 5.2 summarizes the instability results for the flow at $H_w = 0.8$. It shows parameter values corresponding to the marginal Re (minimal at a fixed m and $\omega_i = 0$) and the critical Re (shown bold and minimal among marginal). The critical Re corresponds to single-helix disturbances, i.e., $m = 1$. No instability was found for $m = 0$. Disturbances with other m are less dangerous than those presented in Table 2. Figure 5.11 depicts the streamline pattern at critical $Re = 2629$ and contours of critical-disturbance squared velocity modulus, Ed = constant; Ed is averaged with respect to time and azimuthal angle and normalized by its maximal value, Ed_m.

Re	**2629**	2664	2715	2667
m	**1**	2	3	4
ω_r	**0.204**	0.615	1.054	1.376

Table 5.2 Critical (bold) and marginal parameters of the flow instability at $H_w = 0.8$.
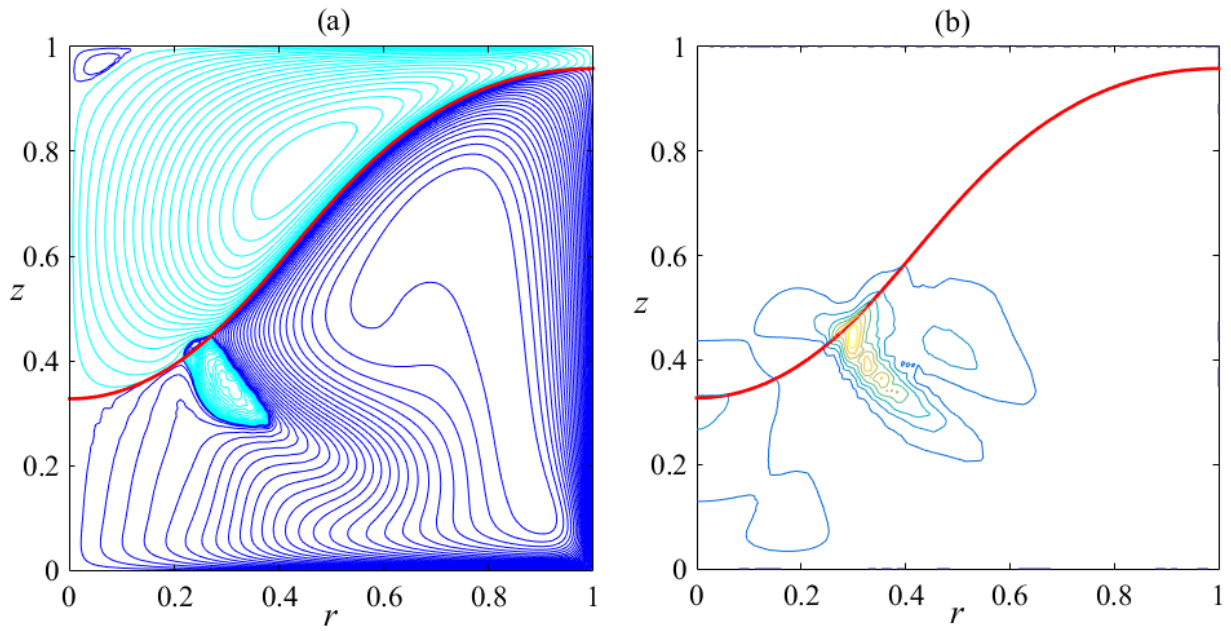
Figure 5.11 Streamline pattern (a) and disturbance energy contours (b) at critical $Re = 2629$ for $H_w = 0.8$.

The Ed peak is located in the water domain at $r = r_m = 0.298$ and $z = z_m = 0.437$. Ed is localized near the peak: the outmost Ed contour corresponds to $Ed_m/10$ in Figure 5.11(b). These features help understand the instability nature. The flow pattern in Figure 5.11(a) visualizes the jet development near the rotating bottom disk where streamlines are packed. This jet forms in the Kármán boundary layer, turns upward and goes near the sidewall, reaches the interface and turns toward the axis along the interface. The convergence to the axis accelerates the jet that compensates the entrainment-caused widening thus making the jet width nearly constant as Figure 5.11(a) shows near the interface middle. The situation changes as the jet approaches the VB bubble. The jet turns down and away from the axis and diverges where the disturbance energy peaks. We guess that these jet deceleration and divergence near the VB region cause the shear-layer instability typical of jet flows [109].
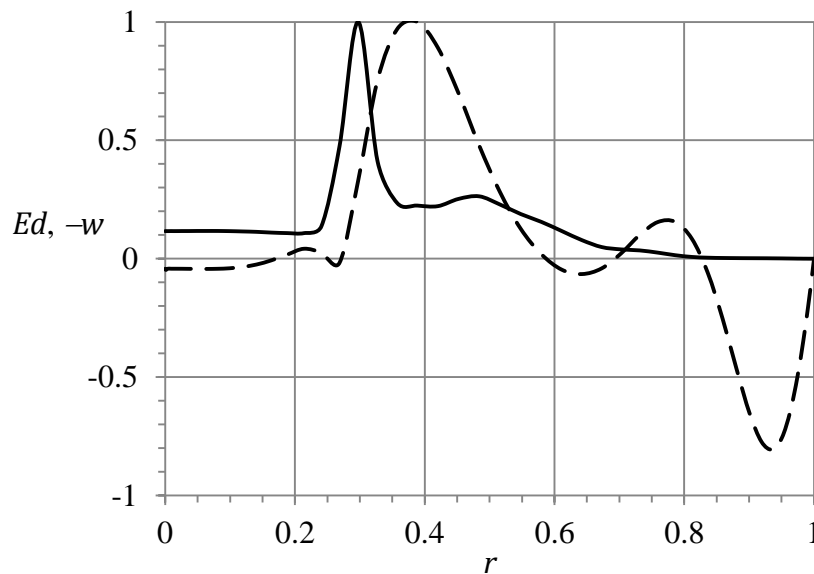
Figure 5.12 Profiles of the disturbance energy (solid curve) and base-flow velocity (dashed curve) at $z = z_m$. Both energy and velocity are normalized by their maximum values.

Figure 5.12 supports this conjecture by depicting the r-distribution of the disturbance energy

Ed (solid curve) and the base-flow w-velocity (dashed curve) at $z = z_m$. Since the jet is directed downward near the interface, we depict $-w$, normalized by its maximal magnitude, for convenient discussion of Figure 5.12. The w-profile indeed has a jet-like shape near $r = 0.4$ with inflection points located near $r = 0.3$ and $r = 0.5$ in Figure 5.12. The disturbance energy peaks near the $r = 0.3$ inflection point and has a local maximum near the $r = 0.5$ inflection point. These features indicate that the instability likely is of the shear-layer type.

The multi-helix instability with $m = 2$ and 4 develop for higher Re than that with $m = 1$ according to Table 5.2, but the marginal Re values are close to the critical Re. This can lead to polygonal patterns observed in experiments ([145], [146], see also references there). For this reason, Figure 5.13 depicts the *Ed* distribution for the marginal disturbances with $m = 2$ and 4 presented in Table 5.2. The energy of these disturbances is less localized (especially at $m = 2$) than that for the $m = 1$ disturbance as comparison of Figure 5.11(b) and Figure 5.13 illustrates. Nevertheless, the marginal disturbance also located in the water domain, where the jet "reflects" from the VB region in Figure 5.11(a).

To summarize, the stability results reveal that the topological metamorphoses occur in the stable steady axisymmetric flow. The instability develops as the interface becomes strongly deformed and approaches the top disk of container (Figure 5.11(a)). The analysis of the base-flow pattern and the energy distribution at the critical Re indicates that the instability likely is of the shear-layer type.
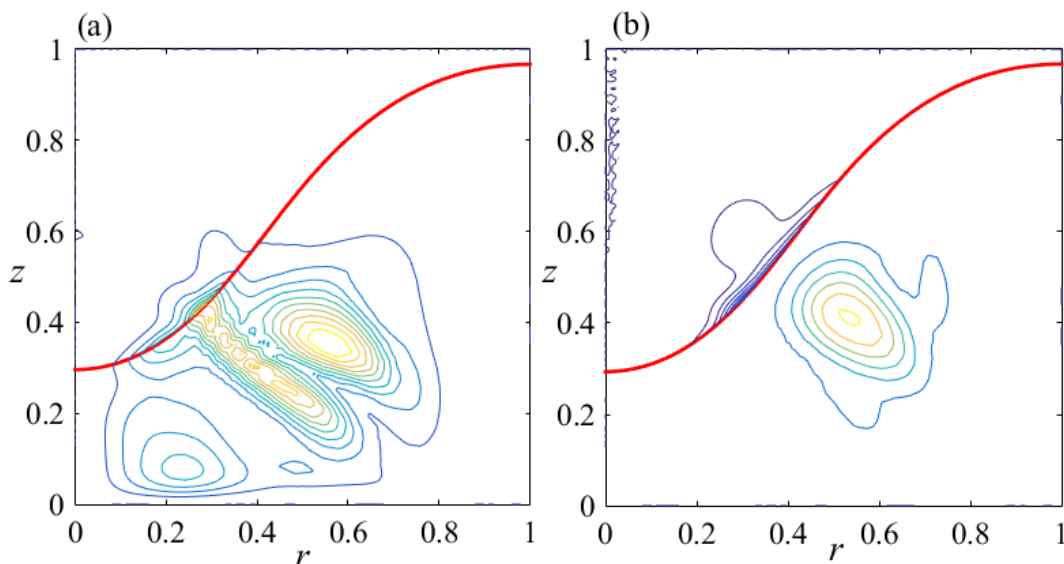
Figure 5.13 Energy contours for marginal disturbance with $m = 2$ (a) and 4 (b) at $H_w = 0.8$.

5.5. Moderately deep whirlpool

Now we describe changes in the flow topology occurring as Re increases at the equal volumes of water and air, $H_w = 0.5$, and examine the flow stability.

5.5.1. Flow reversal near the interface

Figure 5.14 depicts the streamlines patterns at $Re = 250$ (a) and 300 (b). The pattern shown in Figure 5.14(a) is similar to that shown in Figure 5.2(a). The difference is that the outmost Moffatt eddy ME is observed in Figure 5.14while it is not seen in Figure 5.2 being unresolved by our standard grid.

Moffatt [132] revealed that a flow in a corner (between two inclined planes with a sufficiently small angle) has an infinite set of eddies whose strength and scale diminish to zero as the edge is

approached. Since the eddy size is small compared with the cylinder radius (see ME in Figure 5.14), the sidewall can be approximated by a tangential plane thus reducing the cylindrical geometry to the corner between orthogonal planes.

The corner angle, 90°, is sufficiently small for the Moffatt eddies to occur. The air circulation in CR2 generates the Moffatt corner eddies. Among them, only the outmost eddy is resolved by our standard grid and denoted as ME in the upper-right corner of the air flow in Figure 5.14.
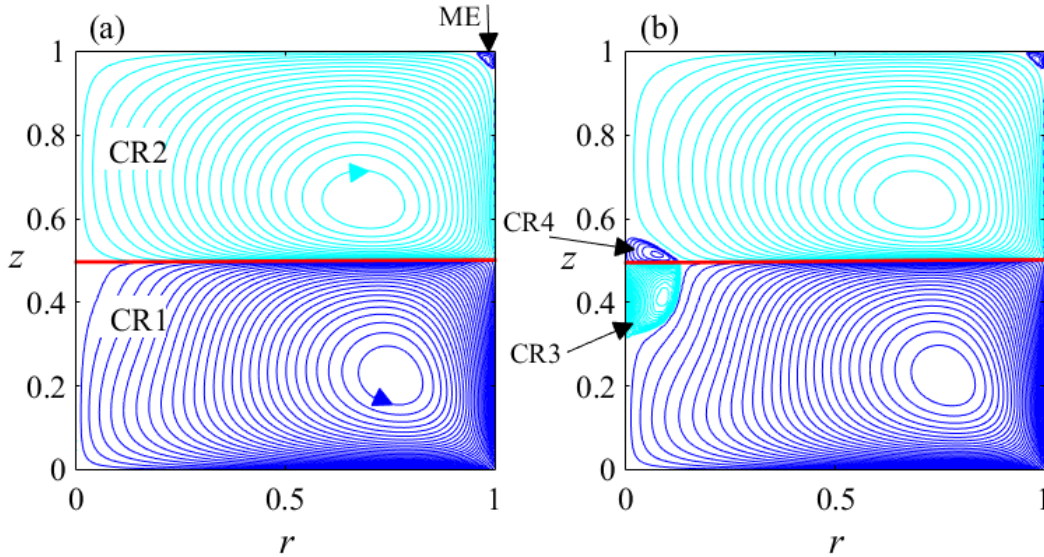
Figure 5.14 Streamline patterns at $H_w = 0.5$ for $Re = 250$ (a) and 300 (b) show the outmost Moffatt eddy ME and the emergence of circulation regions CR3 and CR4.
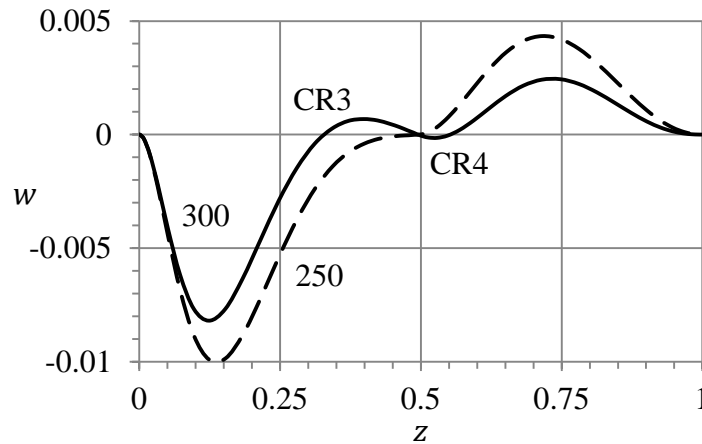
Figure 5.15 Distributions of velocity w at the axis, $r = 0$, for $Re = 250$ (dashed curve) and 300 (solid curve) show the emergence of circulation regions CR3 and CR4, see Fig. 14(b), in the water (air) region $0 < z < z_i$ ($z_i < z < 1$); $z_i = 0.497$ (0.495) at $Re = 250$ (300).

The Moffatt eddies can also develop in a flow inside a cone if cone half-angle $\theta_c < 80.9°$ [147]. A cone becomes a plane at $\theta_c = 90°$. This angle is too large for the Moffatt eddies to occur. Accordingly, no eddy exists near the top disk and axis intersection.
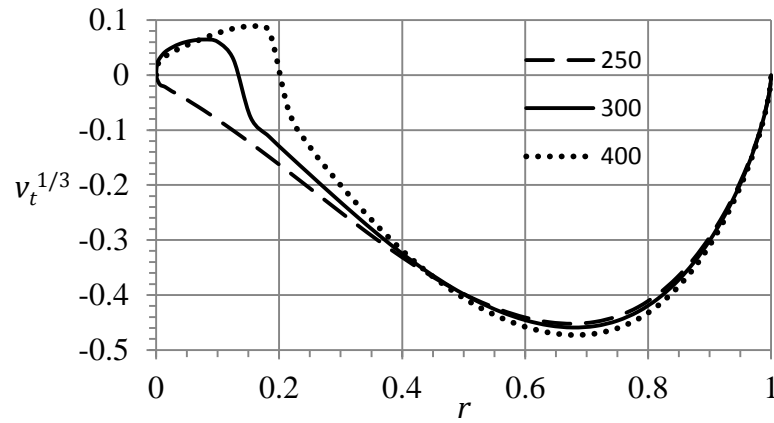
Figure 5.16 Profiles of meridional velocity on the interface v_t at $Re = 250$, 300, and 400 illustrate the emergence and radial expansion of regions CR3 and CR4 (where $v_t > 0$) as Re increases.

Figure 5.14(a) remains topologically invariant as Re decreases down to zero. In contrast as Re increases, a local flow reversal occurs near the axis-interface intersection point, $r = 0$ and $z = z_i = 0.497$, and a two-fluid VB bubble, CR3 and CR4, emerges as Figure 5.14(b) shows. The topological scenarios differ: the VB occurs in the water depth for $H_w = 0.8$, but at the interface for $H_w = 0.5$. Figure 5.15 depicts the distribution on the axis of velocity w for Re values shown near the curves. At $Re = 250$, the velocity is negative in the range, $0 < z < z_i$, that corresponds to water region CR1, and positive in the range, $z_i < z < 1$ that corresponds to air region CR2 in Figure 5.14(a).

At $Re = 300$, w changes its signs near the interface in both water, $0.33 < z < z_i = 0.495$, and air, $z_i < z < 0.551$, flows. These z-ranges respectively correspond to CR3 and CR4 shown in Figure 5.14(b). Interpolating yields that CR3 and CR4 simultaneously emerge at $Re = Re_{1m} = 257$. The leading event is the appearance of region CR3 in water which is a corner bubble. The emergence of region CR4 in air is a sequence of v_t reversal near the axis which accompanies the CR3 development. Figure 5.16 depicts $v_t^{1/3}$ to better observe small positive values of v_t near the axis at $Re = 300$ (curve 2) and 400 (curve 3). Velocity v_t becomes positive for $Re > 257$ and the $v_t > 0$ range, corresponding to CR3 and CR4 in Figure 5.14(b), expands as Re increases (Figure 5.16). The emergence of the two-fluid VB bubble is the first change in the flow topology at $H_w = 0.5$.

5.5.2. Flow reversal near the upper wall
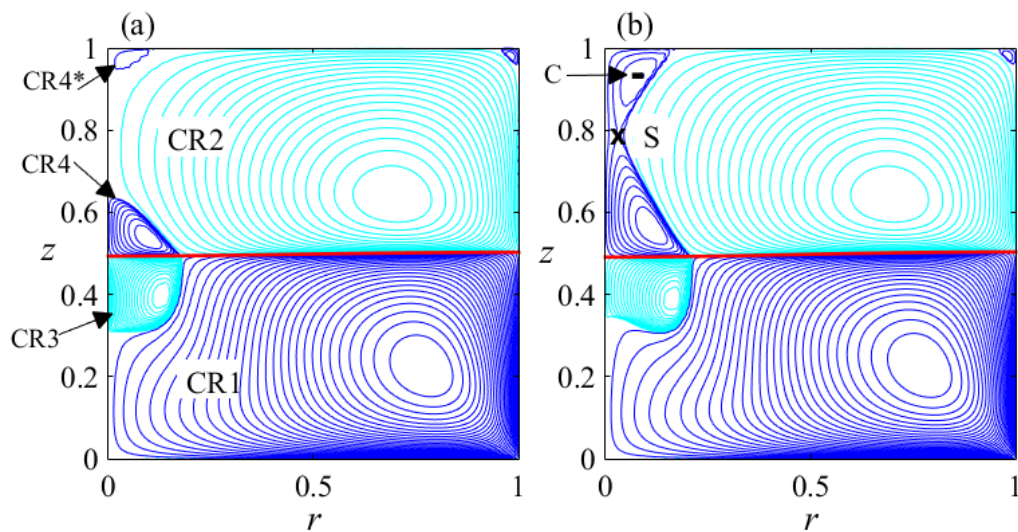
Figure 5.17 Streamline patterns at (a) $Re = 350$ and (b) 400 shows (a) the emergence of circulation region CR4* and (b) merger of CR4 and CR4*.
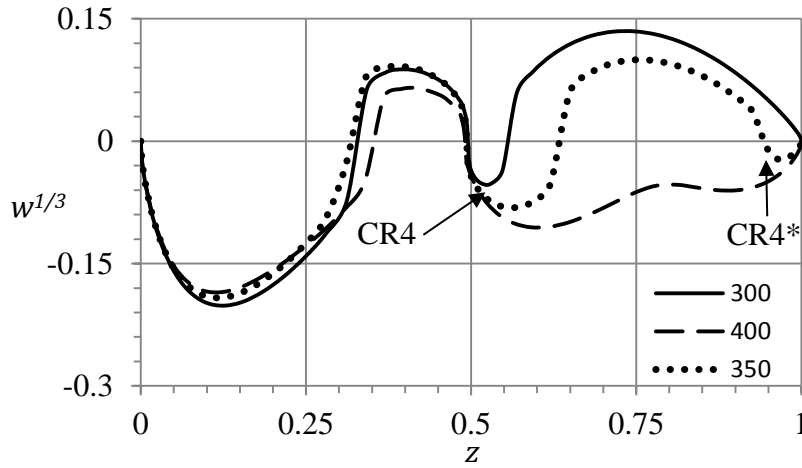
Figure 5.18 Distributions of velocity w at the axis at $Re = 300$, 350, and 400 illustrate the emergence of circulation region CR4* (curves 300 and 350) and merging of CR4 and CR4* (curves 350 and 400, see also Fig. 17).

The second change in the flow topology as Re increases is the development of local counter-circulation of air near the center of the top disk at $Re = Re_{2m}= 347$. Figure 5.17(a) depicts this region (CR4*) at $Re = 350$. The physical reasoning for CR4* emergence is the Bödewadt pumping similar to that in the $H_w= 0.8$ case.

Figure 5.18 depicts the distribution of velocity w at the axis at $Re = 300$, 350 and 400. We plot $w^{1/3}$ to better observe circulation region CR4 (in the range $0.495 < z < 0.632$ for curve 350) and the emergence of circulation region CR4* (in the range $0.947 < z < 1$ for curve 350) where $|w|$ is small. Comparison of curves 300 and 350 in Figure 5.18 helps understand how region CR4* emerges.

5.5.3. Merging of anticlockwise circultation regions in air flow

The third change in the flow topology as Re increases is the merging of regions CR4 and CR4* at $Re = Re_{3m} = 393$. The two saddle stagnation points in Figure 5.17(a), located on the axis between regions (i) CR2 and CR4 and (ii) CR2 and CR4*, coalesce at $Re = 393$ in one saddle point S, which separates from the axis for $Re > 393$ as Figure 5.17(b) shows at $Re = 400$. The merged region, denoted again as CR4, extends from the interface up to the top disk for $Re > 393$.

Comparison of Figure 5.17(a) and Figure 5.17(b) shows how the streamline pattern changes. Figure 5.18 depicts the corresponding change in the velocity distribution at the axis: ranges CR4 and CR4*, where $w < 0$ in the air flow (curve 350), merge into the range, $z_i < z < 1$ (curve 400), as Re increases.

The anticlockwise circulation in the merged region CR4 in Figure 5.19(a) is driven by two factors: (i) positive meridional velocity at the interface, $v_t > 0$, and (ii) Bödewadt pumping. In contrast to the opposite effects of v_t and swirl in region CR2 for $Re < 325$, factors (i) and (ii) cooperate in region CR4 for $Re > 303$ and result in the radial expansion of CR4 as Figure 5.19 illustrates. Saddle S and center C stagnation points of the meridional flow in Figure 5.19(a) merge and disappear in Figure 5.19(b) via the saddle-center bifurcation [144].
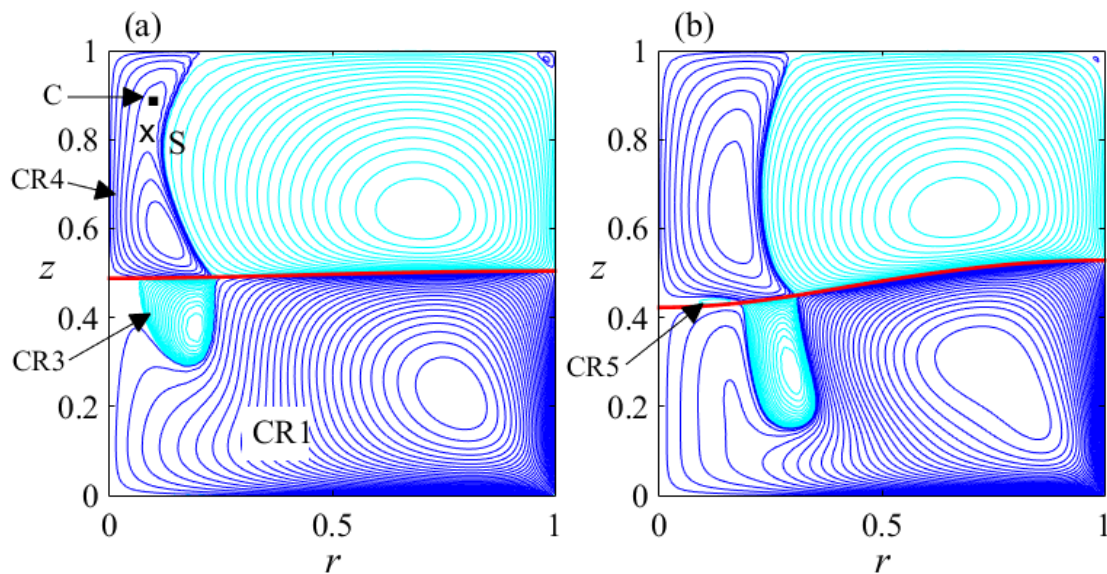
Figure 5.19 Streamline patterns at (a) $Re = 450$ and (b) 1000 show the separation of region CR3 from axis and the emergence of region CR5.

5.5.4. Separation of water VB region from the axis

The forth change in the flow topology is the separation of water VB region CR3 from the axis at $Re = Re_{4m} = 434$. Comparison of Figure 5.17(a) and Figure 5.17(b) shows that the boundary between regions CR1 and CR3 moves upward near the axis as Re increases. The boundary reaches the interface at $Re = 434$ and the separation occurs. Figure 5.19(a) depicts the streamline pattern and separated region CR3 at $Re = 450$.
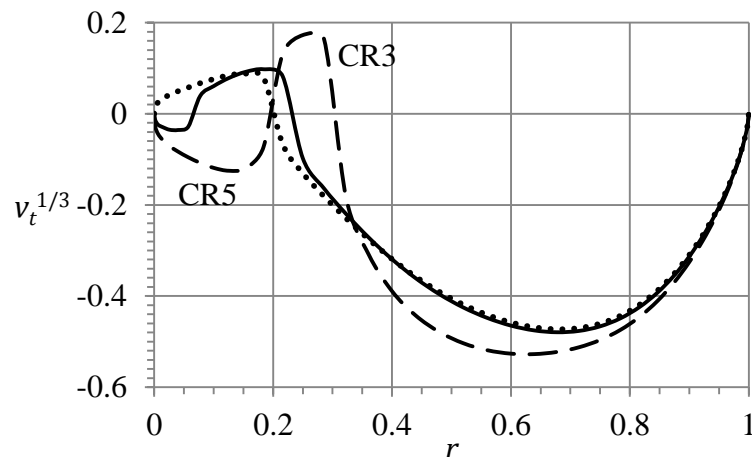
Figure 5.20 Distribution of meridional velocity on the interface v_t at $Re = 400$ (dotted curve), 450 (solid curve), and 1000 (dashed curve) shows the emergence (solid curve) and expansion (dashed curve) of region CR5 shown in Fig. 19(b).

Figure 5.20 depicts the distribution of meridional velocity at the interface v_t at $Re = 400$ (dotted curve), 450 (solid curve), and 1000 (dashed curve), and illustrates one more reversal of v_t which becomes negative near the axis for $Re > 434$. The $v_t > 0$ range of curve 2 in Figure 5.20 corresponds to region CR3 in Figure 5.19(a) and the left $v_t < 0$ range verifies that region CR3 is indeed separated from the axis at $Re = 450$.

This near-axis $v_t < 0$ range corresponds to new region CR5 which radially expands as Re

increases (curve 1000 in Figure 5.20). Region CR5, located in the air flow above the interface, is so thin, that it is invisible in Figure 5.19(a), and hardly observed in the streamline pattern even at $Re = 1000$ as Figure 5.19(b) illustrates. Figure 5.8(a) schematically shows the arrangement of regions CR1-CR5 in the range $434 = Re_{4m} < Re < Re_{5m} = 1183$.

The negative v_t near the sidewall, $r = 1$, (Figure 5.20) agrees with the clockwise circulation of air in region CR2 (Figure 5.14(a)). In contrast, the negative v_t near the axis (solid and dashed curves in Figure 5.20) corresponds to a counter flow with respect to the anticlockwise circulation of air in region CR4 as Figure 5.19(a) shows. Therefore, one more circulation region (CR5) must exist in air, separating regions CR1 and CR4 as Figure 5.8(a) schematically depicts.

Re	z_i	z_s	$z_s - z_i$
$Re_{4m} = 434$	0.4898	0.4898	0
450	0.4879	0.491	0.0037
525	0.4820	0.502	0.0020
600	0.4762	0.502	0.0257
1000	0.4219	0.439	0.0171
1100	0.4030	0.413	0.0106
$Re_{5m} = 1183$	0.3927	0.3927	0
1300	0.3582	0.242	–0.1159
1500	0.3020	0.130	–0.1715
1800	0.185	0.087	–0.0978

Table 5.3 Values of z for the interface (z_i) and separatrix (z_s) on the axis, and axial range ($z_s - z_i$) of CR5 for $Re_{4m} < Re < Re_{5m}$ and of CR6 for $Re > Re_{5m}$.

Table 5.3 lists values of z on the axis, corresponding to the interface (z_i) and the boundary separating regions CR4 and CR5 (z_s). In addition, the axial extent of region CR5 ($z_s - z_i$) is shown in range $434 = Re_{4m} < Re < Re_{5m} = 1183$.

The flow topology, depicted in Figure 5.19 and Figure 5.8(a), remains unchanged in the range, $434 < Re < 1183$. Figure 5.8(a) shows thin curves, separating regions (a) CR4 and CR5, (b) CR1 and CR3, and (c) CR2 and CR4, which can be considered as parts of the united curve, "separatrix". The separatrix originates on the axis at $z = z_s$ and twice intersects the interface in Figure 5.8(a). The number of separatrix-interface intersections grows as Re increases, as shown below.

5.5.5. Emergence of the second VB region in water

The fifth change in the flow topology is the development of the second vortex breakdown bubble (CR6) in the water flow near the axis-interface intersection at $Re = Re_{5m} = 1183$. This development at $H_w = 0.5$ differs with that at $H_w = 0.8$. Figure 5.21 is a schematic showing the flow topology for $Re > 1183$. Table 5.3 indicates that z_s decreases and becomes smaller than z_i for $Re > 1183$ (compare Figure 5.8(a) and Figure 5.21). Figure 5.22 (Figure 5.23) depicts the streamline pattern (v_t) at $Re = 1500$ where circulation region CR6 is well observed.
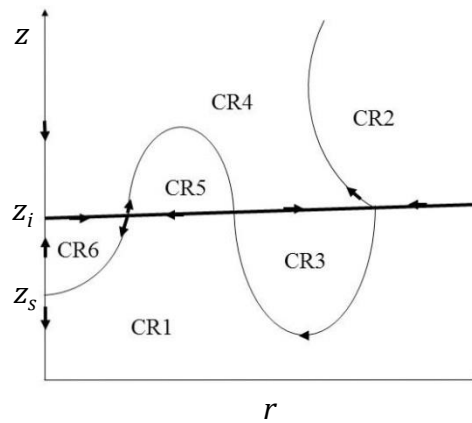
Figure 5.21Schematic of circulation regions CR1-CR6 at $Re > Re_{5m} = 1183$ (see Figure 5.22). The bold line denotes the interface, the thin curve is separatrix, and the arrows show flow directions.
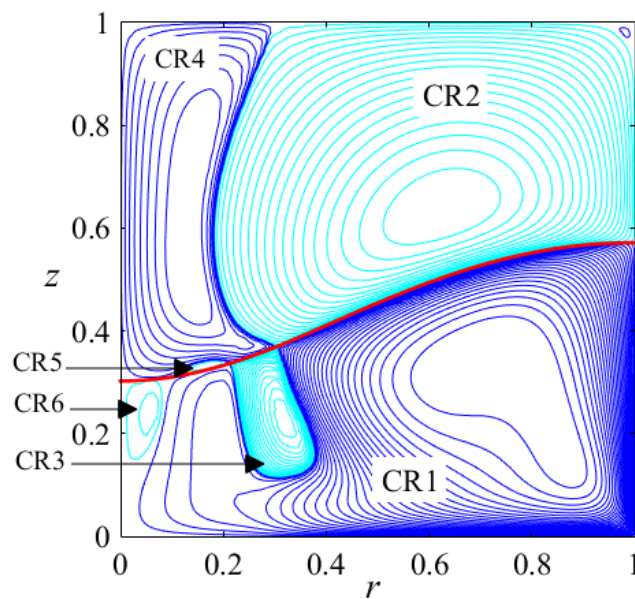
Figure 5.22 Streamline patterns at $Re = 1500$ corresponds to schematic in Figure 5.21.

The axial extent of region CR6 $(z_i - z_s)$ is shown in Table 5.3 for $Re > 1183$. Water VB cells CR3 and CR6 are wide while air cell CR5 is thin in the z-direction (Figure 5.22). This feature is due to CR3 and CR6 are generated by the water rotation while CR5 is generated by v_t. Figure 5.23 indicates that v_t is very small in CR5 that explains why CR5 is thin. Thus, a chain of near-interface cells develops depicted in Figure 5.21 and Figure 5.22.
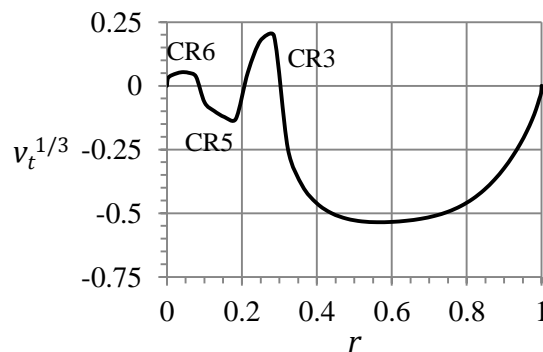
Figure 5.23Distribution of meridional velocity at the interface v_t at $Re = 1500$ characterizes local circulation regions, CR3 $(v_t > 0)$, CR5 $(v_t < 0)$, and CR6 $(v_t > 0)$, adjacent to interface (Figure 5.21 and Figure 5.22).

5.5.6. Reduction of VB cells in the air flow

Figure 5.24 depicts the further flow transformations as Re increases. Regions CR2 and CR5, shown in Figure 5.22, approach each other (Figure 5.24(a)), touch, and merge (Figure 5.24(b), the seventh change). The transition from the pattern in Figure 5.24(a) to that in Figure 5.24(b) have similar intermediate changes in the flow topology as those for the transition from Figure 5.10(a) to Figure 5.10(b) [144]. Next, region CR4, shown in Figure 5.22, separates into the upper and lower parts (Figure 5.24(c), the eighth change) and the lower part shrinks and disappears (Figure 5.24(d), the ninth change). These transformations at $H_w = 0.5$ are similar to those at $H_w = 0.8$. Figure 5.24(d) corresponds to the critical Re according to Table 5.4.
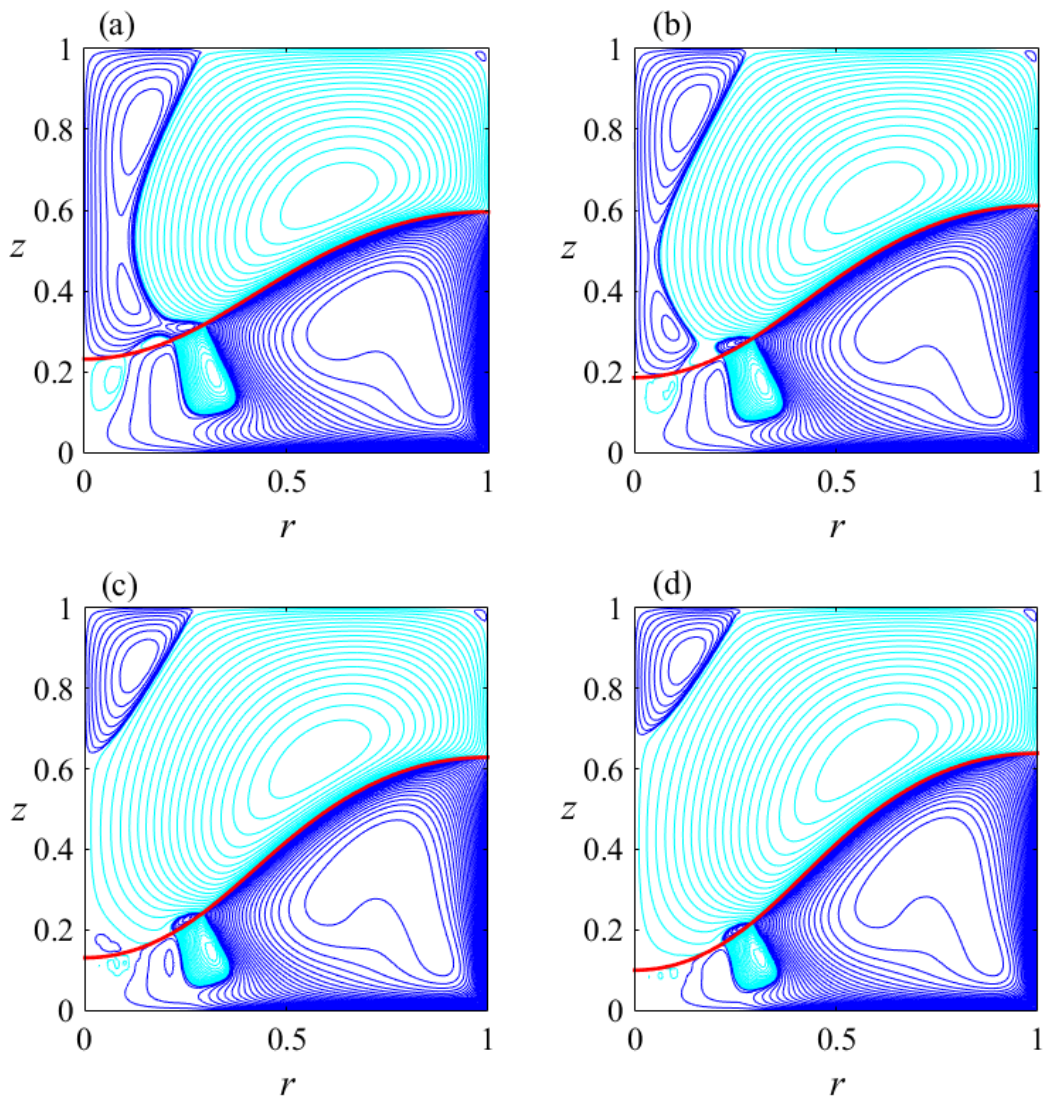
Figure 5.24 Streamline patterns at $Re = 1700$ (a), 1800 (b), 1900 (c) and 1950 (d).

5.5.7. Instability of $H_w = 0.5$ flow

In addition to the critical instability with respect to single-helix disturbances, there is the marginal instability with respect to two-helix disturbances, according to Table 5.4. For larger Re, the interface reaches the bottom. Our numerical procedure is not applicable for such flow patterns. Figure 5.25 shows Ed contours for the critical disturbance.

Re	**1950**	2088
m	**1**	2
ω_r	**0.259**	0.994

Table 5.4 Critical (bold) and marginal parameters of the flow instability at $H_w = 0.5$.
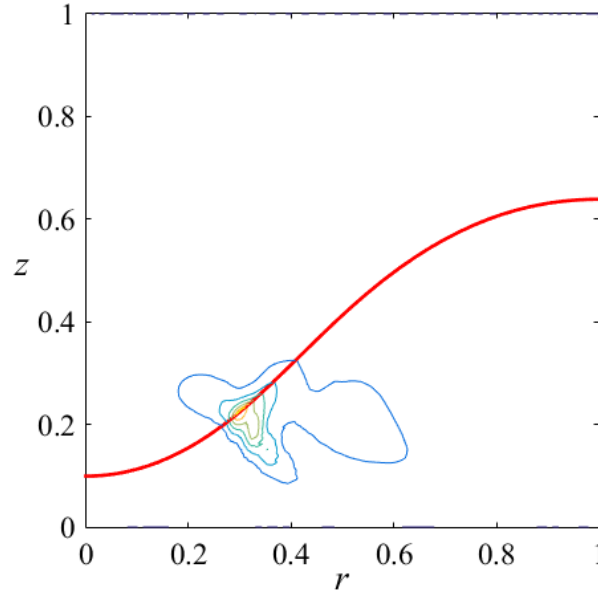
Figure 5.25 Energy contours indicate where the critical disturbance mostly grows in the flow depicted in Fig. 24(d).

The energy peak is located at $r = 0.296$ and $z = 0.222$ that is very close to the interface where the jet-like water flow converging toward the axis along the interface meets the VB bubble (Figure 5.24(d)). This feature is similar to that at $H_w = 0.8$. The outmost contour in Figure 5.25 corresponds to 0.1 of the energy maximal value and therefore the disturbance energy is localized near its peak.

5.6. Shallow whirlpool

Here we describe changes in the flow topology occurring as Re increases in the shallow whirlpool at $H_w = 0.3$ and examine the flow stability.

5.6.1. Flow reversal near the top disk

The streamline pattern at $Re = 150$, depicted in Figure 5.26(a), is similar to that shown in Figure 5.14(a) and remains topologically invariant as Re diminishes to zero. In contrast as Re increases, VB emerges in the air domain near the center of the top disk at $Re = Re_{s1} = 174$. Figure 5.26(b) depicts the new-born VB region CR3 at $Re = 200$. The arrows show the flow direction.
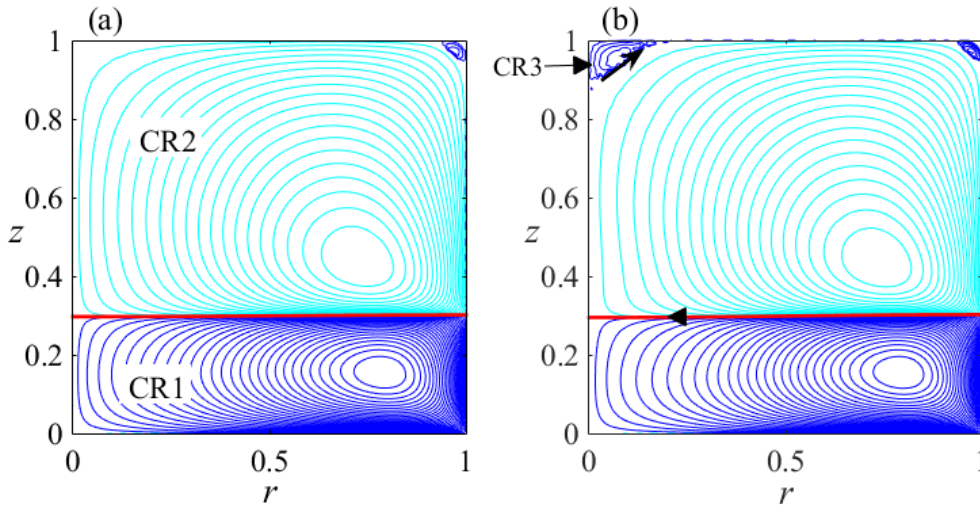
Figure 5.26 Streamline patterns at Re = 150 (a) and 200 illustrate the emergence of CR3.

The physical reasoning behind the CR3 development is the Bödewadt pumping similar to that discussed in section 5.4.3. As Re increases, this pumping enlarges region CR3 in the radial and axial directions. Expanding downward, region CR3 touches the interface at the axis resulting in that region CR2 transforms from a bubble into a bubble-ring as discussed in more detail below.

5.6.2. Development of the first robust bubble-ring

To detect robust bubble rings (RBRs) we analyze (a) streamline patterns, (b) distribution of meridional velocity at the interface $v_t(r)$, (c) distribution of velocity $w(z)$ on the axis, and (d) numerical values of z_i and z_s where $w = 0$ at $r = 0$. Table 5.5 lists values of z at which the axis intersects the interface (z_i) and the boundary separating regions CR2 and CR3 (z_s) as shown in Figure 5.26(b). The (a)-(d) results help us to recognize the existence of RBRs in the ranges of Re specified below.

As Re increases, CR3 expands downward according to Table 5.5, which shows that $z_s - z_i$ decreases and becomes zero at $Re = Re_{s2} = 690$. At this Re, region CR3 touches the interface at the axis. Near the entire interface, the flow is still directed toward the axis (i.e., $v_t(r) < 0$ in the entire range, $0 < r < 1$, at $Re = 690$) driven by the Kármán pumping in CR1. The converging-to-axis water flow entrains adjacent air resulting in that the interface remains to be the boundary between regions CR1 and CR2 only. Therefore, region CR2 continues to be extended from the sidewall up to the axis and touches the axis at the single point, $z = z_i$, at $Re = 690$. This proves that region CR2 is a bubble for $Re < 690$ and becomes a bubble-ring at $Re = 690$.

Now consider what occurs for $Re > 690$. According to the algebra rule, two real roots of a smooth function (here $w(z)$) typically disappear (become complex) after merging. However in a two-fluid flow, z_i cannot disappear due to the physical limitation that the interface cannot detach from the axis except at the end disks. Under this limitation, there are three options: roots z_i and z_s can (i) split back to their $Re < 690$ arrangement, (ii) separate reversing their positions and (iii) stay merged. Case (i) is not observed in this paper. Case (ii) is described in section 5.5.3, where $z_s - z_i$ changes its sign as Re increases (Table 5.3). Case (iii) is achieved here as Table 5.5 shows that $z_i = z_s$ in the wide range, $690 \leq Re \leq 1500$.

Re	z_i	z_s	$z_s - z_i$
0	0.3	1	0.7
$Re_{s1} = 174$	0.2969	1	0.7031
200	0.2949	0.9134	0.6185
250	0.2925	0.3510	0.0585
300	0.2896	0.3198	0.0302
400	0.2822	0.2967	0.0144
600	0.2599	0.2637	0.0038
$Re_{s2} = 690$	0.2449	0.2449	0
$Re_{s3} = 829$	0.2216	0.2216	0
900	0.2067	0.2067	0
1100	0.1571	0.1571	0
1300	0.0946	0.0946	0
$Re_{s5} = 1500$	0.0174	0.0174	0

Table 5.5 Axial values for the interface-axis (z_i) and separatrix-axis (z_s) intersections. Value of ($z_s - z_i$) is the z-extent of CR2 at the axis for $Re < 829$.

Table 5.5 and the feature that $v_t < 0$ at the entire interface indicate that region CR2 remains to be a bubble-ring for $Re > 690$ as well. Figure 5.27(a) depicts the streamline pattern at $Re = 700$ where region CR2 is the new-born bubble-ring. Region CR2 extends from the sidewall up to the axis being a very thin layer in the range $0 < r < 0.35$ where it separates regions CR1 and CR3 in Figure 5.27(a) (see also Figure 5.37(a)). It is explained below why this layer is so thin that it is invisible in Figure 5.27(a).
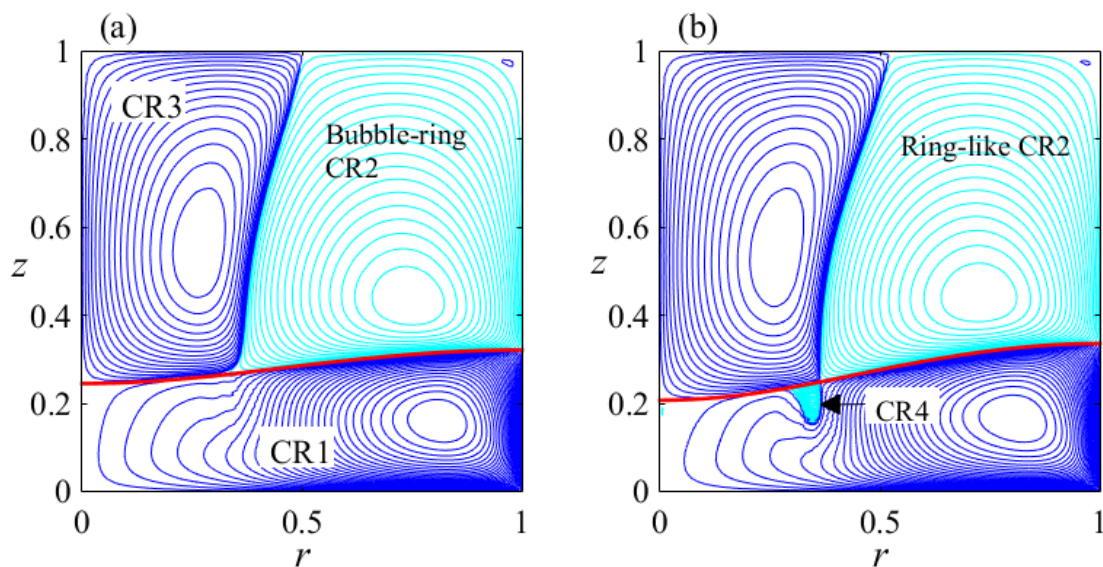
Figure 5.27 Streamline patterns at $Re = 700$ (a) and 900 (b) illustrate how CR2 transforms from bubble (Figure 5.26) in bubble-ring (a) and then in ring (b). Emergence of off-axis VB region CR4 is also shown.

The important difference in the VB scenarios for $H_w = 0.5$ and $H_w = 0.3$ is that

$z_s - z_i$ becomes (does not become) negative as Re increases according to Table 5.3 (Table 5.5). Physical reasoning behind this difference is that an air (water) flow cannot (can) easily reverse a water (air) flow due to the small density ratio, $\rho_r = 0.00122$. For Re slightly exceeding 690, the air flow in region CR3, shown in Figure 5.27(a), is not capable to reverse the interface meridional motion, which is driven by the water flow. For this reason, region CR3 touches the interface only at a single point, namely at the axis, where $v_t = 0$. The Bödewadt pumping extends region CR3 from the axis along the interface in Figure 5.27(a), but cannot overcome the converging motion at the interface, leaving a thin layer of CR2 region, where the air meridional velocity reverses from being directed toward the axis at the interface into being directed away from the axis at the CR3 lower boundary.

To mathematically investigate, why region CR2 is thin between CR1 and CR3 in Figure 5.27(a), consider the Stokes stream function, Ψ, near the axis-interface intersection. With no loss of generality, we can apply the representation,

$$\Psi = r^2[z\!-\!F(r)]\Psi_1(r,z), \qquad\qquad\qquad 5.9$$

where Ψ_1 is a bounded function.

Presentation (5.9) takes into account the boundary conditions at the axis, $r = 0$, and the interface, $z = F(r)$. Since the axis is a streamline, we can put $\Psi = 0$ at $r = 0$. The regularity requirement yields that $\partial\Psi/\partial r = 0$ at $r = 0$ and, therefore, Ψ is proportional to r^2. The interface, $z = F(r)$, is a stream surface, where $\Psi = 0$, that explains the presence of expression in the rectangular brackets in (8). The boundary between regions CR2 and CR3, e. g., in Figure 5.27(a), $z = F_s(r)$, is also a stream surface where $\Psi = 0$. Therefore for $Re > Re_{s1} = 174$, we can use the presentation, $\Psi_1(r,z) = [z\!-\!F_s(r)]\Psi_2(r,z)$, where Ψ_2 is a bounded function.

Due to the axial symmetry, both $F(r)$ and $F_s(r)$ are even functions of r and their power-law expansions are $F(r) = z_i + a_i r^2 + O(r^4)$ for the interface and $F_s(r) = z_s + a_s r^2 + O(r^4)$ for separatrix near the axis, where $r \ll 1$. Here subscripts "i" and "s" denote the interface and separatrix, respectively.

Both the interface and separatrix are normal to the axis at the intersection points, $r = 0$, $z = z_i$ and $z = z_s$, where $w = 0$. This feature remains valid after merging of z_i and z_s, i.e., the interface and separatrix are tangential at $r = 0$. This tangency is a mathematical reason why region CR2 is thin near the axis in Figure 5.27(a).
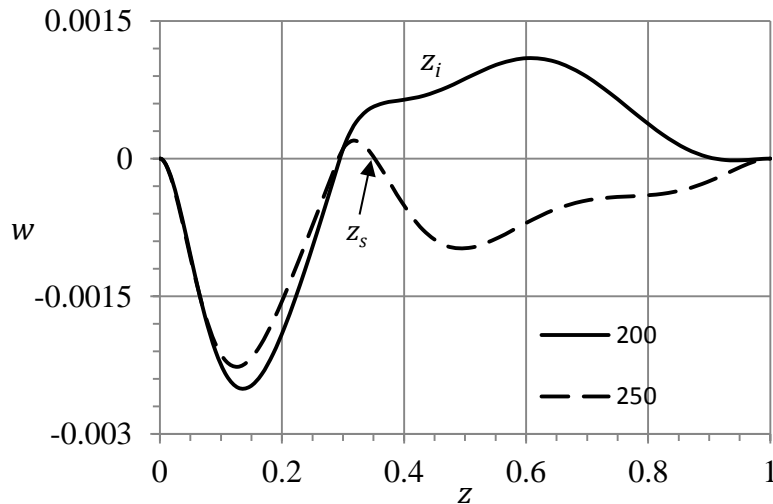
Figure 5.28 Profiles of velocity w on axis show how $w > 0$ range shrinks as Re increases from 200 (solid curve) to 250 (dashed curve).

Figure 5.28 and Figure 5.29 depict how the distribution of velocity on the axis, $w(z)$ at $r = 0$, changes as the roots z_i and z_s merge. At $Re = 200$ (the solid curve in Figure 5.28), w is positive in the air flow, corresponding to the CR2 circulation, except in the $w < 0$ range, $0.9134 = z_s < z < 1$, corresponding to the CR3 circulation in Figure 5.26(b).
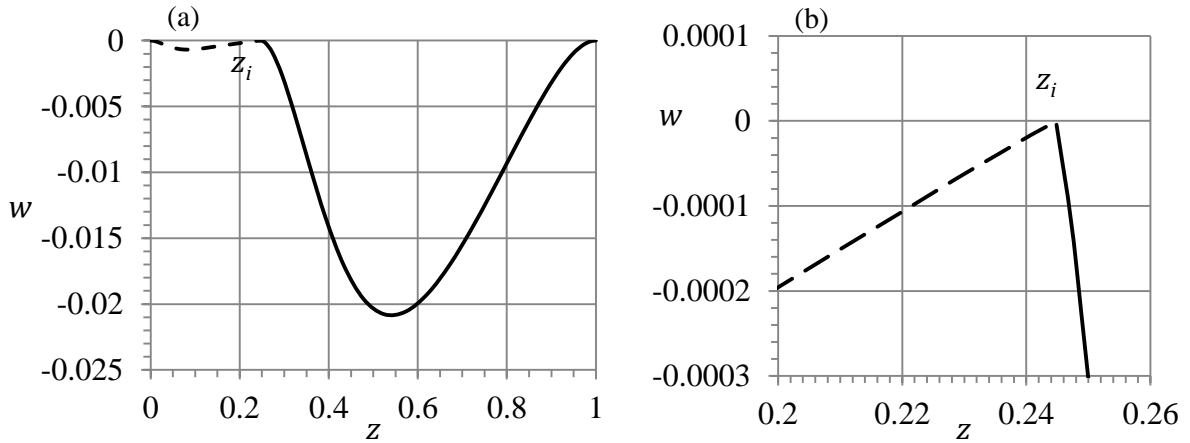
Figure 5.29 (a) Velocity on axis at $Re = 700$, (b) close up of interface (z_i) vicinity.
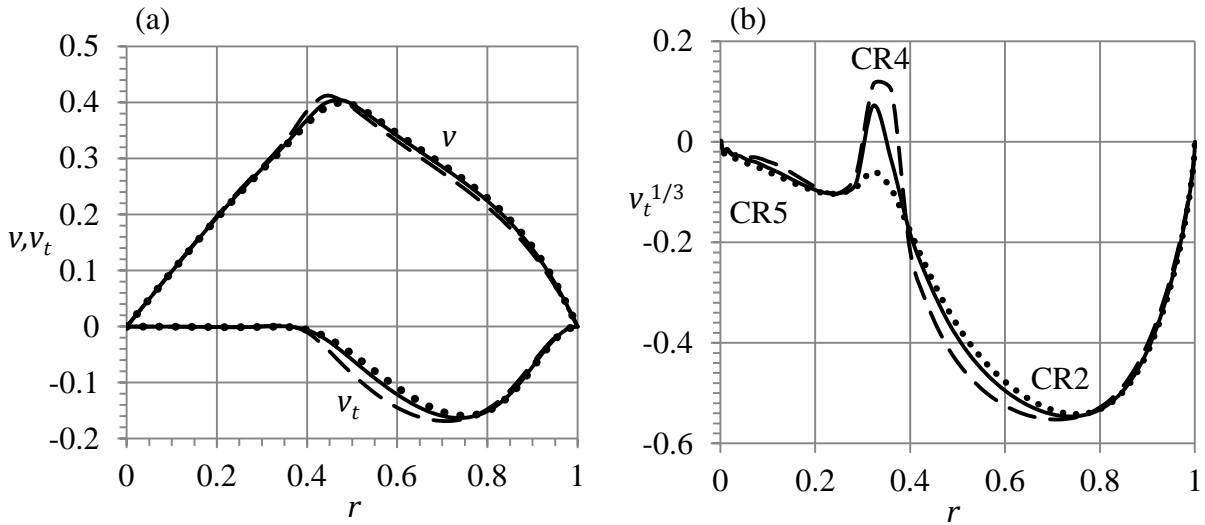
Figure 5.30 (a) Distributions of swirl v and meridional v_t velocities at the interface at $Re = 800$ (dotted curves), 900 (solid curves), and 1100 (dashed curves); (b) distributions of $v_t^{1/3}$ reveal the appearance of $v_t > 0$ range, CR4 and CR5 as Re increases.

The boundary, separating CR2 and CR3 (referred to as "separatrix" here), intersects the axis at $z = z_s$. At Re = 250 (dashed curve in Figure 5.28), the $w > 0$ range, $z_i < z < z_s$ (corresponding to CR2), is small compared with the $w < 0$ range, $z_s < z < 1$ (corresponding to CR3). The $w > 0$ range collapses at $Re = Re_{s2} = 690$.

Figure 5.29 depicts the velocity distribution on the axis at $Re = 700$ where z_i and z_s are merged (Table 5.5). The dashed (solid) curves correspond to the water (air) flow in Figure 5.29. Curve $w(z)$ looks tangential to line $w = 0$ at $z = z_i$ in Figure 5.29(a). However, the close up of the interface vicinity, depicted in Figure 5.29(b), reveals that the curve and the line are indeed not tangential. Despite the curve does touch the line at $z = z_i$, the derivative, $\partial w/\partial z$, is not zero and has a jump at $z = z_i$.

The jump follows from the normal stress balance (equation 5.6) and the different properties of air and water. A jump in $\partial w/\partial z$ at the interface is a specific feature occurring in a two-fluid flow where the fluid density and viscosity are not continuous at the interface.

The presence of region CR2 (or other flow cells described below) is necessary in order to separate CR1 and CR3 which have the same circulation direction and therefore can only touch each other at a saddle point on the interface. One such point is located at the axis in Figure 5.27(a). Other saddle points, located away from the axis for $Re \geq Re_{s3} = 829$, are discussed below.

5.6.3. Off-axis vortex breakdown in water flow

The third topological transformation is the VB emergence in water away from the axis at $Re = Re_{s3} = 829$. This topological change occurs due to the air flow which locally reverses the meridional velocity at the interface, v_t. Figure 5.30 depicts the distributions of swirl v and meridional v_t velocities at the interface at $Re = 800$ (dotted curves), 900 (solid curves), and 1100 (dashed curves). For $Re < 829$, the meridional velocity is directed toward the axis: $v_t < 0$ in $0 < r < 1$, as the dotted curves in Figure 5.30 show. For $Re > 829$, a range of $v_t > 0$ exists. We reveal this by plotting $v_t^{1/3}$ in Figure 5.30(b) in order to better observe regions CR4 and CR5, located in the range $0 < r < 0.4$, where v_t is very small in Fig. 30(a).
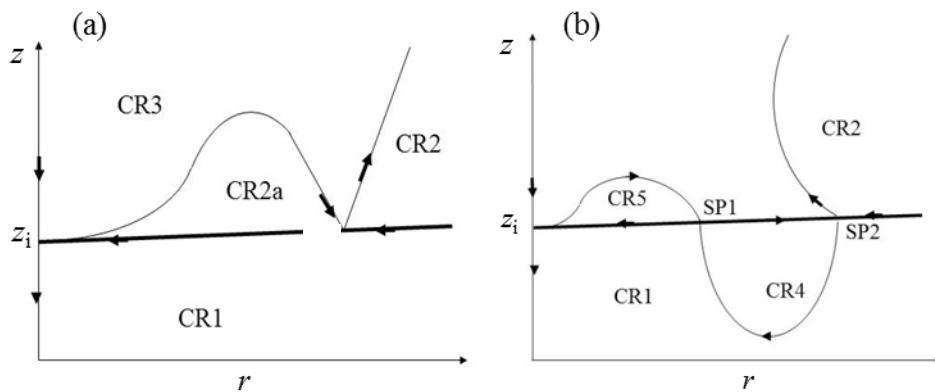
Figure 5.31 Schematics show the flow topology at $Re = 829$ (a) and $Re > 829$ (b). The bold lines denote the interface and the arrows indicate the flow direction.

Figure 5.30(a) shows that the distribution of swirl velocity v is nearly linear (solid-body-rotation) and meridional velocity v_t is negligibly small compared with v in the range, $0 < r < 0.4$. Therefore, this part of the interface acts like a rotating disk for adjacent air. The Kármán pumping pushes air away from the axis near the interface. The air meridional velocity is maximal near $r = 0.35$, where air-flow streamlines converge and are maximally close to the interface in region CR3 (Figure 5.27). This explains why the air flow reverses v_t and a small portion of the water flow near $r = 0.35$ as Re increases.

Figure 5.30(b) shows that there is a local maximum of v_t near $r = 0.35$, whose value is negative at $Re = 800$ and positive at $Re = 900$. Interpolation yields that the maximum value is zero at $Re = Re_{s3} = 829$. At this Re, the boundary between regions CR2 and CR3 touches the interface at point SP as Figure 5.31(a) schematically shows. SP is a saddle point where the meridional motion stagnates, $v_t = 0$, but $v \neq 0$. CR2 becomes divided into two regions: (i) near-sidewall part (denoted again as CR2) which has the ring shape, as Figure 5.27(b) shows, and (ii) near-axis part denoted as CR2a in Figure 5.31(a) which inherits the bubble-ring shape.

At $Re > 829$, SP splits in two saddle points SP1 and SP2, located on the interface as Figure 5.31(b) shows. The interval between SP1 and SP2, where the flow goes away from the axis in Figure 5.31(b), corresponds to the $v_t > 0$ range in Figure 5.30. The v_t reversal results in the appearance of two new cells: CR4 in water and CR5 in air existing for $Re > 829$ as Figure 5.31(b)

illustrates. Thus, an off-axis VB occurs resulting in the emergence of VB ring CR4 which expands as Re increases being well observed at $Re = 900$ in Figure 5.27(b).
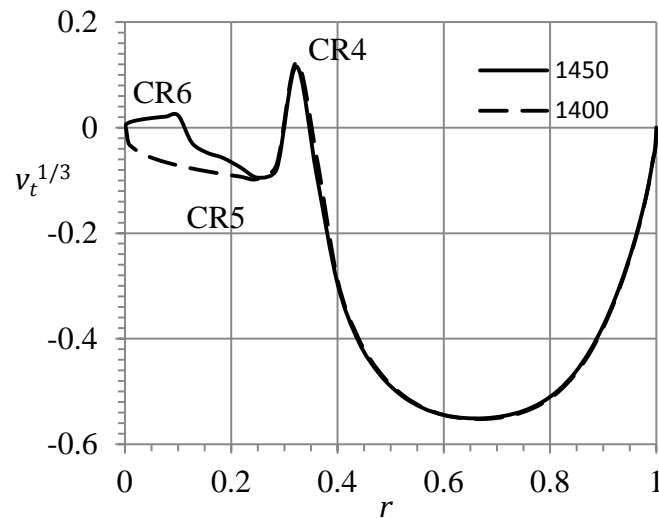
Figure 5.32 Distribution of meridional velocity on the interface at $Re = 1400$ and 1450 shows reversal of v_t near axis and appearance of region CR6.

In contrast, region CR5 (former region CR2a) remains thin; it is a near–axis part separated from former region CR2 shown in Figure 5.27(a). Region CR5 is depicted large in Figure 5.31(b) just for convenient observation. Indeed, region CR5 is so thin that it is not visible at $Re = 900$ in Figure 5.27(b). The CR5 existence follows from the above analysis of flow topology for $Re > 829$ and from the v_t distribution depicted in Figure 5.30(b), where region CR5 corresponds to the near-axis range where $v_t < 0$. Thus, the third change in the flow topology transforms CR2 from a bubble-ring into a ring and results in the emergence of two new circulation regions: (i) VB ring CR4 in water and (ii) bubble-ring CR5 in air.

5.6.4. Chain of VB regions

The fourth and fifth topology transformations occur as the interface approaches the bottom disk. Figure 5.32 depicts the second reversal of the meridional velocity on the interface, which occurs near the axis at $Re = Re_{s4} \approx 1440$. This reversal results in the appearance of the $v_t > 0$ near-axis range, CR6, in Figure 5.32 and the second VB bubble, CR6, in water.

As Re exceeds Re_{s5}, which is slightly less than 1500, the third reversal of the meridional velocity separates region CR6 from the axis, where the new $v_t < 0$ range, CR7, emerges, as Figure 5.33 depicts. Figure 5.34 shows the streamline patterns at (a) $Re = 1300$ (as a reference) and (b) $Re = 1500$ where the new-born VB ring CR6 is observed in the water flow.
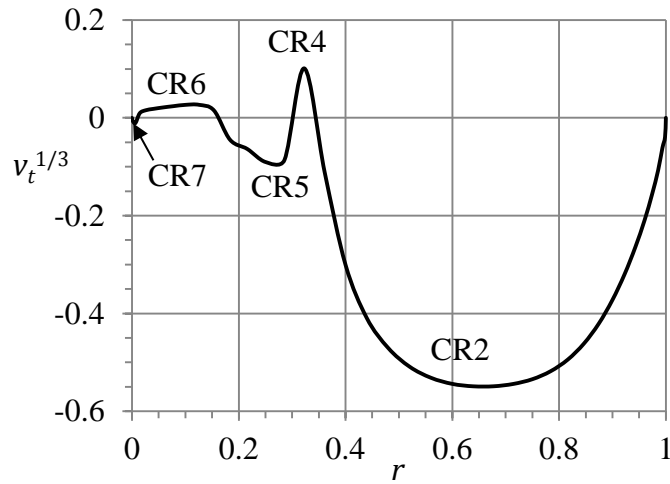
Figure 5.33 Distribution of meridional velocity on the interface at $Re = 1500$ shows the appearance of region CR7.

Thin circulation layers CR5 and CR7, located in air, are not visible in Figure 5.34(b). They are much thinner than water VB cells CR4 and CR6 due to the small air-to-water density ratio, $\rho_r = 0.00122$. Being a close-up of Fig. 34(b), Figure 5.34(c) reveals layer CR5, but its resolution is poor despite we use the fine grid here. Region CR7 is too thin to be observed even in Figure 5.34(c); its existence follows from the v_t distribution depicted in Figure 5.33.
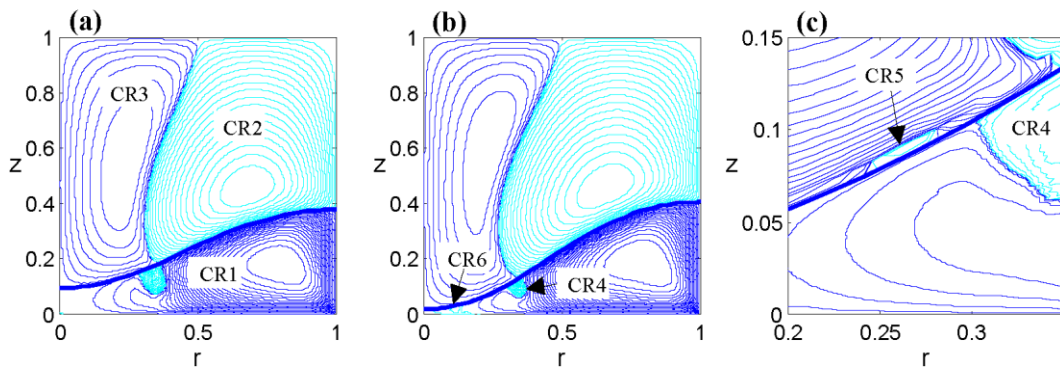
Figure 5.34 Streamline patterns at $Re = 1300$ (a) and 1500 (b) show appearance of circulation region CR6; (c) is close-up of (b) visualizing region CR5.

Based on the above analysis, we interpret the flow pattern in the left-lower corner of Figure 5.34(b) as the zipper-like near-interface chain of VB regions schematically shown in Figure 5.35. The chain develops as the interface approaches the bottom disk similar to the chain development at $H_w = 0.5$ (Figure 5.21 and Figure 5.22).
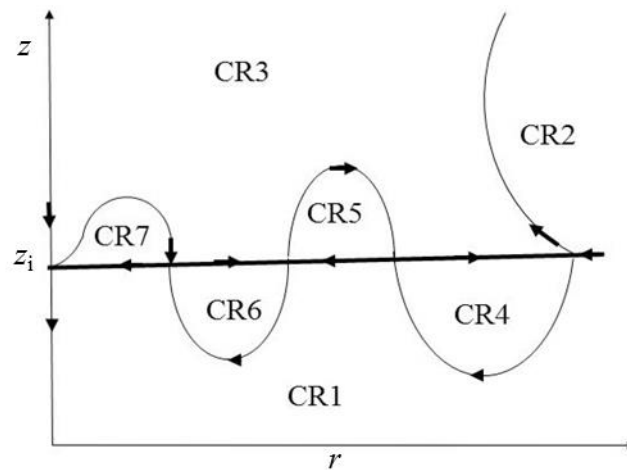
Figure 5.35 Schematic shows the zipper-like topology of shallow whirlpool for $Re \geq 1500$ (see Figure 5.33). The bold line is the interface and arrows indicate flow direction.

5.6.5. Reduction of VB cells by interface deformation

As the interface deformation becomes remarkable, it reduces vortex breakdown cells in both fluids. Figure 5.34 illustrates this effect: region CR4 shrinks as Re increases from 1300 in Figure 5.34(a) to 1500 in Figure 5.34(b). The physical reasoning behind this trend is the swirl decay mechanism (Shtern et al. [114]). The interface deformation enlarges the axial extent of both air and water domains. The enlarged axial extent increases the trajectory length and travel time of fluid particles transporting the angular momentum from the rotating disk to the interface in the water flow and from the interface to the axis in the air flow. This enhances the momentum losses due to viscous diffusion and friction, thus weakening the mechanism of vortex breakdown development.

5.6.6. Instability of $H_w = 0.3$ flow

Similarly to the $H_w = 0.5$ case, the $H_w = 0.3$ flow has the critical instability with respect to single-helix ($m = 1$) disturbances and the marginal instability with respect to two-helix ($m = 2$) disturbances, according to Table 5.6. For larger Re, the interface reaches the bottom near the axis that makes our numerical technique inapplicable.

Figure 5.36 shows (a) base-flow streamlines and (b) energy contours for the critical disturbance at critical $Re = 1547$. The energy peak is located at $r = 0.383$ and $z = 0.1295$ that is very close to the interface where the jet-like water flow, converging toward the axis along the interface, meets the VB bubble (Figure 5.36). This feature is similar to that at $H_w = 0.8$ and 0.5.

Re	1547	1583
m	1	2
ω_r	0.673	1.297

Table 5.6 Critical (bold) and marginal parameters of the flow instability at $H_w = 0.3$.
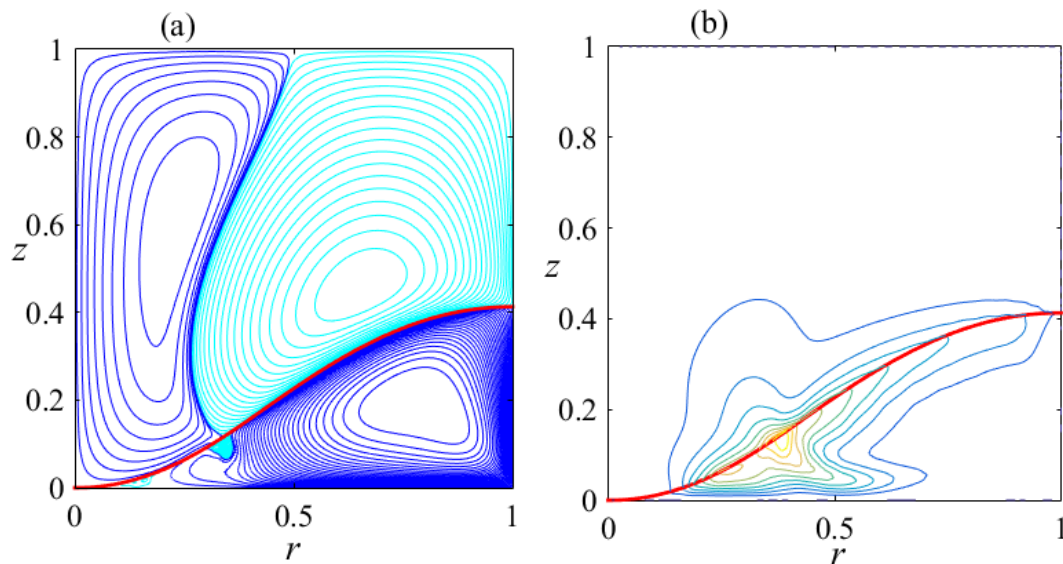
Figure 5.36 (a) Base-flow streamlines and (b) energy contours of critical disturbance at $H_w = 0.3$ and $Re = 1547$.

5.7. Conclusions

5.7.1. Robust bubble-rings

An interesting finding of this paper is that robust bubble-ring circulation cells (RBRs) emerge in a whirlpool flow as the rotation speeds up. In general, a bubble-ring is a transitional shape. A variation of a control parameter (e.g., Re) typically transforms a bubble-ring into a bubble or into a ring. In contrast in the whirlpool flow, we have revealed a few RBRs, existing in the ranges of Re listed below. The bubble-rings are robust here because of (a) the physical limitation that the interface cannot separate from the axis away from the end disks and (b) an air flow cannot easily reverse a water flow due to small air-to-water density ratio. The RBRs are found in the deep ($H_w = 0.8$) and shallow ($H_w = 0.3$) whirlpools.

In the $H_w = 0.8$ whirlpool, bubble-ring CR5, schematically shown in Figure 5.8(a), exists for $1779 < Re < 2348$ (Table 5.1). In the $H_w = 0.3$ whirlpool, the first RBR, CR2 in Figure 5.27(a), is observed in the range, $690 < Re < 829$ (Table 5.5). The second RBR (CR5) emerges at $Re = 829$ being separated from CR2 by a local reversal of meridional velocity on the axis (Figure 5.31 and Figure 5.32). The third RBR (CR7) emerges near the interface-axis intersection at $Re = Re_{s5} \approx 1500$ (Figure 5.33 and Figure 5.35). All these RBRs (CR2, CR5, and CR7) occur in the air flow and are adjacent to the interface.
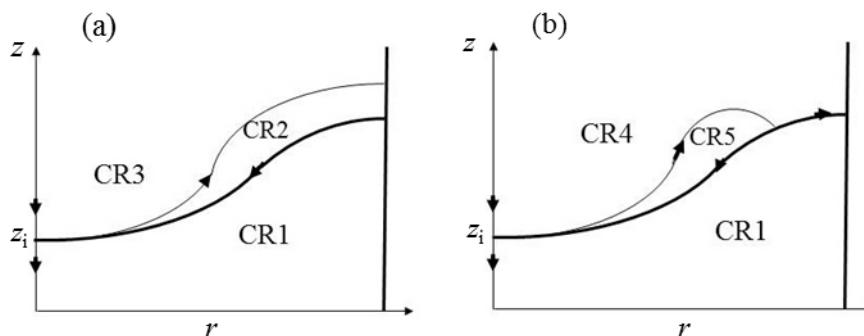
Figure 5.37 (a) Global CR2 and (b) local CR5 kinds of bubble-ring cells. The bold curves depict the interface and the bold lines depict the sidewall.

Two kinds of RBRs are observed: (a) global, extending from the axis up to the sidewall, CR2 in Figure 5.27(a) and Figure 5.37(a), and (b) local, bounded by the interface and separatrix, CR5 in Figure 5.37(b). The bold curves (vertical lines) denote the interface (sidewall) and the thin curves denote the boundaries between CR2 and CR3 in Figure 5.37(a), and CR4 and CR5 in Figure 5.37(b). The local RBR is shown large for convenient observation in Figure 5.37(b), but the radial extent of a local RBR can be small, e.g., $0 < r < 0.011$ for region CR7 at $Re = 1500$ (Figure 5.33 and Figure 5.35).

5.7.2. Multiple changes in flow topology

N	*Re*	Event	Figure
1	359	Emergence of VB bubble CR3 deep in water	Figure 5.2
2	365	Emergence of two-fluid VB bubble CR3-CR4	Figure 5.5(a)
3	377	Emergence of VB bubble CR4* in air	Figure 5.5(b)
4	394	Merger of CR4 and CR4* in air	Figure 5.6(a)
5	873	Separation of CR3 from the axis	Figure 5.7(a)
6	1779	Emergence of RBR CR5 in air	Figure 5.7(b) and Figure 5.8
7	2348	Transformation of RBR CR5 into a bubble	Figure 5.9
8	≈ 2400	Merger of CR2 and CR5	Figure 5.10(b)
9	≈ 2450	Splitting of CR4 into CR4a and CR4b	Figure 5.10(c)
10	≈ 2600	Disappearance of CR4b	Figure 5.10(d)
	2629	Instability development	Figure 5.11

Table 5.7 Changes in flow topology as Re increases at $H_w = 0.8$.

The second interesting finding is a rich variety of topological metamorphoses in the whirlpool flow. Topological scenarios depend on the water volume fraction H_w. Vortex breakdown (VB) first emerges in (i) the air flow near the top disk center at $H_w = 0.3$, (ii) at the interface-axis intersection at $H_w = 0.5$, and (iii) deep in water near the axis at $H_w = 0.8$.

Table 5.7 Changes in flow topology as Re increases at $H_w = 0.8$. lists the ten flow topological transformations found as Re increases in the deep whirlpool, $H_w = 0.8$. We also found the nine (five) transformations at $H_w = 0.5$ ($H_w = 0.3$); the number of topological changes increases with H_w. The plurality of metamorphoses is due to flow cells emerge, change, and disappear in both fluids.

5.7.3. Chain of VB regions

The third interesting finding is the development of VB cell chain adjacent to the interface as the water depth near the axis becomes small. At $H_w = 0.3$, there are four VB cells arranged in a zipper-like pattern attached to the interface near the axis (Figure 5.35). At $H_w = 0.5$, the chain consists of three VB cells (Figure 5.22). At $H_w = 0.8$, the chain consists of two VB cells observed in Figure 5.10(a).

5.7.4. Effect of large deformation of the interface
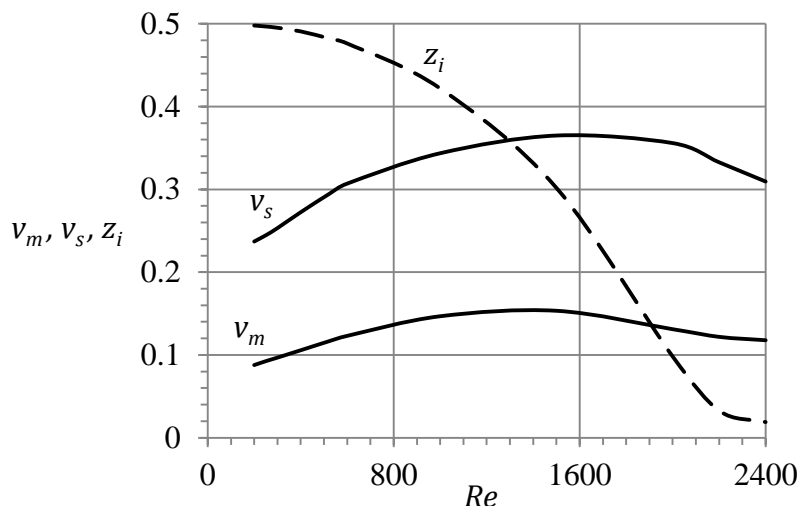
Figure 5.38 Dependence on Re of the maximal magnitudes of meridional v_m and swirl v_s velocities at the interface. Curve z_i shows the interface height at the axis. $H_w = 0.5$.

The forth interesting finding is that the interface deformation (ID), when it becomes remarkable, suppresses VB in both fluids. Figure 5.10 illustrates this effect: VB region CR3 shrinks as ID increases. The physical reasoning behind this feature is the swirl decay mechanism (SDM) (Shtern et al. [114]). SDM plays an important role in the development of vortex breakdown, counterflows, and double counterflows in vortex devices ([109]). According to SDM, a value of Re, at which VB emerges, increases together with the aspect ratio.

The aspect-ratio and ID effects are analogous because ID enlarges the axial extent of both lower and upper fluid domains. The enlarged axial extent increases the trajectory length and travel time of fluid particles transporting the angular momentum from the rotating disk to the interface near the sidewall. This enhances the momentum losses due to viscous friction and diffusion, thus reducing the maximal velocity magnitude at the interface and weakening the mechanism of VB development.

The largest increase in the axial extent of air and water domains occurs at $H_w = 0.5$. Figure 5.38 illustrates the ID effect at $H_w = 0.5$ by depicting the dependence on the Reynolds number of the maximal magnitudes of meridional v_m and swirl v_s velocities at the interface as well as the interface height at the axis z_i. As Re increases from zero, v_m and v_s initially grow because the convective transport intensifies while viscous losses remain nearly the same. As Re further increases and z_i becomes remarkably reduced compared with its no-flow value 0.5, the amplified ID makes larger the trajectory lengths and, therefore, viscous losses. For this reason, first v_m and then v_s start to decrease.

5.7.5. Instability

The instability develops in the water flow because the kinematic viscosity of air is fifteen times that of water and the maximal velocity of air motion (achieved at the interface) is significantly smaller than that of water (achieved at the rotating disk) as Figure 5.38 illustrates.

It is striking that the multi-cellular flows, studied here are stable. The instability develops when the number of flow cells decreases as the interface becomes significantly deformed and approaches either the top (at $H_w = 0.8$) or bottom (at $H_w = 0.3$ and 0.5) disk. The instability occurs with respect to helical disturbances with the azimuthal wave number $m = 1, 2, 3$ and 4. The critical Re values (Table 5.8) correspond to $m = 1$ disturbances.

H_w	0.3	0.5	0.8
Re	1547	1950	2628
ω_r	0.673	0.259	0.204
m	1	1	1

Table 5.8 Dependence on water fraction of critical parameters of the whirlpool instability.

As Table 5.8 shows, the critical Reynolds number grows and the disturbance frequency drops as the water volume fraction H_w increases. The instability develops in a jet-like boundary layer. It originates near the rotating disk, propagates along the sidewall and goes to the axis near the interface, e.g., see Figure 5.11(a). The critical disturbance starts to grow where the jet meets VB region, decelerates and diverges. The disturbance energy peaks are located near the jet inflection points (Figure 5.12). This indicates that the instability likely is of shear-layer type.

The obtained results seem of fundamental interest and might be useful for aerial bioreactors.

6. STABILITY OF AN AIR-WATER FLOW IN A SEMISPHERICAL CONTAINER

This numerical study analyzes the stability of a steady axisymmetric air-water flow driven by a rotating top disk in a sealed semispherical container. A motivation is possible applications in aerial bioreactors. The centrifugal force pushes the air to periphery near the disk, downward near sidewall, toward the axis near the interface, and upward near the axis. This meridional circulation of air drives the water counter-circulation while the centrifugal force tends to induce the water co-circulation. Their competition results in the development of a three-eddy pattern as the rotation intensifies. The air circulation and the water co-circulation are separated by a thin layer of water counter-circulation. It is shown that the time-oscillatory helical instability emerges when the three-eddy pattern is well formed. The azimuthal wave number is $m = 1$ in the shallow-water case and $m = 2$ otherwise. The analysis of flow patterns and critical-disturbance energy distributions indicates that the instability emerges in the air domain and likely is of the shear-layer type.

6.1. Introduction

An intriguing and important fluid-mechanics phenomenon is the emergence of a local circulation cell in a swirling flow, often referred to as vortex breakdown (VB). VB applications include delta-wing aircraft, where VB is dangerous causing an abrupt change in lift and drag, combustion chambers, where VB is beneficial stabilizing flame, and natural swirling jets like tornadoes, where VB decreases the twister strength. Escudier [108] performed a comprehensive review of early VB studies. More recent works, including VB control strategies, are discussed in Ref. [109].

Vogel [136]and Escudier [121] initiated fundamental VB studies in a sealed cylindrical container with one end disk rotating. An advantage is the closed domain with well-defined and controlled boundary conditions allowing for meaningful comparisons of experimental and numerical results. They well agree as was first shown by Lopez [137]. The analysis of the Vogel-Escudier flow helps understand the VB nature. A recent view is that VB develops via the swirl-decay mechanism [113], [114].

While single-fluid VB flows have been studied rather in detail, two-fluid VB flows have not attracted much attention until recent time. The situation changed with the development of aerial bioreactors where air-water flows are used for the growth of tissue culture [138]. The air flow transports the oxygen, required for tissue growth, to the interface and the water circulation enhances mixing of the dissolved oxygen with other ingredients. The tissue fraction is small compared with that of water and is neglected in the studies of flow patterns. The bioreactor applications stimulated the experimental investigations by Lo Jacono *et al*. [115]and the numerical simulations by Liow *et al*. [51], [128]. Early numerical studies modeled the gas-liquid interface as a symmetry plane [139] and as a deformable stress-free surface [140]. The first work, which is free from these idealizations of the interface, was performed by Brady *et al*. [116], [117].

Further research has revealed that two-fluid VB flows have a number of interesting features absent in single-fluid flows. One striking feature, observed also in the current study, is the existence of a thin circulation layer (TCL) adjacent to the interface. A TCL attached to the entire interface

from below was found in water-spout flows occurring in cylindrical [118] and semispherical [148] containers.

Another striking feature is the emergence of an off-axis VB ring in the depth of a lower fluid away from the interface, axis, and walls [141]. Since eddies arise in both fluids, their variety is rich and transformations are numerous. For example, eighteen topological metamorphoses follow each other as the water volume fraction increases in a truncated conical container where a creeping air-water flow is induced by the slowly rotating top disk [129]. The diversity of flow cells and their metamorphoses is even more enriched by the Moffatt eddies [132], which develop near intersections of the end and side walls [130].

The resulting rather complicated topology raises a question about the flow stability. The stability of one-fluid VB flows in a cylindrical container has been investigated rather in detail. The numerical study of Gelfgat *et al.* [119], [120] showed that the Vogel-Escudier flow can become unstable at either smaller or larger *Re* than that, at which VB emerges, depending on the length-to-radius ratio, *H*. The experimental and numerical studies by Escudier [121] and Sorensen *et al.* [122]–[124] documented that, as *Re* increases, the steady axisymmetric VB bubble first develops for $H < 3.2$. For larger *H*, the flow first becomes unstable with respect to 3D time-oscillatory disturbances with $m = 3$ for $3.2 < H < 4.3$, $m = 2$ for $4.3 < H < 5.2$, and $m = 4$ for $5.2 < H < 5.5$; m is the azimuthal wave number. Herrada *et al.* [113] found that this instability is of the shear-layer type developing for $H > 5.5$ as well. Unsteady three-dimensional flows resulting from the instability were studied in Refs. [149]–[151].

Here we numerically investigate the stability of air-water flow in a semispherical container studied by Balci *et al.* [148]. This flow seems the most appropriate for bioreactor applications since the number of eddies, which can damage the tissue, is minimal here. In the cylindrical bioreactors [115],[51], [128],[139], a set of eddies is located near the sidewall-bottom intersection [118]. This eddies are absent in a semispherical container. One more advantage is that semispherical geometry enhances the streamline convergence toward the axis. This convergence strengthens swirl and therefore the centrifugal force, which drives the meridional circulation. Thus, the near-stagnant corner region is removed and the global circulation of ingredients is enhanced.

There is a technical difficulty of studying the stability of a two-fluid flow: the linearization of a rather complicated relation describing the balance of normal stresses at the bent interface. To overcome this problem, an efficient routine was elaborated [1], which in addition facilitates numerical simulations. The routine includes (i) mappings, converting the time-dependent upper and lower fluid regions onto fixed squared domains, (ii) a symbolic toolbox to calculate the analytical Jacobians, and (iii) the Chebyshev grid in both radial and axial directions. Herrada & Montanero proved the method efficiency in their study of liquid-bridge dynamics [1]. Here this numerical technique, being modified and applied for the hemispherical problem, helps investigate and understand the instability nature.

6.2.   Problem formulation

6.2.1. Flow geometry
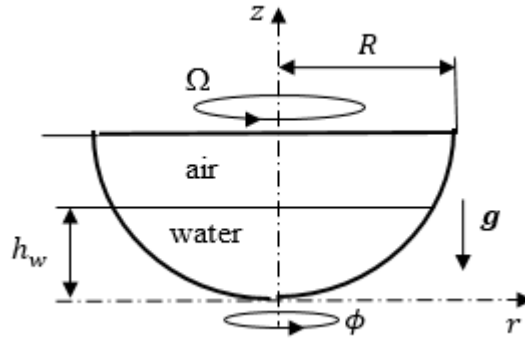
Figure 6.1 Schematic of the problem. The lid only rotates.

Figure 6.1 is a problem schematic. The lower part, $0 < z < h_w$, of the semispherical container is filled with water, the upper part, $h_w < z < R$, is filled with air; r, ϕ, and z are cylindrical coordinates; and $\boldsymbol{g}$ is the gravitational acceleration. The interface is depicted by the thin horizontal line, $z = h_w$. The semispherical wall is stationary. The disk lid, located at $z = R$, rotates with angular velocity Ω; R is the disk and hemisphere radius, which serves as a length scale. The dimensionless control parameters are the water fraction, characterized by the water height $H_w = h_w/R$, and the Reynolds number, $Re = \Omega R^2/\nu_w$, characterizing the rotation strength; ν_w is the kinematic viscosity of water. One our goal is to explore (i) the development of flow instability, as Re increases at a fixed H_w, and (ii) how the critical parameters depend on the water fraction. To this end, we consider $H_w = 0.2$, 0.4, 0.6, and 0.8.

6.2.2. Governing equations

Using R, $1/\Omega$, ΩR, and $\rho_w \Omega^2 R^2$ as scales for length, time, velocity, and pressure, respectively, renders all variables dimensionless. We consider a flow of two viscous incompressible immiscible fluids governed by the Navier-Stokes equations,

$$\frac{1}{r}\frac{\partial(ru)}{\partial r} + \frac{1}{r}\frac{\partial v}{\partial \phi} + \frac{\partial w}{\partial z} = 0, \tag{6.1}$$

$$\frac{\partial u}{\partial t} + u\frac{\partial u}{\partial r} + \frac{v}{r}\frac{\partial u}{\partial \phi} + w\frac{\partial u}{\partial z} - \frac{v^2}{r} = -\rho_n\frac{\partial p}{\partial r} + \frac{\nu_n}{Re}\left(\nabla^2 u - \frac{u}{r^2} - \frac{2}{r^2}\frac{\partial v}{\partial \phi}\right) \tag{6.2}$$

$$\frac{\partial v}{\partial t} + u\frac{\partial v}{\partial r} + \frac{v}{r}\frac{\partial v}{\partial \phi} + w\frac{\partial v}{\partial z} + \frac{uv}{r} = -\frac{\rho_n}{r}\frac{\partial p}{\partial \phi} + \frac{\nu_n}{Re}\left(\nabla^2 v - \frac{v}{r^2} + \frac{2}{r^2}\frac{\partial u}{\partial \phi}\right) \tag{6.3}$$

$$\frac{\partial w}{\partial t} + u\frac{\partial w}{\partial r} + \frac{v}{r}\frac{\partial w}{\partial \phi} + w\frac{\partial w}{\partial z} = -\rho_n\frac{\partial p}{\partial z} + \frac{\nu_n}{Re}\nabla^2 w \tag{6.4}$$

where $\nabla^2 \equiv \frac{1}{r}\frac{\partial}{\partial r}\left(r\frac{\partial}{\partial r}\right) + \frac{1}{r^2}\frac{\partial^2}{\partial \phi^2} + \frac{\partial^2}{\partial z^2}$ is the Laplace operator for a scalar field, (u, v, w) are the velocity components in cylindrical coordinates (r, ϕ, z), t is time, and p is pressure. The coefficients, ρ_n and ν_n, are both equal 1 at $n = 1$ (in the water) while $\rho_n = \rho_w/\rho_a$ and $\nu_n = \nu_a/\nu_w$ at $n = 2$ (in the air).

We denote the list (u, v, w, p) as V, and look for a solution of the system (6.1)-(6.4) in the form

$$V = V_b(r, z) + \varepsilon V_d(r, z)e^{(im\phi - i\omega t)} + c.c., \qquad\qquad 6.5$$

where subscripts "b" and "d" denote the base flow and a disturbance, respectively; $c.c.$ denotes the complex conjugate of the preceding term; $\varepsilon \ll 1$ is an amplitude; integer m is an azimuthal wave number; and $\omega = \omega_r + i\omega_i$ is a complex number to be found, with frequency ω_r and growth rate of disturbance ω_i. For a decaying (growing) disturbance, ω_i is negative (positive). The equations governing the base flow result from substituting (6.5) in system (6.1)-(6.4) and setting $\varepsilon = 0$. The terms of order $O(\varepsilon)$ constitute equations governing infinitesimal disturbances.

6.2.3. Boundary conditions

Equations (6.1)-(6.4) are solved under the following boundary conditions:
(i)   Regularity at the axis, $0 < z < R,\ r = 0$:

         a) $u = v = 0, \partial w/\partial r = 0$ (basic flow and $m = 0$ disturbances),

         b) $w_d = 0, u_d + mv_d = 0, \partial u_d/\partial r = 0$ ($m = 1$ disturbances)

         c) $w_d = u_d = v_d = 0$ ($m > 1$ disturbances)

(ii)   No-slip at the walls: $u = v = w = 0$ at the spherical wall, $0 < r < 1$, $z = 1 - (1-r^2)^{1/2}$ and $u = w = 0$, $v = r$ at the rotating disk, $0 < r < 1$, $z = R$.
(iii)   Continuity of all the velocity and stress components at the interface. In particular, the balance for the normal stresses yields that

$$p_w - p_a = \frac{1}{We}\nabla.\boldsymbol{n} - \frac{1}{Re}\boldsymbol{n}.(\boldsymbol{\tau}_w - \mu_r\boldsymbol{\tau}_a).\boldsymbol{n} - \frac{1}{Fr}(1 - \rho_r)z, \qquad\qquad 6.6$$

         where $\boldsymbol{n}$ is the unit vector perpendicular to the interface, $\boldsymbol{\tau}_w$ and $\boldsymbol{\tau}_a$ are tensors of the viscous stresses in the heavy and light fluids, respectively, and μ_r and ρ_r are the light-to-heavy fluid ratios of the dynamic viscosities and densities, respectively.

(iv)   The kinematic equation for the interface shape, $z_{interface} = G(s, \phi, t)$ and $r_{interface} = F(s, \phi, t)$, are:

$$\left(u - \frac{\partial F}{\partial t}\right)\frac{\partial G}{\partial s} - \left(w - \frac{\partial G}{\partial t}\right)\frac{\partial F}{\partial s} + \frac{v}{F}\left(\frac{\partial G}{\partial \phi}\frac{\partial f}{\partial s} - \frac{\partial F}{\partial \phi}\frac{\partial G}{\partial s}\right) = 0, \qquad\qquad 6.7$$

$$\frac{\partial G}{\partial s}\frac{\partial^2 G}{\partial s^2} + \frac{\partial F}{\partial s}\frac{\partial^2 F}{\partial s^2} = 0, \qquad\qquad 6.8$$

         where s is the arc length coordinate along the interface. We look for a solution in the form

$$z_{interface} = G_b(s) + \varepsilon G_d(s)e^{(im\phi - i\omega t)} + c.c, r_{interface} = F_b(s) + \varepsilon F_d(s)e^{(im\phi - i\omega t)} + c.c. \qquad\qquad 6.9$$

6.3. Numerical procedure

6.3.1. Approach

The numerical scheme used to simulate both the nonlinear problem for the basic flow and the generalized eigenvalue problem for disturbance is a variation of that described in [1]. It includes first the mapping of water and air regions onto standard square domains, $0 \leq \eta_{(w,a)} \leq 1, 0 \leq s \leq 1$, by means of two coordinate transformations (see Section 6.3.2). Then, each variable (velocities, pressure, and the two variables, G and F, required to describe the interface shape) and all its temporal and spatial derivatives, which appear in the transformed equations, are composed as a single symbolic vector. The next step is to use a symbolic toolbox to calculate the analytical Jacobians of all the equations with respect to the symbolic vectors. MATLAB tool matlabFunction is used to convert these symbolic Jacobians and equations into MATLAB functions. These functions are evaluated point-by-point in the squared domains every time when it is required to compute either the numerical Jacobian, used in the Newton procedure to solve the nonlinear problem of the basic flow, or the matrices associated with the eigenvalue problem. The structure of these matrices is determined by the spatial and temporal discretization of the derivatives of the variables in the numerical domains. In this work, the water and air domains are discretized using forth order finites differences in a set of n_w and n_a collocation points in the η direction (along the η_w and η_a axes, respectively). By the other hand, the domains are also discretized using forth order finites differences in a set of n_s collocation points in the s direction. The second-order backward finite differences are used to compute the time derivatives for the basic flow. Since the basic flow is axisymmetric, all the azimuthal derivatives are set to zero. For disturbances, we obtain the temporal and azimuthal derivatives using the representation (equation 6.5).

To summarize, the numeric procedure includes the mapping of water and air regions, the proper spatial and temporal discretization, creating the discrete Jacobian matrix for the Newton procedure for the basic flow and two more matrices for the generalized eigenvalue problem for disturbances. For the basic flow, we get the final steady solution though using an unsteady process. Starting from the rest and selecting a time step, dt, the solution is advanced in time until a steady state is reached. Since the nonlinear procedure used to compute the basic flow is fully implicit, dt can be taken sufficiently large to quickly reach the steady solution. Once the base flow is computed, at given an azimuthal wave number m, we use MATLAB subroutine *eigs* to calculate the eigenvalues (ω) of the system of discrete linear equations.

Most of the simulations presented here are done using $n_w = 111$, $n_a = 41$, and $n_s = 111$ (standard grid) and $dt = 10, 20$ and 50, but some runs for flows, having small circulation regions, are performed with more fine grids.

To analyze the flow topology, we use the Stokes stream function Ψ, $w = \frac{1}{r} \partial \Psi / \partial r$ and $u = -\frac{1}{r} \partial \Psi / \partial z$, and plot streamlines of the meridional motion, i.e., contours Ψ = constant.

6.3.2. Mapping

In the water region the following mapping has been applied

$$z = G(s, \phi, t)\eta_w, r = F(s, \phi, t)\eta_w + s[sin(acos\{1 - g_0\eta_w\}) - f_0\eta_w], \qquad 6.10$$

where $g_0 = G(s = 1, \phi, t)$, and $f_0 = sin(acos\{1 - g_0\})$.

By the other hand, the air region the following mapping has been used

$$= G(s, \phi, t)(1 - \eta_a) + \eta_a, \qquad r = F(s, \phi, t)\eta_a + s[sin(acos\{1 - g_0\eta_a\}) - f_0\eta_a] \qquad 6.11$$

Note that both mappings are defined by variables F and G which describe the radial and axial position of the interface as a function of the arc length s $(0 \leq s \leq 1)$ and by variables η_w, $(0 \leq \eta_w \leq 1)$ and η_a, $(0 \leq \eta_a \leq 1)$. Equations (6.7) and (6.8) allow the determination of F and G. Note that in the case of a completely flat interface, $G = H_w$ and $F = f_0 s$, the mapping in the water region becomes

$$z = Hw\,\eta_w, \qquad r = s\left[sin\left(acos\{1 - Hw\,\eta_w\}\right)\right], \qquad 6.12$$

while in the gas region

$$z = Hw\left(1 - \eta_a\right) + \eta_a, \qquad r = s[sin(acos\{1 - Hw\,\eta_a\})] \qquad 6.13$$

Figure 6.2 shows an example of mesh generated by the mapping for a case with a deformable artificial interface (F and G given by the red line)
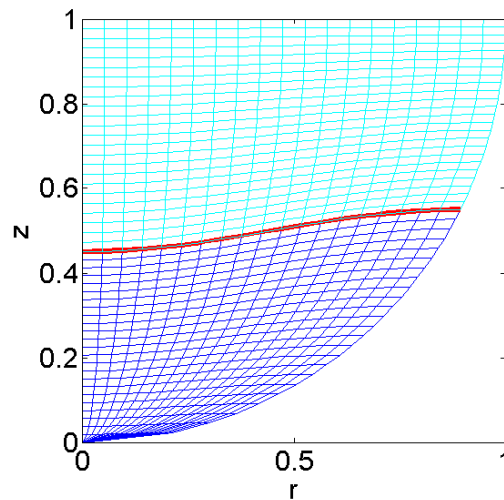
Figure 6.2 Mesh generated using $\eta_w = 25$, $\eta_a = 25$, $n_s = 20$ with G(s) = 0.5-cos(π s) and F(s)= $f_0 s$.

6.4. Discussion of stability results

6.4.1. Deep-water flow at $H_w = 0.8$

It is reasonable to start the stability analysis with the case $H_w = 0.8$, where the base flow was investigated in Ref. [148]. Figure 9(a) of Ref. [148]shows that the creeping flow has the four-eddy pattern with one large cell and one small cell in each of the water and air domains. All four cells are adjacent to the interface. As Re increases, the small air cell shrinks and disappears, while the small water cell extends along the entire interface forming a thin counter-circulation layer. Thus, the four-

eddy pattern of the creeping flow transforms into the three-eddy pattern, as the disk rotation speeds up. Figures 9(c) and 9(d) of Ref. [148] show this pattern at $Re = 10000$ and 18000 respectively. Figure 6.3(a) of our study depicts the three-eddy pattern at $Re = 55700$, at which the interface is remarkably deformed upward near the axis and downward near the sidewall, and the flow becomes unstable.
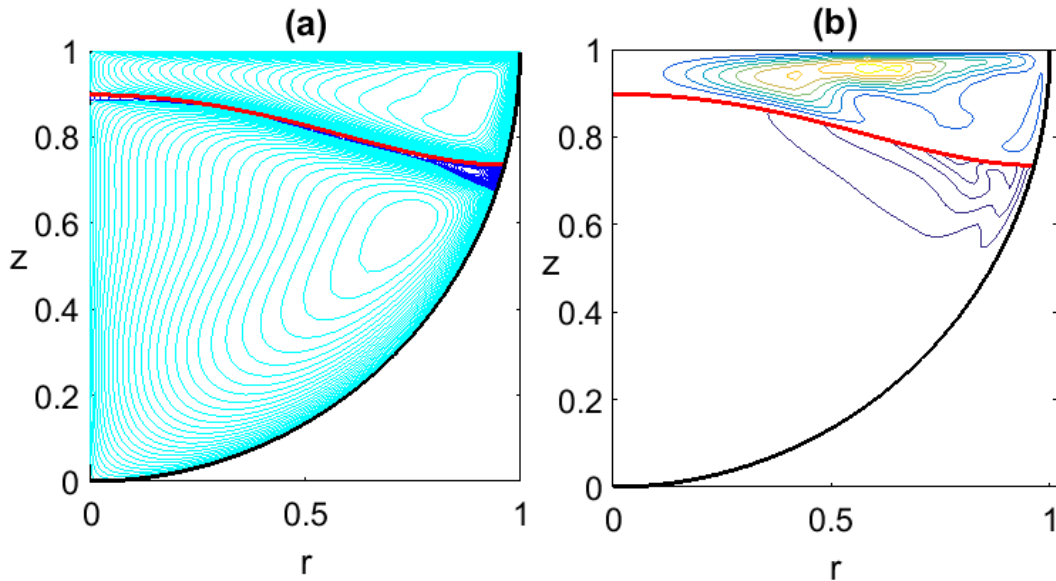
Figure 6.3 (a) The base-flow pattern and (b) critical-disturbance energy distribution at $H_w = 0.8$.

The critical characteristics are found using the interpolation as Figure 6.4 illustrates for the critical Re. The cross symbols correspond to the numerical results, the curve and formula show the fitting polynomial. The critical value is determined as the polynomial root where $\omega_i = 0$. A similar procedure is used to find the critical value of ω_r. The obtained critical characteristics are: $m = 2$, $Re = 55700$, $\omega_r = -0.0176$, $\omega_i = 0$, $Re_a = 3713$, and $Re_w = 813$.

In addition to Re, which is convenient to use in the numerical procedure, we calculate the Reynolds number, $Re_a = Re/\nu_n$, based on the air viscosity and therefore characterizing the strength of the air flow; $\nu_n = 15$ is the air-to-water kinematic viscosity ratio. To characterize the strength of the water flow, we also calculate $Re_w = \nu_{si}Re$; ν_{si} is the maximal (dimensionless) swirl velocity at the interface. Here $\nu_{si} = 0.0146$ is small compared with 1, which is the maximum velocity of the rotating disk.
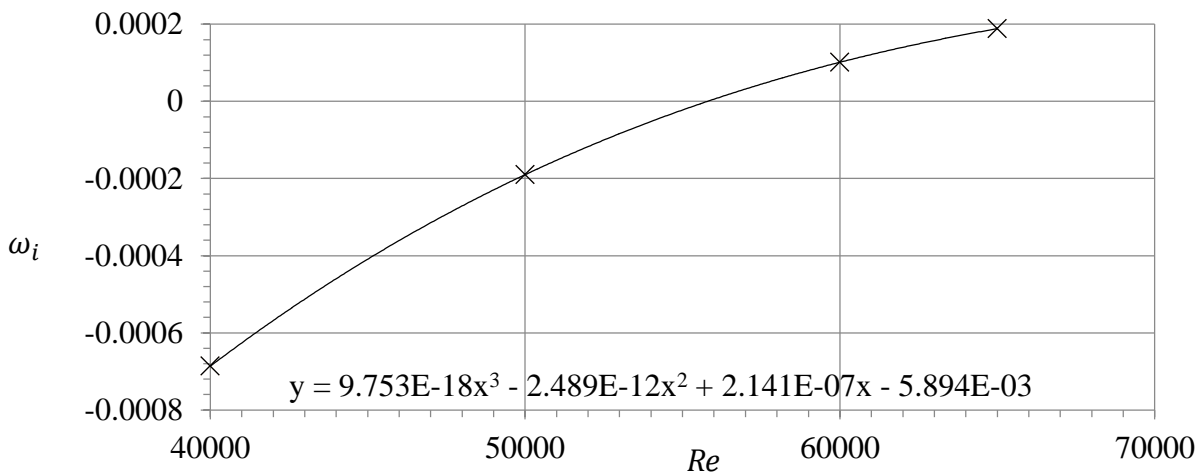
Figure 6.4 Finding the critical Re by interpolation. The crosses present the numerical results. The curve and formula show the fitting polynomial.
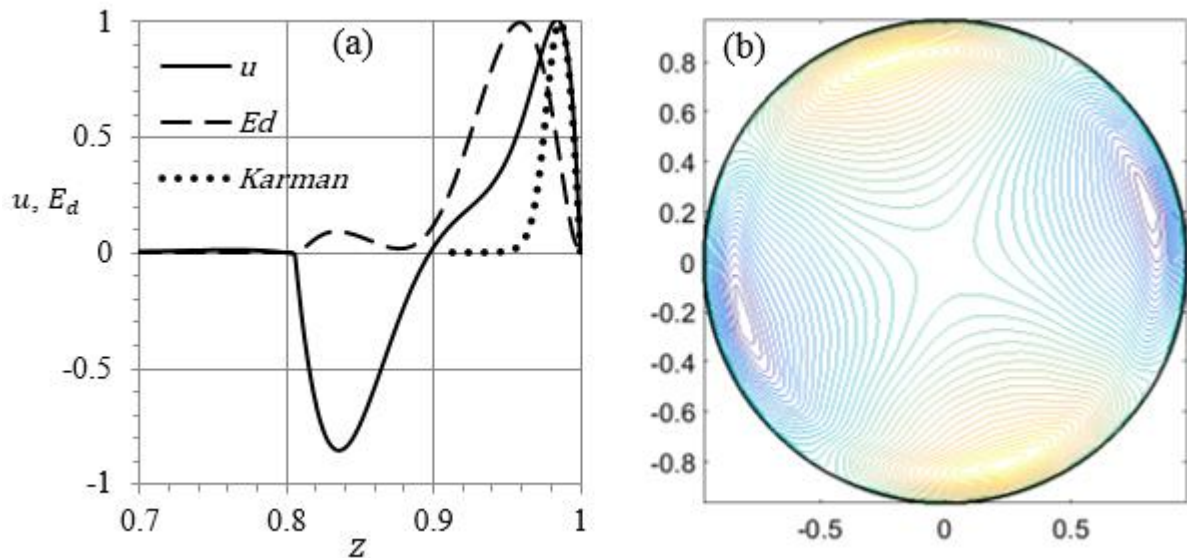
Figure 6.5 (a) The z-profiles of the base-flow radial velocity u (solid curve) and E_d (dashed curve) near the lid at $r = 0.618$ $H_w = 0.8$. The dotted curve depicts the Kármán solution for u. (b) Contours of the disturbance axial velocity at the interface (color online).

This small value of v_{si} results in that $Re_a > Re_w$ that helps explain why the critical disturbance is focused in the air domain, as Figure 6.3(b) illustrates. It depicts contours of squared velocity magnitude, $E_d(r,z) = $ constant, calculated for the critical disturbance; $E_d = < |u_d|^2 + |v_d|^2 + |w_d|^2 >$ is normalized by its maximal value in the air and water domains respectively; brackets, $<>$, denote averaging with respect to t and ϕ.

We depict a few contours of E_d with the outermost contour corresponding to $E_d = 0.1E_{dmax}$. This contour encompasses a flow region where the disturbance energy mostly is focused. In Figure 6.3(b), E_d reaches its peak value at $r = r_m = 0.618$ and $z = z_m = 0.957$, i.e., near the rotating lid.

At $r = r_m$, Figure 6.5(a) depicts the axial distribution of the base-flow radial velocity u (solid curve) and of E_d (dashed curve) near the lid. For convenient presentation, u is normalized by its maximal value, $u_m = 0.1065$, in Figure 6.5(a), which reveals that both u and E_d are very small in the water flow (for $z < 0.8$) compared with their maximal values in the air flow.

The profile of u in Figure 6.5(a) agrees with the streamline pattern in Figure 6.3(a). The rotating disk pushes the air to the periphery (the Kármán pump) forming a jet-like motion near the lid. The dotted curve in Figure 6.5(a) corresponds to the Kármán boundary layer solution as $Re_a \to \infty$ [127]. The near-lid parts (up to the u peak) of the boundary layer and numerical solutions are close. For smaller z, the effect of the air circulation (the counterflow in Figure 6.5(a)) makes the difference. The fact that the E_d peak is located near the inflection point of $u(z)$ in Figure 6.5(a) indicates that the instability likely is of the shear-layer type.

The E_d distribution in Figure 6.5(a) suggests that the air-flow instability does not necessarily disturb the water flow. A reason could be the large water-to-air density ratio. The E_d contours shown in Figure 6.3(b) reveal that the E_d peak in the water domain is located far away from the E_d peak in the air domain. The E_d peak in the water is likely induced by the counterflow in the thin water cell observed in Figure 6.3(a). Figure 6.5(b) depicts contours of critical-disturbance axial velocity at the interface. The bright (orange online) and dark (blue online) regions correspond to the interface deformation upward and downward, respectively. The locations of maximal $|w_d|$ in Figure 6.5(b) agree with the location of E_d peak in the water in Figure 6.3(b). According to $m = 2$, Figure 6.5(b) corresponds to two bumps and two dimples at the interface. As time increases, the picture in Figure 6.5(b) makes precession around the axis with the angular velocity ω_r/m in the direction opposite to the base-flow rotation.

6.4.2. Flow at H_w = 0.6
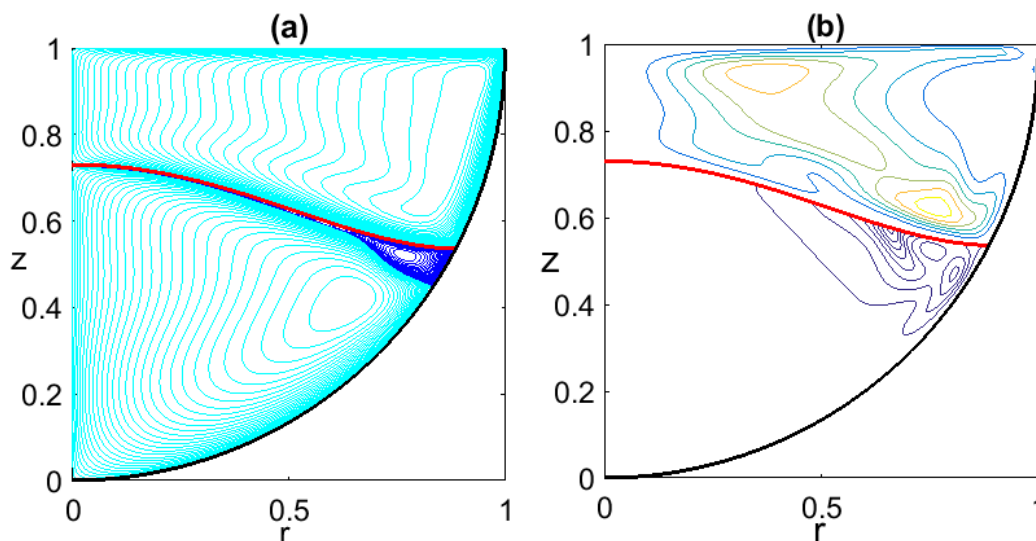
Figure 6.6 (a) The base-flow streamlines and (b) critical disturbance energy contours at $H_w = 0.6$.
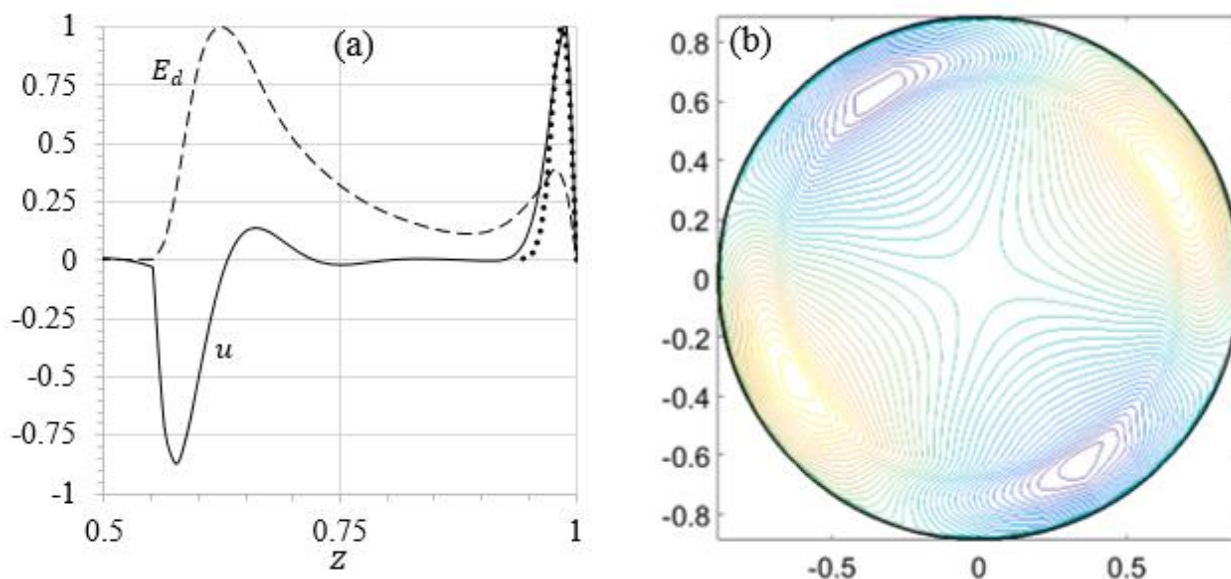
Figure 6.7 (a) The z-profiles of the base-flow radial velocity u (solid curve) and E_d (dashed curve) in the air domain at $r = 0.76$ and $H_w = 0.6$. The dotted curve depicts the Kármán solution for u. (b) Contours of the disturbance axial velocity at the interface (color online).

At $H_w = 0.6$, the critical parameters are $Re = 76430$, $\omega_r = -0.01295$, $\omega_i = 0$, $m = 2$, $Re_a = 5095$, and $Re_w = 876$. The critical Reynolds numbers increase at $H_w = 0.6$ compared to those at $H_w = 0.8$. Figure 6.6(a) depicts the base-flow pattern at the critical Re and reveals that the Kármán boundary layer near the lid, where streamlines are packed, is now well separated, by a large region of slowly ascending air, from the near-interface boundary layer, corresponding to the radially converging jet-like air flow, where streamlines also are parked.

The z-profile of u in Figure 6.7(a) has the jet-like peak, corresponding to the Kármán boundary layer (dotted curve) near the lid and a jet-like valley, corresponding to the near-interface boundary layer. Figure 6.6(b) reveals that E_d has peaks in both boundary layers near their inflection points of the u profile that indicates the shear-layer nature of instability. The near-interface jet diverges near the E_d peak that stimulates the shear-layer instability [109]. Closer to the axis, this divergence is compensated by the radially converging motion. This explains why the E_d peak in the near-interface jet is located close to the sidewall. Figure 6.7(b) depicts contours of critical-disturbance axial velocity at the interface whose features are similar to those in Figure 6.5(b).

6.4.3. Flow at $H_w = 0.4$
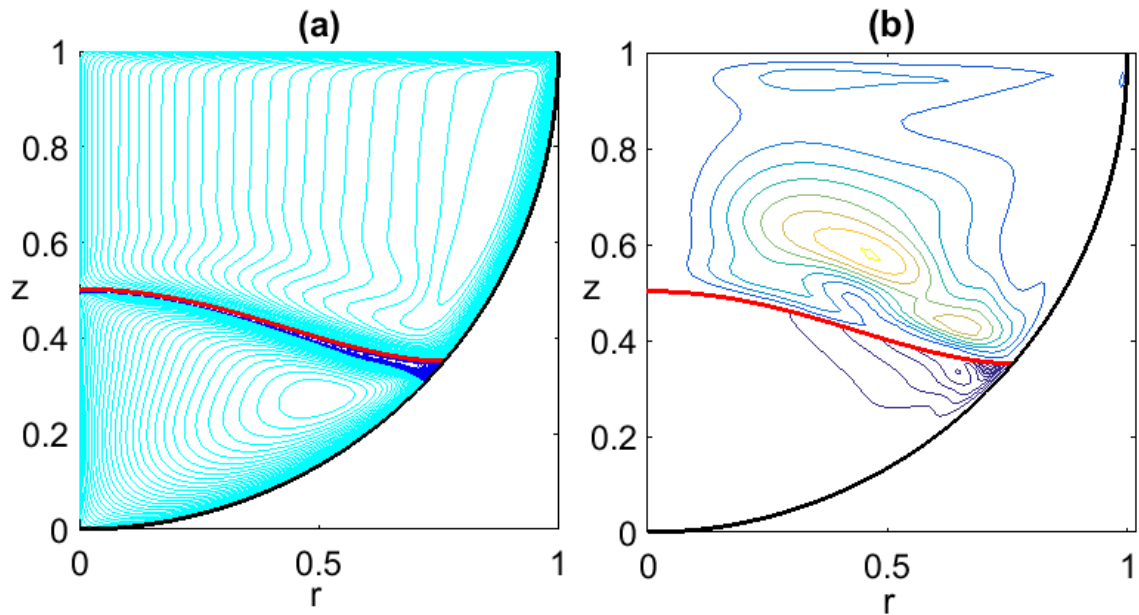
Figure 6.8 (a) The base-flow streamlines and (b) critical disturbance energy contours at $H_w = 0.4$.

At $H_w = 0.4$, the critical parameters are $Re = 100620$, $\omega_r = -0.0113$, $\omega_i = 0$, $m = 2$, $Re_a = 6708$, and $Re_w = 1078$. The critical Re numbers increase at $H_w = 0.4$ compared to those at $H_w = 0.6$. Figure 6.8(a) depicts the base-flow pattern at the critical Re. It reveals that the Kármán boundary layer near the lid, where streamlines are packed, is now even more, than in the $H_w = 0.6$ case, separated from the near-interface boundary layer. There is the axially elongated region in Figure 6.8(a) where the air streamlines are nearly parallel to the z = axis. This motion is induced by the Kármán boundary layer [127], which sucks the ambient air.
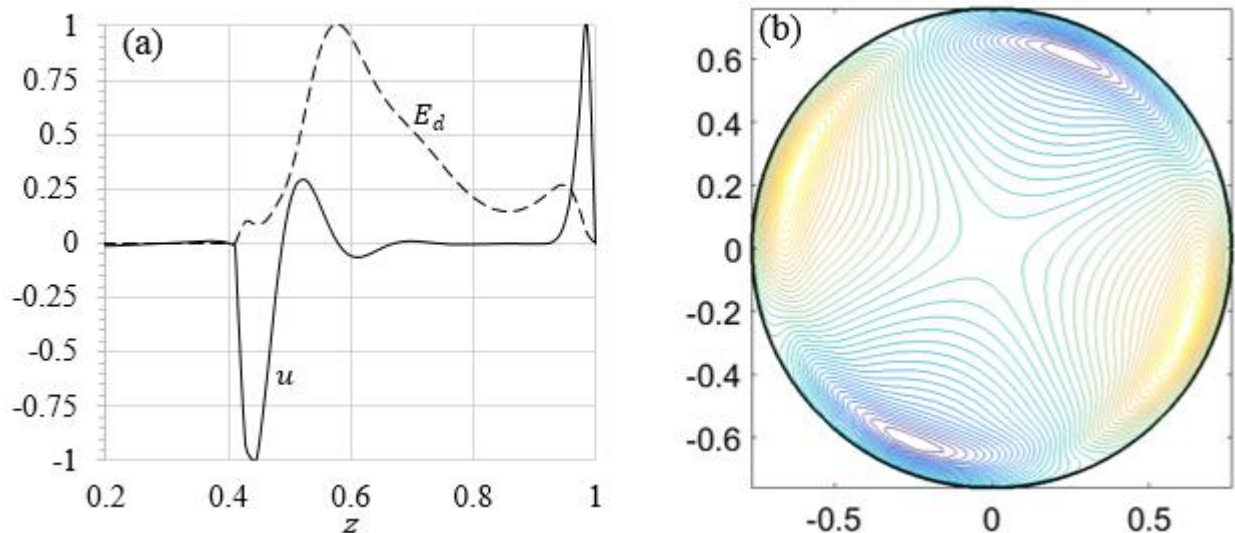
Figure 6.9 The z-profiles of the base-flow radial velocity u (solid curve) and E_d (dashed curve) in the air domain at $r = 0.469$ and $H_w = 0.4$. (b) Contours of the disturbance axial velocity at the interface (color online).

Figure 6.9(a) depicts the z-profile of radial velocity u, normalized by its maximal value, $u_m = 0.0676$, at $r = 0.469$ and $H_w = 0.4$. Near the interface, at $z > 0.41$, the multi-layer counterflow of air is formed where u oscillates. The nature of these oscillations is similar to that for the secondary flow near a wall normal to a rotating fluid, first described by Bödewadt [134].
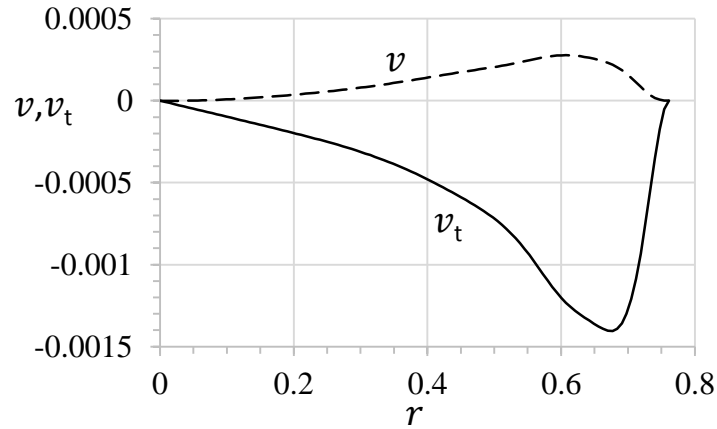
Figure 6.10 The r-profiles of the base-flow azimuthal v and meridional v_t velocities at the interface for $H_w = 0.4$.

Since both azimuthal and meridional velocities are very small at the interface compared with their maximal magnitudes, as Figure 6.10 illustrates, the interface acts as a wall for the air flow. Away from the interface, the radial pressure gradient is balanced by the centrifugal force, $\partial p/\partial r = \rho v^2/r$. Near the interface, the centrifugal force is drastically reduced while the pressure gradient is not and, being unbalanced by the centrifugal force, pushes the fluid to the axis. The radial convergence of air accumulates the swirl vorticity near the axis that develops a local minimum of pressure. The minimal pressure sucks the ambient fluid, decelerates the downstream air flow, and reverses the radial velocity (see the peak of u near $z = 0.5$ in Figure 6.9(a)), i.e., the swirl-decay mechanism [113] works, generating the oscillations of u.

The jet-like air flow near $z = 0.5$ in Figure 6.9(a) has (i) inflection points and (ii) radially diverges. These two features, (i) and (ii), cause the strong shear-layer instability [109] that helps explains the location of the E_d peak in Figure 6.8(b), where $r_m = 0.469$ and $z_{m=} = 0.572$, and in Figure 6.9(a), where the E_d peak is located near the inflection point where u is positive. Figure 6.9(b) depicts contours of critical-disturbance axial velocity at the interface whose features are similar to those in Figure 6.5(b).

6.4.4. Flow at $H_w = 0.2$
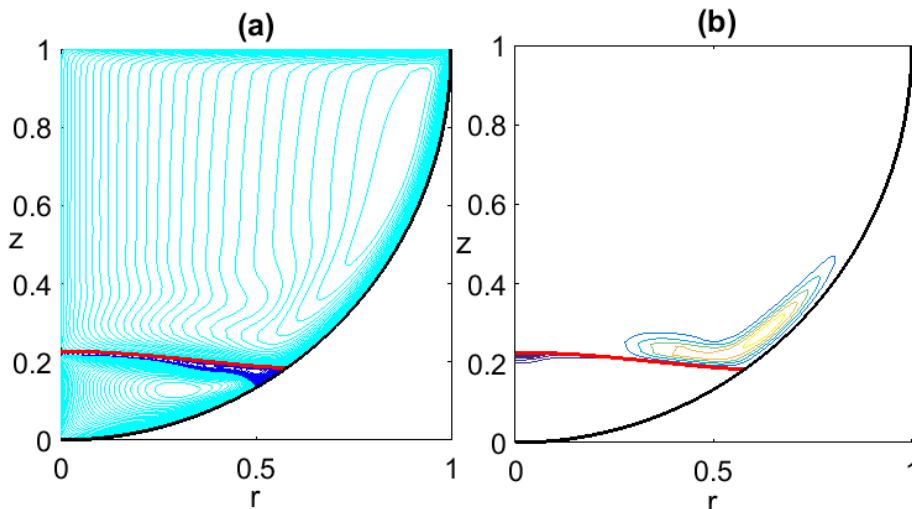
Figure 6.11 (a) The base-flow streamlines and (b) critical disturbance energy contours at $H_w = 0.2$.

In the shallow-water case, $H_w = 0.2$, the disturbance with $m = 1$ becomes the most dangerous with the critical values: $Re = 95350$, $\omega_r = -0.842$, $\omega_i = 0$, $Re_a = 6357$, and $Re_w = 713$.

Disturbances with $m = 2$ and $m = 3$ also become growing, but for larger values of Re. The critical Re numbers slightly decrease at $H_w = 0.2$ compared to those at $H_w = 0.4$. Figure 6.11(a) depicts the base-flow pattern at the critical Re.
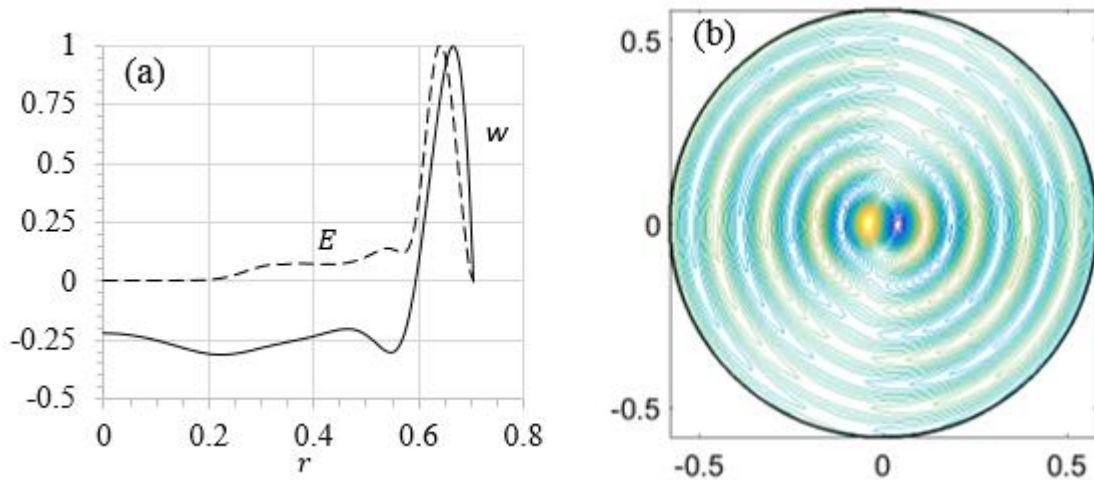
Figure 6.12 (a) The r-profiles of the base-flow normalized axial velocity w (solid curve) and E_d (dashed curve) in the air domain at $z = 0.289$ and $H_w = 0.2$. (b) Contours of the disturbance axial velocity at the interface (color online).

Figure 6.11(b) depicts the E_d distribution and reveals that the growing disturbance now is focused in the region where the near-wall jet-like air flow approaches the interface and decelerates. The deceleration enhances the shear-layer instability [109]. The E_d peak is located at $r = r_m = 0.638$ and $z = z_m = 0.289$. Figure 6.12(a) shows the radial distribution of E_d (dashed curve) and the axial velocity w, normalized by its minimal value, $w_{min} = -0.0532$, (solid curve) at $z = z_m$. The E_d peak is located near the inflection point of $w(r)$ that indicates the shear-layer nature of the instability. Figure 6.12(b) depicts contours of critical-disturbance axial velocity at the interface. This pattern is spiral with the most high and low points located near the axis.

6.5. Concluding remarks

The goal of this study is to explore the instability nature of the air-water flow in the semispherical container driven by the rotating lid. The study reveals that the instability develops in the air domain. The disturbance energy E_d in the water is very small compared with the E_d maximal magnitude in the air flow. At critical values of the Reynolds number, the flow has the well-developed three-eddy pattern: (i) the global meridional circulation of air is separated from (ii) the water co-circulation by (iii) the thin layer of water counter-circulation, which serves as a liquid bearing. The air circulation is concentrated in the jet-like boundary layer, (a) radially diverging near the lid (the Kármán flow), (b) descending near the sidewall, and (c) radially converging near the interface. The instability is caused by the inflection points in the boundary-layer velocity profile enhanced by the jet divergence and deceleration. The location of E_d peak depends on the water volume fraction characterized by the depth-to-radius ratio H_w. For the deep water, the instability focuses near the rotating lid (Section 6.4.1). As H_w decreases, the E_d peak shifts downward (Sections 6.4.2 and 6.4.3) and concentrates near the interface-sidewall intersection for the shallow water (Section 6.4.4). The instability is time-oscillatory and helical with the azimuthal wave number $m = 2$ except in the shallow water case, where $m = 1$. Since E_d drastically drops below the interface, it is not expected that the air-flow instability can significantly affect the bulk water motion. The results could have possible applications for aerial bio-reactors.

7. MEAN FLOW PRODUCED BY SMALL-AMPLITUDE VIBRATIONS OF A LIQUID BRIDGE WITH ITS FREE SURFACE COVERED WITH AN INSOBLUBLE SURFACTANT

As is well known, confined fluid systems subject to forced vibrations produce mean flows, called in this context streaming flows. These mean flows promote an overall mass transport in the fluid that has consequences in the transport of passive scalars and surfactants, when these are present in a fluid interface. Such transport causes surfactant concentration inhomogeneities that are to be counterbalanced by Marangoni elasticity. Therefore, the interaction of streaming flows and Marangoni convection is expected to produce new flow structures that are different from those resulting when only one of these effects is present. The present chapter focuses on this interaction using the liquid bridge geometry as a paradigmatic system for the analysis. Such analysis is based on an appropriate post-processing of the results obtained via direct numerical simulation of the system for moderately small viscosity, a condition consistent with typical experiments of vibrated millimetric liquid bridges. It is seen that the flow patterns show a nonmonotone behavior as the Marangoni number is increased. In addition, the strength of the mean flow at the free surface exhibits two well-defined regimes as the forcing amplitude increases. These regimes show fairly universal power-law behaviors.

7.1. Introduction

Oscillatory flows in confined and low-viscosity fluid systems develop oscillatory boundary layers near solid walls and interfaces. Reynolds stresses exhibit nonzero temporal mean values in these layers, where they drive a mean flow. This interesting effect was first shown in a pioneering work by Lord Rayleigh [152] when explaining the anomalous sand accumulation at the bottom of a vertically vibrated container, observed 50 years earlier by Faraday [153]. Rayleigh also noted that the same mechanism was seemingly responsible for nonuniform dust accumulation (known as Kundt figures) at the walls of sound tubes [154] and for the formation of steady vortical structures in vibrated soap films, already observed by Sedley Taylor [155]. This latter problem has been more recently studied by Vega et al. [156]. They concluded that, under reasonableassumptions and according to Rayleigh's insight, the observed vortical structures are most seemingly due to the streaming flow in the air surrounding the soap film. Rayleigh made a careful analysis of the (nowadays called) boundary layer attached to a (no-slip) solid boundary, obtaining the steady mean flow responsible for sand or dust nonuniform accumulation near the boundary. Rayleigh's work was completed 50 years later by Schlichting [157] (see also Ref. [158]), who noticed that the streaming flow velocity was nonzero at the internal edge of the boundary layer, which is a driving mechanism for the generation of mean flows in the fluid bulk. Longuet-Higgins [159] made a similar analysis for the streaming flow within the boundary layer attached to a free surface, which again was nonzero at the internal edge of the layer and thus also responsible for the generation of a global mean flow in the bulk. An important well-known property is that the time-averaged velocity or stress converges to a generally nonzero

value as viscosity goes to zero, while it would vanish if viscosity were identically zero (i.e., when the boundary layer is absent) [125]. This seemingly surprising effect is explained by the singular perturbation character of the inviscid limit.

More recently, the mean flow (also called steady or acoustic streaming [160], [161]) has been studied in various contexts. In particular, the streaming flow induced by no-slip boundaries has been studied in connection with flows in blood vessels [162], generation of mean motions in the ear [163], interaction of sound waves with bodies [164], flows around vibrating bodies [165], and streaming-flow-jets produced by acoustic waves [166]. On the other hand, the streaming flow produced in the boundary layer attached to a vibrating free surface has an effect on the dynamics of oscillating bubbles [167], is of interest in water wave theory [168]–[172], and has been shown to play a role in the instability of the ocean Langmuir circulations [173]. In different contexts, the streaming flow has been studied in microfluidic systems [174] and in conjunction with thermal effects for various purposes, including the control of thermocapillary convection at low viscosity [175]–[178] and cooling in narrow channels [179]. For nearly resonant systems at small viscosity, the streaming flow is not just a byproduct of the primary waves, but generally affects the dynamics of those waves, as repeatedly shown for various flow configurations and vibrating devices [180]–[184]. This is because the streaming flow velocity scales with the square of the wave amplitude and produces an effect in the amplitude equations governing the dynamics of the primary waves that is proportional to the product of the primary waves amplitude and the streaming flow velocity. Thus, this latter effect scales as the cube of the primary waves amplitude, which is the order of magnitude of the cubic nonlinearity that saturates the dynamics in these systems [185].

The streaming flow is responsible for the effective mass transport in the fluid system and, in particular, for the overall motion of passive scalars and surfactants. Therefore, the mean flow is expected to exhibit a nontrivial interaction with Marangoni convection. The understanding of this interaction has been pursued in a number of papers. For instance, Martin and Vega [186] included the effect of Marangoni elasticity in a previous theory for clean free surfaces [182] to study the drift stability of standing Faraday waves in annular containers, previously found experimentally by Douady et al. [187]. More recently, Strickland et al. [188] have pointed out that materials (such as crude oil, biogenic slicks, or industrial and medical surfactants) absorbed at the fluid free surface are expected to move in response to surface waves. They have experimentally studied such effect for Faraday waves in a shallow cylindrical container with an insoluble surfactant monolayer. They distinguished the effects of the meniscus waves near the boundaries and the travelling waves in the far field, which resulted in very complex spatiotemporal patterns. The case of Faraday waves in a rectangular container was considered in Ref. [189], where no specific surfactant was added. In this study, surface contamination was seemingly present due to the use of tap water, which is easily contaminated. In fact, water contamination was also most probably responsible for some striking mean flow effects due to wave-maker oscillations that have been recently reported [190].

The streaming flow theory and systems mentioned above all deal with the low-viscosity limit, in which the thickness of the oscillatory boundary layers is very small compared to the characteristic lengths of the primary surface waves. This sets an upper limit to the surface waves oscillation frequency. If that condition does not hold, the streaming flow can still be analyzed by appropriate time-averaging of the trajectories of fluid elements calculated via direct numerical simulation. This task has not been addressed in the literature, to our knowledge.

As mentioned above, Faraday waves in vibrating containers may produce meniscus oscillations that further complicate the dynamics, and may mask the interaction between the streaming flow and Marangoni convection. To overcome this difficulty, we consider a vibrating liquid bridge with the contact lines attached to the edges of the supporting disks, as we have done in other related works dealing with surfactant monolayer dynamics [191], [192]. This geometry has the additional advantage that direct numerical simulation is feasible at a reasonable computational price. The liquid bridge geometry has already been considered in connection with the streaming flow produced by vibrations, focusing on weakly nonlinear oscillations [193] and the effect of free surface waves [194]. However, these studies dealt with the low viscosity limit. On the contrary, viscosity is not

necessarily small in the present study. Our analysis is based on direct numerical simulation for arbitrary values of that parameter.

Concerning the interaction of the streaming flow with Marangoni convection, we may anticipate here that there is a tradeoff between both. Without Marangoni elasticity (the surfactant is treated as a passive scalar), the surfactant is transported by the streaming flow, which gives rise to nonuniform passive scalar concentrations at the free surface. However, Marangoni elasticity reacts against surfactant concentration gradients, decreasing the tangential velocity at the free surface and counterbalancing the effect of the streaming flow alone. Thus, the resulting streaming flow patterns are expected to be highly affected by Marangoni stresses, at least near the free surface.

The main object of this investigation is to analyze the interaction between the streaming flow and Marangoni elasticity in a vibrated liquid bridge using direct numerical simulation. For simplicity, we consider an insoluble surfactant monolayer on top of the interface of a vibrating liquid bridge. We ignore gravity, consider the symmetric case in which the disks supporting the bridge have equal radii, and neglect surface viscosities. The streaming flow velocity and the time average of both the liquid bridge shape and the surfactant distribution will be calculated in two ways, one asymptotic assuming that the oscillatory flow intensity goes to zero, and another "exact" that does not take that assumption into account. In the former case, the streaming flow velocity is calculated as the sum of the mean Eulerian velocity and the Stokes drift, while in the latter case that velocity is obtained through the time-averaging of the trajectories of the fluid elements. These two approaches rely on the appropriate post-processing of the results obtained by direct numerical simulation, and their outcomes will be used for cross-checking.

7.2. Theoretical background

As anticipated, the analysis of the interaction between the streaming flow and Marangoni stress will be conducted by post-processing "exact results" obtained upon direct numerical simulation. The theoretical background in Sec. 7.2.1 includes the problem formulation, the description of the numerical solver, and the nondimensional parameter range considered. The post-processing formulas to compute the streaming flow is derived and discussed in Sec. 7.2.2.

7.2.1. Governing equations and numerical solver

We consider a liquid bridge (sketched in Figure 7.1) of length L and volume $\mathcal{V}$, held between two circular disks of equal radius R, and surrounded by another fluid medium of negligible density and viscosity. Nondimensionalization of the governing equations is made by using R and $t_0 = (\rho R^3/\sigma_0)^{1/2}$ as units for length and time, respectively, where ρ is the liquid density and σ_0 is the equilibrium (initial) surface tension. For axisymmetric flows, the incompressible Navier-Stokes equations are

$$(ru)_r + rw_r = 0 \tag{7.1}$$

$$u_t + uu_r + wu_z = -p_r + C\left[u_{rr} + \left(\frac{u}{r}\right)_r + u_{zz}\right] \tag{7.2}$$

$$w_t + uw_r + ww_z = -p_z + C\left[w_{rr} + \frac{w_r}{r} + w_{zz}\right] \tag{7.3}$$

where r and z are the radial and axial cylindrical coordinates, respectively, t is the time variable, the
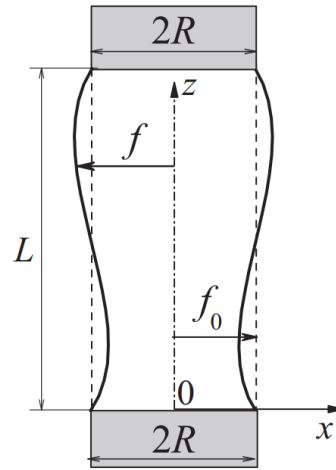
Figure 7.1 Liquid bridge configuration

subscripts r, z, and t denote hereinafter partial derivatives with respect to those variables, u and w are the radial and axial velocity components, respectively, p is the (hydrostatic) reduced pressure, and $C = \mu(\rho\sigma_0 R)^{-1/2}$ is the volumetric Ohnesorge number defined in terms of the bulk viscosity μ.

As boundary conditions, we consider the regularity conditions $u = w_r = p_r = 0$ at the symmetry axis $r = 0$, as well as the kinematic compatibility condition

$$f_t + f_z w - u = 0 \tag{7.4}$$

and the equilibrium of normal and tangential stresses,

$$p - B(t)z - \hat{\sigma}\kappa - \frac{2C\left[u_r - f_z(w_r + u_z) + f_z^2 w_z\right]}{1 + f_z^2} = 0 \tag{7.5}$$

$$C\frac{\left[1 - f_z^2\right](w_r + u_z) + 2f_z(u_r - w_z)}{1 + f_z^2} = \frac{\hat{\sigma}_z}{\sqrt{1 + f_z^2}} \tag{7.6}$$

at the free surface, $r = f(z,t)$. It must be noted that these boundary conditions do not apply if overturning takes place, which may occur just before the pinch-off for vibration amplitudes larger than those considered in this paper. In the above equations,

$$\kappa = \frac{1 + f_z^2 - f f_{zz}}{f\left(1 + f_z^2\right)^{3/2}} \tag{7.7}$$

is (twice) the mean curvature of the free surface, $B(t)$ is the unsteady Bond number defined in Eq. (7.12), and $\hat{\sigma} = \sigma/\sigma_0$ is the ratio of the local surface tension value σ to its equilibrium value σ_0. The dependence of the surface tension on the surfactant concentration obeys differentrelationships, depending on the surfactant. Here, we shall use the Szyskowski-Frumkin equation of state [195],

$$\hat{\sigma} = 1 + Ma \ln\left(\frac{1 - \hat{\gamma}}{1 - \hat{\gamma}_0}\right) \tag{7.8}$$

where $\hat{\gamma} = \gamma/\gamma_\infty$ and $\hat{\gamma}_0 = \gamma_0/\gamma_\infty$ are the local surface coverage and the equilibrium surface coverage, respectively. These quantities are defined in terms of the local surfactant surface concentration γ, its equilibrium value γ_0, and its maximum value γ_∞ corresponding to the maximum

surfactant packing density. In addition, $Ma = \gamma_\infty R_g T_e / \sigma_0$ is the (Marangoni) elasticity number defined in terms of γ_∞, the gas constant R_g, the temperature T_e, and the equilibrium surface tension σ_0. On the other hand, the surfactant concentration along the free surface must obey the surfactant conservation equation [192],

$$\left[f\left(1 + f_z^{\,2}\right)^{1/2} \hat{\gamma} \right]_t + \left[f\left(1 + f_z^{\,2}\right)^{1/2} w\hat{\gamma} \right]_z = \left[\frac{f}{Pe^S} \frac{\hat{\gamma}_z}{\sqrt{1 + f_z^{\,2}}} \right]_z \quad at \; r = f(z,t), \tag{7.9}$$

where $Pe^S = R^2/(t_0 D^S)$ is the surface Peclet number, and D^S is the surface diffusion coefficient.

The boundary condition Eq. (7.5) and the conservation Eq. (7.9) must be complemented with the anchoring condition for the free surface and impenetrability of the surfactant at the liquid bridge disks,

$$f = 1 \; and \; \hat{\gamma}_z = 0 \; at \; z = 0 \; and \; 2\Lambda, \tag{7.10}$$

where $\Lambda = L/(2R)$ is the slenderness. Also, the nondimensional volume $V \equiv \mathcal{V}/(\pi R^2 L)$ and the total amount of surfactant are both conserved, namely

$$\int_0^{2\Lambda} f^2 dz = \int_0^{2\Lambda} f_0^2 dz = 2\Lambda V, \quad \int_0^{2\Lambda} \sqrt{1 + f_z^{\,2}} f\hat{\gamma} dz = \sqrt{1 + f_z^{\,2}} f_0 \hat{\gamma}_0 dz, \tag{7.11}$$

where f_0 is the initial value of the free surface position.

The initial liquid bridge shape is calculated by integrating the Young-Laplace equation, and the initial surfactant concentration is set as spatially constant. For $t \geq 0$, a rigid-solid acceleration with magnitude $a\omega^2 e^{i\omega t} + c.c.$ is applied, where a and ω are the forcing amplitude and frequency, respectively, i is the imaginary unit, and $c.c.$ stands hereinafter for the complex conjugate. Therefore, the unsteady Bond number becomes

$$B(t) = \hat{B} e^{i\omega t} + c.c., \tag{7.12}$$

where $\hat{B} = \rho a\omega^2 R^2 / \sigma_0$ is the dynamical Bond number. The above theoretical model is formulated in terms of the eight nondimensional parameters:

$$\Lambda, V, C, Pe^S, Ma, \hat{\gamma}_0, \omega, and \; \hat{B}. \tag{7.13}$$

We have selected the values of those parameters according to the following considerations:

(i)   Because of the large dimension of the parameter space, the analysis will be restricted to (equilibrium) cylindrical shapes ($V = 1$) with $\Lambda = 1.25$.

(ii)   The volumetric Ohnesorge number will be selected as $C = 0.01$, which corresponds to a typical experimental realization with millimetric water liquid bridges. To analyze the influence of the liquid viscosity, the volumetric Ohnesorge number $C = 0.001$ will be considered too.

(iii)   The surfactant surface diffusivity is typically of the order of 10^{-10}–10^{-9} mm^2/s [195], which leads to surface Peclet numbers in the range 10^5–10^6 when those surfactants are added to millimetric liquid bridges. Thus, the influence of surface diffusion on the liquid bridge dynamics can be ignored. However, ignoring surface diffusion makes the surfactant conservation Eq. (7.9) (hyperbolic and) quite stiff. Because the physics of the high-Peclet-number limit is well captured using much smaller values of Pe^S, we will

consider $Pe^S = 1000$ in the numerical simulations.

(iv)   The elasticity number $Ma = 1$ corresponds to a strong surfactant. For this reason, we will consider the interval $0 \leq Ma \leq 1$.

(v)   The formation of micelles for $\hat{\gamma} \geq 1$ may add rheological effects not considered in this paper. For this reason, the value $\hat{\gamma}_0 = 0.5$ will be selected as typical for the surfactant concentration.

(vi)   The main goal of this paper is the analysis of the influence of the Marangoni convection on the streaming flow caused by the liquid bridge oscillation modes. However, both the thickness of the boundary layers and the axial characteristic length decrease as the oscillation frequency increases, which leads to a considerable increase of the spatial resolution required in the simulations. For this reason, all the calculations will be made for forcing frequencies around the first resonance frequency of the liquid bridge. The value of this quantity is about 2.1 for the equilibrium shape considered in the first item.

(vii)   The strength of the oscillation must be not too large for the quasi-linear theory developed in this paper to be valid. In particular, the steepness of the free surface deflection must be sufficiently small. Taking into account these considerations, $0 < \hat{B} < 0.05$ is an appropriate range for the dynamical Bond number.

Summarizing the above, the following values of the nondimensional parameters listed in Eq. (7.13) will be considered in most of this chapter:

$$\Lambda = 1, V = 1, C = 0.01 \; or \; 0.001, Pe^S = 1000, 0 \leq Ma \leq 1, \hat{\gamma}_0 = 0.5, \tag{7.14}$$

$$2 \leq \omega \leq 2.2, and \; 0 < \hat{B} < 0.05.$$
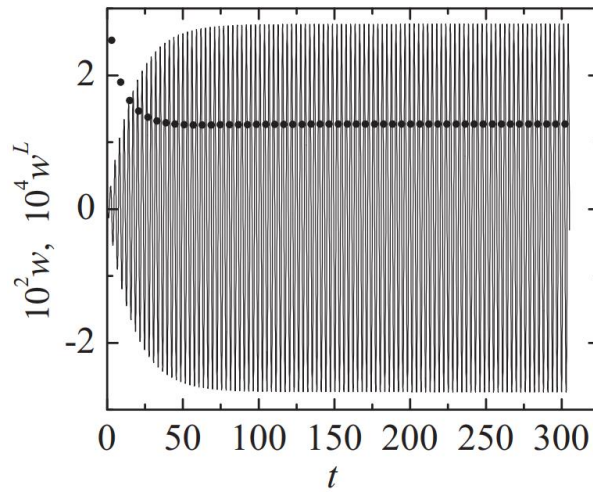
Figure 7.2 Time evolution of the axial component w of the velocity numerically calculated (solid line) and of the axial component w^L of the Lagrangian mean velocity (dots). These quantities were evaluated at the liquid bridge position ($r = 1, z = 3\Lambda/2$). The component w^L was obtained from the difference between the fluid element positions at the instants t and $t - T$ [Eq. (7.24)]. The simulation was conducted for $\Lambda = 1.25, V = 1, C = 0.01, Ma = 0, \omega = 2.1$, and $\hat{B} = 0.005$.

The problem formulated above will be solved with the numerical method recently proposed in Ref. [1]. The timedependent fluid domain is mapped onto a fixed rectangular domain ($0 \leq \eta \leq 1, 0 \leq z \leq 2\Lambda$) through the radial coordinate transformation $\eta = r/f(z, t)$. The numerical domain is discretized (after some calibration) using $n_\eta = 41$ and $n_z = 101$ grid points along the η and z directions, respectively. The spatial derivatives are calculated with fourth-order finite differences. The (implicit) time advancement is performed using second-order backward-differences with a fixed

time step $t = T/80$, where $T = 2\pi/\omega$ is the period of the forced oscillation. At each time step, the resulting set of algebraic equations are solved with the iterative Newton-Raphson technique. The elements of the Jacobian of the discretized system of equations are computed via standard symbolic software at the outset, before running the simulation. These functions are evaluated numerically in the Newton-Raphson iterations to find the solution at each time step, which reduces considerably the required CPU time. The initial guess for the iterations at each time step is the solution at the previous instant.

7.2.2. Streaming flow

Under the conditions mentioned above, we assume that the oscillatory flow velocity and free surface deflection are both conveniently small. Thus, after a transient stage (see Fig. 2), this flow is assumed to be quasilinear, periodic, and quasimonochromatic with the forcing frequency ω. To the approximation relevant in this paper, the velocity components, the free surface deflection, and the surfactant concentration can be written as

$$(u, w) = \varepsilon\big[(U(r,z), W(r,z))e^{i\omega t} + c.c\big] + \varepsilon^2\big[(U_2(r,z), W_2(r,z))e^{2i\omega t} + c.c + \big(u^m(r,z), w^m(r,z)\big)\big] + (O\varepsilon^3),$$
(7.15)

$$f - f_0 = \varepsilon F(z)e^{i\omega t} + c.c. + \varepsilon^2\big[F_2(z)e^{2i\omega t} + c.c + f^m(z)\big] + (O\varepsilon^3),$$
(7.16)

$$\hat{\gamma} - \hat{\gamma}_0 = \varepsilon\hat{\Gamma}(z)e^{i\omega t} + c.c. + \varepsilon^2\big[\hat{\gamma}_2(z)e^{2i\omega t} + c.c + \hat{\gamma}^m(z)\big] + (O\varepsilon^3),$$
(7.17)

where ε is small. The leading-order terms collect the "exact" first harmonic of the periodic oscillation, which can be computed from the exact solution as

$$\varepsilon(U(r,z), W(r,z)) = \frac{1}{T}\int_0^T (u(r,z,t), w(r,z,t))e^{-i\omega t}dt,$$
(7.18)

$$\varepsilon\left(F(z), \hat{\Gamma}(z)\right) = \frac{1}{T}\int_0^T (f(z,t), \hat{\gamma}(z,t))e^{-i\omega t}dt,$$
(7.19)

In addition to the second harmonic, the second-order terms in Eqs. (7.15) – (7.17) comprise the mean values of the velocity field, $\varepsilon^2\big(u^m(r,z), w^m(r,z)\big)$, the free surface deflection, $\varepsilon^2 f^m(z)$, and the surfactant concentration $\varepsilon^2\hat{\gamma}^m(z)$. These mean values are calculated in terms of the exact fields as

$$(u^E, w^E) = \varepsilon^2\big(u^m(r,z), w^m(r,z)\big) = \frac{1}{T}\int_0^T (u(r,z,t), w(r,z,t))dt,$$
(7.20)

$$(f^E, \hat{\gamma}^E) = \varepsilon^2(f^m(z), \hat{\gamma}^m(z)) = \frac{1}{T}\int_0^T (f(z,t) - f_0(z), \hat{\gamma}(z,t) - \hat{\gamma}_0(z))dt,$$
(7.21)

As can be seen, computing these values requires an accuracy $0(\varepsilon^2)$ in the numerical solver.

Equation (7.20) defines the components (u^E, w^E) of the mean Eulerian velocity. However, the effective mass transport is not given by that quantity, but by the mean Lagrangian velocity defined as the time-averaged velocity along the trajectories of the fluid elements, namely,

$$(u^L(r_0, z_0), w^L(r_0, z_0)) = \frac{1}{T}\int_0^T (r'(t), z'(t))dt,$$
(7.22)

Here, (r_0, z_0) is the point where the mean Lagrangian velocity is calculated, and the primes denote the time derivatives. The trajectory $(r(t), z(t))$ of the fluid element passing through (r_0, z_0) is calculated by integrating the kinematic equations for the velocity field, $(u, w) = (u(r, z, t), w(r, z, t))$, as

$$r'(t) = u(r(t), z(t), t), \quad rz'(t) = w(r(t), z(t), t), \quad r(0) = r_0 \ and \ z(0) = z_0 \tag{7.23}$$

Equation (7.22) shows that the exact value of the mean Lagrangian velocity is

$$(u^L(r_0, z_0), w^L(r_0, z_0)) = \frac{(r(T) - r_0, z(T) - z_0)}{T} \tag{7.24}$$

However, and as explained below, this is not a good equation to obtain that quantity. Instead, we may perform a classical asymptotic analysis (as the intensity of the oscillatory flow goes to zero) considering Eq. (7.22) and the Taylor expansions of the right-hand sides of the kinematic Eqs. (7.23), namely,

$$r'(t) = u(r_0, z_0, t) + u_r(r_0, z_0, t)[r(t) - r_0] + u_z(r_0, z_0, t)[z(t) - z_0] + \cdots, \tag{7.25}$$

$$z'(t) = w(r_0, z_0, t) + w_r(r_0, z_0, t)[r(t) - r_0] + w_z(r_0, z_0, t)[z(t) - z_0] + \cdots, \tag{7.26}$$

Substituting Eq. (7.15) into Eqs. (7.25) and (7.26), replacing the resulting equations into Eq. (7.23), and integrating the result gives

$$r(t) - r_0 = \varepsilon U(r_0, z_0) \frac{e^{i\omega t} - 1}{i\omega} + c.c. + O(\varepsilon^2) \tag{7.27}$$

$$z(t) - r_0 = \varepsilon W(r_0, z_0) \frac{e^{i\omega t} - 1}{i\omega} + c.c. + O(\varepsilon^2) \tag{7.28}$$

where only the leading order terms have been retained. These equations show that $|r(T) - r(0)| \sim |z(T) - z(0)| \sim \varepsilon^2$. In other words, calculating the "exact" mean Lagrangian velocity via Eq. (7.24) is a difficult task because it requires computations that are exact to this order (errors small compared to ε2). Instead, we may complete the asymptotic calculation by substituting Eqs. (7.27), (7.28), and (7.15) into Eqs. (7.25) and (7.26), and the resulting equation into Eq. (7.22), which yields

$$(u^L, w^L) = \varepsilon^2 (u^m, w^m) + \varepsilon^2 \left[\frac{1}{i\omega} (\bar{U}_r U + \bar{U}_z W, \bar{W}_r U + \bar{W}_z W) + c.c. \right] + O(\varepsilon^3) \tag{7.29}$$

Hereinafter, the overbar stands for the complex conjugate. In addition, we have taken into account that

$$\int_0^T e^{m\omega t} dt = 0 \quad if \ m = \pm 1, \pm 2, \dots \tag{7.30}$$

Equation (7.29) is a classical result: the mean Lagrangian velocity equals the mean Eulerian velocity plus the Stokes drift [196], i.e.,

$$(u^L, w^L) = (u^E, w^E) + (u^{SD}, w^{SD}) \tag{7.31}$$

where the Stokes drift velocity components are given by

$$(u^{SD}, w^{SD}) \equiv \frac{\varepsilon^2}{i\omega} (\bar{U}_r U + \bar{U}_z W, \bar{W}_r U + \bar{W}_z W) + c.c. \tag{7.32}$$

In contrast to most works mentioned above, the formulas derived here does not rely on the nearly inviscid approximation, but only on the quasilinear approximation Eqs. (7.15)–(7.17), which only requires that the oscillatory field be small. In this approximation, the mean Lagrangian velocity field is given to the leading order by Eq. (7.29) with (U, W) and (u^m, w^m) calculated in terms of the (numerically computed) unsteady velocity components (u, w) from Eqs. (7.18) and (7.20), respectively. Alternatively, the mean Lagrangian velocity can be calculated using Eq. (7.24), which is much more computationally demanding. This calculation will be used for the validation of the asymptotic formulas. Similarly, the mean values of the free surface deflection and the surfactant concentration along the free surface are given by Eq. (7.21).

Using the formulas derived above in the computational domain is somewhat tricky. Note that the calculation of the mean Langrangian velocity must be performed within the physical domain $0 \leq r \leq f_0 + f^E$, which corresponds to the time-averaged liquid bridge shape. In addition, such calculation must be done for fixed r and z, which requires the time-dependent interpolation from the computational domain to the physical one. On the other hand, the computation of the fluid element trajectory used in Eq. (7.24) requires a double time-dependent interpolation: one to calculate the velocity field at $(r(t), z(t))$ from the velocities at the nodes of the fixed computational mesh, and another to integrate the kinematic equations in the (r, z) plane. These details are described in the Appendix.

To illustrate the formulas derived above, we calculated the streaming flow for $C = 0.01$, $Ma = 0$, $\omega = 2.1$, and $\hat{B} = 0.005$. We considered a moderately small viscosity, and ignored the Marangoni stress for simplicity. In addition, we selected a representative value of the forcing frequency ω and amplitude $\hat{B}$. Figure 7.2 shows the time evolution of the axial component of both the actual time-dependent velocity numerically calculated and the mean Lagrangian velocity. These quantities are evaluated at a representative point next to the mean free surface. As can be seen, the time-dependent velocity reaches a strictly periodic state after the transient stage $0 \leq t \leq 100$, while the mean Lagrangian velocity becomes stationary for $t \geq 50$. Consistently with the quasilinear assumption implicit in Eq. (7.15), $w \sim \varepsilon \sim 0.05$ is small, and $w^L \sim \varepsilon^2$ is much smaller than w in the periodic regime. Interestingly, the Lagrangian flow reaches its asymptotic value somewhat before the time-dependent velocity becomes periodic, which implies that the mean flow is not a slave of the surface waves. This seemingly means that the streaming flow does affect the dynamics of the primary surface waves, as shown in Refs. [180]–[184] for small viscosity.

The remaining calculations in this chapter will be conducted in the periodic regime arising after the initial transient stage, whose length varies from one case to another. The spatial structure of the streaming flow in the periodic regime is considered in Figure 7.3, where a comparison between the "exact" and asymptotic formulas [Eqs. (7.24) and (7.29), respectively] is made. The results calculated in these two ways are consistent with each other, which constitutes a stringent test for the numerical procedure. It must be noted that nothing similar to these computations has been performed so far, to our knowledge. As can be seen in Figure 7.3(a), the streaming flow is reflection-symmetric in about the mean plane $z = 1.25$, which is consistent with the invariance of the governing equations under this symmetry. Also, the streamlines show six counter-rotating vortices where the forcing effect of the boundary layers near the disks and the free surface is evident. The free surface boundary layer produces four vortices, which is consistent with the fact that Eq. (7.29) is quadratic in U and W. The first resonant mode of the liquid bridge was excited in this case owing to the selected value of the forcing frequency ω. This mode exhibits two time-dependent vortices associated with the free surface oscillation. As can be seen, quadratic effects double the number of vortices appearing in the streaming flow. The thickness of the boundary layers scales as $\sqrt{C}/\omega \sim 0.07$ in the present case. This value is not small enough for the asymptotic formulas commonly used in the literature to apply. On the other hand, the blow ups in Figs. Figure 7.3(b)–Figure 7.3(d) illustrate how elongated the

fluid trajectories can be, and how small the drift is compared to the widths of those trajectories. These remarks are consistent with the above mentioned difficulties encountered in these computations.
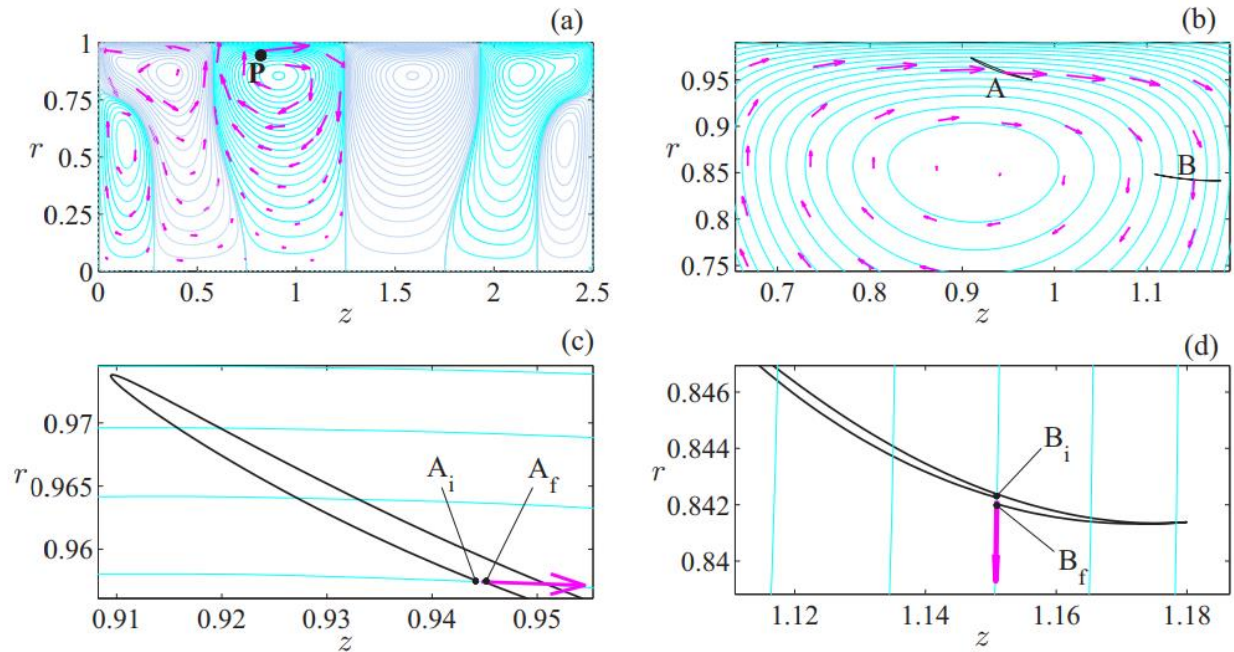
Figure 7.3 (a) Streamlines of the mean Lagrangian velocity field.The cyan lines (first, third, and fifth vortex starting from the left) and gray lines (second, fourth, and sixth vortex starting from the left) indicate clockwise and anticlockwise rotations, respectively. The arrows are the mean Lagrangian velocities calculated from Eq. (7.24). (b) Magnification of plot (a) near the point $(r = 0.85, z = 0.9)$.The black lines indicate the time-dependent trajectories of the fluid particles A and B calculated from the integration of Eqs. (7.23). (c and d) Magnification of plot (b) to show the trajectories of the fluid particles A and B. The subindexes i and f indicate the initial and final positions of the fluid particles in a cycle, respectively. The maximum value of the velocity field is $v_{max} = 1.77 \times 10^{-4}$. The velocity magnitude at the points P, A, and B are $0.92v_{max}$, $0.98v_{max}$, and $0.43v_{max}$, respectively. The values of the governing parameters are the same as those in Figure 7.2, namely, $\Lambda = 1.25$, $V = 1$, $C = 0.01$, $\gamma_0 = 0.5$, $Ma = 0$, $\omega = 2.1$, and $\hat{B} = 0.005$.

The mean free surface deflection and the mean surfactant concentration for the case analyzed in Figure 7.3 are given in Figure 7.4. Note that both are reflection symmetric about the mean plane $= \Lambda$, which is consistent with the invariance of the problem under this symmetry. The left plot indicates that the free surface position is no longer uniform due to the oscillations, although the induced deformation is small. In fact, the mean free surface deflection plays only a secondary role in the context of this paper, and thus it will not be further considered for the sake of brevity. It is interesting to note that $f^E(z) < 0$ for all z, which could be seen as surprising if one takes the conservation of volume into account. However, the liquid bridge volume depends quadratically on f [see Eq. (7.11)], which means that the time-averaged volume (which must be conserved) does not generally coincide with the volume of the time-averaged free surface location. This well-known artifact produced by nonlinear terms is, in fact, similar to what happens with the time-averaged velocity, which is generally nonzero and produces the streaming flow. Note that the volume of the time-averaged free surface location is smaller than its initial value in the present case. The mean surfactant concentration peaks at the liquid bridge center and at the supporting disks and exhibits two minima near $z = \Lambda/2$ and $3\Lambda/2$ (right plot). This behavior is consistent with Figure 7.3, which shows that convection caused by the streaming flow vortices empties the free surface in the regions $z \cong \Lambda/2$ and $3\Lambda/2$ and fills both the central part of the liquid bridge and the sorroundings of the supporting disks.
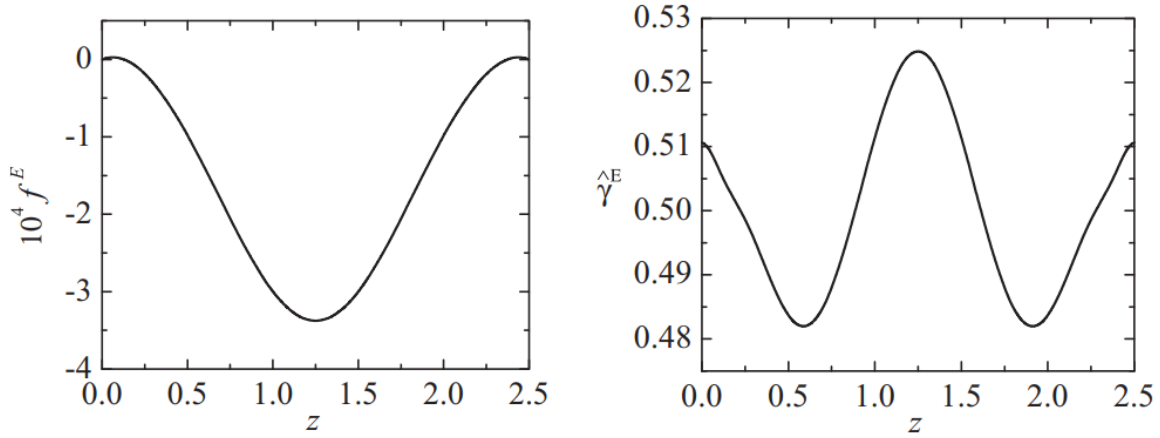
Figure 7.4 Mean free surface deflection $f^E(z)$ (left) and mean surfactant concentration $\hat{\gamma}^E(z)$ (right). The values of the governing parameters are the same as those in Fig. 2, namely, $\Lambda = 1.25$, $V = 1$, $C = 0.01$, $\hat{\gamma}_0 = 0.5$, $Ma = 0$, $\omega = 2.1$, and $\hat{B} = 0.005$.

The simulation illustrated in Figs. Figure 7.3 and Figure 7.4 was conducted for Ma = 0. Therefore, the surfactant does not alter the surface tension and behaves as a passive scalar in that case. If the scalar were a surface active substance ($Ma > 0$), then this concentration distribution would cause Marangoni convection in the direction opposite to that of the streaming flow, which would alter significantly both the mean surfactant concentration distribution and the mean flow pattern. This effect will be analyzed in the next section.

7.3. Results on the interaction of the streaming flow and Marangoni convection

All the results shown in this section were obtained for the values Eq. (7.14) of the governing parameters. The strength of the oscillatory and mean flows are measured using RMS values instead of values at particular points, which would be less robust and less appropriate to obtain scaling laws when different configurations are considered. Specifically, the intensity of the oscillatory flow is defined as

$$I_{osc}^{bulk} = \sqrt{\frac{1}{\Lambda V} \int_0^{2\Lambda} \int_0^{f^E} [|U(r,z)|^2 + |W(r,z)|^2] r \, dr \, dz} \tag{7.33}$$

where U and W are given by Eq. (7.18). The counterpart of Eq. (7.33) for the streaming flow in the bulk is defined as

$$I_{mf}^{bulk} = \sqrt{\frac{1}{\Lambda V} \int_0^{2\Lambda} \int_0^{f^E} [|u^L(r,z)|^2 + |w^L(r,z)|^2] r \, dr \, dz} \tag{7.34}$$

In addition, the intensity of the mean flow in the free surface is defined as

$$I_{mf}^{interf} = \sqrt{\frac{1}{L_s} \int_0^{2\Lambda} [|u^L|^2 + |w^L|^2]_{r=f^E} dz} \tag{7.35}$$

where

$$L_s = \int_0^{2\Lambda} \sqrt{1 + |f_z^E|^2}\, dz \tag{7.36}$$

is the length of the time-averaged free surface. Finally, the strength of the mean flow along the axial coordinate is given by

$$I_{mf}^{axial}(z) = \sqrt{2 \int_0^{f^E} [|u^L(r,z)|^2 + |w^L(r,z)|^2]\, r\, dr} \tag{7.37}$$

The components uL and wL of the mean Lagragian velocities in Eqs. (7.34), (7.35), and (7.37) are given by Eq. (7.29).

In the following two subsections, we consider the influence on the streaming flow of the two main parameters: the Marangoni number and the strength of the oscillatory flow. As will be seen, the Marangoni number affects the shape of the flow patterns, while the strength of the oscillatory flow influences quantitatively the intensity of the mean flow. We aim at uncovering the main physical effects of Marangoni convection on the streaming flow, rather than a full account of the results obtained as the values of the governing parameters are varied.

7.3.1. Influence of the Marangoni number on the flow patterns

In this section, we consider the dependence of the streaming flow on the Marangoni number for the parameter values listed in Eq. (7.14). We are mainly interested in illustrating how Marangoni stresses completely change the streaming flow pattern, without intending an exhaustive description of those patterns. For this reason, we will restrict ourselves to the Ohnesorge number $C = 0.01$ and the forcing frequency $\omega = 2.1$. Smaller values of C would give flow patterns that are more concentrated near the disks and the free surface. The forcing frequency $\omega = 2.1$ is close (but not equal) to the first resonance frequency of the liquid bridge for $Ma = 0$, which means that the oscillatory flow intensity is very sensitive to the value of the dynamical Bond number $\hat{B}$. After some calibration, $\hat{B}$ has been chosen such that the maximum over a cycle of $\varepsilon W e^{i\omega t} + c.c.$ at the center of the liquid bridge is 0.05. This choice makes the intensity of the streaming flow for $Ma = 0$ comparable to the strength of the Marangoni convection in the considered range of Ma. It must be noted that the values of $\hat{B}$ resulting from this criterion are physically realistic since they correspond to accelerations that can be easily produced in experiments [197].

Figure 7.5 shows the counterpart of Figure 7.3 for the indicated values of the Marangoni number. As can be seen, all the flow patterns are reflection-symmetric about the mid plane of the liquid bridge. However, and surprisingly at first sight, the streaming flow patterns do not show a monotone behavior as Ma increases. Instead, the six counter-rotating eddies that are present for $Ma = 0$ first merge for $Ma = 0.001$, 0.005, and 0.05, and then give rise to just two counter-rotating eddies for $Ma = 0.1$ and 0.2. As Ma increases further, new eddies appear leading to a flow pattern for $Ma = 1$ (very strong Marangoni stress) that is qualitatively similar to that obtained for amuch smaller value $Ma = 0.001$. This unexpected behavior is a consequence of the trade off between two mechanisms: nonuniformities in the surfactant concentration at the free surface, and the intensity of the oscillatory flow.
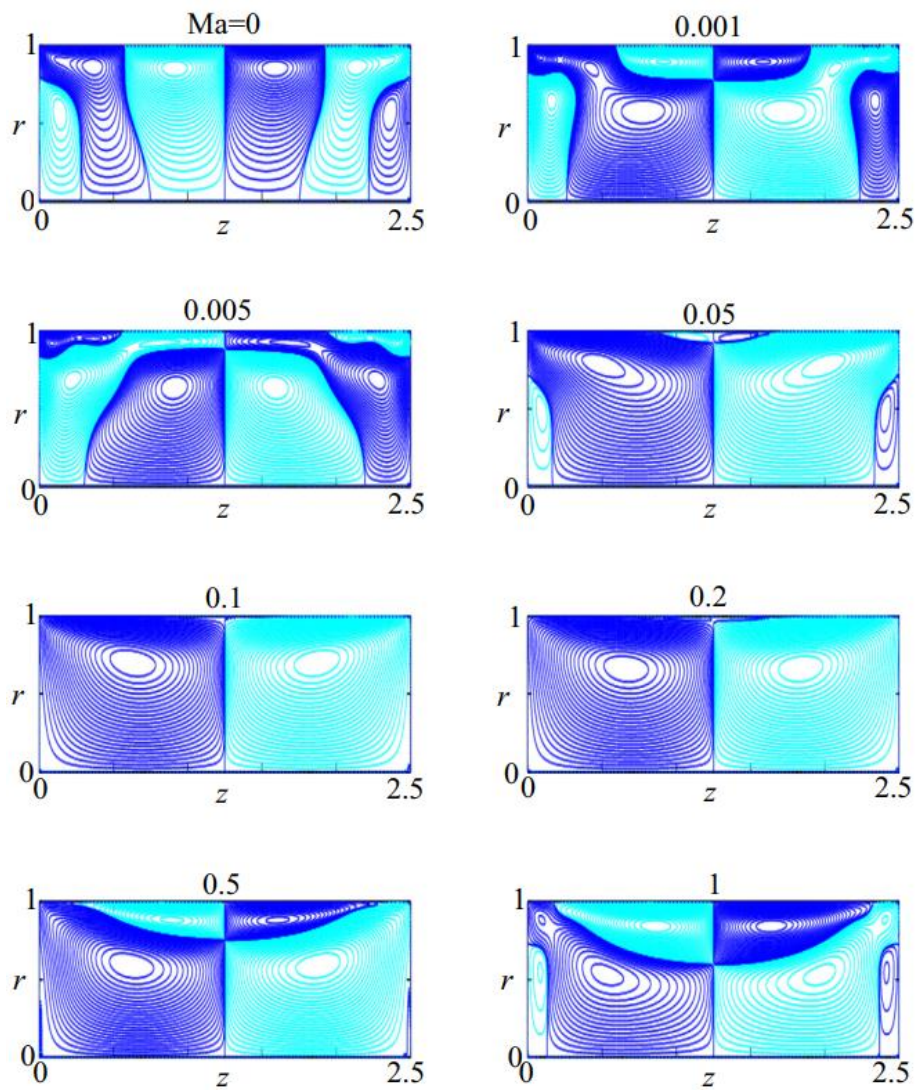
Figure 7.5 Counterpart of Fig. 3 for different Marangoni numbers as indicated by the labels in the figure. The values of the governing parameters are $\Lambda = 1.25$, $V = 1$, $C = 0.01$, $\hat{\gamma}_0 = 0.5$, and $\omega = 2.1$
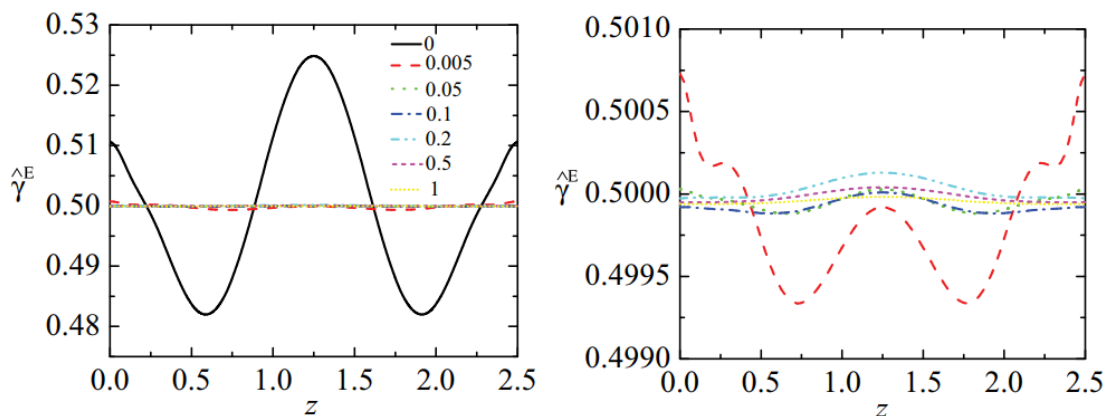
Figure 7.6 Mean surfactant concentration $\hat{\gamma}^E(z)$. The colors (and types of lines) correspond to the different Marangoni numbers as indicated in the left-hand graph. The values of the rest of governing parameters are $\Lambda = 1.25$, $V = 1$, $C = 0.01$, $\hat{\gamma}_0 = 0.5$, and $\omega = 2.1$

The surfactant concentration along the free surface is shown in Figure 7.6 for the same values of

the Marangoni number considered in Figure 7.5. As can be seen, the surfactant concentration becomes almost spatially uniform for very small Marangoni stress. This is due to the strong stabilizing effect of this stress, and is consistent with our guess at the end of Sec. 7.2.2. This behavior explains the streaming flow patterns shown in Figure 7.5 for $Ma = 0.001, 0.005,$ and 0.05. However, as Ma is increased further, the strength of the oscillatory flow increases, peaks at $Ma \cong 0.2$, and decreases again [Figure 7.7(a)]. This is due to the fact that the forcing frequency matches the resonance frequency of the contaminated liquid bridge for $Ma \cong 0.2$. Since the intensity of the streaming flow depends on that of the oscillatory flow, they follow similar trends, as the comparison between Fig. Figure 7.7(a) and Figs. Figure 7.7(b) and Figure 7.7(c) shows.
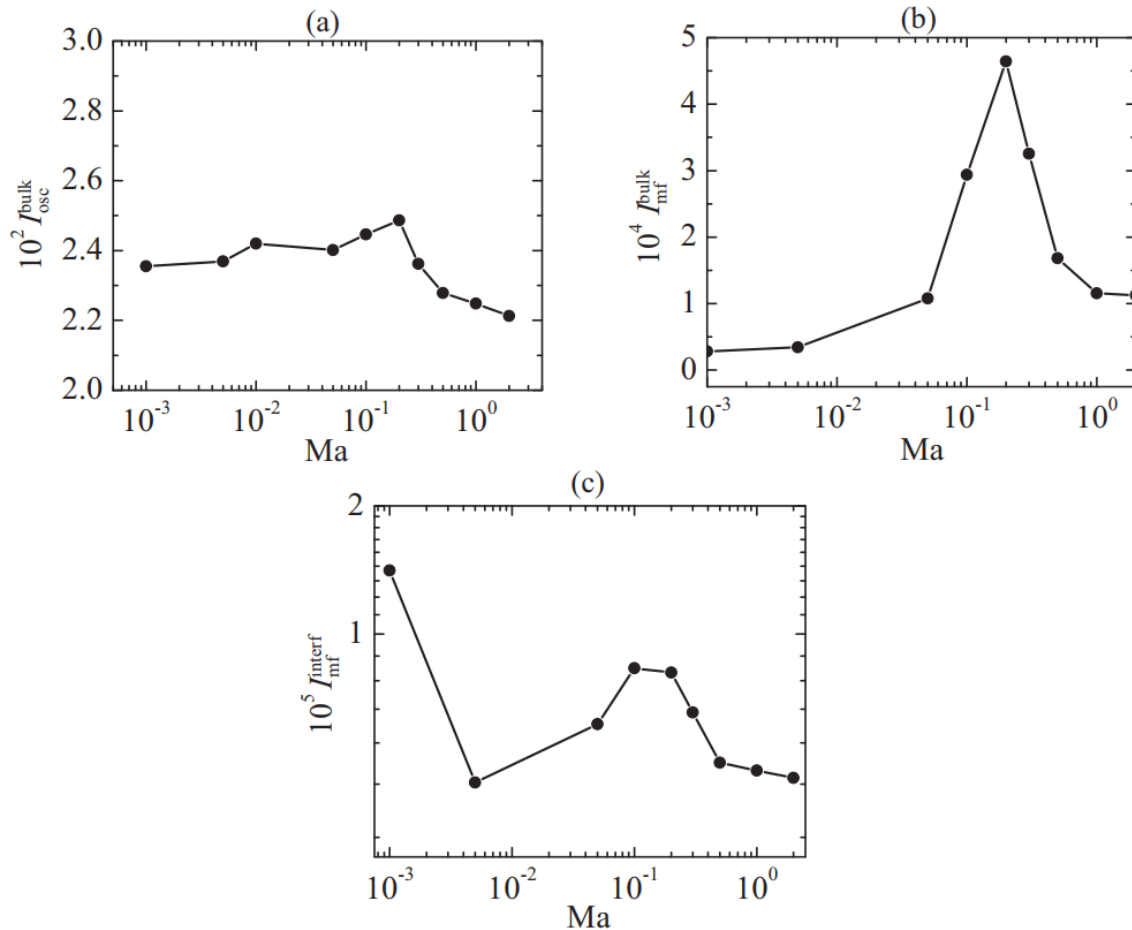
Figure 7.7 Intensities I_{osc}^{bulk} (a), I_{mf}^{bulk} (b), and I_{mf}^{interf} (c) of the oscillatory flow, the mean flow in the bulk and the mean flow in the interface, respectively, for the Marangoni numbers considered in Figure 7.5. The values of the rest of governing parameters are $\Lambda = 1.25$, $V = 1$, $C = 0.01$, $\hat{\gamma}_0 = 0.5$, and $\omega = 2.1$.

Summarizing the above, the Marangoni stress has a great quantitative and qualitative influence on the streaming flow patterns. As Ma increases, these patterns do not behave monotonously due to the fairly complex behavior of both the surfactant concentration at the free surface and the strength of the nearly resonant oscillation.

7.3.2. Influence of the oscillatory flow intensity

In this section, we analyze the influence of the oscillatory flow intensity on the streaming flow intensity for the parameter values listed in Eq. (7.14). This analysis is more involved than that presented in the previous section due to the larger number of parameters considered, and the fact that hysteresis could be present because viscous effects are small and the forcing frequency is close to the

resonant one. The results are obtained by varying the dynamical Bond number. However, and to uncover the underlying scaling laws for the intensity of streaming flow in the bulk and the interface, these quantities are plotted in terms of the oscillatory flow intensity.
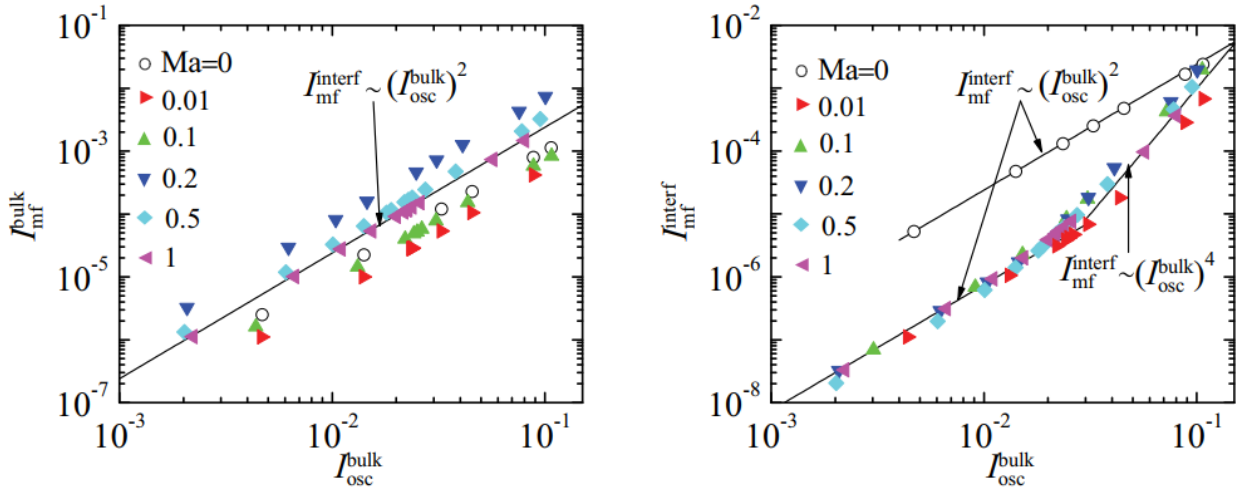
Figure 7.8 I_{mf}^{bulk} (left) and I_{mf}^{interf} (right) vs. I_{osc}^{bulk} for the indicated Marangoni numbers. The values of the rest of governing parameters are $\Lambda = 1.25$, $V = 1$, $C = 0.01$, $\hat{\gamma}_0 = 0.5$, and $\omega = 2.1$.

Figure 7.8 shows the influence of I_{osc}^{bulk} on I_{mf}^{bulk} and I_{mf}^{interf} for the indicated Marangoni numbers, $C = 0.01$ and $\omega = 2.1$. As can be seen, I_{mf}^{bulk} scales as $(I_{osc}^{bulk})^2$ for all values of Ma. This quadratic scaling law can be expected in view of Eq. (7.29). The curves I_{mf}^{bulk} versus I_{osc}^{bulk} are parallel to each other. The maximum and minimum values of the scaling factor differ by one order of magnitude. This factor does not behave monotonously as Ma increases, but first decreases and then increases. This is consistent with the non-monotone behavior of the streaming flow patterns as Ma increases (Figure 7.5). The curves I_{mf}^{interf} versus I_{osc}^{bulk} clearly show two power-law regimes: one for small I_{osc}^{bulk} and another for large I_{osc}^{bulk}, with a fairly well defined threshold at $I_{osc}^{bulk} \cong 0.02$. Morover, the curves for $Ma > 0$ are very close to each other, and clearly deviate from that for $Ma = 0$.
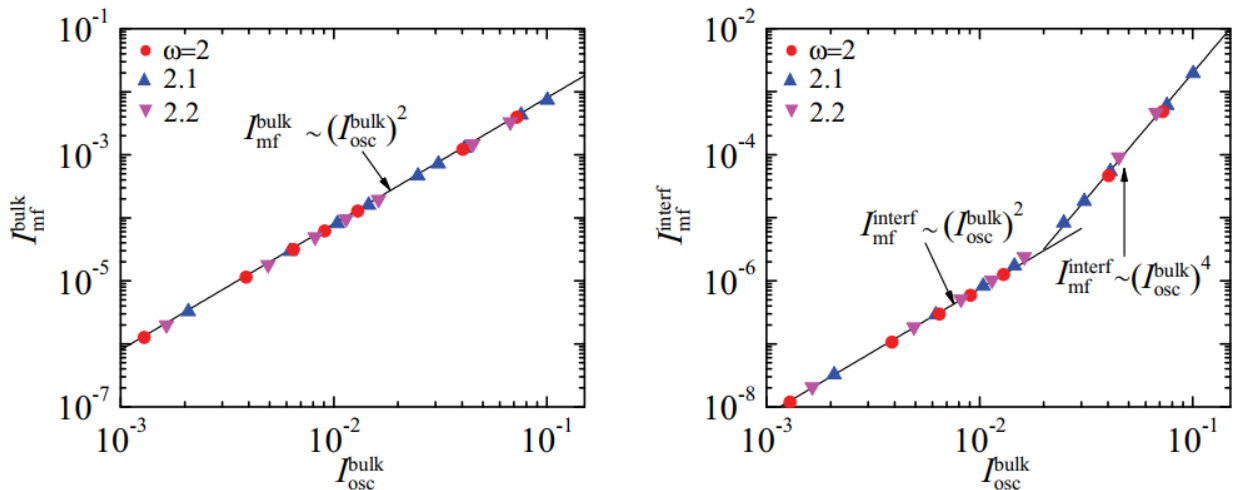
Figure 7.9 Counterpart of Figure 7.8 for the indicated oscillation frequencies. The values of the rest of governing parameters are $\Lambda = 1.25$, $V = 1$, $C = 0.01$, $\hat{\gamma}_0 = 0.5$, and $Ma = 0.2$.
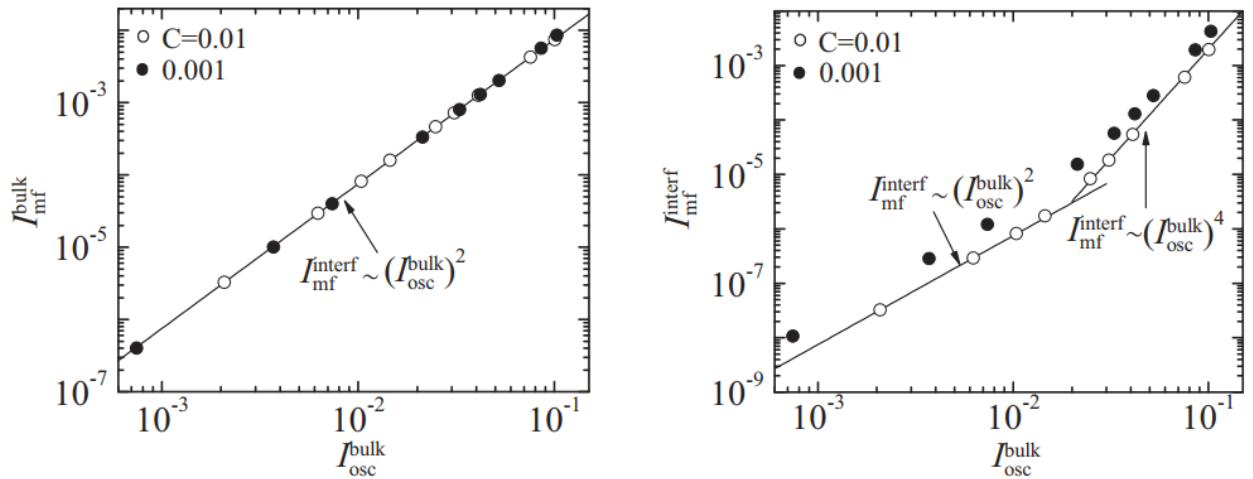
Figure 7.10 Counterpart of Figure 7.8 for the indicated values of C. The values of the rest of governing parameters are $\Lambda = 1.25$, $V = 1$, $\hat{\gamma}_0 = 0.5$, $Ma = 0.2$, and $\omega = 2.1$.

The same behavior is found for other forcing frequencies, as shown in Figure 7.9 for $Ma = 0.2$. As in the previous cases, this figure shows a unique scaling law for I_{mf}^{bulk} and two scaling laws for I_{mf}^{bulk} with a well defined threshold in I_{osc}^{bulk}. This threshold is very close to that in Figure 7.8. In addition, the scaling laws almost coincide for the three values of ω, which suggests that these laws show a fairly weak dependence on the forcing frequency.

The scaling behavior found in Figs. Figure 7.8 and Figure 7.9 is also present for smaller values of C, as shown in Figure 7.10. As can be seen, the scaling laws for I_{mf}^{bulk} and I_{mf}^{interf} coincide with their counterparts in the previous cases. Moreover, the curve I_{mf}^{bulk} versus I_{osc}^{bulk} almost coincide for the two values of C, in spite of the fact that these are disparate. On the other hand, the curves I_{mf}^{interf} versus I_{osc}^{bulk} slightly deviate from each other. The transition between the two scaling behaviors is less sharp for the smallest value of C.

Summarizing the above, the intensity of the streaming flow in the interface shows two well defined power-law behaviors, one for small oscillatory flow intensity and another for larger values of this quantity. These behaviors are fairly universal, since they show the same exponents and the same transition threshold for the considered values of the Marangoni number, forcing frequency, and Ohnesorge number. Such regimes are reminiscent of those found in Ref. [189] (see Fig. 4 in that paper) for the streaming flow produced by Faraday waves in a rectangular container with tap water. However, we cannot ensure that there is a plain analogy between our problem and those experiments for two reasons. First, the data in Ref. [[189], Fig. 4] were not plotted on log-log scale, meaning that the power law for small oscillatory flow intensity could not be uncovered in that paper. In addition, tap water was most seemingly contaminated with a soluble surfactant in those experiments.

Finally, we aim at elucidating whether hystheresis is present as the dynamic Bond number is varied. As already mentioned, this could occur since viscous effects are weak and the forcing frequency is close to the first resonant frequency. Figure 7.11 shows the intensities of the oscillatory and mean flows in the bulk obtained when the periodic regime is reached starting from equilibrium, as well as starting from the previous point while increasing or decreasing progressively the dynamical Bond number $\hat{B}$. As can be seen, the liquid bridge oscillations do not not exhibit hystheresis, i.e., they do not depend on the liquid bridge history.
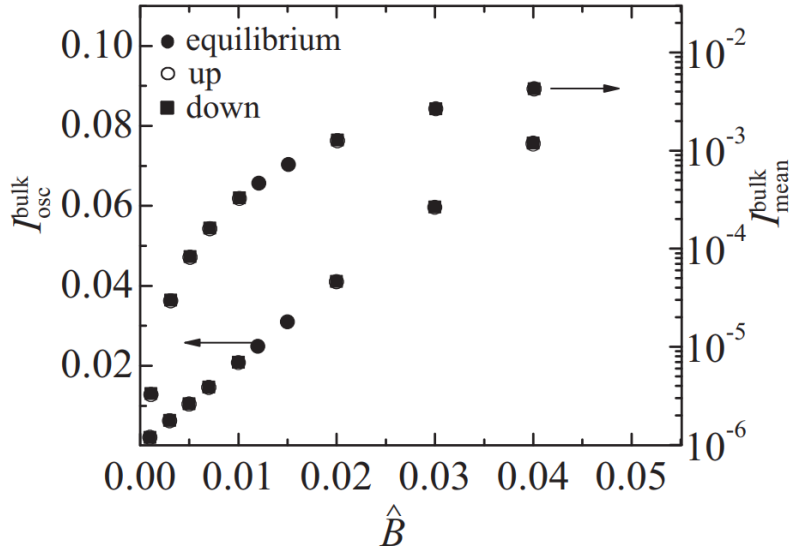
Figure 7.11 I_{osc}^{bulk} and I_{mf}^{bulk} as a function of the dynamical Bond number $\hat{B}$ starting from equilibrium, as well as starting from the previous point while increasing (up) and decreasing (down) progressively the dynamical Bond number. The symbols overlap. The values of the governing parameters are $\Lambda = 1.25$, $V = 1$, $C = 0.01$, $\hat{\gamma}_0 = 0.5$, $Ma = 0.2$, and $\omega = 2.1$.

7.4. Conclusions

We have developed a consistent theory of the interaction between the streaming flow produced by axial vibrations in a liquid bridge and Marangoni convection due to the presence of an insoluble surfactant monolayer. In contrast to previous papers in the field, this theory does not rely on any nearly inviscid formulation, but only on the assumption that the forcing amplitude is sufficiently low for the steepness of the free surface deflection to be small. The streaming flow intensities have been calculated from fully nonlinear direct numerical simulations. Two sets of formulas have been derived and used for cross-checking: one "exact" and based on the average along the trajectories of the fluid elements and another asymptotic and based on the addition of the Eulerian mean velocity and Stokes drift. After validation, the (computationally cheaper) asymptotic formulas have been used in the rest of computations. The main results of this investigation were obtained for a realistic set of parameter values. In particular, the forcing frequency was very close to the first resonant frequency of the liquid bridge.

The following general conclusions can be established:

(i) The streaming flow pattern is highly affected by Marangoni stress even for very small values of Ma. Moreover, the flow patterns show a nonmonotonous behavior as Ma is increased, which is seemingly due to two main effects: the tendency of Marangoni stresses to oppose any surfactant inhomogeneities in the free surface and the nonmonotonous oscillatory response of the liquid bridge due to resonance peaks whose frequencies depend on Ma.

(ii) The strength of the streaming flow shows a "universal" behavior with a unique power law for the intensity in the bulk and a transition between two power laws for the intensity in the free surface. This could be seen as somewhat similar to some recent findings in the literature [189].

The above conclusions are expected to apply to other vibrating systems despite the peculiarities of the primary oscillating flow producing the mean flow. In fact, we have selected the liquid bridge geometry only because it shows fairly simple oscillatory flow patterns when the first resonant mode is excited. This allowed us to focus on the main involved physical mechanisms.

The scaling laws obtained in the present analysis require that the forcing amplitude be small. For larger amplitudes, the dynamics are fully nonlinear and much more complex. In this case, the

oscillatory and mean flow components of the state variables are not expected to be related by simple laws. On the other hand, the somewhat small viscous effects considered in this paper might also play a role. Although the quadratic dependence of the mean flow on the vibrating amplitude also holds for more viscous fluids, the interaction with Marangoni convection may change that dependence for not too small vibrating amplitudes. The analysis of this possibility is beyond the scope of this study, where only realistic values of the parameters have been considered.

Most of surface-active substances in nature are water-soluble. Surfactant solubility makes our analysis less general and does affect the results of the study quantitatively (in particular, the scaling laws). However, there is a large set of surfactants characterized by adsorption and desorption time scales much larger than the liquid bridge capillary time. The results presented here can be extended to such substances. In any case, the fact that Marangoni elasticity opposes surfactant inhomogeneities produced by the streaming flow remains valid for soluble surfactants as well.

7.5. Appendix: Computation of the lagrangian mean velocities in the numerical domain

As explained in Sec. 7.2.1, the computational spatial coordinates are $\eta \equiv r/f(z,t)$ and z. The counterparts of Eqs. (7.15), (7.18), and (7.20) for the velocity components are

$$(\tilde{u}, \tilde{w}) = \varepsilon\left[\left(\tilde{U}(\eta, z), \tilde{W}(\eta, z)\right)e^{i\omega t} + c.c\right] + \varepsilon^2\left[\left(\tilde{U}_2(\eta, z), \tilde{W}_2(\eta, z)\right)e^{2i\omega t} + c.c + \left(\tilde{u}^m(\eta, z), \tilde{w}^m(\eta, z)\right)\right] + (O\varepsilon^3), \tag{7.38}$$

$$\varepsilon\left(\tilde{U}(\eta, z), \tilde{W}(\eta, z)\right) = \frac{1}{T}\int_0^T (\tilde{u}(\eta, z, t), \tilde{w}(\eta, z, t))e^{-i\omega t}dt \tag{7.39}$$

$$\varepsilon^2\left(\tilde{U}_2(\eta, z), \tilde{W}_2(\eta, z)\right) = \frac{1}{T}\int_0^T (\tilde{u}(\eta, z, t), \tilde{w}(\eta, z, t))dt \tag{7.40}$$

where the tilde indicates that the quantity is evaluated in the fixed numerical domain. In addition, Eq. (7.16) implies that

$$\eta = \frac{r}{f} = \frac{r}{f_0} - \varepsilon\left[\frac{rF}{f_0^2}e^{i\omega t} + c.c.\right] + (O\varepsilon^2) \tag{7.41}$$

The Eulearian mean velocity at a fixed point (r, z) can be calculated from the velocity field in the numerical domain as

$$(u^E(r, z), w^E(r, z)) = \frac{1}{T}\int_0^T (\tilde{u}(r/f(t), z, t), \tilde{w}(r/f(t), z, t))dt \tag{7.42}$$

This calculation involves the evaluation of the velocity field at a moving point (r/f (t),z) of the numerical domain in the course of the oscillation. To avoid this evaluation, the above integral is expanded in the following way

$$\frac{1}{T}\int_0^T (\tilde{u}(r/f(t),z,t),\tilde{w}(r/f(t),z,t))dt \tag{7.43}$$

$$= \frac{1}{T}\int_0^T \left(\tilde{u}\left(\frac{r}{f_0},z,t\right),\tilde{w}\left(\frac{r}{f_0},z,t\right)\right)dt$$

$$- \varepsilon^2\left[\frac{r\bar{F}(z)}{f_0^2}\left(U_\eta\left(\frac{r}{f_0},z\right),W_\eta\left(\frac{r}{f_0},z\right)\right) + c.c\right] + (O\varepsilon^3)$$

Therefore, the Eulearian mean velocity at a fixed point (r,z) can be obtained as

$$(u^E,w^E) = \varepsilon^2\left[(\tilde{u}^m(\eta_0,z),\tilde{w}^m(\eta_0,z)) - \frac{\eta_0\bar{F}(z)}{f_0(z)}\left(\tilde{U}_\eta(\eta_0,z),\tilde{W}_\eta(\eta_0,z)\right) + c.c\right] \tag{7.44}$$
$$+ (O\varepsilon^3)$$

where $\eta_0 \equiv r/f_0(z)$ is a fixed coordinate in the numerical domain. To leading order, $\tilde{U}(r/f,z) = \tilde{U}(r/f_0,z)$ and $\tilde{W}(r/f,z) = \tilde{W}(r/f_0,z)$. Therefore, the Lagrangian mean velocity at a fixed point (r,z) can be calculated as

$$(u^L,w^L) = \varepsilon^2(\tilde{u}^m,\tilde{w}^m) \tag{7.45}$$
$$+ \varepsilon^2\left[-\frac{\eta_0\bar{F}}{f_0}(\tilde{U}_\eta,\tilde{W}_\eta) + \frac{1}{i\omega}\left(\bar{\tilde{U}}_\eta\tilde{U} + \bar{\tilde{U}}_z\tilde{W},\bar{\tilde{W}}_\eta\tilde{U} + \bar{\tilde{W}}_z\tilde{W}\right) + c.c.\right]$$
$$+ O(\varepsilon^3)$$

where all the functions are evaluated at (η_0,z). Finally, the kinematic Eqs. (7.23) are rewritten as

$$\frac{d\eta}{dt} = \frac{\tilde{u}(\eta,z,t)}{f(z,t)} - \frac{\eta f_z(z,t)\tilde{w}(\eta,z,t)}{f(z,t)} - \frac{\eta f_t(z,t)}{f(z,t)}, \quad \frac{dz}{dt} = \tilde{w}(\eta,z,t) \tag{7.46}$$

8. INFLUENCE OF THE DYNAMICAL FREE SURFACE DEFORMATION ON THE STABILITY OF THERMAL CONVECTION IN HIGH-PRANDTL-NUMBER LIQUID BRIDGES

W e analyze theoretically the stability of the thermal convection in high-Prandtl-number liquid bridges. The steady axisymmetric base flow, as well as its corresponding linear non-axisymmetric eigenmodes, are calculated taking into account the free surface deformation caused by both that flow and the perturbations. The stability limits and the oscillation frequencies obtained from the linear stability analysis satisfactorily agree with previous experimental data. The dynamical free surface deformation produced by the base flow approximately coincides with that measured in the experiments. When the deformations are normalized with their corresponding values of the Capillary number, they collapse onto a single curve. The dependence of the free surface oscillation amplitude with respect to the axial coordinate approximately also coincides with that measured in previous experiments under similar conditions. Our results show that the dynamical free surface deformation has very little effect on the eigenvalues, and, therefore, on the stability limits.

8.1. Introduction

Convective flows in systems with free surfaces have attracted attention both at the fundamental and practical levels over the last decades. A good example of this is the thermocapillary convection in liquid bridges under microgravity conditions, where flow sets in due to variations of the surface tension along the free surface caused by the temperature difference ΔT applied between the two supporting rods. For small ΔT, an axisymmetric steady flow evolves driven by thermocapillarity. For $\Delta T > \Delta T_c$ and high-Prandtl-number liquids, this flow bifurcates into a three-dimensional oscillatory one (Velten et al., [198]).

There have been numerous both theoretical and experimental studies of thermocapillary convection in cylindrical liquid bridges. Attention has mainly been paid to the examination of the onset of instability and, more recently, the formation of Particle Accumulation Structures (PAS) (Schwabe et al., [199]). Direct numerical simulations of the three-dimensional, time-dependent problem (Shevtsova et al., [200]) have enabled the description of the supercritical regimes arising as ΔT increases above its critical value. These studies have been extended to normal gravity conditions and non-cylindrical volumes ($\mathcal{V} \neq 1$, $\mathcal{V}$ being the liquid bridge volume divided by that of the cylinder enclosed by the supporting rods). In almost all the cases, the numerical simulations have been conducted with a statically deformed free surface calculated for $\Delta T = 0$ from the equilibrium Young-Laplace equation. For high-Prandtl-number liquids, one typically obtains a stability diagram $\Delta T_c(\mathcal{V})$ which consists of two branches that approach each other at very high values of the critical temperature difference ΔT_c when the liquid bridge volume $\mathcal{V}$ tends to a value around unity.

The approximation of static free surface deformation is expected to be valid only for small enough values of the Capillary number, defined as the ratio of the dynamical to the capillary pressure. The free surface deformation induced by the flow, the so-called dynamical free deformation, has received some attention over the last years. In fact, the roled played by this factor in the instability mechanisms is still a subject of discussion for high Prandtl numbers. It has been speculated that both the formation caused by the underlying base flow and the free surface oscillation are important in the development of the oscillatory instability for high-Prandtl numbers fluids. In this case, the main driving force is confined within a small region near the hot corner, where the free surface temperature gradient considerably increases. It is believed that this force may be significantly disturbed by small-amplitude deformations of the free surface (Komatoni et al.,[201]). Komatoni et al. [202] have shown experimentally that the heat loss across the free surface considerably affects the critical temperature difference of the thermocapillary convection in high-Prandtl-number liquids, and have suggested that the dynamic free surface deformation near the hot wall may be responsible for that effect too.

Kuhlmann and Nienhuser [203] have studied theoretically the dynamic free surface deformation induced by thermocapillarity in low-Prandtl-number liquid bridges in the limit of small Capillary numbers. They concluded that the leading-order dynamic deformation does not feed back to the leading-order thermocapillary flow. The dynamic free surface deformation induced by a thermocapillary flow was qualitatively measured by Li et al. [204] using interferometry. Montanero et al. [205] and Ferrera et at. [206] were probably the first to measure quantitatively the free surface perturbation associated with the axisymmetric base flow and oscillations, respectively. Yano et al. [207] have recently determined the amplitude of the free surface oscillatons arising in microgravity experiments on board of the International Space Station (ISS). These oscillatons resulted from both the oscillatory Marangoni convection and g-jitter, whose effects on the liquid bridge behavior can be noticeable due to large sensitivity of the centimeter liquid bridges formed in space (Ferrera et al. [208]). Direct numerical simulations have considered the steady dynamic free surface deformation both in the absence (Zhou and Huai, [209]; Yang et al., [210]) and in the presence ((Herrada et al., [211]; Matsunaga et al., [212]; Yang et al., [213], [214]) of an external air flow. This latter factor has been proposed as a way to control the threshold of the oscillatory flow (Shevtsova et al., [215]). Marangoni shear stresses and/or those exerted by the downwards outer stream drive the liquid towards the bottom (cold) solid end, increasing the hydrostatic pressure there. As a result, the liquid bridge bulges in that region, and shrinks in the upper part.

Linear stability analysis has demonstrated to be a useful tool to describe the instability of the thermal convection in liquid bridges (Neitzel et al., [216]; Kuhlmann and Rath, [217]; Wanschura et al., [218], [219]; Ermakov and Ermakova, [220]; Xun et al., [221]; Nishino et al., [222]). Wanschura et al. [219] showed that the character of this instability in weightless cylindrical liquid bridges depends on the Prandtl number: the bifurcation is stationary for low values of this parameter, while a pair of counter-propagating hydrothermal waves arises in the opposite case. Kuhlmann and Rath [217] examined the linear stability of the thermal convection in cylindrical liquid bridges with a rigid free surface. They analyzed the influence on the stability boundaries of the heat transfer across the free surface, the liquid bridge aspect ratio, and the buoyancy force. This last factor stabilizes the axisymmetric flow in high-Prandtl-number liquids for both heating and cooling from below (Wanschura et al., [218]). It is well known that the equilibrium free surface deformation has a pronounced effect on the stability of the thermocapillary convection in liquid bridges (Sumner et al., [223]). Ermakov and Ermakova [220] reproduced the two branches of the stability diagram $\Delta T_c(\mathcal{V})$ from the linear stability analysis of the thermocapillary convection in liquid bridges with highly deformed free surfaces. These theoretical results are also in good agreement with experimental data measured under microgravity conditions (Nishino et al., [222]).

In all the theoretical analyses mentioned above, the free surface deformation was that given by the liquid bridge equilibrium shape. In this work, we analyze, for the first time, the linear stability analysis of the thermal convection in liquid bridges with a high Prandtl number including the effects of the dynamical free surface deformation. We will quantify this deformation and will examine its

effect on the flow stability. The spatial structure of the dominant eigenmode will be studied, including the shape of the supercritical free surface oscillations.

8.2. Formulation of the problem

The liquid bridge configuration considered in this work (Figure 8.1) is a drop of liquid of volume $\tilde{V}$ delimited by two coaxial supporting rods of diameter D and placed a distance L apart. The triple contact lines anchor perfectly to the edges of those rods. The force of gravity acts along the liquid bridge axis, g being its magnitude per unit mass. The dynamical effects of the outer medium are neglected. The lower and upper solid supports are kept at the temperatures T_0 and $T_0 + \Delta T$ ($\Delta T > 0$), respectively. In most experimental runs, the liquid bridge upper rod is progressively heated up while keeping the lower rod temperature constant, so that a certain range of ΔT values is covered. For this reason, we choose T_0 as the reference temperature of the problem. The heat flux q' across the free surface is given by the expression $q' = h(T_s - T_{amb})$, where h is the (constant) heat flux coefficient, T_s is the free surface element temperature, and T_{amb} is the ambient temperature. The center of the lower rod is chosen as the origin of the cylindrical coordinate system ($\tilde{r}$; θ; $\tilde{z}$). The function $\tilde{F}$ (θ; $\tilde{z}$; $\tilde{t}$) measures the distance between a free surface element and liquid bridge axis ($\tilde{z}$ axis) at the instant $\tilde{t}$.

The liquid thermal conductivity κ and diffusivity are assumed to be constant. The dependence of the liquid density ρ and surface tension σ upon the liquid temperature T are given by the linear functions

$$\rho = \rho_0[1 - \beta(T - T_0)], \qquad \sigma = \sigma_0 - \sigma_T(T - T_0) \tag{8.1}$$
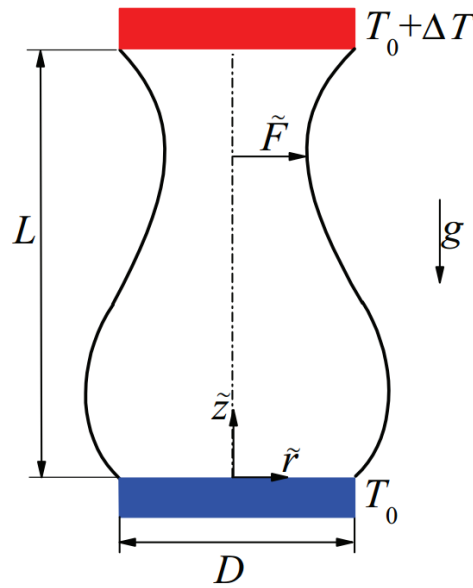
Figure 8.1 Liquid bridge configuration. The dynamical free surface deformation has been exaggerated.

where ρ_0 and σ_0 are the values of these properties at the reference temperature T_0, while and β and σ_T are the thermal expansion and surface tension coefficients, respectively. The temperature dependence of the kinematic viscosity ν is given by the nonlinear function Nishino et al. [222]

$$\nu = \nu_0 f^{(\nu)}, \qquad f^{(\nu)} = exp\left(-\alpha_\nu \frac{T - T_0}{T}\right) \tag{8.2}$$

whose linearization around $T = T_0$ gives

$$v = v_0 - \frac{v_0 \alpha_v}{T_0}(T - T_0) \tag{8.3}$$

Following Ref. Ermakov and Ermakova [220], we choose the characteristic length, time, pressure and temperature as L, L^2/v_0, $\rho_0 v_0^2/L^2$ and ΔT, respectively. According to this choice, the problem is formulated in terms of the dimensionless volume $\mathcal{V} = 4\tilde{\mathcal{V}}/(\pi D^2 L)$, aspect ratio $AR = L/D$, Prandtl number $Pr = v_0/\alpha$, Froude number $Fr = gL^3/v_0^2$, Biot number $Bi = hL/\kappa$, Weber number $We = \rho_0 v_0^2/(\sigma_0 L)$, temperature difference $\Theta_{amb} = (T_{amb} - T_0)/\Delta T$, Grashof number $Gr = g\beta\Delta T L^3/v_0^2$, and Reynolds number $Re = \sigma_T \Delta T L/(\rho_0 v_0^2)$. The viscosity function can be re-written as

$$f^{(v)} = exp\left(-\alpha_v \frac{\Theta}{\Theta + T_0^*}\right) \tag{8.4}$$

Where $\Theta = (T - T_0)/\Delta T$ is the temperature difference field, and $T_0^* = T_0/\Delta T$. The linearization (8.3) of the function involves the single dimensionless parameter $R_v \equiv \frac{\alpha_v}{T_0^*} = \frac{\alpha_v \Delta T}{T_0}$. The resulting set of governing parameters is $\{\mathcal{V}, AR, Pr, Fr, Bi, We, \alpha_v, \Theta_{amb}, Gr, Re, T_0^*\}$. The four last parameters involve the driving temperature difference ΔT.

8.3. Governing equations and numerical method

8.3.1. Governing equations

The liquid bridge motion is described by the Boussinesq approximation:

$$\frac{(rU)_r}{r} + \frac{V_\theta}{r} + W_z = 0 \tag{8.5}$$

$$U_t + UU_r + V\frac{U_\theta}{r} + WU_z - \frac{V^2}{r} \tag{8.6}$$
$$= -p_r + f^{(v)}\left[\frac{(rU_r)_r}{r} + \frac{U_{\theta\theta}}{r^2} + U_{zz} - \frac{U}{r^2} - \frac{2V_\theta}{r^2}\right] + A_r$$

$$V_t + UV_r + \frac{UV}{r} + V\frac{V_\theta}{r} + WV_z \tag{8.7}$$
$$= -p_\theta + f^{(v)}\left[\frac{(rV_r)_r}{r} + \frac{V_{\theta\theta}}{r^2} + V_{zz} - \frac{V}{r^2} + \frac{2U_\theta}{r^2}\right] + A_\theta$$

$$W_t + UW_r + V\frac{W_\theta}{r} + WW_z = -p_z + f^{(v)}\left[\frac{(rW_r)_r}{r} + \frac{W_{\theta\theta}}{r^2} + W_{zz}\right] + Gr\Theta + A_z \tag{8.8}$$

$$\Theta_t + U\Theta_r + V\frac{\Theta_\theta}{r} + W\Theta_z = \frac{1}{Pr}\left[\frac{(r\Theta_r)_r}{r} + \frac{\Theta_{\theta\theta}}{r^2} + \Theta_{zz}\right] \tag{8.9}$$

where $r \equiv \tilde{r}/L$, $z \equiv \tilde{z}/L$ and $t \equiv \tilde{t}v_0/L^2$ are the dimensionless spatial and temporal coordinates, $\mathbf{v}(r, z, \theta; t) = U(r, z, \theta; t)\mathbf{e_r} + V(r, z, \theta; t)\mathbf{e_\theta} + W(r, z, \theta; t)\mathbf{e_z}$ and $p(r, z, \theta; t) = P(r, z, \theta; t) +$

$Fr\,z$ are the velocity and reduced pressure fields, respectively, and $P(r, z, \theta; t)$ the hydrostatic pressure. In addition, the subscripts stand for the partial derivatives with respect to the corresponding variables. The terms A_r, A_z and A_θ account for the viscosity spatial variations, and are given by the expressions

$$A_r = 2f_\Theta^{(v)}\Theta_r U_r + \frac{f_\Theta^{(v)}\Theta_\theta}{r}\left(\frac{U_\theta}{r} + V_r - \frac{V}{r}\right) + f_\Theta^{(v)}\Theta_z(U_z + W_r) \tag{8.10}$$

$$A_\theta = f_\Theta^{(v)}\Theta_r\left(\frac{U_\theta}{r} + V_r - \frac{V}{r}\right) + \frac{2}{r^2}f_\Theta^{(v)}\Theta_\theta(V_\theta + U) + f_\Theta^{(v)}\Theta_z\left(V_z + \frac{W_\theta}{r}\right) \tag{8.11}$$

$$A_z = f_\Theta^{(v)}\Theta_r(U_z + W_r) + \frac{f_\Theta^{(v)}\Theta_\theta}{r}\left(V_z + \frac{W_\theta}{r}\right) + 2f_\Theta^{(v)}\Theta_z W_z \tag{8.12}$$

where $f_\Theta^{(v)} \equiv df^{(v)}/d\Theta$.

The above equations are integrated considering the kinematic compatibility condition at the dimensionless free surface position $r = F(\theta, z; t)$ ($F \equiv \tilde{F}/L$):

$$F_t - U + \frac{F_\theta}{F}V + F_z W = 0 \tag{8.13}$$

The equilibrium of both normal and tangential stresses on the two sides of the free surface yields

$$\tau_n = \left(\frac{1}{We} - Re\,\Theta\right)\nabla.\mathbf{e_n}, \qquad \tau_{t1} = \frac{Re\,\Theta_z}{C_t}, \qquad \tau_{t2} = \frac{Re\,\Theta_\theta}{C_\theta} \tag{8.14}$$

Here, τ_n, τ_{t1} and τ_{t2} are the sum of hydrostatic pressure and viscous stresses on the inner side of the free surface along the normal and two tangential directions, respectively. These stresses are given by the expressions

$$\tau_n = p - Fr\,z - \frac{2f^{(v)}}{C_n^2}\left\{U_r + F_z(F_z W_z - U_z - W_r) \right. \tag{8.15}$$
$$\left. - \frac{F_\theta}{F}\left[-\frac{F_\theta}{F^2}(U + V_\theta) + \frac{U_\theta}{F} + V_r - \frac{V}{F} - F_z\left(V_z + \frac{W_\theta}{F}\right)\right]\right\}$$

$$\tau_{t1} = \frac{f^{(v)}}{C_n C_t}\left\{2F_z(U_r - W_z) + (1 - F_z^2)(W_r + U_z) \right. \tag{8.16}$$
$$\left. - \frac{F_\theta}{F}\left[V_z + \frac{W_\theta}{F} + F_z\left(\frac{U_\theta}{F} + V_r - \frac{V}{F}\right)\right]\right\}$$

$$\tau_{t2} = \frac{f^{(v)}}{C_n^2 C_t}\left\{\frac{2F_\theta}{F}\left[U_r - (1 + F_z^2)\frac{U + V_\theta}{F} + F_z(F_z W_z - U_z - W_r)\right] \right. \tag{8.17}$$
$$\left. + \left(1 + F_z^2 - \frac{F_\theta^2}{F^2}\right)\left[\frac{U_\theta}{F} + V_r - \frac{V}{F} - F_z\left(V_z + \frac{W_\theta}{F}\right)\right]\right\}$$

where C_n, C_t, C_θ are functions of the instantaneous liquid bridge shape given by the equations

$$C_n = \left(1 + F_z^2 + \frac{F_\theta^2}{F^2}\right)^{1/2}, \qquad C_t = (1 + F_z^2)^{1/2}, \qquad C_\theta = \left(1 + \frac{F_\theta^2}{F^2}\right)^{1/2} \tag{8.18}$$

In addition, $\mathbf{e_n} = \frac{1}{FC_n}[(F_\theta sin\theta + Fcos\theta)\mathbf{e_r} - (F_\theta cos\theta + Fsin\theta)\mathbf{e_\theta} - FF_z\mathbf{e_z}]$ is the outward unit vector perpendicular to the free surface, and

$$\nabla.\mathbf{e_n} = \frac{1}{FC_n} + \frac{1}{FC_n^3}\left[\frac{F_\theta}{F}\left(\frac{F_\theta}{F} + 2F_zF_{\theta z}\right) - C_t^2\frac{F_{\theta\theta}}{F} - C_\theta^2FF_{zz}\right] \tag{8.19}$$

is the local mean curvature. The condition for the temperature at the free surface is

$$\nabla\Theta.\mathbf{e_n} + Bi(\Theta - \Theta_{amb}) \tag{8.20}$$

The anchorage, no-slip and temperature boundary conditions,

$$F(\theta, 0; t) = F(\theta, L; t) = (2\,AR)^{-1} \tag{8.21}$$

$$\mathbf{v}(r, 0, \theta; t) = \mathbf{v}(r, L, \theta; t) = 0 \tag{8.22}$$

$$\Theta(r, 0, \theta; t) = 0, \qquad \Theta(r, L, \theta; t) = 1 \tag{8.23}$$

are imposed at the solid supports. Finally, periodic boundary conditions in the angular direction are prescribed for all the variables.

The steady axisymmetric base flow is characterized by the velocity $\mathbf{v_b}(r, z) = U_b(r, z)\mathbf{e_r} + W_b(r, z)\mathbf{e_z}$, reduced pressure $p_b(r, z)$ and temperature $\Theta_b(r, z)$ fields. The function $F_b(r, z)$ is the distance between a surface element and the z axis, and allows one to calculate the liquid bridge volume

$$\mathcal{V} = 4\,AR^2\int_0^1 F_b^2 dz \tag{8.24}$$

To calculate the linear global modes, one assumes the spatio-temporal dependence

$$U(r, z, \theta; t) = U_b(r, z) + \epsilon\widehat{U}(r, z)e^{-i\omega t + m\theta} \tag{8.25}$$

$$V(r, z, \theta; t) = V_b(r, z) + \epsilon\widehat{V}(r, z)e^{-i\omega t + m\theta} \tag{8.26}$$

$$W(r, z, \theta; t) = W_b(r, z) + \epsilon\widehat{W}(r, z)e^{-i\omega t + m\theta} \tag{8.27}$$

$$p(r, z, \theta; t) = p_b(r, z) + \epsilon\widehat{p}(r, z)e^{-i\omega t + m\theta} \tag{8.28}$$

$$\Theta(r, z, \theta; t) = \Theta_b(r, z) + \epsilon\widehat{\Theta}(r, z)e^{-i\omega t + m\theta} \tag{8.29}$$

$$F(z, \theta; t) = F_b(z) + \epsilon\widehat{F}(z)e^{-i\omega t + m\theta} \tag{8.30}$$

where $\epsilon \ll 1$, $\{\widehat{U}, \widehat{V}, \widehat{W}, \widehat{p}, \widehat{\Theta}, \widehat{F}\}$ stand for the eigenmode spatial dependence of the corresponding quantities, while $\omega = \omega_r + i\omega_i$ is the eigenfrequency and m is the azimuthal wave number. The eigenmode regularity conditions at the symmetry axis $r = 0$ are

$$\widehat{U}(0, z) = \widehat{V}(0, z) = \widehat{W}_r(0, z) = \widehat{\Theta}_r(0, z) = 0 \quad for \quad m = 0 \tag{8.31}$$

$$\hat{U}(0,z) + i\hat{V}(0,z) = \hat{W}(0,z) = \hat{\Theta}(0,z) = 0 \quad for \quad m = 1 \tag{8.32}$$

$$\hat{U}(0,z) = \hat{V}(0,z) = \hat{W}(0,z) = \hat{\Theta}(0,z) = 0 \quad for \quad m \geq 2 \tag{8.33}$$

Both the eigenfrequencies and the corresponding eigenmodes are calculated as a function of the governing parameters. The dominant eigenmode is that with the largest growth factor ω_i. If that growth factor is positive, the base flow is unstable. For sufficiently large temperature differences, the axisymmetric flow becomes unstable and gives rise to an unsteady three-dimensional motion.

In the previous works, the linear stability analyses have been conducted by assuming that the liquid bridge free surface is rigid, i.e., it does not deform due to the flow. To take this approximation, we replace $F(\theta, z; t)$ with the equilibrium free surface contour $F_0(z)$ calculated from the Young-Laplace and volume equations

$$p - Fr\,z = We^{-1}\nabla.\mathbf{e_n}\,, \qquad \mathcal{V} = 4\,AR^2\int_0^1 F_0^2 dz \tag{8.34}$$

and eliminate both the kinematic compatibility condition [Eq. (8.13)] and the balance of normal stresses at the free surface [Eq. (8.14)-left] from the system of equations. This is equivalent to take an infinitely small (large) value of the Weber number We (equilibrium surface tension σ_0) with a finite Bond number $B = FrWe = \rho g L^2/\sigma_0$.

8.3.2. Numerical method

In order to calculate both the base flows and the corresponding eigenmodes, we apply the boundary fitted method. The liquid domain is mapped onto a quadrangular domain through a time-dependent coordinate transformation which accounts for the instantaneous location of the liquid bridge free surface. The hydrodynamic equations are discretized in the radial and axial directions using fourth-order finite differences with 91 points. These points are accumulated near the two solid surfaces and the free surface (Figure 8.2) where the gradients of the hydrodynamic quantities are expected to increase. The accumulation of grid points next to the upper (hot) solid rod is especially important due to the flow complexity in that region.
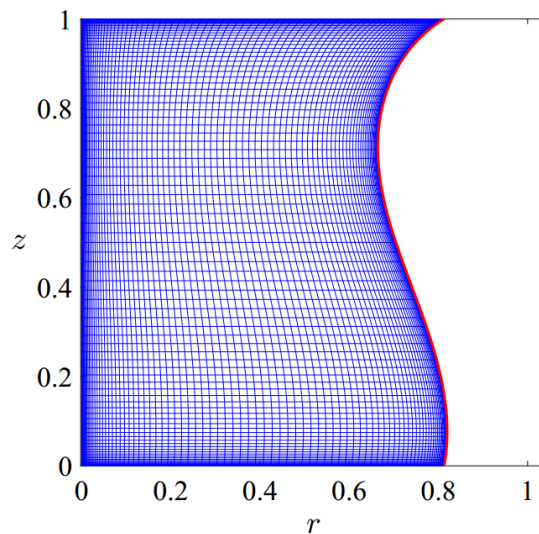
Figure 8.2 Details of the grid used in the simulations

Consider the Jacobian $\mathcal{J}^{(p,q)}$ corresponding to the discretized system of equations $\mathcal{J}^{(p,q)}\mathcal{U}_b^{(q)} = \mathcal{F}^{(p)}$, where $\mathcal{U}_b^{(q)}$ $(q = 1,2,...,n \times N)$ stand for the values of the n base flow unknowns at the N

grid points, and $\mathcal{F}^{(p)}$ represents the inhomogeneous part of the equations. Both the elements of $\mathcal{J}^{(p,q)}$ and $\mathcal{F}^{(p)}$ are computed analytically before running the simulation using a symbolic software. The resulting functions are evaluated numerically over the Newton-Raphson iterations, which greatly reduces the CPU time. In each of those iterations, one first evaluates the Jacobian $\mathcal{J}_b^{(p,q)} = \mathcal{J}^{(p,q)}\left(\mathcal{U}_b^{(q)}\right)$ and the inhomogeneous part $\mathcal{F}_b^{(p)}\left(\mathcal{U}_b^{(q)}\right)$ for the updated value of $\mathcal{U}_b^{(q)}$. Then, one calculates the inverse matrix $\mathcal{J}_b^{-1(p,q)}$ with an algorithm which takes advantage of the high sparsity of the matrix. Finally, the correction vector $\delta\mathcal{U}_b^{(q)}$ is obtained as $\delta\mathcal{U}_b^{(q)} = -\mathcal{J}_b^{-1(p,q)}\mathcal{F}_b^{(p)}$.

The above numerical procedure can be easily adapted to solve the eigenvalue problem which determines the linear modes of the system. The spatial dependence of the linear perturbation $\hat{\mathcal{U}}^{(q)}$ is the solution to the generalized eigenvalue problem $\mathcal{J}_b^{(p,q)}\hat{\mathcal{U}}^{(q)} = i\omega Q^{(p,q)}\hat{\mathcal{U}}^{(q)}$, where $\mathcal{J}_b^{(p,q)}$ is the Jacobian of the system evaluated with the base solution $\mathcal{U}_b^{(q)}$, and $Q^{(p,q)}$ accounts for the temporal dependence of the problem. This matrix is calculated with essentially the same procedure as that for $\mathcal{J}_b^{(p,q)}$. Therefore, the numerical algorithm developed for the base flow problem can also be applied to the linear stability analysis. More details of the numerical method can be found elsewhere (Herrada and Montanero, [1]).

We have validated the numerical method from comparison with previous simulation results for a rigid free surface. The average difference between the critical Reynolds numbers and oscillation frequencies shown in Tables 1 and 3 of Ref. Shevtsova et al. [200] and our corresponding values are 0.2% and 0.6%, respectively. The difference between the critical Rayleigh number shown in Table 1 of Ref. Kuhlmann and Rath [217] for the natural convection in a liquid bridge with $AR = 0.5$ and that predicted by our simulation is less than 0.5%. Finally, the difference between the critical Reynolds number shown in Table 1 of Ref. (Prange et al., [224]) in the absence of a magnetic field and our result is less than 0.5%.

8.4. Results

It is believed that the onset of instability under microgravity conditions is determined by the Marangoni $Ma = RePr = \sigma_T\Delta TL/(\rho_0 v_0\alpha)$. and Capillary $Ca = ReWe = \sigma_T\Delta T/\sigma_0$ numbers rather than by the Reynolds and Weber numbers, which naturally arise from the characteristic quantities introduced in Sec. 8.2. For this reason, we will adopt

$$\{\mathcal{V}, AR, Pr, Fr, Bi, \alpha_v, \Theta_{amb}, Gr, Ma, Ca, T_0^*\} \tag{8.35}$$

as the set of governing parameters. The last five numbers involve the temperature difference ΔT. Now, the Capillary number is the single parameter that includes the equilibrium surface tension σ_0, and, therefore, it can be regarded as a measure of the free surface rigidity. In fact, the limit $Ca \to 0$ ($\sigma_0 \to \infty$) corresponds to the rigid free surface approximation commonly made in the theoretical analyses.

Given the large dimension of the parameter space, we will restrict ourselves to liquid bridges of 5-cSt silicone oil, characterized by a high Prandtl number ($Pr =67$) and very frequently used in experiments. The physical properties of this liquid measured at $T_0 = 25$ °C by Nishino et al. ([206]): $\rho_0 = 915$ kg/m^3, $\beta = 1.09 \times 10^{-3}$ 1/K, $v_0= 5.0 \times 10^{-6}$ m^2/s, $\alpha_v = 5.892$, $\sigma_0 = 19.7 \times 10^{-3}$ N/m, $\sigma_T = 6.58 \times 10^{-5}$ N/(m·K), $\kappa = 0.12$ W/(m·K) and $\alpha = 7.46 \times 10^{-8}$ m^2/s.

Figure 8.3 shows a comparison between the experimental values and our numerical predictions for the critical Marangoni number $Ma^* = \sigma_T\Delta T\left(\frac{D}{2}\right)/(\rho\bar{v}\alpha)$ and the dimensionless oscillation frequency $\omega_r^* = \widetilde{\omega}_r\left(\frac{D}{2}\right)^2/(\alpha\sqrt{Ma^*})$ of liquid bridges with different aspect ratios under microgravity conditions ($Fr = Gr =0$) (Fig. 6 of Ref. Nishino et al. ([206])). Here, $\bar{v}$ and $\widetilde{\omega}_r$ are the

kinematic viscosity for $T = T_0 + \Delta T/2$ and the dimensional oscillation frequency, respectively. In our simulations, the instability for $AR = 0.17$ and 0.325 was caused by the growth of the $m = 2$ mode, while the dominant mode for the rest of aspect ratios was that with $m = 1$. There is good agreement between the theoretical and experimental results for the Biot numbers $Bi = 0.15$ and 0.3 proposed by Nishino et al. [206]. This agreement is similar to that exhibited by the linear stability analysis presented by in that work. In particular, the simulation reproduces the sharp decrease of the oscillation frequency for $AR = 1.25$.
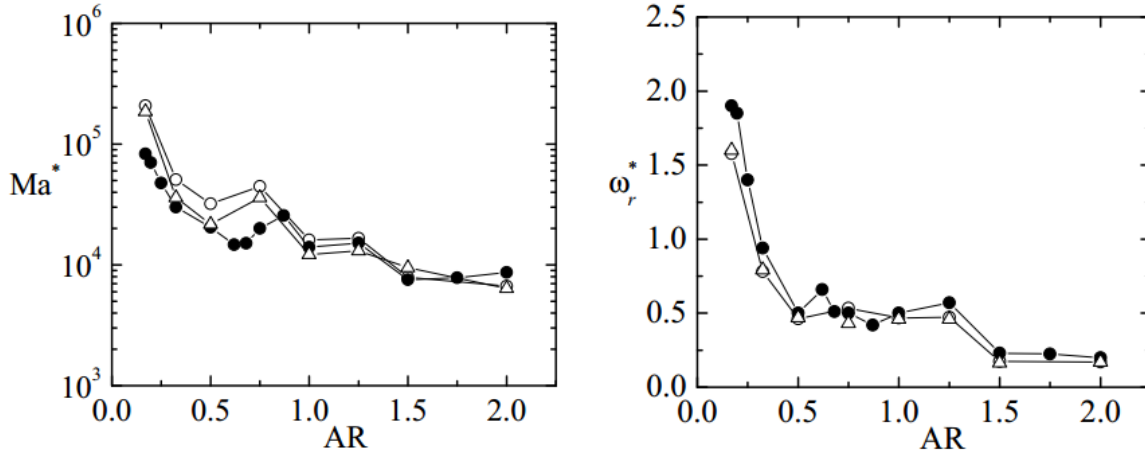
Figure 8.3 Experimental (solid symbols) and numerical (open symbols) values of the critical Marangoni number Ma^* (left-hand graph) and the oscillation frequency ω_r^* (right-hand graph) for liquid bridges with different aspect ratios AR under microgravity conditions ($Fr = Gr = 0$) (see Fig. 6 of Ref. (Nishino et al., [206])). The circles and triangles correspond to the numerical results calculated with $Bi = 0.15$ and 0.3, respectively.

Montanero et al. [205] studied experimentally the dynamical free surface deformation arising in the thermal convection of 5-cSt silicone oil liquid bridges. In those experimental runs, the liquid bridge was formed at the ambient temperature $T_{amb} = 25°C$, and then the upper rod was progressively heated up while keeping the lower rod temperature $T_0 = 25°C$ constant, so that a certain range of ΔT values was covered. The dimensionless number $\{AR = 0.615, Pr = 67, \alpha_v = 5.892, Fr = 1.973 \times 10^4, \Theta_{amb} = 0\}$ were kept constant, while $\{V, Gr, Ma, Ca, T_0^*\}$ varied with ΔT. The free surface location was accurately measured in the course of the experiment with a sub-pixel resolution technique. The liquid thermal expansion produced variations of the liquid bridge volume $\Delta V \sim 10^{-2}$, which caused free surface deformations comparable to those produced by the flow. We will devote the rest of this section to examine numerically the first experimental run conducted in that work (the other produced very similar results). In that case, the instability was caused by the $m = 1$ mode for $\Delta T = 16.8°C$, which corresponds to a critical Marangoni number $Ma = 1.196 \times 10^4$. In order to take into account thermal expansion, our simulations were conducted with the liquid bridge volumes measured in the experiment for the corresponding value of ΔT (see Fig. 10b of Ref. (Montanero et al., [205])).

Figure 8.4 shows the base flows corresponding to the experimental run I in Ref. Montanero et al. [205] with $\Delta T = 15.20$ and $21.76°C$, which correspond to subcritical and supercritical conditions, respectively. In both cases, the streamlines show the formation of four vortices. The two anticlockwise vortices near the free surface are driven by the Marangoni stress, while the other two clockwise rotations are caused by the buoyancy force. A thin recirculation cell arises in contact with the upper rod, where the temperature gradient reaches higher values. As can be observed, a large number of grid points are required in that region and next to the free surface to reproduce the flow accurately. The only qualitative difference between the flow patterns in the subcritical and supercritical cases is the growth of the vortex next to the center of the lower rod as the temperature difference increases.

We have verified that neither the base flow nor its linear stability are significantly affected by the Biot number. Specifically, the critical Marangoni number $Ma = 1.159 \times 10^4$ calculated for $Bi=0.15$ differed in less than 0.5% from that calculated for $Bi=0.3$. Those values deviated in less than 3.6% from that measured in the experiment. We will set $Bi=0.15$ in the rest of the simulations. As occurred in the experiment, instability was caused by the $m = 1$ mode.
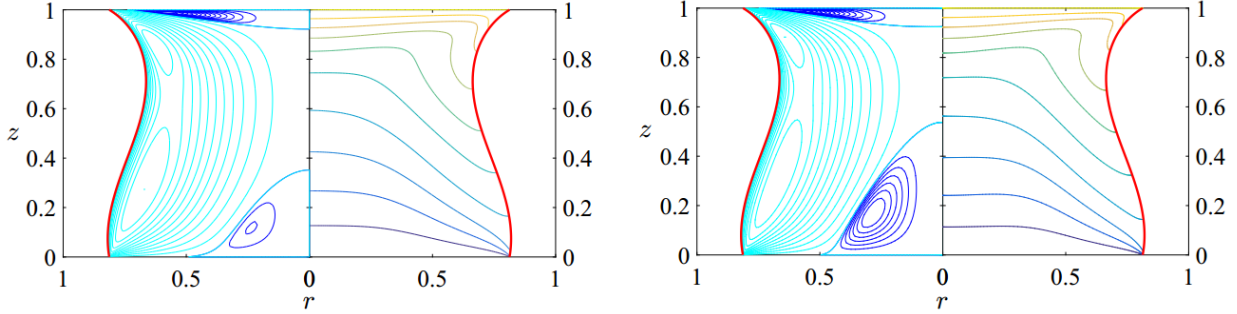
Figure 8.4 Streamlines (left) and temperature isolines (right) for $\{AR = 0.615, Pr = 67, \alpha_v = 5.892, Fr = 1.973 \times 10^4, \Theta_{amb} = 0, Bi = 0.15\}$ and $\{\mathcal{V} = 0.8265, Gr = 326.9, Ma = 1.082x10^4, Ca = 0.0508, T_0^* = 1.645\}$(left) and $\{\mathcal{V} = 0.8298, Gr = 468, Ma = 1.549x10^4 Ca = 0.0727, T_0^* = 1.149\}$ (right). The blue and cyan lines in the left-hand figure indicate clockwise and anticlockwise rotations, respectively.

As mentioned above, Montanero et al. [205] described the free surface deformation of a 5-cSt silicone oil liquid bridge when a temperature difference ΔT was applied between two solid supports of the same diameter. For ΔT = 0, the equilibrium liquid bridge contour is characterized by the function $F_0(z)$ which obeys the Young-Laplace equation (8.34). The deformation $F_0(z) - (2\,AR)^{-1}$ with respect to the cylinder delimited by the two supports results from the competition between gravity and surface tension, and from the difference between the liquid bridge volume and that of the cylinder. An axisymmetric steady flow arises in the liquid bridge when a temperature difference ΔT is applied between the supports. The corresponding free surface contour $F_b(z)$ differs from the equilibrium shape $F_0(z)$ by the perturbation $F_b(z) - F_0(z)$, which is at least one order of magnitude smaller than the deformation $F_0(z) - (2\,AR)^{-1}$ at equilibrium under normal gravity conditions (Montanero et al., [205]). This perturbation is caused by the liquid thermal expansion, the surface tension variation over the free surface, and the hydrodynamic effects on that surface. The three effects are commensurate with each other. When ΔT exceeds a certain critical value ΔT_c, the axisymmetric steady flow evolves towards a non-axisymmetric oscillatory regime. In this regime, the free surface contour $F(\theta, z; t)$ can be seen as the sum of those corresponding to the underlying base flow, $F_b(z)$, and to the oscillations. In the experiments, the oscillation contribution $F(\theta, z; t) - F_b(z)$ was a periodic or quasi-periodic function of time, and at least one order of magnitude smaller than $F_b(z) - F_0(z)$ for the range of ΔT explored (Ferrera et al., [206]). The underlying base flow contour $F_b(z)$ for $\Delta T > \Delta T_c$ can be approximately measured by averaging $F(\theta, z; t)$ over an oscillation cycle (Montanero et al., [205]).

To summarize, one must bear in mind the following hierarchy of deformations for the thermal convection in liquid bridges:

$$|F(\theta, z; t) - F_b(z)| \ll |F_b(z) - F_0(z)| \ll |F_0(z) - (2\,AR)^{-1}| \ll (2\,AR)^{-1}$$

(8.36)
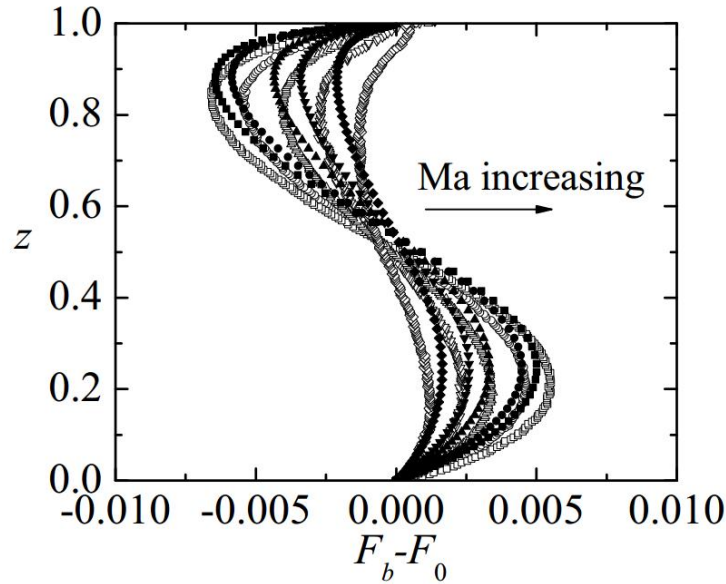
Figure 8.5 Experimental (open symbols) and numerical (solid symbols) free Surface deformation $F_b - F_0$ of the base flow $\{AR = 0.615, Pr = 67, \alpha_v = 5.892, Fr = 1.973 \times 10^4, \Theta_{amb} = 0, Bi = 0.15\}$ and $\{\mathcal{V} = 0.8200, Gr = 117.4, Ma = 3.885x10^3, Ca = 0.0182, T_0^* = 4.579\}$ (diamonds), $\{\mathcal{V} = 0.8241, Gr = 237.7, Ma = 7.863x10^3, Ca = 0.0369, T_0^* = 2.262\}$ (down-triangles), $\{\mathcal{V} = 0.8265, Gr = 326.9, Ma = 1.082x10^4, Ca = 0.0508, T_0^* = 1.645\}$ (up-triangles), $\{\mathcal{V} = 0.8298, Gr = 468, Ma = 1.549x10^4, Ca = 0.0727, T_0^* = 1.149\}$ (circles) and $\{\mathcal{V} = 0.8405, Gr = 544.8, Ma = 1.803x10^4, Ca = 0.0846, T_0^* = 0.987\}$ (squares).

Figure 8.5 shows $F_b(z) - F_0(z)$ both measured experimentally (Montanero et al., [205]) and obtained from our numerical simulations. As mentioned above, the simulation was conducted with the liquid bridge volume determined in the experiment for the corresponding value of ΔT to account for thermal expansion. In both the experiments and simulations, the function $F_0(z)$ was calculated from the integration of the Young-Laplace equation (8.34) with that volume and the surface tension value σ_0. Therefore, $F_b(z) - F_0(z)$ indicates the free surface deformation caused by the surface tension variation over the free surface and the hydrodynamic effects on that surface. There is good agreement between the theoretical predictions and experiments. In all the cases, the deviation of the numerical contour from its experimental counterpart is smaller than the (dimensionless) size 2.3 x 10⁻³ of the pixels in the images acquired in the experiments (Montanero et al., [205]). Part of that deviation can be attributed to the small differences between the nominal geometry and the real one (eccentricity, difference between the diameters of the rods, . . .), which may commensurate with the dynamical perturbation $F_b(z) - F_0(z)$ [Eq. (8.36)].

The free surface deformation induced by the base flow exhibits similar shapes for the temperature differences considered in Figure 8.5. In fact, the maximum and minimum deformations are reached at practically the same heights. This can be clearly appreciated in Figure 8.6, where the free surface deformation has been divided by the Capillary number. As can be seen, the maximum free surface deformation is one order of magnitude smaller than the corresponding value of the Capillary number. The normalized deformations do not perfectly match probably due to the influence of the liquid bridge equilibrium shape $F_0(z)$. This shape is different in each case due to the thermal expansion, as quantified by the volume   . To verify this hypothesis, we have run all the simulations keeping constant that parameter, and, therefore, the equilibrium contour $F_0(z)$. The results are shown in the right-hand graph of Figure 8.6. The normalized free surface deformations fall on a single curve $\mathcal{F}(z)$, which indicates that $F_b(z) - F_0(z) = Ca\,\mathcal{F}$ for $Ca \lesssim 0.1$ (provided that the volume remains constant). This means that the dynamical free surface deformation can be seen as a linear steady perturbation with respect to the liquid bridge equilibrium shape. We have explored the validity of the above linear relationship by conducting simulations with larger values of the Capillary number

(applied temperature difference). The above linear law underestimates the dynamical free surface deformation for $Ca \gtrsim 0.15$, which corresponds to the supercritical regime.

tr
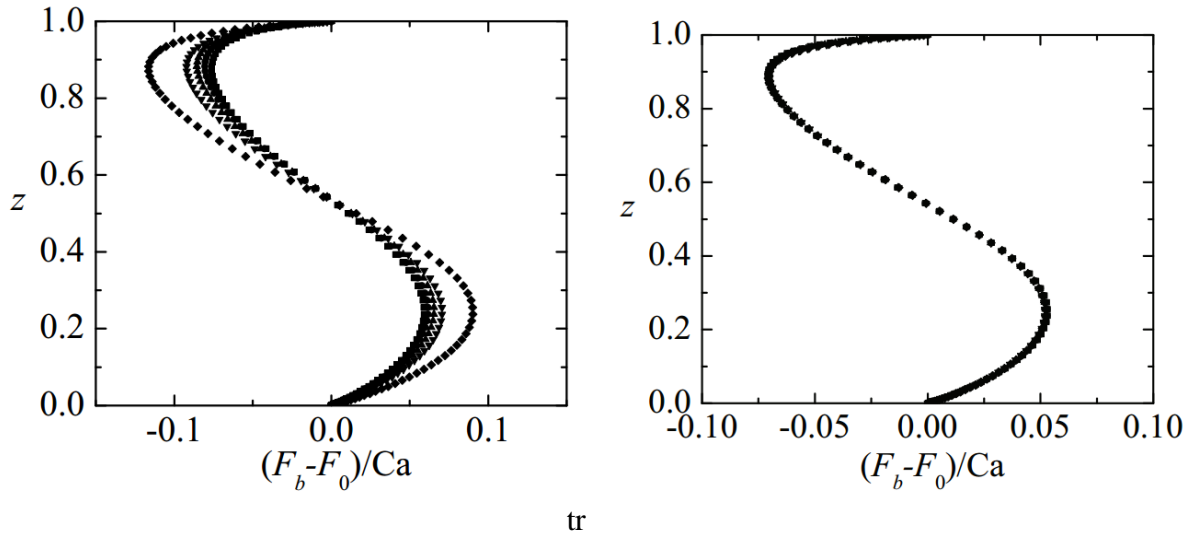
Figure 8.6 (Left) Free Surface deformation normalized with the Capillary number, $(F_b - F_0)/Ca$, for the configurations considered in Figure 8.5: $\{AR = 0.615, Pr = 67, \alpha_v = 5.892, Fr = 1.973 \times 10^4, \Theta_{amb} = 0, Bi = 0.15\}$ and $\{\mathcal{V} = 0.8200, Gr = 117.4, Ma = 3.885x10^3, Ca = 0.0182, T_0^* = 4.579\}$ (diamonds), $\{\mathcal{V} = 0.8241, Gr = 237.7, Ma = 7.863x10^3, Ca = 0.0369, T_0^* = 2.262\}$ (down-triangles), $\{\mathcal{V} = 0.8265, Gr = 326.9, Ma = 1.082x10^4, Ca = 0.0508, T_0^* = 1.645\}$ (up-triangles), $\{\mathcal{V} = 0.8298, Gr = 468, Ma = 1.549x10^4, Ca = 0.0727, T_0^* = 1.149\}$ (circles) and $\{\mathcal{V} = 0.8405, Gr = 544.8, Ma = 1.803x10^4, Ca = 0.0846, T_0^* = 0.987\}$ (squares).

Figure 8.7. (Left-hand image) Isolines of kinetic energy $1/2(\widehat{U}^2 + \widehat{V}^2 + \widehat{W}^2)$ (left) and magnitude of $|\hat{p}|$ of reduced pressure (right). (Right-hand image) Isolines of magnitude of the temperature field, $|\widehat{\Theta}(r,z)|$ (left), and amplitude $|\widehat{F}(z)|$ of the free surface oscillation. The latter has been magnified to show clearly its axial dependence. The results correspond to the eigenmode $m = 1$ responsible for instability at $\{AR = 0.615, Pr = 67, \alpha_v = 5.892, Fr = 1.973 \times 10^4, \Theta_{amb} = 0, Bi = 0.15\}$ and $\{\mathcal{V} = 0.828, Gr = 350.2, Ma = 1.159x10^4, Ca = 0.0544, T_0^* = 1.535\}$

Figure 7 shows the spatial structure of the dominant eigenmode for the marginally stable base flow of the experimental run analyzed in this section. The perturbation kinetic energy sharply increases in the region next to the free surface where the liquid flows between the two vortices driven by the Marangoni stress (Figure 8.4). The magnitude of the reduced pressure perturbation increases close to the triple contact line anchored to the upper rod. The upper part of the free surface oscillates more than the lower part. The shape of the free surface oscillation amplitude is very akin to that measured experimentally by Ferrera et al. [206] under similar conditions (see Fig. 9 of that

reference). It also resembles the experimental results obtained more recently by Yano et al. [207] for the oscillatory Marangoni convection under microgravity conditions (see Fig. 10 of that reference). It must be pointed out that the linear stability analysis cannot predict the magnitude of the free surface oscillations, but only the relative dependence of the amplitude with respect to the axial coordinate.
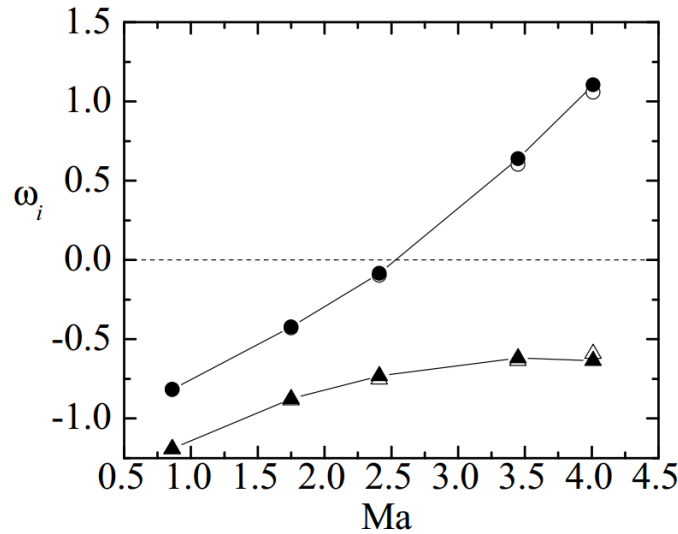
Figure 8.8 Eigenvalues characterizing the m=1 (circles) and 2 (triangles) linear modes for the configurations considered in Figure 8.5: $\{AR = 0.615, Pr = 67, \alpha_v = 5.892, Fr = 1.973 \times 10^4, \Theta_{amb} = 0, Bi = 0.15\}$ and $\{V = 0.8200, Gr = 117.4, Ma = 3.885x10^3, Ca = 0.0182, T_0^* = 4.579\}$, $\{V = 0.8241, Gr = 237.7, Ma = 7.863x10^3, Ca = 0.0369, T_0^* = 2.262\}$, $\{V = 0.8265, Gr = 326.9, Ma = 1.082x10^4, Ca = 0.0508, T_0^* = 1.645\}$, $\{V = 0.8298, Gr = 468, Ma = 1.549x10^4, Ca = 0.0727, T_0^* = 1.149\}$ and $\{V = 0.8405, Gr = 544.8, Ma = 1.803x10^4, Ca = 0.0846, T_0^* = 0.987\}$. The open and solid symbols were calculated with dynamical free surface deformation and the equilibrium contour, respectively.

Figure 8.8 shows the eigenvalues characterizing the $m = 1$ and 2 linear modes for the liquid bridge in Figure 8.5 at the marginal stability. The solid symbols are the results calculated when the free surface contour is assumed to be rigid and the same as that at equilibrium ($\Delta T = 0$). As can be observed, there is no signicant influence of the dynamical free surface deformation on the liquid bridge stability: the growth factors of both the $m = 1$ and $m = 2$ modes are hardly affected by that deformation.

In order to extend our analysis to a variety of liquid bridge shapes, we simulated the same experimental run as that analyzed in this section but with different diameters of the supporting rods (aspect ratios) and the same dimensionless volume $V = 1$ (neglecting the increase of volume due to thermal expansion).
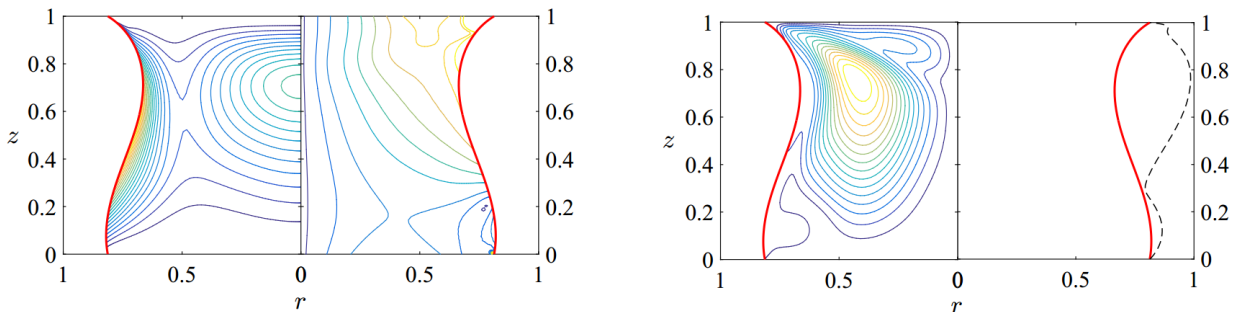
Figure 8.9 shows the spatial dependence of both the temperature field perturbation and the amplitude of the free surface oscillation for marginally stable liquid bridges. The location of the temperature perturbation maximum moves away from the upper rod as the aspect ratio decreases for $AR \geq 0.75$ (lower graphs). However, the height of that point exhibits a non-monotonous behavior for $AR \leq 0.615$. The amplitude of the free surface oscillation in the liquid bridge upper part increases with AR, i.e., with the deformation of the base flow free surface with respect to the cylinder. In fact, the upper part of the free surface oscillates more than the lower part for well-deformed equilibrium shapes (large values of AR).

Finally, we verified whether the dynamical free surface deformation affects the thermal convection stability for different aspect ratios. Figure 8.10 shows the critical Marangoni number and oscillation frequency obtained with both the dynamical free surface deformation and the rigid free surface approximation. As can be observed, there is little influence of the dynamical free surface deformation on the liquid bridge stability for the all the aspect ratios considered.
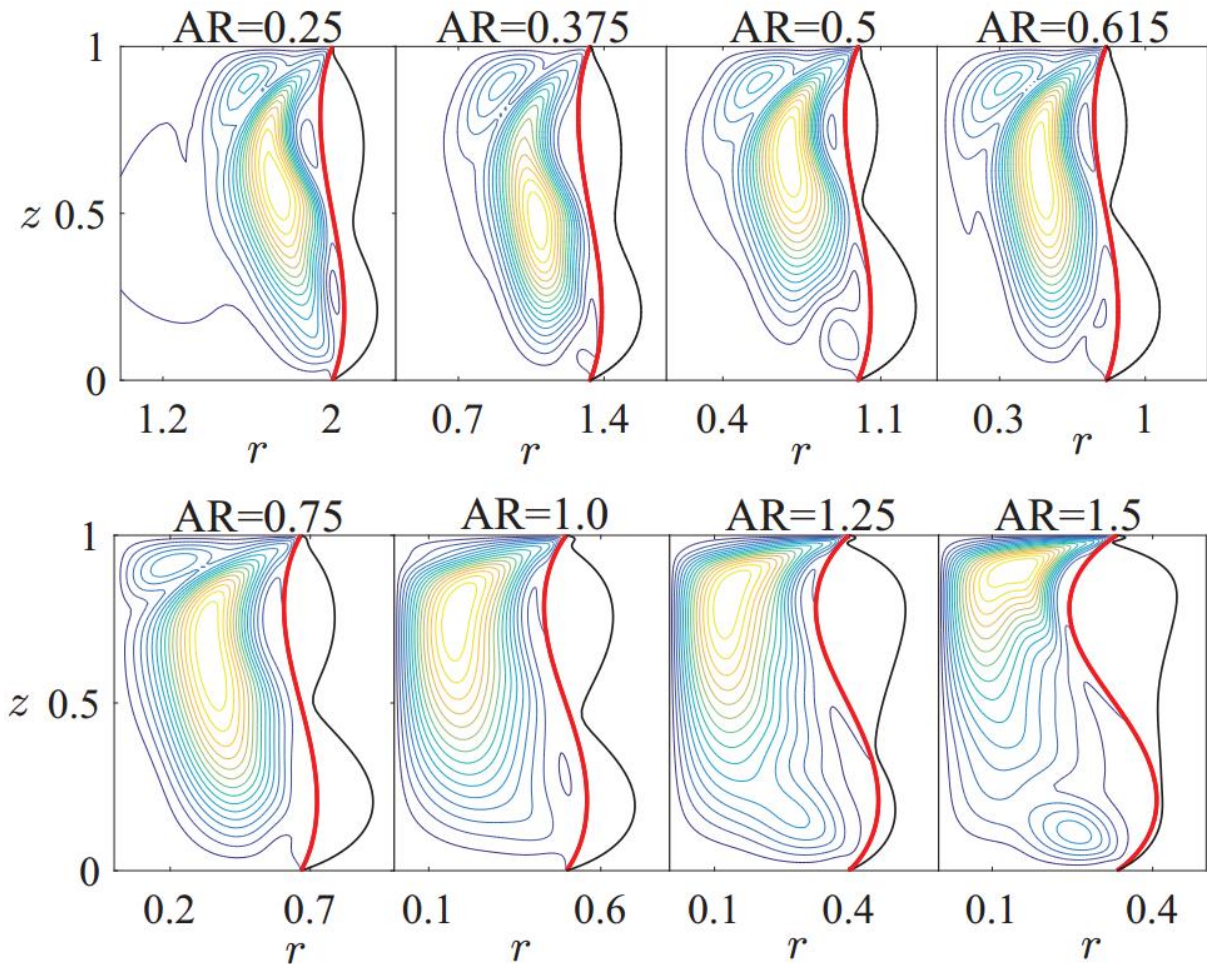
Figure 8.9 Spatial dependence of the temperature field perturbation and free surface oscillation amplitude for marginally stable liquid bridges with different aspect ratios. The calculations were conducted for 5-cSt silicone oil liquid bridges with $L = 3.69$ mm and $\mathcal{V} = 1$. The free surface oscillation amplitude has been magnified to show clearly its axial dependence.
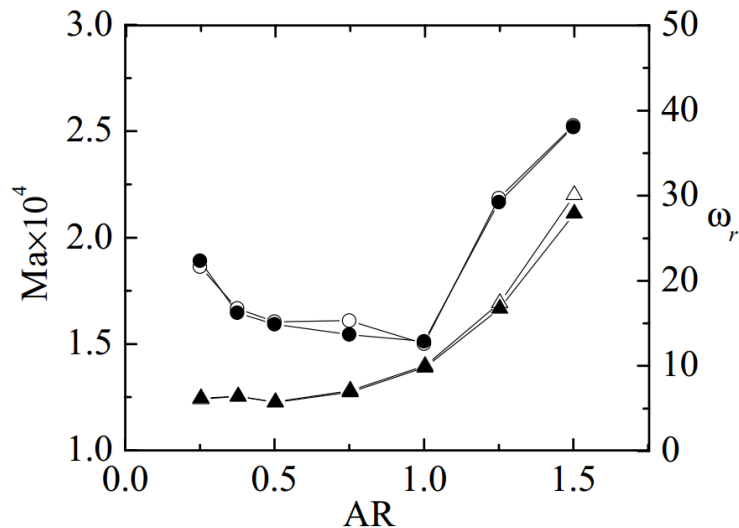
Figure 8.10 Critical Marangoni number Ma (circles) and oscillation frequency ω_r (triangles) as a function of the aspect ratio AR for 5-cSt silicone oil liquid bridges with $L = 3.69$ mm and $\mathcal{V} = 1$. The results were calculated with the dynamical free surface deformation (open symbols) and the rigid free surface approximation (solid symbols).

8.5. Conclusions

In this investigation, we have studied numerically the thermal convection in liquid bridges with high Prandtl numbers. Both the base flow and its eigenmodes have been calculated accounting for the effect of the dynamical free surface deformation. This includes not only the steady axisymmetric deformation caused by the base flow, but also the small-amplitude non-axisymmetric oscillations produced by the growth/decay of the linear modes. We have restricted ourselves to the parameter space corresponding to 5-cSt silicone oil liquid bridges due to its popularity among experimentalists. The comparison between the linear stability analysis predictions and the experimental results measured on board of the ISS (Nishino et al., [222]) shows reasonable agreement, similar to that exhibited by the numerical calculations of Nishino et al. [222].

Our efforts have mainly focused on reproducing a representative experimental run among those conducted in Ref. (Montanero et al., [205]), where the dynamical free surface deformation was accurately measured. We find good agreement between the numerical and experimental results for both the dynamical free surface deformation and the critical Marangoni number. If the deformations caused by the base flows are normalized with the corresponding values of the Capillary number, they approximately collapse onto a single curve. This means that the dynamical free surface deformation can be seen as a steady perturbation with respect to the equilibrium shape, which increases linearly with the Capillary number.

We have described the complex spatial structure of the dominant eigenmode responsible for instability. The amplitude of the free surface oscillation is very similar to that measured by Ferrera et al. [206]. We have described the dependence of both the temperature field perturbation and free surface oscillation amplitude upon the liquid bridge aspect ratio.

One of the major conclusions of the present work is the fact that the dynamical free surface deformation has little effect on the eigenvalues characterizing the linear modes, and, therefore, on the thermal convection stability. Considering the liquid bridge free surface as a rigid boundary constitutes an accurate approximation. This conclusion must not be necessarily expected given the complex structure of the base flow next to the free surface, especially in the vicinity of the upper hot rod.

BIBLIOGRAPHY

[1]   M. A. Herrada and J. M. Montanero, "A numerical method to study the dynamics of capillary fluid systems," *J. Comput. Phys.*, vol. 306, pp. 137–147, Feb. 2016.

[2]   J.-C. Tsai *et al.*, "Vortex-induced morphology on a two-fluid interface and the transitions," *Phys. Rev. E*, vol. 92, no. 3, p. 031002, Sep. 2015.

[3]   S. Fujimoto and Y. Takeda, "Topology changes of the interface between two immiscible liquid layers by a rotating lid," *Phys. Rev. E*, vol. 80, no. 1, p. 015304, Jul. 2009.

[4]   C. E. Brennen, *Fundamentals of multiphase flow*. Cambridge: Cambridge University Press, 2005.

[5]   C. T. Crowe, J. D. Schwarzkopf, M. Sommerfeld, and Y. Tsuji, *Multiphase Flows with droplets and particles*, Second Ed. Boca Raton: CRC Press, 2012.

[6]   Y. Taitel and D. Barnea, "Two-Phase Slug Flow," *Adv. Heat Transf.*, vol. 20, no. C, pp. 83–132, 1990.

[7]   G. F. Hewitt and N. S. Hall-Taylor, *Annular Two-phase Flow*, First Ed. Edinburgh: Pergamon Press, 1970.

[8]   W. D. Bachalo, "Experimental methods in multiphase flows," *Int. J. Multiph. Flow*, vol. 20, no. SUPPL. 1, pp. 261–295, 1994.

[9]   O. Shoham and Society of Petroleum Engineers of AIME., *Mechanistic modeling of gas-liquid two-phase flow in pipes*. Society of Petroleum Engineers, 2006.

[10]   A. Prosperetti and G. Tryggvason, *Computational Methods of Multiphase Flow*. New York: Cambridge University Press, 2007.

[11]   S. Chandrasekhar, *Hydrodynamic and hydromagnetic stability*. New York: Dover Publications, 2013.

[12]   W. Criminale, T. Jackson, R. Joslin, and R. Joslin, *Theory and computation of hydrodynamic stability*. Cambridge: Cambridge University Press, 2003.

[13]   P. Drazin and W. Reid, *Hydrodynamic stability*, 2nd edn. Cambridge: Cambridge University Press, 2004.

[14]   M. Ishii and T. Hibiki, *Thermo-fluid dynamics of two-phase flow*. Springer, 2011.

[15]   M. P. Juniper, A. Hanifi, and V. Theofilis, "Modal Stability Theory," *Appl. Mech. Rev.*, vol. 66, no. 2, p. 024804, Mar. 2014.

[16]   H. F. FASEL, U. RIST, and U. KONZELMANN, "Numerical investigation of the three-dimensional development in boundary-layer transition," *AIAA J.*, vol. 28, no. 1, pp. 29–37, Jan. 1990.

[17]   L. Kleiser and T. A. Zang, "Numerical Simulation of Transition in Wall-Bounded Shear Flows," *Annu. Rev. Fluid Mech.*, vol. 23, no. 1, pp. 495–537, Jan. 1991.

[18]   F. Charru and P. de Forcrand-Millard, *Hydrodynamic Instabilities*. Cambridge: Cambridge University Press, 2011.

[19]   Lord Rayleigh, "On The Instability Of Jets," *Proc. London Math. Soc.*, vol. s1-10, no. 1, pp. 4–13, Nov. 1878.

[20]   P. Huerre, "Spatio-Temporal Instabilities in Closed and Open Flows," in *Instabilities and*

Nonequilibrium Structures, Dordrecht: Springer Netherlands, 1987, pp. 141–177.

[21]   A. Georgescu, *Hydrodynamic stability theory*, vol. 9. Dordrecht: Springer Netherlands, 1985.

[22]   S. (Subrahmanyan) Chandrasekhar, *Hydrodynamic and hydromagnetic stability*. Dover Publications, 1981.

[23]   P. Huerre and P. A. Monkewitz, "Local and Global Instabilities in Spatially Developing Flows," *Annu. Rev. Fluid Mech.*, vol. 22, no. 1, pp. 473–537, Jan. 1990.

[24]   T. Herbert, "PARABOLIZED STABILITY EQUATIONS," *Annu. Rev. Fluid Mech.*, vol. 29, no. 1, pp. 245–283, Jan. 1997.

[25]   C. C. Yen and N. L. Messersmith, "Application of Parabolized Stability Equations to the Prediction of Jet Instabilities," *AIAA J.*, vol. 36, no. 8, pp. 1541–1544, Aug. 1998.

[26]   F. P. Bertolotti and T. Herbert, "Analysis of the linear stability of compressible boundary layers using the PSE," *Theor. Comput. Fluid Dyn.*, vol. 3, no. 2, pp. 117–124, Nov. 1991.

[27]   Y. Zhang and H. Zhou, "Verification of parabolized stability equations for its application to compressible boundary layers," *Appl. Math. Mech.*, vol. 28, no. 8, pp. 987–998, Aug. 2007.

[28]   P. Moin and K. Mahesh, "DIRECT NUMERICAL SIMULATION: A Tool in Turbulence Research," *Annu. Rev. Fluid Mech.*, vol. 30, no. 1, pp. 539–578, Jan. 1998.

[29]   M. R. Malik, "Hypersonic Flight Transition Data Analysis Using Parabolized Stability Equations with Chemistry Effects," *J. Spacecr. Rockets*, vol. 40, no. 3, pp. 332–344, May 2003.

[30]   M. A. Herrada, C. Del Pino, and R. Fernandez-Feria, "Stability of the boundary layer flow on a long thin rotating cylinder," *Phys. Fluids*, vol. 20, no. 3, p. 034105, Mar. 2008.

[31]   V. Theofilis, "Global Linear Instability," *Annu. Rev. Fluid Mech.*, vol. 43, no. 1, pp. 319–352, Jan. 2011.

[32]   V. Theofilis, "Advances in global linear instability analysis of nonparallel and three-dimensional flows," *Prog. Aerosp. Sci.*, vol. 39, no. 4, pp. 249–315, May 2003.

[33]   R. T. Pierrehumbert, "Universal Short-Wave Instability of Two-Dimensional Eddies in an Inviscid Fluid," *Phys. Rev. Lett.*, vol. 57, no. 17, pp. 2157–2159, Oct. 1986.

[34]   R.-S. Lin and M. R. Malik, "On the stability of attachment-line boundary layers. Part 1. The incompressible swept Hiemenz flow," *J. Fluid Mech.*, vol. 311, no. 1, p. 239, Mar. 1996.

[35]   R. S. Heeg and B. J. Geurts, "Spatial Instabilities of the Incompressible Attachment-Line Flow Using Sparse Matrix Jacobi–Davidson Techniques," *Appl. Sci. Res.*, vol. 59, no. 4, pp. 315–329, 1997.

[36]   J. de Vicente, J. Basley, F. Meseguer-Garrido, J. Soria, and V. Theofilis, "Three-dimensional instabilities over a rectangular open cavity: from linear stability analysis to experimentation," *J. Fluid Mech.*, vol. 748, pp. 189–220, Jun. 2014.

[37]   G. A. BRÈS and T. COLONIUS, "Three-dimensional instabilities in compressible flow over open cavities," *J. Fluid Mech.*, vol. 599, pp. 309–339, Mar. 2008.

[38]   T. Tatsumi and T. Yoshimura, "Stability of the laminar flow in a rectangular duct," *J. Fluid Mech.*, vol. 212, no. 1, p. 437, Mar. 1990.

[39]   R. R. Kerswell and A. Davey, "On the linear instability of elliptic pipe flow," *J. Fluid Mech.*, vol. 316, no. 1, p. 307, Jun. 1996.

[40]   F. GIANNETTI and P. LUCHINI, "Structural sensitivity of the first instability of the cylinder wake," *J. Fluid Mech.*, vol. 581, p. 167, Jun. 2007.

[41]   R. Natarajan and A. Acrivos, "The instability of the steady flow past spheres and disks," *J.*

Fluid Mech., vol. 254, no. 1, p. 323, Sep. 1993.

[42] J.-C. Tsao, A. Rothmayer, and A. Ruban, "Stability of air flow past thin liquid films on airfoils," in *Theroretical Fluid Mechanics Conference*, 1996.

[43] A. Tezuka and K. Suzuki, "Three-Dimensional Global Linear Stability Analysis of Flow Around a Spheroid," *AIAA J.*, vol. 44, no. 8, pp. 1697–1708, Aug. 2006.

[44] S. BAGHERI, P. SCHLATTER, P. J. SCHMID, and D. S. HENNINGSON, "Global stability of a jet in crossflow," *J. Fluid Mech.*, vol. 624, p. 33, Apr. 2009.

[45] F. Giannetti, P. Luchini, and L. Marino, "Linear stability analysis of three-dimensional lid-driven cavity flow," *Atti 19th Congr. AIMETA Mecc. Teor. Appl., Ancona, Italy, Art. No. 738. Ancona, Italy Aras Ed.*, 2009.

[46] G. Lian, C. Thornton, and M. J. Adams, "A Theoretical Study of the Liquid Bridge Forces between Two Rigid Spherical Bodies," *J. Colloid Interface Sci.*, vol. 161, no. 1, pp. 138–147, Nov. 1993.

[47] S. L. Anna, N. Bontoux, and H. A. Stone, "Formation of dispersions using 'flow focusing' in microchannels," *Appl. Phys. Lett.*, vol. 82, no. 3, pp. 364–366, Jan. 2003.

[48] A. M. Gañán-Calvo and J. M. Gordillo, "Perfectly Monodisperse Microbubbling by Capillary Flow Focusing," *Phys. Rev. Lett.*, vol. 87, no. 27, p. 274501, Dec. 2001.

[49] Z.-M. Huang, Y.-Z. Zhang, M. Kotaki, and S. Ramakrishna, "A review on polymer nanofibers by electrospinning and their applications in nanocomposites," *Compos. Sci. Technol.*, vol. 63, no. 15, pp. 2223–2253, Nov. 2003.

[50] J. Doshi and D. H. Reneker, "Electrospinning process and applications of electrospun fibers," *J. Electrostat.*, vol. 35, no. 2–3, pp. 151–160, Aug. 1995.

[51] K. Liow, B. Tan, … G. T.-M. P. L., and U. 2009, "CFD modeling of the steady-state momentum and oxygen transport in a bioreactor that is driven by an aerial rotating disk," *Mod. Phys. Lett. B*, vol. 23, no. 2, pp. 121–127, 2009.

[52] M. A. Herrada, A. M. Gañán-Calvo, and P. Guillot, "Spatiotemporal instability of a confined capillary jet," *Phys. Rev. E*, vol. 78, no. 4, p. 046312, Oct. 2008.

[53] J. M. GORDILLO, M. PÉREZ-SABORID, and A. M. GAÑÁN-CALVO, "Linear stability of co-flowing liquid–gas jets," *J. Fluid Mech.*, vol. 448, pp. 23–51, Dec. 2001.

[54] A. Sevilla, "The effect of viscous relaxation on the spatiotemporal stability of capillary jets," *J. Fluid Mech.*, vol. 684, pp. 204–226, Oct. 2011.

[55] E. Castro-Hernández, F. Campo-Cortés, and J. M. Gordillo, "Slender-body theory for the generation of micrometre-sized emulsions through tip streaming," *J. Fluid Mech.*, vol. 698, pp. 423–445, 2012.

[56] G. I. Taylor, "Conical free surfaces and fluid interfaces," in *Applied Mechanics*, Berlin, Heidelberg: Springer Berlin Heidelberg, 1966, pp. 790–796.

[57] J. M. Gordillo, A. Sevilla, and F. Campo-Cortés, "Global stability of stretched jets: conditions for the generation of monodisperse micro-emulsions using coflows," *J. Fluid Mech.*, vol. 738, pp. 335–357, 2014.

[58] M. Rubio-Rubio, A. Sevilla, and J. M. Gordillo, "On the thinnest steady threads obtained by gravitational stretching of capillary jets," *J. Fluid Mech.*, vol. 729, pp. 471–483, Aug. 2013.

[59] J. Eggers and T. F. Dupont, "Drop formation in a one-dimensional approximation of the Navier–Stokes equation," *J. Fluid Mech.*, vol. 262, pp. 205–221, Oct. 1994.

[60] F. J. García and A. Castellanos, "One- dimensional models for slender axisymmetric viscous liquid jets," *Phys. Fluids*, vol. 6, no. 8, pp. 2676–2689, Aug. 1994.

[61]   A. Prosperetti and G. Tryggvason, *Computational Methods for Multiphase Flow*. Cambridge: Cambridge University Press, 2007.

[62]   C. . Hirt and B. . Nichols, "Volume of fluid (VOF) method for the dynamics of free boundaries," *J. Comput. Phys.*, vol. 39, no. 1, pp. 201–225, Jan. 1981.

[63]   K. M. T. Kleefsman, G. Fekken, A. E. P. Veldman, B. Iwanowski, and B. Buchner, "A Volume-of-Fluid based simulation method for wave impact problems," *J. Comput. Phys.*, vol. 206, no. 1, pp. 363–393, Jun. 2005.

[64]   J. H. Jeong and D. Y. Yang, "Finite element analysis of transient fluid flow with free surface using VOF (volume-of-fluid) method and adaptive grid," *Int. J. Numer. Methods Fluids*, vol. 26, no. 10, pp. 1127–1154, Jun. 1998.

[65]   S. Osher and J. A. Sethian, "Fronts propagating with curvature-dependent speed: Algorithms based on Hamilton-Jacobi formulations," *J. Comput. Phys.*, vol. 79, no. 1, pp. 12–49, Nov. 1988.

[66]   J. A. Sethian, "A fast marching level set method for monotonically advancing fronts.," *Proc. Natl. Acad. Sci. U. S. A.*, vol. 93, no. 4, pp. 1591–5, Feb. 1996.

[67]   T. Ménard, S. Tanguy, and A. Berlemont, "Coupling level set/VOF/ghost fluid methods: Validation and application to 3D simulation of the primary break-up of a liquid jet," *Int. J. Multiph. Flow*, vol. 33, no. 5, pp. 510–524, May 2007.

[68]   M. Sussman and E. G. Puckett, "A Coupled Level Set and Volume-of-Fluid Method for Computing 3D and Axisymmetric Incompressible Two-Phase Flows," *J. Comput. Phys.*, vol. 162, no. 2, pp. 301–337, Aug. 2000.

[69]   T. Yabe, F. Xiao, and T. Utsumi, "The Constrained Interpolation Profile Method for Multiphase Analysis," *J. Comput. Phys.*, vol. 169, no. 2, pp. 556–593, May 2001.

[70]   D. Jacqmin, "Calculation of Two-Phase Navier–Stokes Flows Using Phase-Field Modeling," *J. Comput. Phys.*, vol. 155, no. 1, pp. 96–127, Oct. 1999.

[71]   S. McKee *et al.*, "The MAC method," *Comput. Fluids*, vol. 37, no. 8, pp. 907–930, Sep. 2008.

[72]   G. Tryggvason *et al.*, "A Front-Tracking Method for the Computations of Multiphase Flow," *J. Comput. Phys.*, vol. 169, no. 2, pp. 708–759, May 2001.

[73]   K. H. Bendiksen, D. Maines, R. Moe, and S. Nuland, "The Dynamic Two-Fluid Model OLGA: Theory and Application," *SPE Prod. Eng.*, vol. 6, no. 02, pp. 171–180, May 1991.

[74]   M. Ishii and K. Mishima, "Two-fluid model and hydrodynamic constitutive relations," *Nucl. Eng. Des.*, vol. 82, no. 2–3, pp. 107–126, Oct. 1984.

[75]   M. Ishii and T. Hibiki, *Thermo-fluid dynamics of two-phase flow*. Springer, 2011.

[76]   G. R. Liu and M. B. Liu, *Smoothed Particle Hydrodynamics*. WORLD SCIENTIFIC, 2003.

[77]   R. A. Gingold and J. J. Monaghan, "Smoothed particle hydrodynamics: theory and application to non-spherical stars," *Mon. Not. R. Astron. Soc.*, vol. 181, no. 3, pp. 375–389, Dec. 1977.

[78]   J. J. Monaghan and A. Kocharyan, "SPH simulation of multi-phase flow," *Comput. Phys. Commun.*, vol. 87, no. 1–2, pp. 225–235, May 1995.

[79]   S. Chen and G. D. Doolen, "LATTICE BOLTZMANN METHOD FOR FLUID FLOWS," *Annu. Rev. Fluid Mech.*, vol. 30, no. 1, pp. 329–364, Jan. 1998.

[80]   X. He and L.-S. Luo, "Theory of the lattice Boltzmann method: From the Boltzmann equation to the lattice Boltzmann equation," *Phys. Rev. E*, vol. 56, no. 6, pp. 6811–6817, Dec. 1997.

[81]   Q. Li, K. H. Luo, Q. J. Kang, Y. L. He, Q. Chen, and Q. Liu, "Lattice Boltzmann methods for multiphase flow and phase-change heat transfer," *Prog. Energy Combust. Sci.*, vol. 52, pp. 62–105, Feb. 2016.

[82] X. He, S. Chen, and R. Zhang, "A Lattice Boltzmann Scheme for Incompressible Multiphase Flow and Its Application in Simulation of Rayleigh–Taylor Instability," *J. Comput. Phys.*, vol. 152, no. 2, pp. 642–663, Jul. 1999.

[83] L. Chen, Q. Kang, Y. Mu, Y.-L. He, and W.-Q. Tao, "A critical review of the pseudopotential multiphase lattice Boltzmann model: Methods and applications," *Int. J. Heat Mass Transf.*, vol. 76, pp. 210–236, Sep. 2014.

[84] A. K. Gunstensen, D. H. Rothman, S. Zaleski, and G. Zanetti, "Lattice Boltzmann model of immiscible fluids," *Phys. Rev. A*, vol. 43, no. 8, pp. 4320–4327, Apr. 1991.

[85] M. J. Fritts, D. E. Fyfe, and E. S. Oran, "Numerical Simulations of Fuel Droplet Flows Using a Lagrangian Triangular Mesh.," *NASA CR-168263*, 1984.

[86] L. Lee and R. J. LeVeque, "An Immersed Interface Method for Incompressible Navier--Stokes Equations," *SIAM J. Sci. Comput.*, vol. 25, no. 3, pp. 832–856, Jan. 2003.

[87] J. F. Thompson, Z. U. . Warsi, and C. Wayne Mastin, "Boundary-fitted coordinate systems for numerical solution of partial differential equations—A review," *J. Comput. Phys.*, vol. 47, no. 1, pp. 1–108, Jul. 1982.

[88] T. J. Chung, *Computational fluid dynamics*. Cambridge University Press, 2010.

[89] S. Shiratori, H. C. Kuhlmann, and T. Hibiya, "Linear stability of thermocapillary flow in partially confined half-zones," *Phys. Fluids*, vol. 19, no. 4, p. 044103, Apr. 2007.

[90] M. Morzynski and F. Thiele, "Numerical stability analysis of a flow about a cylinder," *Zeitschrift für Angew. Math. und Mech.*, vol. 71, pp. T424–T428, 1991.

[91] G. A. BRÈS and T. COLONIUS, "Three-dimensional instabilities in compressible flow over open cavities," *J. Fluid Mech.*, vol. 599, pp. 309–339, Mar. 2008.

[92] C. J. Mack and P. J. Schmid, "A preconditioned Krylov technique for global hydrodynamic stability analysis of large-scale compressible flows," *J. Comput. Phys.*, vol. 229, no. 3, pp. 541–560, Feb. 2010.

[93] Y. Ding and M. Kawahara, "Three-dimensional linear stability analysis of incompressible viscous flows using the finite element method," *Int. J. Numer. Methods Fluids*, vol. 31, no. 2, pp. 451–479, Sep. 1999.

[94] L. González, V. Theofilis, and R. Gómez-Blanco, "Finite Element Methods for Viscous Incompressible BiGlobal Instability Analysis on Unstructured Meshes," *AIAA J.*, vol. 45, no. 4, pp. 840–854, Apr. 2007.

[95] M. Morzynski and F. Thiele, "Finite Element Method for Global Stability Analysis of 3D Flow," in *4th Flow Control Conference*, 2008.

[96] Y. Ding and M. Kawahara, "Linear Stability of Incompressible Flow Using a Mixed Finite Element Method," *J. Comput. Phys.*, vol. 139, no. 2, pp. 243–273, Jan. 1998.

[97] M. Sahin and R. G. Owens, "A novel fully-implicit finite volume method applied to the lid-driven cavity problems Part II: Linear stability analysis," *Int. J. Numer. Methods Fluids*, vol. 42, no. 1, pp. 79–88, May 2003.

[98] A. Y. Gelfgat, "Stability of convective flows in cavities: solution of benchmark problems by a low-order finite volume method," *Int. J. Numer. Methods Fluids*, vol. 53, no. 3, pp. 485–506, Jan. 2007.

[99] M. Sahin and H. J. Wilson, "A parallel adaptive unstructured finite volume method for linear stability (normal mode) analysis of viscoelastic fluid flows," *J. Nonnewton. Fluid Mech.*, vol. 155, no. 1–2, pp. 1–14, Nov. 2008.

[100] H. A. Dijkstra, "On the structure of cellular solutions in Rayleigh–Bénard–Marangoni flows in small-aspect-ratio containers," *J. Fluid Mech.*, vol. 243, no. 1, p. 73, Oct. 1992.

[101] M. Y. Hussaini, D. A. Kopriva, and A. T. Patera, "Spectral collocation methods," *Appl. Numer. Math.*, vol. 5, no. 3, pp. 177–208, May 1989.

[102] R. T. Pierrehumbert and S. E. Widnall, "The two- and three-dimensional instabilities of a spatially periodic shear layer," *J. Fluid Mech.*, vol. 114, no. 1, p. 59, Jan. 1982.

[103] A. Zebib, "Stability of viscous flow past a circular cylinder," *J. Eng. Math.*, vol. 21, no. 2, pp. 155–165, 1987.

[104] D. Rodríguez and V. Theofilis, "Massively Parallel Solution of the BiGlobal Eigenvalue Problem Using Dense Linear Algebra," *AIAA J.*, vol. 47, no. 10, pp. 2449–2459, Oct. 2009.

[105] J. M. B. N.Syred, "Combustion in swirling flows: a review," *Combust. Flame*, vol. 23, pp. 143–201, 1974.

[106] P. J. Zandbergen and D. Dijkstra, "Von Karman Swirling Flows," *Annu. Rev. Fluid Mech.*, vol. 19, no. 1, pp. 465–491, Jan. 1987.

[107] M.P. Escudier; J. Keller, "Recirculation in swirling flow-a manifestation of vortex breakdown," *AIAA J.*, vol. 23, no. 1, pp. 111–116, 1985.

[108] M. P. Escudier, "Vortex breakdown: Observations and explanations," *Prog. Aerosp. Sci.*, vol. 25, pp. 189–229, 1988.

[109] V. N. Shtern, *Counterflows: Paradoxical fluid mechanics phenomena*. New York: Cambridge University Press, 2012.

[110] V. Shtern and F. Hussain, "Collapse, symmetry breaking, and hysteresis in swirling flows," *Annu. Rev. Fluid Mech.*, vol. 31, no. 1, pp. 537–566, Jan. 1999.

[111] Peckham D.H and Atkinson S.A., "Preliminary results of low speed wind tunnel tests on a gothic wing of aspect ratio 1.0," *A.R.C. Tech. Rep. C.P.*, no. No. 508. TN No. Aero. 2504, 1957.

[112] V. S. and A. Borissov, "Counter-flow driven by swirl decay," *Phys. Fluids*, vol. 22, p. 034107, 2010.

[113] M. A. Herrada, V. N. Shtern, and M. M. Torregrosa, "The instability nature of the Vogel–Escudier flow," *J. Fluid Mech.*, vol. 766, pp. 590–610, Mar. 2015.

[114] V. N. Shtern, M. del Mar Torregrosa, and M. A. Herrada, "Effect of swirl decay on vortex breakdown in a confined steady axisymmetric flow," *Phys. Fluids*, vol. 24, no. 4, p. 043601, Apr. 2012.

[115] D. Lo Jacono, M. Nazarinia, and M. Brøns, "Experimental vortex breakdown topology in a cylinder with a free surface," *Phys. Fluids*, vol. 21, no. 11, p. 111704, Nov. 2009.

[116] P. T. Brady, M. Herrmann, and J. M. Lopez, "Two-fluid confined flow in a cylinder driven by a rotating end wall," *Phys. Rev. E*, vol. 85, no. 1, p. 016308, Jan. 2012.

[117] P. T. Brady, M. Herrmann, and J. M. Lopez, "Addendum to 'Two-fluid confined flow in a cylinder driven by a rotating endwall,'" *Phys. Rev. E*, vol. 85, no. 6, p. 067301, Jun. 2012.

[118] M. A. Herrada, V. N. Shtern, and J. M. López-Herrera, "Vortex breakdown in a water-spout flow," *Phys. Fluids*, vol. 25, no. 9, p. 093604, Sep. 2013.

[119] A. Y. Gelfgat, P. Z. BarYoseph, and A. Solan, "Stability of confined swirling flow with and without vortex breakdown," *J. Fluid Mech.*, vol. 311, pp. 1–36, 1996.

[120] A. Y. Gelfgat, P. Z. BarYoseph, and A. Solan, "Three-dimensional instability of axisymmetric flow in a rotating lid–cylinder enclosure," *J. Fluid Mech.*, vol. 438, pp. 1–36, 2001.

[121] M. P. Escudier, "Observations of the flow produced in a cylindrical container by a rotating endwall," *Exp. Fluids*, vol. 2, no. 4, pp. 189–196, 1984.

[122] J. N. Sørensen, I. V. Naumov, and R. Mikkelsen, "Experimental investigation of three-dimensional flow instabilities in a rotating lid-driven cavity," *Exp. Fluids*, vol. 41, no. 3, pp. 425–440, Aug. 2006.

[123] J. N. Sørensen, A. Y. Gelfgat, I. V. Naumov, and R. F. Mikkelsen, "Experimental and numerical results on three-dimensional instabilities in a rotating disk–tall cylinder flow," *Phys. Fluids*, vol. 21, no. 5, p. 054102, May 2009.

[124] J. N. Sørensen, I. V. Naumov, and V. L. Okulov, "Multiple helical modes of vortex breakdown," *J. Fluid Mech.*, vol. 683, pp. 430–441, 2011.

[125] G. K. (George K. Batchelor, *An introduction to fluid dynamics*. Cambridge University Press, 1999.

[126] M. R. Khorrami, "A Chebyshev spectral collocation method using a staggered grid for the stability of cylindrical flows," *Int. J. Numer. Methods Fluids*, vol. 12, no. 9, pp. 825–833, May 1991.

[127] T. V. Kármán, "Über laminare und turbulente Reibung," *ZAMM - J. Appl. Math. Mech. / Zeitschrift für Angew. Math. und Mech.*, vol. 1, no. 4, pp. 233–252, Jan. 1921.

[128] K. Y. S. Liow, G. A. Thouas, B. T. Tan, M. C. Thompson, and K. Hourigan, "Modelling the Transport of Momentum and Oxygen in an Aerial-Disk Driven Bioreactor Used for Animal Tissue or Cell Culture," in *13th International Conference on Biomedical Engineering*, Berlin, Heidelberg: Springer Berlin Heidelberg, 2009, pp. 1672–1675.

[129] A. Balci, M. Brøns, M. A. Herrada, and V. N. Shtern, "Vortex breakdown in a truncated conical bioreactor," *Fluid Dyn. Res.*, vol. 47, no. 6, p. 065503, Dec. 2015.

[130] M. Herrada and V. Shtern, "Patterns of a creeping water-spout flow," *J. Fluid Mech.*, vol. 744, pp. 65–88, Apr. 2014.

[131] V. N. Shtern and A. A. Borissov, "Nature of counterflow and circulation in vortex separators," *Phys. Fluids*, vol. 22, no. 8, p. 083601, Aug. 2010.

[132] H. K. Moffatt, "Viscous and resistive eddies near a sharp corner," *J. Fluid Mech.*, vol. 18, no. 01, p. 1, Jan. 1964.

[133] V. Shtern, "Moffatt eddies at an interface," *Theor. Comput. Fluid Dyn.*, vol. 28, no. 6, pp. 651–656, Dec. 2014.

[134] U. T. Bödewadt, "Die Drehströmung über festem Grunde," *ZAMM - Zeitschrift für Angew. Math. und Mech.*, vol. 20, no. 5, pp. 241–253, Jan. 1940.

[135] L. Carrión, M. A. Herrada, and V. N. Shtern, "Instability of a water-spout flow," *Phys. Fluids*, vol. 28, no. 3, p. 034107, Mar. 2016.

[136] HU Vogel, "Experimentelle Ergebnisse über die laminare Strömung in einem Zylindrischen Gehäuse mit darin rotierender Scheibe," *Max-Planck-Institut für Strömungsforschung, Göttigen, Bericht. 6.*, 1968.

[137] J. M. Lopez, "Axisymmetric vortex breakdown Part 1. Confined swirling flow," *J. Fluid Mech.*, vol. 221, no. 1, p. 533, Dec. 1990.

[138] Y. A. Ramazanov, V. I. . Kislykh, I. P. . Kosyuk, N. V. . Bakuleva, and V. V. Shchurikhina, "Industrial Production of Vaccines Using Embryonic Cells in Gas-Vortex," in *In book "New Aspects of Biotechnology and Medicine,"* A. M. Egorov, Ed. 2007, pp. 87–91.

[139] J. M. Lopez, "Unsteady swirling flow in an enclosed cylinder with reflectional symmetry," *Phys. Fluids*, vol. 7, no. 11, pp. 2700–2714, Nov. 1995.

[140] R. Bouffanais and D. Lo Jacono, "Unsteady transitional swirling flow in the presence of a moving free surface," *Phys. Fluids*, vol. 21, no. 6, p. 064107, Jun. 2009.

[141] M. A. Herrada, V. N. Shtern, and J. M. López-Herrera, "Off-axis vortex breakdown in a shallow whirlpool," *Phys. Rev. E*, vol. 87, no. 6, p. 063016, Jun. 2013.

[142] J. Mougel, D. Fabre, and L. Lacaze, "Waves in Newton's bucket," *J. Fluid Mech.*, vol. 783, pp. 211–250, Nov. 2015.

[143] M. BRØNS, L. K. VOIGT, and J. N. SØRENSEN, "Topology of vortex breakdown bubbles in a cylinder with a rotating bottom and a free surface," *J. Fluid Mech.*, vol. 428, p. S0022112000002512, Feb. 2001.

[144] M. Brøns, "Topological fluid dynamics of interfacial flows," *Phys. Fluids*, vol. 6, no. 8, pp. 2730–2737, Aug. 1994.

[145] R. BERGMANN, L. TOPHØJ, T. A. M. HOMAN, P. HERSEN, A. ANDERSEN, and T. BOHR, "Polygon formation and surface flow on a rotating fluid surface," *J. Fluid Mech.*, vol. 679, pp. 415–431, Jul. 2011.

[146] L. Tophøj, J. Mougel, T. Bohr, and D. Fabre, "Rotating Polygon Instability of a Swirling Free Surface Flow," *Phys. Rev. Lett.*, vol. 110, no. 19, p. 194502, May 2013.

[147] S. Wakiya, "Axisymmetric flow of a viscous fluid near the vertex of a body," *J. Fluid Mech.*, vol. 78, no. 04, p. 737, Dec. 1976.

[148] A. Balci, M. Brøns, M. A. Herrada, and V. N. Shtern, "Patterns of a slow air–water flow in a semispherical container," *Eur. J. Mech. - B/Fluids*, vol. 58, pp. 1–8, Jul. 2016.

[149] A. H. Hirsa, J. M. Lopez, and R. Miraghaie, "Symmetry breaking to a rotating wave in a lid-driven cylinder with a free surface: Experimental observation," *Phys. Fluids*, vol. 14, no. 6, pp. L29–L32, Jun. 2002.

[150] J. M. LOPEZ, F. MARQUES, A. H. HIRSA, and R. MIRAGHAIE, "Symmetry breaking in free-surface cylinder flows," *J. Fluid Mech.*, vol. 502, pp. 99–126, Mar. 2004.

[151] J. M. LOPEZ and F. MARQUES, "Mode competition between rotating waves in a swirling flow with reflection symmetry," *J. Fluid Mech.*, vol. 507, pp. 265–288, May 2004.

[152] Lord Rayleigh, "On the Circulation of Air Observed in Kundt's Tubes, and on Some Allied Acoustical Problems," *Philosophical Transactions of the Royal Society of London*, vol. 175. Royal Society, pp. 1–21, 1884.

[153] FARADAY and M., "On the forms and states assumed by fluids in contact with vibrating elastic surfaces," *Philos. Trans. R. Soc. London*, vol. 121, pp. 39–346, 1831.

[154] J. Rayleigh, *The theory of sound*, vol. 1. New: Dover, 1945.

[155] S. Taylor, "IV. Experiments on the colours shown by thin liquid films under the action of sonorous vibrations," *Proc. R. Soc. London*, vol. 27, no. 185–189, pp. 71–76, Jan. 1878.

[156] J. M. VEGA, F. J. HIGUERA, and P. D. WEIDMAN, "Quasi-steady vortical structures in vertically vibrating soap films," *J. Fluid Mech.*, vol. 372, p. S0022112098002225, Oct. 1998.

[157] H. Schlichting, "Berechnung ebener periodischer Grenzschichtströmungen," *Phys. Zeit*, vol. 33, p. 327, 1932.

[158] H. Schlichting, *Boundary-Layer Theory*. New York: McGraw-Hill, 1968.

[159] M. S. Longuet-Higgins, "Mass Transport in Water Waves," *Philos. Trans. R. Soc. A Math. Phys. Eng. Sci.*, vol. 245, no. 903, pp. 535–581, Mar. 1953.

[160] S. J. Lighthill, "Acoustic streaming," *J. Sound Vib.*, vol. 61, no. 3, pp. 391–418, Dec. 1978.

[161] N. Riley, "Steady streaming," *Annu. Rev. Fluid Mech.*, vol. 33, no. 1, pp. 43–65, Jan. 2001.

[162] N. Padmanabhan and T. J. Pedley, "Three-dimensional steady streaming in a uniform tube with an oscillating elliptical cross-section," *J. Fluid Mech.*, vol. 178, no. 1, p. 325, May 1987.

[163] J. Lighthill, "Acoustic streaming in the ear itself," *J. Fluid Mech.*, vol. 239, no. 1, p. 551, Jun. 1992.

[164] N. Riley, "Acoustic streaming about a cylinder in orthogonal beams," *J. Fluid Mech.*, vol. 242, no. 1, p. 387, Sep. 1992.

[165] B. Yan, D. B. Ingham, and B. R. Morton, "Streaming flow induced by an oscillating cascade of circular cylinders," *J. Fluid Mech.*, vol. 252, no. 1, p. 147, Jul. 1993.

[166] B. Moudjed, V. Botton, D. Henry, H. Ben Hadid, and J.-P. Garandet, "Scaling and dimensional analysis of acoustic streaming jets," *Phys. Fluids*, vol. 26, no. 9, p. 093602, Sep. 2014.

[167] M. S. Longuet-Higgins, "Viscous streaming from an oscillating spherical bubble," *Proc. R. Soc. London. Ser. A Math. Phys. Eng. Sci.*, vol. 454, no. 1970, pp. 725–742, Feb. 1998.

[168] M. Kubota and M. Kubota, "A Mechanism for the Accumulation of Floating Marine Debris North of Hawaii," *J. Phys. Oceanogr.*, vol. 24, no. 5, pp. 1059–1064, May 1994.

[169] A. D. D. Craik, *Wave interactions and fluid flows*. Cambridge: Cambridge University Press, 1988.

[170] A. D. D. Craik, "The drift velocity of water waves," *J. Fluid Mech.*, vol. 116, no. 1, p. 187, Mar. 1982.

[171] A.-K. Liu and S. H. Davis, "Viscous attenuation of mean drift in water waves," *J. Fluid Mech.*, vol. 81, no. 01, p. 63, Jun. 1977.

[172] O. M. Phillips, *The Dynamics of the Upper Ocean*. Cambridge: Cambridge University Press, 1977.

[173] S. Leibovich, "On wave-current interaction theories of Langmuir circulations," *J. Fluid Mech.*, vol. 99, no. 04, p. 715, Aug. 1980.

[174] T. M. Squires and S. R. Quake, "Microfluidics: Fluid physics at the nanoliter scale," *Rev. Mod. Phys.*, vol. 77, no. 3, pp. 977–1026, Oct. 2005.

[175] J. A. Nicolá, D. Rivas;, and J. M. Vega;, "The interaction of thermocapillary convection and low-frequency vibration in nearly-inviscid liquid bridges," *Zeitschrift für Angew. Math. und Phys.*, vol. 48, no. 3, p. 389, 1997.

[176] D. Lyubimov, T. Lyubimova, and B. Roux, "Mechanisms of vibrational control of heat transfer in a liquid bridge," *Int. J. Heat Mass Transf.*, vol. 40, no. 17, pp. 4031–4042, Oct. 1997.

[177] J. A. NICOLÁS, D. RIVAS, and J. M. VEGA, "On the steady streaming flow due to high-frequency vibration in nearly inviscid liquid bridges," *J. Fluid Mech.*, vol. 354, p. S0022112097007519, Jan. 1998.

[178] T. P. Lyubimova, R. V. Scuridin, A. Cröll, and P. Dold, "Influence of high frequency vibrations on fluid flow and heat transfer in a floating zone," *Cryst. Res. Technol.*, vol. 38, no. 7-8, pp. 635–653, Jul. 2003.

[179] Q. Wan, T. Wu, J. Chastain, W. L. Roberts, A. V. Kuznetsov, and P. I. Ro, "Streaming in a narrow channel established by a vibrating piezoelectric bimorph," *Flow Turbul. Combust*, vol. 74, p. 195, Jan. 2005.

[180] C. Martel, E. Knobloch, and J. M. Vega, "Dynamics of counterpropagating waves in parametrically forced systems," *Phys. D Nonlinear Phenom.*, vol. 137, no. 1–2, pp. 94–123, Mar. 2000.

[181] M. Higuera, J. A. Nicolás, and J. M. Vega, "Weakly nonlinear nonaxisymmetric oscillations of capillary bridges at small viscosity," *Phys. Fluids*, vol. 14, no. 9, pp. 3251–3271, Sep.

2002.

[182] E. MARTÍN, C. MARTEL, and J. M. VEGA, "Drift instability of standing Faraday waves," *J. Fluid Mech.*, vol. 467, pp. 57–79, Sep. 2002.

[183] Higuera, Vega, and Knobloch, "Coupled Amplitude-Streaming Flow Equations for Nearly Inviscid Faraday Waves in Small Aspect Ratio Containers," *J. Nonlinear Sci.*, vol. 12, no. 5, pp. 505–551, Oct. 2002.

[184] M. Higuera, E. Knobloch, and J. M. Vega, "Dynamics of nearly inviscid Faraday waves in almost circular containers," *Phys. D Nonlinear Phenom.*, vol. 201, no. 1–2, pp. 83–120, Feb. 2005.

[185] M. C. Cross and P. C. Hohenberg, "Pattern formation outside of equilibrium," *Rev. Mod. Phys.*, vol. 65, no. 3, pp. 851–1112, Jul. 1993.

[186] E. MARTÍN and J. M. VEGA, "The effect of surface contamination on the drift instability of standing Faraday waves," *J. Fluid Mech.*, vol. 546, no. 1, p. 203, Dec. 2005.

[187] S. Douady, S. Fauve, and O. Thual, "Oscillatory Phase Modulation of Parametrically Forced Surface Waves," *Europhys. Lett.*, vol. 10, no. 4, pp. 309–315, Oct. 1989.

[188] S. L. Strickland, M. Shearer, and K. E. Daniels, "Spatiotemporal measurement of surfactant distribution on gravity–capillary waves," *J. Fluid Mech.*, vol. 777, pp. 523–543, Aug. 2015.

[189] N. Périnet, P. Gutiérrez, H. Urra, N. Mujica, and L. Gordillo, "Streaming patterns in Faraday waves," *J. Fluid Mech.*, vol. 819, pp. 285–310, May 2017.

[190] H. Punzmann, N. Francois, H. Xia, G. Falkovich, and M. Shats, "Generation and reversal of surface flows by propagating waves," *Nat. Phys.*, vol. 10, no. 9, pp. 658–663, Sep. 2014.

[191] M. A. Herrada, J. M. Montanero, and J. M. Vega, "The effect of surface shear viscosity on the damping of oscillations in millimetric liquid bridges," *Phys. Fluids*, vol. 23, no. 8, p. 082102, Aug. 2011.

[192] A. Ponce-Torres, M. A. Herrada, J. M. Montanero, and J. M. Vega, "Linear and nonlinear dynamics of an insoluble surfactant-laden liquid bridge," *Phys. Fluids*, vol. 28, no. 11, p. 112103, Nov. 2016.

[193] J. A. NicoláS and J. M. Vega, "Weakly nonlinear oscillations of nearly inviscid axisymmetric liquid bridges," *J. Fluid Mech.*, vol. 328, no. 1, p. 95, Dec. 1996.

[194] D. V. Lyubimov, T. P. Lyubimova, R. V. Skuridin, G. Chen, and B. Roux, "Numerical investigation of meniscus deformation and flow in an isothermal liquid bridge subject to high-frequency vibrations under zero gravity conditions," *Comput. Fluids*, vol. 31, no. 4–7, pp. 663–682, May 2002.

[195] Y.-M. Tricot, "Surfactants: Static and Dynamic Surface Tension," in *Liquid Film Coating*, Dordrecht: Springer Netherlands, 1997, pp. 99–136.

[196] G. G. Stokes, "On the theory of oscillatory waves," *Trans. Cambridge Phil. Soc*, vol. 8, p. 441, 1847.

[197] C. Ferrera, M. G. Cabezas, and J. M. Montanero, "An experimental analysis of the linear vibration of axisymmetric liquid bridges," *Phys. Fluids*, vol. 18, no. 8, p. 082105, Aug. 2006.

[198] R. Velten, D. Schwabe, and A. Scharmann, "The periodic instability of thermocapillary convection in cylindrical liquid bridges," *Phys. Fluids A Fluid Dyn.*, vol. 3, no. 2, pp. 267–279, Feb. 1991.

[199] D. Schwabe, A. I. Mizev, M. Udhayasankar, and S. Tanaka, "Formation of dynamic particle accumulation structures in oscillatory thermocapillary flow in liquid bridges," *Phys. Fluids*, vol. 19, no. 7, p. 072102, Jul. 2007.

[200] V. M. Shevtsova, D. E. Melnikov, and J. C. Legros, "Three-dimensional simulations of hydrodynamic instability in liquid bridges: Influence of temperature-dependent viscosity," *Phys. Fluids*, vol. 13, no. 10, pp. 2851–2865, Oct. 2001.

[201] Y. Kamotani, S. Matsumoto, and S. Yoda, "Recent Developments in Oscillatory Marangoni Convection," 2007.

[202] Y. Kamotani, L. Wang, S. Hatta, A. Wang, and S. Yoda, "Free surface heat loss effect on oscillatory thermocapillary flow in liquid bridges of high Prandtl number fluids," *Int. J. Heat Mass Transf.*, vol. 46, no. 17, pp. 3211–3220, Aug. 2003.

[203] H. C. Kuhlmann and C. Nienhüser, "Dynamic free-surface deformations in thermocapillary liquid bridges," *Fluid Dyn. Res.*, vol. 31, no. 2, pp. 103–127, Aug. 2002.

[204] X. Li, K. Nishino, and S. Yoda, "Temporal speckle pattern interferometry for measuring micron-order surface motion of a liquid bridge," *Meas. Sci. Technol.*, vol. 15, no. 11, pp. 2284–2294, Nov. 2004.

[205] J. M. Montanero, C. Ferrera, and V. M. Shevtsova, "Experimental study of the free surface deformation due to thermal convection in liquid bridges," *Exp. Fluids*, vol. 45, no. 6, pp. 1087–1101, Dec. 2008.

[206] C. Ferrera, J. M. Montanero, A. Mialdun, V. M. Shevtsova, and M. G. Cabezas, "A new experimental technique for measuring the dynamical free surface deformation in liquid bridges due to thermal convection," *Meas. Sci. Technol.*, vol. 19, no. 1, p. 015410, Jan. 2008.

[207] T. Yano *et al.*, "Report on Microgravity Experiments of Dynamic Surface Deformation Effects on Marangoni Instability in High-Prandtl-Number Liquid Bridges," *Microgravity Sci. Technol.*, vol. 30, no. 5, pp. 599–610, Oct. 2018.

[208] C. Ferrera, M. A. Herrada, and J. M. Montanero, "Analysis of a resonance liquid bridge oscillation on board of the International Space Station," *Eur. J. Mech. - B/Fluids*, vol. 57, pp. 15–21, May 2016.

[209] X. Zhou and X. Huai, "Free Surface Deformation of Thermo-Solutocapillary Convection in Axisymmetric Liquid Bridge," *Microgravity Sci. Technol.*, vol. 27, no. 1, pp. 39–47, Feb. 2015.

[210] S. Yang, R. Liang, and J. He, "Oscillating characteristic of free surface from stability to instability of thermocapillary convection for high Prandtl number fluids," *Int. J. Heat Fluid Flow*, vol. 61, pp. 298–308, Oct. 2016.

[211] M. A. Herrada, J. M. López-Herrera, E. J. Vega, and J. M. Montanero, "Numerical simulation of a liquid bridge in a coaxial gas flow," *Phys. Fluids*, vol. 23, no. 1, p. 012101, Jan. 2011.

[212] T. Matsunaga, A. Mialdun, K. Nishino, and V. Shevtsova, "Measurements of gas/oil free surface deformation caused by parallel gas flow," *Phys. Fluids*, vol. 24, no. 6, p. 062101, Jun. 2012.

[213] S. Yang, R. Liang, S. Xiao, J. He, and S. Zhang, "Influence of Ambient Airflow on Free Surface Deformation and Flow Pattern Inside Liquid Bridge With Large Prandtl Number Fluid (Pr > 100) Under Gravity," *J. Heat Transfer*, vol. 139, no. 12, p. 122001, Jun. 2017.

[214] S. Yang *et al.*, "The experimental investigation on dynamic response of free surface for non-isothermal liquid bridge with the varying shear airflow," *Exp. Therm. Fluid Sci.*, vol. 98, pp. 662–673, Nov. 2018.

[215] V. Shevtsova *et al.*, "The jeremi-project on thermocapillary convection in liquid bridges. Part B: overview on impact of co-axial gas flow," *Fluid Dyn. Mater. Process. FDMP.*, vol. 10, pp. 197–240, 2005.

[216] G. P. Neitzel, K. -T. Chang, D. F. Jankowski, and H. D. Mittelmann, "Linear-stability theory

of thermocapillary convection in a model of the float-zone crystal-growth process," *Phys. Fluids A Fluid Dyn.*, vol. 5, no. 1, pp. 108–114, Jan. 1993.

[217]   H. C. Kuhlmann and H. J. Rath, "Hydrodynamic instabilities in cylindrical thermocapillary liquid bridges," *J. Fluid Mech.*, vol. 247, no. 1, p. 247, Feb. 1993.

[218]   M. Wanschura, H. C. Kuhlmann, and H. J. Rath, "Linear stability of two-dimensional combined buoyant-thermocapillary flow in cylindrical liquid bridges," *Phys. Rev. E*, vol. 55, no. 6, pp. 7036–7042, Jun. 1997.

[219]   M. Wanschura, V. M. Shevtsova, H. C. Kuhlmann, and H. J. Rath, "Convective instability mechanisms in thermocapillary liquid bridges," *Phys. Fluids*, vol. 7, no. 5, pp. 912–925, May 1995.

[220]   M. K. Ermakov and M. S. Ermakova, "Linear-stability analysis of thermocapillary convection in liquid bridges with highly deformed free surface," *J. Cryst. Growth*, vol. 266, no. 1–3, pp. 160–166, May 2004.

[221]   B. Xun, P. G. Chen, K. Li, Z. Yin, and W. R. Hu, "A linear stability analysis of large-Prandtl-number thermocapillary liquid bridges," *Adv. Sp. Res.*, vol. 41, no. 12, pp. 2094–2100, Jan. 2008.

[222]   K. Nishino, T. Yano, H. Kawamura, S. Matsumoto, I. Ueno, and M. K. Ermakov, "Instability of thermocapillary convection in long liquid bridges of high Prandtl number fluids in microgravity," *J. Cryst. Growth*, vol. 420, pp. 57–63, Jun. 2015.

[223]   L. B. S. Sumner, G. P. Neitzel, J.-P. Fontaine, and P. Dell'Aversana, "Oscillatory thermocapillary convection in liquid bridges with highly deformed free surfaces: Experiments and energy-stability analysis," *Phys. Fluids*, vol. 13, no. 1, pp. 107–120, Jan. 2001.

[224]   M. PRANGE, M. WANSCHURA, H. C. KUHLMANN, and H. J. RATH, "Linear stability of thermocapillary convection in cylindrical liquid bridges under axial magnetic fields," *J. Fluid Mech.*, vol. 394, p. S0022112099005698, Sep. 1999.